IntechOpen

Impact of Thermal Conductivity on Energy Technologies

Edited by Aamir Shahzad

IMPACT OF THERMAL CONDUCTIVITY ON ENERGY TECHNOLOGIES

Edited by **Aamir Shahzad**

Impact of Thermal Conductivity on Energy Technologies
http://dx.doi.org/10.5772/intechopen.72471
Edited by Aamir Shahzad

Contributors

Dedi ., Indah Primadona, Yang-Yuan David Chen, Ping-Chung Lee Ping-Chung, Chien Chi-Hua, Youngjae Kim, Youngjo Kang, Kazuki Morita, Yoneda Morihiro, Saim Memon, Evgeny Chuvilin, Boris Aleksandrovich Bukhanov, Viktor Cheverev, Rimma Motenko, Erika Grechishcheva, S Manjunatha, K Ganesh Kumar, B J Gireesha, Rudra Swamy N G, Venkatesh P., Krishnamurthy M.R., Gireesha B.J., Teboho Mokhena, Dickson Mubera Andala, Jeremia Shale Sefadi, Mokgaotsa Mochane, Setumo Victor Motloung, Gernot Pottlacher, Peter Pichler, Daisuke Tomida, Aamir Shahzad, Maogang He, Syed Irfan Haider Rizwi

Notice

First published in London, United Kingdom, 2018 by IntechOpen
eBook (PDF) Published by IntechOpen, 2019
IntechOpen is the global imprint of INTECHOPEN LIMITED, registered in England and Wales, registration number: 11086078, The Shard, 25th floor, 32 London Bridge Street
London, SE19SG – United Kingdom
Printed in Croatia

British Library Cataloguing-in-Publication Data
A catalogue record for this book is available from the British Library

Additional hard and PDF copies can be obtained from orders@intechopen.com

Impact of Thermal Conductivity on Energy Technologies
Edited by Aamir Shahzad

p. cm.

Print ISBN 978-1-78923-672-9

Online ISBN 978-1-78923-673-6

eBook (PDF) ISBN 978-1-83881-689-6

Meet the editor

Aamir Shahzad has over 13 years of experience in university research and teaching in Pakistan and abroad, and it is due to his continuous efforts that the thermophysical properties of materials have started to be taught at the graduate and postgraduate levels. He received his postdoctoral and doctoral degrees from the Xi'an Jiaotong University (XJTU), PR China, in Computational and Experimental Fluid Materials, in 2015 and 2012. He proposed novel methods to explore results of complex materials, which show his aptitude to comprehend computational physics, modeling and molecular simulations, and fluid materials together with the understanding of experimental materials. In addition, he is also working in the field of computational semiconductors, fluids/plasmas, solar materials, battery/ionic materials, and energy materials.

Contents

Preface

This edition of our book on thermal conductivity is geared specifically to the needs and background of research students. In reviewing different comments, we have made modifications in some parts of the book to enhance reader understanding of the material. This book focuses on the thermal properties in different materials using novel experimental and computational methods and discloses the exact nature and origin of different approaches of systems. New methods for investigating thermal properties in various devices are required for improving device design and for understanding device physics and technology. Such methods are also required for studying new thermal phenomena in micro- to nano-scale devices made up of novel nanostructures, such as carbon electronics or semiconductor nanowires, nanometer size sensors to detect proteins or single DNA and nanolevel fluidic flow, nanopowder production, nanocrystalline solar cells, and polymer coatings with embedded nano particles. Thermal conductivity, heat process, and their nonlinear effects (non-Newtonian behaviors) are the basic elements of the transport property of complex liquids and are applied for studying their flow, heat, and mass transfer characteristics. Among the changes we have made in this edition are the following. In the first section "Thermal Conductivity of Complex Systems," we have explained the discussion of the thermal conductivity of complex dusty plasma system and discussed the thermal conductivity of non-Newtonian fluid with particle suspension, ionic fluids, and synthetic and regenerated fiber assemblies. In the second section "Thermal Conductivity of Solid and Fluid Systems," we have incorporated material on liquid metals, molten systems at high temperatures, hydrate-bearing porous sediments, and vacuum glazing systems. In the third section "Thermal Conductivity of Nano Systems," we explained the structural and thermoelectric properties of single crystalline nanowire, nonlinear heat transfer of nano particles, and graphite-based polymer.

I hope this book will fulfill all the needs of the research students of different universities and institutions.

Dr. Aamir Shahzad
Assistant Professor
Molecular Modeling and Simulation Laboratory,
Department of Physics
Government College University Faisalabad
Pakistan

Section 1

Thermal Conductivity of Complex Systems

Chapter 1

Introductory Chapter: A Novel Approach to Compute Thermal Conductivity of Complex System

Aamir Shahzad, Syed Irfan Haider, Maogang He and Yan Feng

Additional information is available at the end of the chapter

http://dx.doi.org/10.5772/intechopen.75367

1. Introduction

Thermophysical properties of complex fluids materials (dusty plasmas) have been very actively investigated both experimentally and by computer simulations. These properties describe the physical and chemical behavior of material that remains in terms of fluids formation. Among all of the properties, thermal conductivity is most important; it is an intrinsic property of fluid materials. It is a difficult property from computational point of view because it is sensitive to the internal energy of the system. Its molecular-level observations are becoming more important in dusty plasmas. Dust is abundant in nature. Dust particles coexist in plasmas and then form a complex dusty plasma. Dusty plasmas are ionized gases that contain particulates of condensed matter. Dusty plasmas are of interest as a non-Hamiltonian system of interacting particles and as a means to study generic fundamental physics of self-organization, pattern formation, phase transitions, and scaling. Their discovery has therefore opened new ways of precision investigations in many-particle physics.

2. Dusty plasmas

Dusty plasmas are ionized gases that contain particulates of condensed matter. These particles have different sizes ranging from tens of nanometers to hundreds of microns. The dynamics of these massive charged particles happens at slower timescales than the ordinary plasma ions because charge to mass ratio (e/m) is orders of magnitude smaller that the corresponding (e/m) of either the electrons or ions. They may be in the shape of rods, irregularly shaped pancakes or

spheres. They are made up of dielectric, e.g., SiO_2 *or* Al_2O_3, or conducting materials. Even though the particles are normally solid, they might also be liquid droplets or fluffy ice crystals [1].

3. History of dusty plasmas

Despite almost a century–long history—the first observations of dust in discharges have been reported by Langmuir in 1924. After that, Lyman Spitzer along with Hannes Alfven recognized that dust in the universe was not merely a hindrance to optical observation, but that it was an essential component of the universe. One of the most exciting events in the field of dusty plasmas occurred in early 1980 during the *Voyager 2* flyby of planet Saturn. In 2005, *Cassini* spacecraft took new and improved images of spokes with detail that would provide a better understanding of their origin. In 1992, the European spacecraft *Ulysses* flew by the planet Jupiter and detected the dust particles and measured their masses and impact speed. The current enormous interest in complex plasmas started in the mid-1980s, triggered by laboratory investigation of thermal conductivity of dusty plasmas [2].

4. Types of dusty plasmas

4.1. Weakly vs. strongly coupled dusty plasmas

The vital attention in the investigation of dusty plasmas is whether the particles are in the weakly or strongly coupled state. The description as weakly or strongly coupled denotes the subject of whether the particles average potential energy, due to nearest neighbor interactions, are smaller or larger than their average thermal energy. Coulomb coupling parameter, Γ is defined as the ratio of the interparticle Coulomb potential energy to the (thermal) kinetic energy of the particles:

$$\Gamma = \frac{q^2}{rT} exp\left(\frac{-r}{\lambda_D}\right) \tag{1}$$

where $r = (3/4\pi n)^{1/3}$ is the average interparticle spacing [3].

5. Dusty plasma physics

The brief discussion of the basic principles of dusty plasma physics is given in the following sections.

5.1. Debye shielding

The Debye length is an important physical parameter in a plasma. It provides the distance over which the influence of the electric field of an individual charged particle is felt by other charged particles (such as ions) inside the plasma. The charged particles actually rearrange

themselves in order to shield all electrostatic fields within a Debye distance. In dusty plasmas, the Debye length can be defined as follows [4].

$$\lambda_D = \frac{\lambda_{De}.\lambda_{Di}}{\sqrt{\lambda_{De}^2 + \lambda_{Di}^2}} \tag{2}$$

where $\lambda_{De} = \sqrt{KT_e}/4\pi n_e e^2$ and $\lambda_{Di} = \sqrt{KT_i}/4\pi n_i e^2$ are the Debye lengths associated to electrons and ions, respectively.

5.2. Macroscopic neutrality

Dusty plasmas are characterized as a low-temperature ionized gas whose constituents are electrons, ions, and micron-sized dust particulates. The presence of dust particles (grains) changes the plasma parameters and affects the collective processes in such plasma systems. In particular, the charged dust grains can effectively collect electrons and ions from the background plasma. Thus, in the state of equilibrium, the electron and ion densities are determined by the neutrality condition [5], which is given by

$$en_{i0} - en_{e0} + qn_{d0} = 0 \tag{3}$$

5.3. Inter-grain spacing

In a multicomponent dusty plasma, inter-grain spacing is very important to distinguish between dust in plasma and dusty plasma. Like the dust grain radius, b the inter-grain spacing, r is usually much smaller than the Debye length λ_D. For dust in plasma, $r > \lambda_D$ and the dust particles are completely isolated from their neighbors. For dusty plasmas, $r \leq \lambda_D$ and the dust particles can be considered as massive point particles like multiple-charged negative (or positive) ions in a multispecies plasma where the effect of neighboring particles can be significant.

5.4. Coulomb coupling parameter

Charged dust grains can be either weakly or strong correlated depending on the strength of the Coulomb coupling parameter Eq. (1). When $\Gamma >> 1$, the dust is strongly coupled and this condition is met in several laboratory dusty plasmas, such as dust "plasma crystals". When the dust is weakly coupled, the dispersion relation of waves is not affected by the spatial correlation of the dust grains. A dusty plasma is considered as weakly coupled if $\Gamma << 1$ [6].

5.5. Lattice parameter

In the case of Yukawa interaction, additional screening parameter becomes necessary

$$\kappa = \frac{a_{ws}}{\lambda_D} \tag{4}$$

It is how much effective and protective the shielding out behavior of a single specie against the external or internal stimuli (voltages) that affect inside the plasmas. a_{ws} is the Wigner-Seitz radius which can be estimated as $a_{ws} = (4\pi n/3)^{-1/3}$ [7].

6. The forces on a dust grain in a plasma

The knowledge about various forces acting on dust particles in a plasma is necessary for an understanding of their dynamics and transport.

6.1. Force of gravity, F_g

The dust particle is subject to gravity with a force that is proportional to its mass, but under microgravity condition, it is ignored.

$$\boldsymbol{F}_g = m\boldsymbol{g} = \frac{4}{3}\pi b^3 \rho \boldsymbol{g} \tag{5}$$

where $\boldsymbol{g}$ is the local acceleration due to gravity and ρ is the mass density of the particle [8].

6.2. The electric force, F_e

At a location in the plasma having an electric field $\boldsymbol{E}$, the electric force acting on dust particles of charge q is

$$\boldsymbol{F}_e = q\boldsymbol{E} \tag{6}$$

The electric field is smaller in the bulk of the plasma while it is larger in sheaths next to the plasma wall boundary.

6.3. Neutral drag force, F_n

This force is produced from collisions with the background neutral gas atoms or molecules, and is proportional to the neutral pressure in the vacuum chamber. $\boldsymbol{F}_n$ is given as

$$\boldsymbol{F}_n = Nm_n v^2{}_n \pi b^2 \tag{7}$$

where N is the neutral density, m_n is the mass of the neutral atoms (or molecules), and v_n is the average relative velocity [1].

6.4. Thermophoretic force, F_{th}

This force will be produced due to the temperature gradient in the neutral gas in the plasma, and it's direction is opposite to temperature gradient. This force is given approximately by

$$\boldsymbol{F}_{th} = \frac{16\sqrt{\pi}}{15}\frac{b^2 k_T}{v_{T,n}} \nabla T_n \tag{8}$$

where, $v_{T,n}$ is the thermal speed of the neutral gas, k_T is the translational part of the thermal conductivity, and T_n is the temperature of the neutrals [9].

7. Transport properties

7.1. Diffusion coefficient

The diffusion coefficient is the proportionality constant between molar fluxes which is $J_A = -D\Delta C_A$, where Δ is known as gradient operator, D is known as diffusion coefficient ($m^2.\ s^{-1}$), and C_A is the concentration ($mole/m^3$). In the complex (dusty) plasma, the mass, momentum, and energy are transported through dust particles.

7.2. Shear viscosity

Shear viscosity is the measure of force between different layers of fluid. It is the dynamical property of a material such as liquid, solids, gas and dusty plasmas. For liquid, it is familiar thickness, for example, honey and water have different viscosity. The ideal fluid has no resistance between layers in shear stress. The superfluid has zero viscosity at very low temperature. All other liquids have positive viscosity and are said to be viscous.

7.3. Thermal conductivity

The most vital property of the dusty plasma liquids (DPLs) is thermal conductivity and it is due to the internal energy of the molecules. The energy transference of the DPLs and its dependence on the applied external field can be checked by the thermal conductivity. The complete analysis of it is important and necessary for the designing and manufacturing of numerous heat flow devices. The applications in thermo-electronic devices e.g., in semiconductor systems, the phonon thermal conductivity has got a special attention. Due to the atoms' oscillations, phonons of different wavelengths and frequencies are created in solids, and these phonons would disappear when the oscillations stop. Especially, nanotechnology (nanomaterials) requires the accurate calculation of heat transport features [10, 11]. Molecular simulation is recognized as substantial for micro- and nano-scale heat transport phenomena. Furthermore, the new advances require the complete explanations of phase change and the heat, mass transport in micrometer to nanometer scale regimes.

8. Applications

8.1. Dust is a good thing

In the present era, scientists do not consider the dust as an undesirable pollutant; interestingly its positive impacts lead in manufacturing, designing of new devices and direct new developments in material science. In the plasma-chemical mechanism, fine dust particles are also important and having useful properties related to their size and composition. A few of the applications are given below:

1. The efficiency and lifetime of silicon solar cell was increased by the incorporation of amorphous hydrogenated silicon particles (*a-Si:H*) with the nanocrystalline silicon particles which grow in silane plasmas.
2. Thin films of *TiN* in an amorphous Si_3N_4 matrix prepared by PECVD (plasma enhanced chemical vapor deposition) have enormously high hardness and elastic modulus. A thin film coating is applied to materials to improve surface properties.
3. Diamond whiskers made up by etching in radio frequency (*rf*) plasmas improve electron field emission. The reactive ion etching process used in *rf* plasma devices effectively sharpen the micro tips of diamond [12].

8.2. Dust in plasma processing devices (dust is a bad thing)

At first, it was presumed that the semiconductor surfaces were contaminated during handling of the wafers. To lighten the problem, all fabrication steps were done in clean rooms. Yet even with the best state-of-the art clean rooms, semiconductor wafers showed evidence of contamination. It drove out that the surfaces were being soiled by dust particles generated within the processing plasmas. Complex plasma-enhanced chemical reactions take place within these discharges that produce and grow dust particles. Several experimental devices are used to measure the presence and growth of dust particles such as transmission electron microscope (TEM), scanning electron microscope (SEM), laser light scattering etc. Also, theoretical and computational works are directed to investigate the dust formation, growth, charging, and transport.

9. Computational method

9.1. Simulation technique and parameters

Molecular mechanics dynamic simulation (MMDS) is a simplified approach as compared to other techniques. It allows study of molecular ensembles for thousands of atoms. The MMDS technique works as a core on a simple explanation of force between the individual atoms. Here, HPMD approach is implemented to determine the thermal conductivity of CDPs by applying external perturbation which is modeled by using Yukawa potential model use for the explanation of dust particles interacting with one another. Yukawa potential is used for a system of charged particles. While Green-Kubo relation applies to neutral particles,

$$\phi(|\mathbf{r}|) = \frac{q^2}{4\pi\varepsilon_0}\frac{e^{-|\mathbf{r}|/\lambda_D}}{|\mathbf{r}|}, \tag{9}$$

The plasma phase of Yukawa system is representing three dimensionless parameters [7], plasma coupling parameter $\Gamma = (q^2/4\pi\varepsilon_0)(1/a_{ws}K_BT)$, screening strength $\kappa = a_{ws}/\lambda_D$, and $\boldsymbol{F}_e(t) = (F_z)$ is external perturbation with its normalized value $F^* = F_z a_{ws}/J_{QZ}$, where J_{QZ} is thermal heat energy along *z*-axis. The inverse of plasma frequency $\omega_p = (q^2/2\pi\varepsilon_0 m a_{ws}^3)^{1/2}$ characterizes timescale. Simulations are performed for N = 400–14,400 particles in canonical ensemble with PBCs and minimum

image convention of Yukawa particles. In our case, most of the simulations are performed with $N = 400$ particles. The particles are placed in a unit cell with edge length L_x / L_y and the dimensions of square simulation cell are $L_x a_{ws} \times L_y a_{ws}$. The equations of motions for N-Yukawa dust particles are integrated through the predictor–corrector algorithm with simulation time step of $\Delta t = 0.001\omega_p^{-1}$. In our case, the conductivity calculations are reported for a wide range of plasma coupling ($1 \le \Gamma \le 100$) and screening parameters ($1 \le \kappa \le 4$) of 2D Yukawa system at constant normalized external perturbation F^*.

9.2. HNEMD model and thermal conductivity

The Green-Kubo relations (GKRs) are the mathematical terms for transport coefficients in the form of time integral correlation functions. GKR is for hydrodynamic transport coefficient of neutral particles. This formula gives linear response expression for thermal conductivity. It enables our calculations using a time-series record of motion of individual dust particles. For thermal transport coefficient, it is a time integral of the correlation function of the microscopic flux of heat energy and where the required input includes time series for position and velocity of a dust particle.

$$\lambda = \frac{1}{2 K_B A T^2} \int_0^\infty \left\langle \mathbf{J}_Q(t).\mathbf{J}_Q(0) \right\rangle dt, \tag{10}$$

where A represents the area, T denotes the absolute temperature, K_B is Boltzmann's constant. The relation of microscopic heat energy $\mathbf{J}_Q$ is

$$\mathbf{J}_Q A = \sum_{i=1}^{N} \left[\mathrm{E}_i - \frac{1}{2} \sum_{i=j} (\boldsymbol{ri} - \boldsymbol{rj}).\boldsymbol{Fij} \right].\frac{\boldsymbol{p}_i}{m}, \tag{11}$$

In this equation, $\boldsymbol{r}_{ij} = \boldsymbol{r}_i - \boldsymbol{r}_j$ is the position vector and $\boldsymbol{F}_{ij}$ is the force of interaction on particle i due to j and $\boldsymbol{p}_i$ represents the momentum vector of the i_{th} particle. The energy E_i of particle i is $\mathrm{E}_i = \boldsymbol{p}_i / 2\, m + \frac{1}{2} \Sigma\phi_{ij}$, for $i \neq j$, where ϕ_{ij} is the Yukawa pair potential given in Eq. (9) between particle i and j. According to linear response theory (LRT), the perturbed equations of motion, given by Evans-Gillan [7] is

$$\begin{aligned} \dot{\boldsymbol{r}}_i &= \frac{\boldsymbol{p}_i}{m} \\ \dot{\boldsymbol{p}}_i &= \boldsymbol{F}_i + \mathbf{D}_i(\boldsymbol{r}_i, \boldsymbol{p}_i).\boldsymbol{F}_e(t) \\ \alpha &= \frac{\sum_{i=1}^{N} [\boldsymbol{F}_i + \mathbf{D}_i(\boldsymbol{r}_i, \boldsymbol{p}_i).\boldsymbol{F}_e(t)].\boldsymbol{p}_i}{\sum_{i=1}^{N} p_i^2 / m_i} \end{aligned} \tag{12}$$

The tensorial phase space distribution function $\mathbf{D}_i(\boldsymbol{r}_i, \boldsymbol{p}_i)$ describes the coupling of the system. In the generalization of LRT to a system moving according to non-Hamiltonian dynamics, the response of $\mathbf{D}_i(\boldsymbol{r}_i, \boldsymbol{p}_i)$ [13] is

$$\langle A(t) \rangle - \langle A(0) \rangle = \beta \int_0^t \left\langle A(t)\, \dot{H}_0(t') \right\rangle dt, \tag{13}$$

where $\dot{H}_0$ is the time derivative of the total energy with respect to field-dependent equation of motion [7] and average brackets denote the statistical average and $\beta = 1/K_B T$.

$$\langle \mathbf{J}_Q(t) \rangle = \beta A \int_0^t dt \langle \mathbf{J}_{Q_z}(t').\mathbf{J}_{Q_z}(0) \rangle . \boldsymbol{F}_e(t), \tag{14}$$

When external force is selected parallel to the z-axis $\boldsymbol{F}_e(t) = \boldsymbol{\delta}\ (0, F_z)$, $\boldsymbol{\delta}$ is Dirac delta function. Due to this function, the response of heat energy current is proportional to autocorrelation function itself rather than time integral of this function [14]. The reduced thermal conductivity has the following form:

$$\lambda = \frac{1}{ATF_Z} \int_0^\infty \langle \mathbf{J}_{Q_z}(t').\mathbf{J}_{Q_z}(0) \rangle \, dt, \tag{15}$$

Eq. (15) is the basic formula for evaluation of autocorrelation function of heat energy current by a perturbation method. Here it is important to discuss some other factors that are in association with the thermal conductivity i.e., Ewald sum. It is used to measure force, Yukawa potential energy, heat energy current (GKR). In this scheme, original interaction potential is divided into two parts: the long-range part that converges quickly in reciprocal space, a short-range interaction that converges quickly in the real-space part of Ewald-Yukawa potential [15].

10. HNEMD results and discussion

In this section, the thermal conductivity calculations are obtained through homogenous perturbed MD (HPMD) simulations, using Eq. (15), for 2D complex dusty plasma systems. The thermal conductivity is compared here with appropriate frequency normalization in the limit of a suitable equilibrium low value of normalized external perturbation, for an absolute range of plasma coupling ($\Gamma \geq 1$) and screening strength ($\kappa \geq 1$). For 2D case, the thermal conductivity of complex dusty plasmas may be represented as $\lambda_0 = \lambda/nm\omega_p a_{ws}^2$ (normalized by plasma frequency) or $\lambda^* = \lambda/nm\omega_E a_{ws}^2$ (normalized by plasma frequency). This improved HPMD approach to 2D strongly coupled plasmas enables it possible to compute all the possible range of plasma states (Γ, κ) at a constant value of normalized perturbation $F^* = (F_z a_{ws}/J_{QZ})$. In our case, the possible low value of external perturbation is $F^* = 0.02$ at which 2D complex plasma system gives equilibrium thermal conductivity for all plasma state points. Before the external perturbation F^* is switched on, the system is equilibrated using the Gaussian thermostat which generates the canonical ensemble given in Eq. (12). In practice, it is necessary for the MD system to be thermostated for the removal of additional heat that is generated due to work done by the external perturbation F^* [16]. The results obtained through present HPMD approach are shown in **Figures 1–4**, where we have traced the plasma thermal conductivity through a computation of usual Yukawa particles in 2D within the strongly coupled regime for different screening parameters of $\kappa = 1$, 2, 3, and 4, respectively.

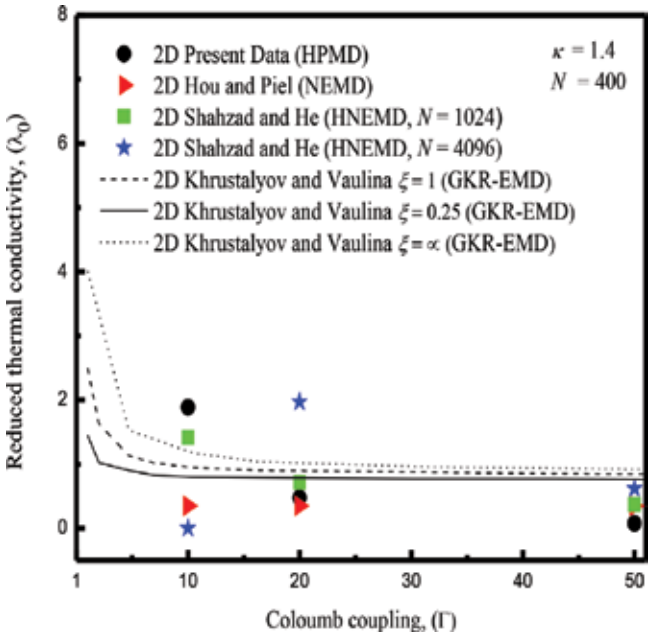

Figure 1. Comparison of results obtained from Yukawa thermal conductivity λ_0 (normalized by ω_p) as a function of plasma coupling Γ ($1 \leq \Gamma \leq 50$) (system temperature) for SCCDPs at $\kappa = 1.4$.

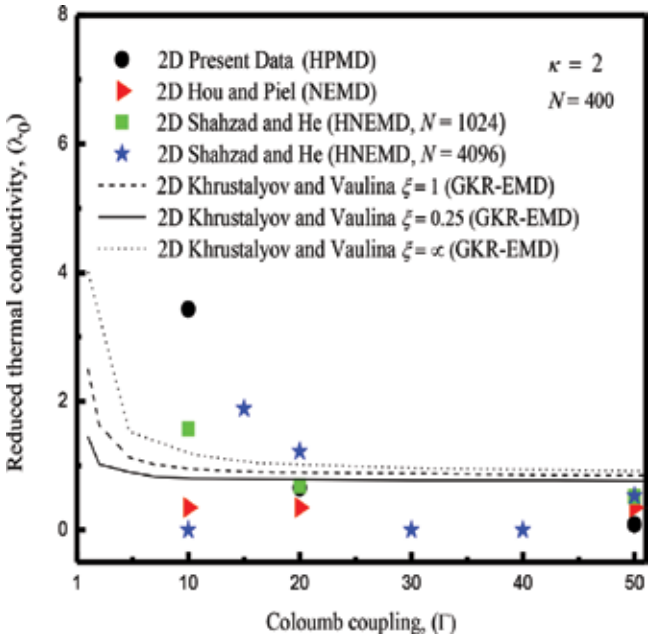

Figure 2. Comparison of results obtained from Yukawa thermal conductivity λ_0 (normalized by ω_p) as a function of plasma coupling Γ ($1 \leq \Gamma \leq 50$) (system temperature) for SCCDPs at $\kappa = 2$.

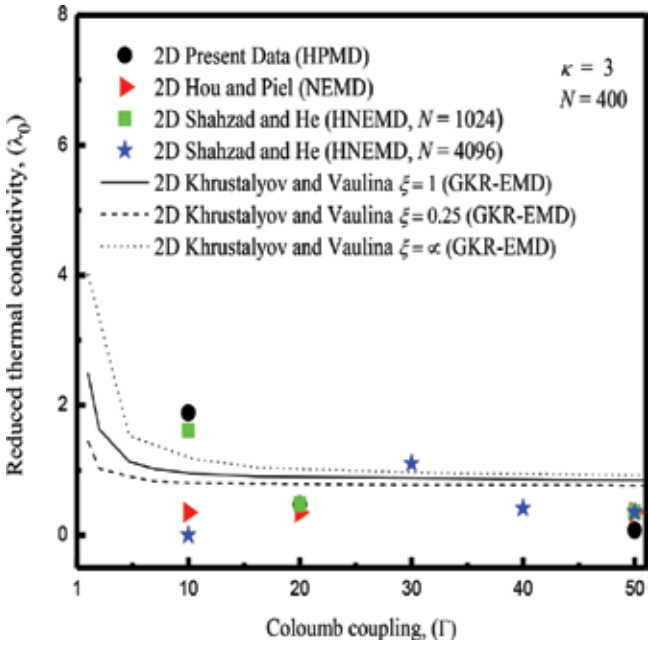

Figure 3. Comparison of results obtained from Yukawa thermal conductivity λ_0 (normalized by ω_p) as a function of plasma coupling Γ ($1 \leq \Gamma \leq 50$) (system temperature) for SCCDPs at $\kappa = 3$.

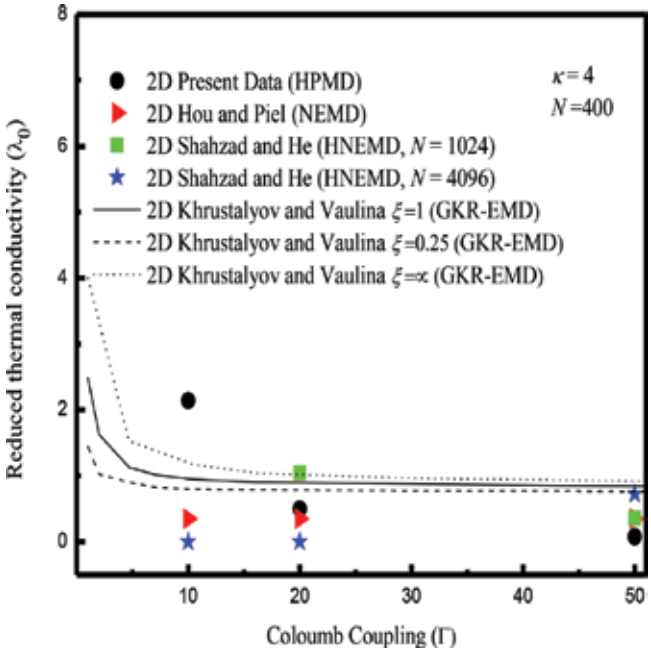

Figure 4. Comparison of results obtained from Yukawa thermal conductivity λ_0 (normalized by ω_p) as a function of plasma coupling Γ ($1 \leq \Gamma \leq 50$) (system temperature) for SCCDPs at $\kappa = 4$.

Figures 1 and **2** show the thermal conductivity for the cases of κ = 1.4 and 2, respectively. For both cases, our simulations cover the appropriate range of Coulomb coupling parameter i.e., from the nearly liquid state to strongly coupled states. It is observed that our investigation of λ_0 at low value of Γ (= 10) is definitely higher than that of GKR-EMD estimations of Khrustalyov and Vaulina [17] and NEMD of Hou and Piel [18] but for κ = 1.4 results are slightly higher than HNMED (N = 1024) simulations of Shahzad and He [19]. It is noted that our result for the low value of Γ shows that particle–particle interactions are very weak and particles have maximum kinetic energy and the effectiveness of screening parameter is large. At intermediate to higher Γ (= 20, 50), the present results lie closer to earlier 2D NEMD simulations [18] and HNMED (N = 4096) computations [19] but slightly less than 2D dissipative Yukawa GKR-EMD numerical results [17]. For both cases, it can be seen that the presented λ_0 is well matched with earlier 2D numerical estimations [19] at intermediate Γ (= 20). It is significant to note that a constant λ_0 is observed at intermediate to higher plasma coupling Γ at constant external perturbation F^* = 0.02; however, it is observed that a very slightly decreasing behavior is observed at higher Γ, contrary to earlier simulations of Shahzad and He [19]. But it is examined that a constant λ_0 is found at intermediate to higher Γ at constant F^*.

Two further set of simulations is plotted to illustrate the plasma λ_0 behaviors of the simulated complex dusty plasmas at a higher value of screening. For this case, **Figures 3** and **4** show the normalized λ_0 computed by the HPMD approach for N = 400 at κ = 3 and 4 and a sequence of different simulations are performed. It is characterized by these figures that the present results lie close to the earlier 2D NEMD results of Hou and Piel [18] at intermediate to higher Γ (= 20, 50). For the κ = 3 at a lower value of Γ, our simulation result is slightly higher than earlier HNMED simulation result, however, for both cases at a lower value of Γ, it is definitely higher than earlier numerical results of NEMD, GKR-EMD.

11. Conclusions

The improved Evan-Gillan HPMD method is used to investigate the thermal conductivity of the 2D strongly coupled complex Yukawa liquid for a suitable range of plasma parameters of screening lengths κ (=1, 4) and Coulomb couplings Γ (=1, 100). Nonequilibrium molecular dynamics method uses the thermal response of heat energy current to calculate the preliminary results of plasma thermal conductivity. The presented method is better than earlier HNEMD and NEMD methods because the very small value of external perturbation (F^* = 0.02) is only imposed on several individual particles each time step. It is concluded that the present approach for evaluating the thermal conductivity from homogenous PMD method yields consistent results and this method is quite accurate and much faster than the previous EMD and NEMD methods. For future work, the system size (N) and external perturbation strength (F^*) can be varied to examine how effectively this improved HPMD algorithm calculates the thermal conductivities of Yukawa and other Coulomb systems. It is suggested that the presented HPMD technique based on Ewald summation described here can be used to explore the ionic and dipolar materials.

Acknowledgements

The authors thank the National Advanced Computing Centre of National Centre for Physics (NCP), Pakistan and National High-Performance Computing Center (NHPCC) of Xian Jiaotong University, P.R. China for allocating computer time to test and run our MD code.

Abbreviations

SCCDPs	strongly coupled complex dusty plasmas
EMD	equilibrium molecular dynamics
HNEMD	homogeneous nonequilibrium molecular dynamics
HPMD	homogeneous perturbed molecular dynamics
MMDS	molecular mechanics dynamic simulation
DPLs	dusty plasma liquids
LRT	linear response theory
GKR	Green-Kubo relation
CDPs	complex dusty plasma
PBCS	periodic boundary conditions
Γ	Coulomb coupling
κ	screening strength
λ_D	Debye length
K_B	Boltzmann constant

Author details

Aamir Shahzad[1,2]*, Syed Irfan Haider[1], Maogang He[2] and Yan Feng[3]

*Address all correspondence to: aamirshahzad_8@hotmail.com

1 Molecular Modeling and Simulation Laboratory, Department of Physics, Government College University Faisalabad (GCUF), Faisalabad, Pakistan

2 Key Laboratory of Thermo-Fluid Science and Engineering, Ministry of Education (MOE), Xi'an Jiaotong University, Xi'an, China

3 Center for Soft Condensed Matter Physics and Interdisciplinary Research, College of Physics, Optoelectronics and Energy, Soochow University, Suzhou, China

References

[1] Shukla PK, Mamun AA. Series in Plasma Physics: Introduction to Dusty Plasma Physics. Bristol: Taylor & Francis group, CRC Press; 2001; ISBN: 9780750306539 – CAT#IP39

[2] Merlino RL. Dusty Plasmas and Applications in Space and Industry. Plasma Physics Applied. 2006; ISBN: 81-7895-230-0

[3] Bellan PM. Fundamentals of Plasma Physics. 1st ed. UK: Cambridge University Press; 2008. ISBN-13: 9780521528009

[4] Shukla PK. Dusty Plasmas: Physics, Chemistry and Technological Impacts in Plasma Processing. In: Bouchoule A. Wiley, New York. 2000; ISBN: 0471973866

[5] Chen FF. Introduction to Plasma Physics and Controlled Fusion. 2nd ed. New York: Springer-Verlag. 2006; 200 p. ISBN: 9780521825689

[6] Thomas H, Morfill GE, Demmel V, Goree J, Feuerbacher B, Möhlmann D. Plasma crystal: Coulomb crystallization in a dusty plasma. Physical Review Letters. 1994;**73**(5):652. DOI: 0031-9007/94

[7] Shahzad A, He M-G. Thermal conductivity calculation of complex (dusty) plasmas. Physics of Plasmas. 2012;**19**(8):083707. DOI: 10.1063/1.4748526

[8] Kikuchi H. Electrohydrodynamics in Dusty and Dirty Plasmas: Gravito-Electrodynamics and EHD. Dordrecht; Boston: Kluwer Academic Publishers; 2001. 207 p. ISBN: 0792368223

[9] Peratt AL. Physics of the Plasma Universe, Appendix C. Dusty and Grain Plasmas. New York: Springer; 1992. ISBN: 0-387-97575-6

[10] Boulos MI, Fauchais P, Pfender E. Thermal Plasmas: Fundamentals and Applications. New York: Springer Science & Business Media; 2013. DOI: 10.1007/978-1-1337-1

[11] Shahzad A, He M-G. Thermal Conductivity and Non-Newtonian Behavior of Complex Plasma Liquids, A Chapter from the Book of Thermoelectrics for Power Generation—A Look at Trends in the Technology. Ri jeka, Croatia: InTech; 2016; 305 p. DOI: 10.5772/65563

[12] Vladimir EF, Gregor EM. Complex and Dusty Plasmas: From Laboratory to Space. Bosa Roca, Uni ted States: Taylor & Francis Inc, CRC Press Inc.; 2010; ISBN-10: 1420083112/ ISBN-13: 9781420083118

[13] Faussurier G, Murillo MS. Gibbs-Bogolyubov inequality and transport properties for strongly coupled Yukawa fluids. Physical Review E. 2003;**67**(4):046404. DOI: 10.1103/ PhysRevE.85.046405

[14] Gillan MJ, Dixon M. The calculation of thermal conductivities by perturbed molecular dynamics simulation. Journal of Physics C: Solid State Physics. 1983;**16**(5):869. DOI: 0022-3719/83/050869

[15] Mazars M. Ewald sums for Yukawa potentials in quasi-two-dimensional systems. The Journal of Chemical Physics. 2007;**126**(5):056101. DOI: 10.1063/1.2431371

[16] Mandadapu KK, Jones RE, Papadopoulos P. A homogeneous nonequilibrium molecular dynamics method for calculating thermal conductivity with a three-body potential. The Journal of Chemical Physics. 2009;**130**(20):204106. DOI: 10.1063/1.3141982

[17] Khrustalyov YV, Vaulina OS. Numerical simulations of thermal conductivity in dissipative two-dimensional Yukawa systems. Physical Review E. 2012;**85**(4):046405. DOI: 10.1103/PhysRevE.85.046405

[18] Hou LJ, Piel A. Heat conduction in 2D strongly coupled dusty plasmas. Journal of Physics A: Mathematical and Theoretical. 2009;**42**(21):214025. DOI: 10.1088/1751-8113

[19] Shahzad A, He MG. Numerical experiment of thermal conductivity in two-dimensional Yukawa liquids. Physics of Plasmas. 2015;**22**(12):123707. DOI: 10.1063/1.4938275

Chapter 2

Thermal Conductivity of Ionic Liquids

Daisuke Tomida

Additional information is available at the end of the chapter

http://dx.doi.org/10.5772/intechopen.76559

Abstract

Ionic liquids (ILs) have attracted great attention as green solvents, heat carriers, and electrolytes. They can be obtained with specific thermophysical properties and functions by changing the kind of species of cations and anions. Knowledge of the fundamental thermophysical properties of ILs, such as their densities, viscosities, and thermal conductivities, is needed to design ILs with desirable thermophysical properties. In this chapter, we will review the various measurement results for the thermal conductivities of the pure components of ILs and methods for predicting the thermal conductivity of an IL, which are based on its structure and physical properties, by conducting correlations between these parameters. In the recent years, the thermal conductivities of IoNano fluids, which comprise of nanoparticles dispersed in an IL, have attracted great attention. Therefore, we will review the unique thermal conductivities of IoNano fluids.

Keywords: thermal conductivity, ILs, nanofluids, correlation, prediction

1. Introduction

ILs are salts that exist in the liquid at ambient temperature, and their characteristics include nonvolatility, flame retardancy, high ionic conductivity, and exhibiting a liquid state at a wide temperature range, among others. Since Wilkes et al. discovered a water-stable IL system using BF_4^-, a nonchloroaluminate anion, in 1992 [1], the study of ILs has drastically increased, and ILs have drawn great attention for a variety of applications, such as an alternative reaction solvent to replace organic solvents, as thermal medium, and as electrolyte in batteries. **Figure 1** shows the cations and anions that are typically used in ILs. There are infinite potential combinations of cations and anions and, additionally, various chemical modifications can be made to the organic moieties of the ions. Thus, there is a possibility of creating ILs tailored for specific purposes; for this reason, ILs are also called "designer solvents."

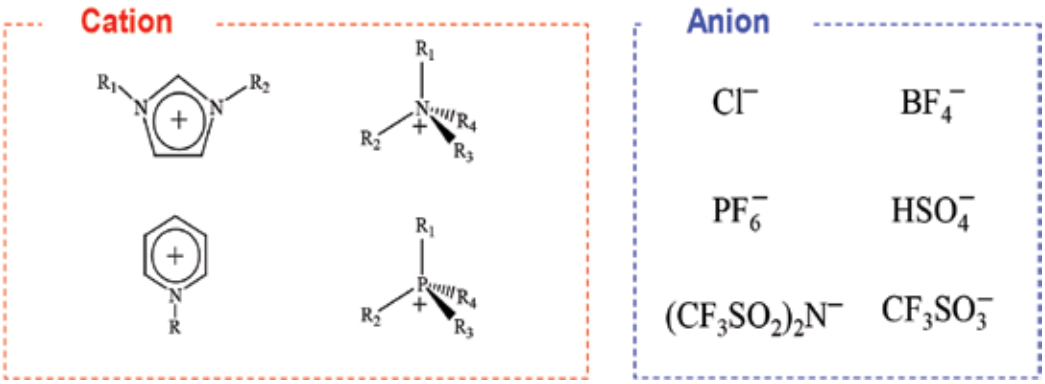

Figure 1. Cations and anions typically used in ILs.

A variety of ILs have been synthesized, many of which have melting points much greater than room temperature. For this reason, ILs are broadly defined as the ones having melting point below 100°C. Numerous ILs have been created; however, the prediction of their thermophysical properties such as the thermal conductivity on the basis of the molecular structure would be useful to develop novel ILs. In this chapter, we review the various measurement results for the thermal conductivities of the pure components of IL, the progress made toward the development of effective methods of correlating and predicting the thermal conductivities, and the thermal conductivities of IoNano fluids, which, in the recent years, have attracted great attention as high-temperature heat mediums.

2. Thermal conductivities of the pure components of ILs

2.1. Investigating the thermal conductivities of ILs

The thermal conductivity of an IL was first reported by Valkenburg et al. [2]. The known thermophysical properties of ILs, including their thermal conductivities, are summarized in ILs database of NIST [3]. During the early stages of IL research, since it was necessary to synthesize an IL to measure its thermophysical properties, there was less number of researches. However, once ILs became commercially available, the amount of information reported about the thermophysical properties of ILs increased drastically. However, the number of the reported thermal conductivity values is fewer than the other thermophysical properties, and it has been reported that two or three component systems have almost no thermal conductivity. Only four research groups have reported the thermal conductivities of binary mixtures [4–7], and only two groups have reported on ternary mixtures containing ILs [6, 8]. The reported thermal conductivity values for various ILs range from 0.106 [4] to 0.238 W/(m K) [7] at 298.15 K (**Figure 2**) and many reported values are around 0.15 W/(m K) [3, 9] (**Figure 3**). The thermal conductivities of ILs were found to be about the same as those of organic solvents, such as methanol and toluene.

http://dx.doi.org/10.5772/intechopen.76559

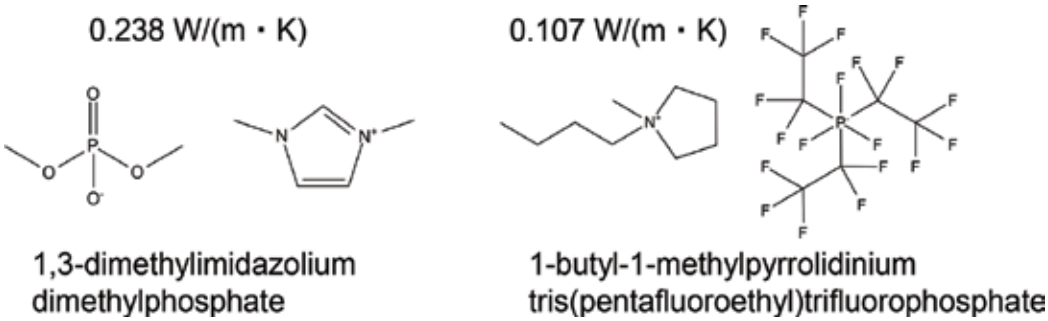

Figure 2. The ILs with the highest thermal conductivity (left) [7] and the lowest thermal conductivity (right) [4] at 298.15 K that have been reported to date.

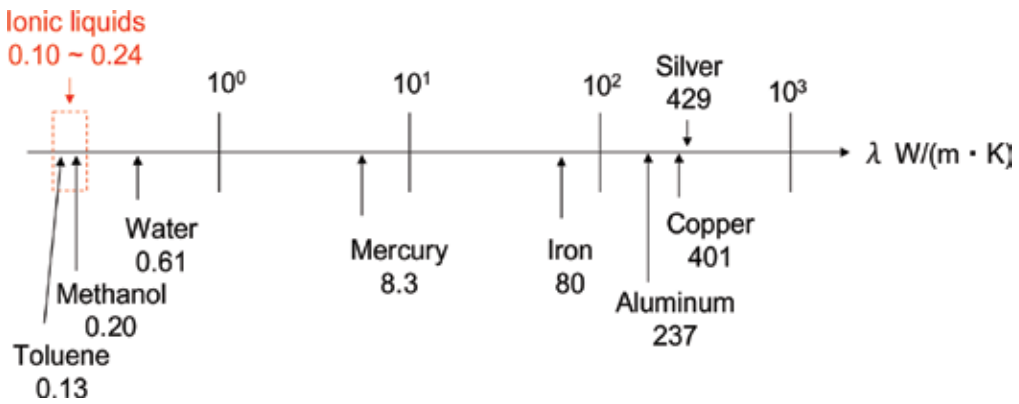

Figure 3. Thermal conductivities of various substances at 298.15 K [3, 9].

It is well known that the thermophysical properties of ILs are influenced by impurities [10]. For example, it has been reported that the viscosity of an IL decreases by about 1% with the addition of only 100 ppm of water [11]. The influence of trace water and chloride on the thermal conductivity of an IL has been reported to be relatively small compared to that on the other thermophysical properties, such as viscosity and density, as reported by Rooney et al. [4] (**Figure 4**). Our group has also investigated the effect of chloride ions on the thermal conductivities of IL [5] by measuring and comparing the thermal conductivity of 1-butyl-3-methylimidazolium tetrafluoroborate with different chloride concentrations of 421 and 4580 ppm; the difference between the thermal conductivities of these ILs was 1.2%.

We additionally investigated the influence of the alkyl chain length on thermal conductivity of ILs [12–16]. **Figure 5** shows the relation between alkyl chain length and thermal conductivity at 293 K. The thermal conductivity of *n*-alkanes was calculated by REFPROP 9.0 [17]. The results indicated that the alkyl chain length does not significantly affect the thermal conductivity. This observation differed from the findings of other studies regarding the thermal conductivities of *n*-alkanes [18] and the influence of the viscosity of the IL [19].

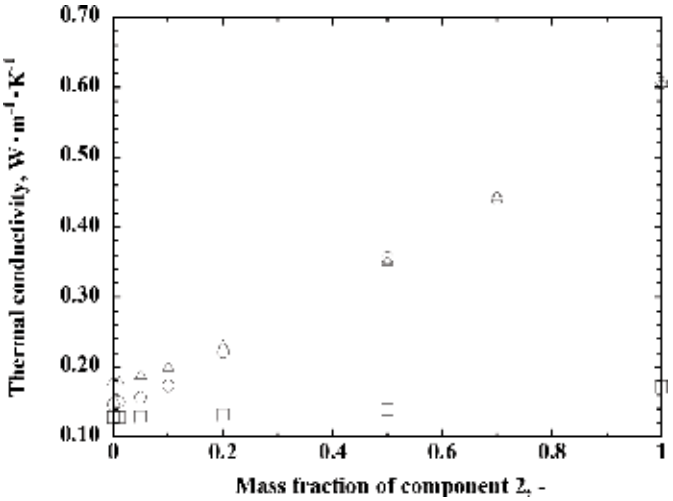

Figure 4. Effects of water and chloride on the thermal conductivities of ILs [4]: °, 1-butyl-3-methylimidazolium trifluoromethanesulfonate (1) + water (2); Δ, 1-ethyl-3-methylimidazolium ethylsulfate (1) + water (2); □, 1-hexyl-3-methylimidazolium bis-(trifluoromethylsulfonyl)imides (1) + 1-hexyl3-methylimidazolium chloride (2).

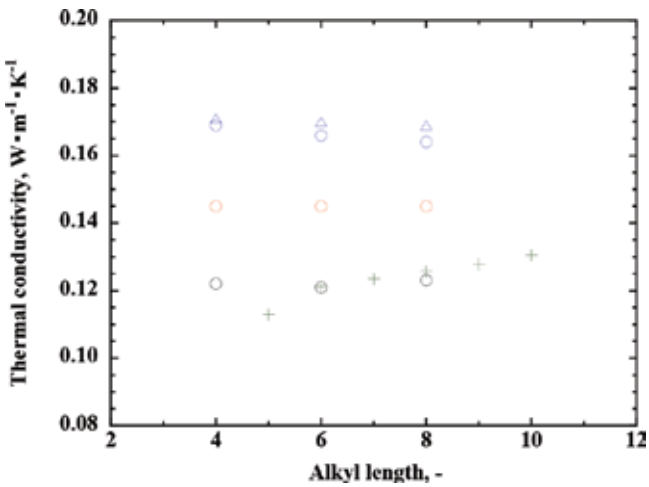

Figure 5. Relationship between the alkyl chain length and the thermal conductivities of various ILs at 293 K: 1-alkyl-3-methylimidazolium hexafluorophosphates; 1-alkyl-3-methylimidazolium tetrafluoroborates; 1-alkyl-3-methylimidazolium bis[(trifluoromethyl)sulfonyl] amides; *N*-alkylpyridinium tetrafluoroborates; and *n*-alkanes [12–17].

The temperature and pressure dependence of the thermal conductivity of ILs has been investigated [12, 14]. **Figure 6** shows a comparison of the temperature dependence of thermal conductivities of various ILs and organic solvents. The results showed that the temperature dependence of the thermal conductivity of each IL is very small in comparison with those of toluene and benzene. This is because the temperature dependence of the density of an IL is small. **Figure 7** shows a comparison of the thermal conductivities of various ILs and organic

http://dx.doi.org/10.5772/intechopen.76559

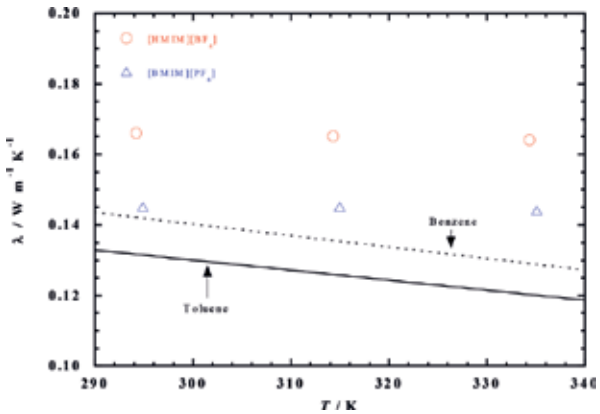

Figure 6. Temperature dependences of the thermal conductivities of various ILs and organic solvents.

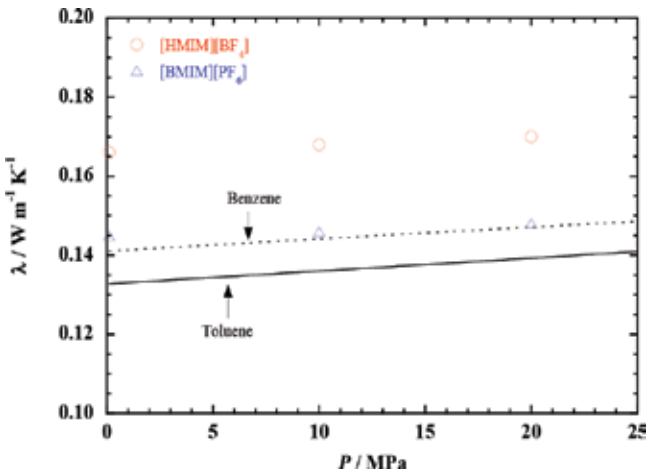

Figure 7. Pressure dependences of the thermal conductivities of various ILs and organic solvents.

solvents as functions of the pressure. It was found that the pressure dependence of the thermal conductivity of each IL is very small (within 20 MPa) in comparison with those of toluene and benzene. This is because the pressure dependence of the density of an IL is small.

2.2. Prediction and correlation of the thermal conductivity of an IL with its physical properties

A variety of ILs has been created as "designer solvents." Therefore, the prediction of the thermal conductivity of an IL based on its structure and other physical properties would be very useful for designing novel ILs. So far, an empirical-prediction method [13, 20, 21], group-contribution method [22–24], quantitative structure-property relationship method [25], prediction

method using a neural network [26, 27], and many other methods [28–35] have been proposed for the prediction of the thermal conductivities of ILs. In this section, the empirical-prediction method based on other physical properties and prediction method using group-contribution method are introduced.

We proposed a correlation equation based on the Mohanty equation [36] to describe the relation between the thermal conductivity and viscosity of an IL [13]:

$$\log\left(M\lambda/\eta\right) = 1.9596 - 0.004499\ M, \tag{1}$$

where M is the molar mass, λ is the thermal conductivity, and η is the viscosity of the IL. However, Eq. (1) was obtained by assuming that the molar mass of the IL is two times larger than the actual value. Fröba et al. proposed another correlation method and described the relation between the thermal conductivity and density of an IL as follows [20]:

$$\lambda M\rho = 0.1244M + 18.84\ , \tag{2}$$

where M is the molar mass, λ is the thermal conductivity, and ρ is the density of the IL. From 45 data points for 36 ILs, the standard deviation and mean absolute deviation of the experimental data relative to the predictions were 7.8 and 6.5%, respectively at 293.15 K and atmospheric pressure. Koller et al. extended this model to calculate the thermal conductivity at any temperature as follows [21]:

$$\lambda(T) = \left(0.0960 + \frac{21.43}{M\rho(T_{ref})}\right)\left(\frac{\rho(T)}{\rho(T_{ref})}\right)^{0.82\epsilon} \tag{3}$$

From 469 data points for 53 different ILs, the mean absolute deviation and root-mean-square deviation of the experimental data relative to the values predicted using Eq. (3) were 4.81 and 6.32%, respectively.

As mentioned above, novel ILs are synthesized and many new substances will be synthesized in the near future. Therefore, it would be very useful to predict the thermophysical properties from the structure of an IL.

Gardas and Coutinho proposed predicting the thermal conductivity of an IL by the group-contribution method [22]. When this method was proposed, few reports were available regarding the thermal conductivities of ILs from which a prediction equation could be derived. However, the following equation was derived to correlate the thermal conductivity to the specific cation and anion and the length of the alkyl chain of the cation:

$$\lambda = A_\lambda - B_\lambda T\ , \tag{4}$$

where T is the temperature in K and A_λ and B_λ are the fitting parameters that can be obtained from the group-contribution approach. These parameters can be derived as follows:

$$A_\lambda = \sum_{i=1}^{k} n_i a_{i,\lambda} \qquad B_\lambda = \sum_{i=1}^{k} n_i b_{i,\lambda} \quad , \tag{5}$$

where n_i is the number of groups of type i, k is the total number of different groups in the molecule, and the parameters $a_{i,\lambda}$, and $b_{i,\lambda}$ estimated for the ILs studied are given in **Table 1**.

Wu et al. proposed a prediction formula in which the group is divided finely so that more ILs can be predicted based on their structures [24]:

$$\lambda = \sum_{i=0}^{2} a_i \left(\sum_{j=1}^{k} n_j \Delta\lambda_{0,j} \right)^i [1 + k_0(1 - T_r)^{2/3}] \quad , \tag{6}$$

where $T_r = T/T_c$ is the reduced temperature, T_c is the critical temperature in K (which is easy to obtain for many ILs by applying the group-contribution method proposed by Valderrama group [37]), k_0 is the temperature-independent constant, n_j is the number of groups of type j, k is the total number of different groups in the molecule, and the parameters a_i and $\Delta\lambda_{0,j}$ are estimated using **Table 2**. The calculated values and those reported in the literature were in agreement for 286 data points for 36 ILs with an average absolute deviation of 1.66%.

Species	$a_{i,\lambda}$	$b_{i,\lambda}$ **(K^{-1})**
Cations		
1,3-dimethylimidazolium (+)	0.1356	1.564×10^{-5}
1,1-dimethylpyrrolidinium (+)	0.1325	1.668×10^{-5}
Tetramethylphosphonium (+)	0.1503	3.230×10^{-5}
Anions		
PF_6^-	0.0173	9.088×10^{-6}
BF_4^-	0.0874	8.828×10^{-5}
Tf_2N^-	0.0039	2.325×10^{-5}
$CF_3SO_3^-$	0.0305	5.284×10^{-5}
$EtSO_4^-$	0.0700	6.552×10^{-5}
Cl^-	0.0166	1.000×10^{-5}
Groups		
CH_2	0.0010	2.586×10^{-6}
CH_3	0.0042	7.768×10^{-6}

Table 1. Group-contribution parameters, $a_{i,j}$ and $b_{i,j}$, for Eq. (5) at 293–390 K [22].

Without rings		With rings		Coefficients	Values
Group	Values of $\Delta\lambda_{ij}$	Group	Values of $\Delta\lambda_{ij}$		
$-CH_3$	−2.66388	>C<	−0.90423	k_0	4.05711
$-CH_2-$ (*with ammonium-*)	0.60575	=CH–	−1.32204	a_0	0.03647
$-CH_2-$ (*with phosphonium-*)	0.71023	$-CH_2-$	−0.49677	a_1	−0.00097
$-CH_2-$ (*with others*)	0.68295	>CH–	2.20488	a_2	0.00003
>C<	−0.36265	–NH–	2.53635		
>CH	5.29795	–N=	0.83850		
–CN	1.51636	>N–/>N<*	−3.22547		
–COO–	1.51468				
–COOH	−10.35869				
>N–/>N<*/–N–*	−1.24392				

Without rings	
Group	Values of $\Delta\lambda_{ij}$
$-NH_2$	−3.20298
$-SO_2$	6.88560
–O–/[–O]*	0.00273
–OH	−1.33002
–F	1.69009
–Cl	−6.92175
–B	−3.97751
–P	−2.50897

Table 2. The coefficient values obtained by the group-contribution method using Eq. (6) [24].

Lazzús proposed a prediction equation to calculate the thermal conductivity of an IL as a function of the temperature and pressure [23]. The experimentally measured thermal conductivities of 41 ILs (including 400 experimental data points) in the range of 0.1–0.22 W/(m K) were used to design the proposed method for the temperature range of 273–390 K and the pressure range of 0.1–20 MPa. The results showed that the proposed group-contribution method can be used to accurately predict the thermal conductivity of an IL as a function of the temperature and pressure present with lower deviations between the predicted and actual values, including an average absolute relative deviation (AARD) of less than 1.90% and an R^2 of 0.9879 for the correlation dataset and AARD of less than 2.33% and R^2 of 0.9754 for the prediction dataset.

3. Thermal conductivities of IoNano fluids

Nanofluids are dispersions of nanoparticles and are expected to be applied as heat transfer media and used for inkjet printing. They were first reported by Choi [38] in 1995. Since then, it has been reported that the thermal conductivity of ethylene glycol is improved by 40% when 0.3 vol% of 10-nm Cu nanoparticles are dispersed in ethylene glycol [39]. A dispersion of nanoparticles in an IL is called an "IoNano fluid," as first dubbed by Castro et al. in 2010 in a

study of the thermal conductivities of nanofluids with carbon nanotubes dispersed in ILs [40, 41]. As described above, the thermal conductivities of ILs have been reported to be about the same as those of ethanol and methanol, which is not high. For this reason, it is expected that the thermal conductivity of an IL can be enhanced by dispersing nanoparticles in it.

It is known that the thermal conductivity of a nanofluid agrees well with the Hamilton-Crosser model [42]:

$$\frac{k_{eff}}{k_0} = \frac{k_p + (n-1)k_0 + (n-1)(k_p - k_0)\phi_p}{k_p + (n-1)k_0 - (k_p - k_0)\phi_p} \tag{7}$$

where k_0, k_{eff}, and k_p are the thermal conductivities of the dispersion medium, nanofluid, and dispersoid, respectively, in W/(m K), n is the particle shape parameter [–], and φ_p is the volume fraction of the dispersoid (also unitless).

Figure 8 shows the calculated enhancement of the thermal conductivity rate based on the Hamilton-Crosser model when silver, alumina, and barium titanate spherical nanoparticles are used as the dispersoid in 1-butyl-3-methylimidazolium tetrafluoroborate ([BMIM][BF_4]) as a representative IL. **Table 3** shows the thermal conductivity of each dispersoid tested. The results show that even with dispersoids with significantly different thermal conductivities, the resulting enhancement in the thermal conductivity does not vary significantly when the volume fraction is about 15% (n = 3). This suggests that, for the case of dispersing spherical nanoparticles in an IL, the thermal conductivity of the dispersoid does not significantly affect the thermal conductivity of the obtained nanofluid. Thus, to further increase the thermal conductivity of an IL using spherical nanoparticles, the volume fraction of the dispersoid must be increased; however, this introduces a problem of flowability. Therefore, while considering the use of a nanofluid as a heating medium, it is necessary to increase the thermal conductivity using the smallest possible volume fraction of nanoparticles. To remarkably increase the thermal conductivity enhancement rate with a low nanoparticle concentration, it is necessary

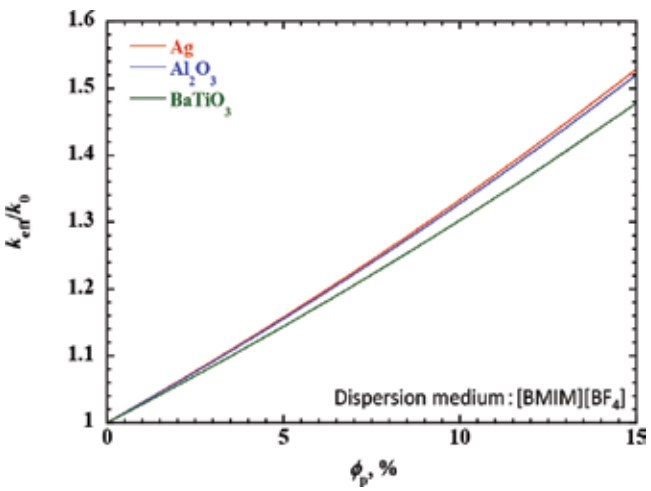

Figure 8. Relationship between the enhancement of the thermal conductivity and the volume fraction of nanoparticles based on the Hamilton-Crosser model at 298 K.

	k_p, W/(m K)
Ag	428
Al_2O_3	36
$BaTiO_3$	6

Table 3. Thermal conductivities of dispersoids.

to increase the particle diameter, n. Increasing n increases the slope; this is possible by using a material with a large aspect ratio.

Wang et al. reported that the thermal conductivity of an IoNano fluid of carbon nanotubes dispersed in 1-hexyl-3-methylimidazolium tetrafluoroborate (**Figure 9**) [43] was improved by more than 10% by adding only 0.03 wt% of graphene. In addition, the results showed that the thermal conductivities of the pure IL component (the dispersion medium) and the IoNano fluid increase with an increase in temperature. **Figure 6** shows the temperature dependence of the thermal conductivities of benzene, toluene, and 1-hexyl-3-methylimidazolium tetrafluoroborate. Usually, the thermal conductivity of a liquid decreases with increasing temperature; it is known that this holds true for ILs and that the temperature dependence of an IL is smaller than those of organic solvents including benzene and toluene. The thermal conductivity values of [HMIM][BF_4] reported by other researchers [40] indicate that the thermal conductivity gradually decreases as the temperature increases. Thus, it is conceivable that the thermal conductivity value reported by Wang et al. was influenced by convection. Assael et al. studied the reported thermal conductivity values of the nanofluid in detail and pointed out that there are many reported cases that are affected by convection [44, 45]. Based on this finding, it is necessary to carefully consider the previously reported thermal conductivity values for nanofluids because they may include the influence of convection.

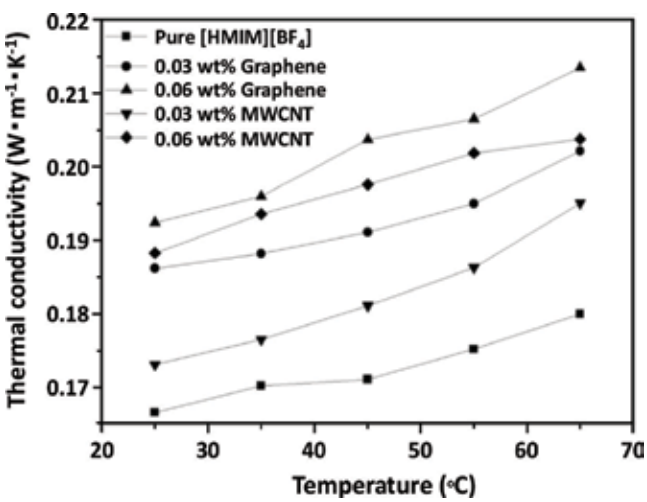

Figure 9. Thermal conductivities of IoNano fluids and [HMIM][BF_4] as functions of temperature [43].

http://dx.doi.org/10.5772/intechopen.76559

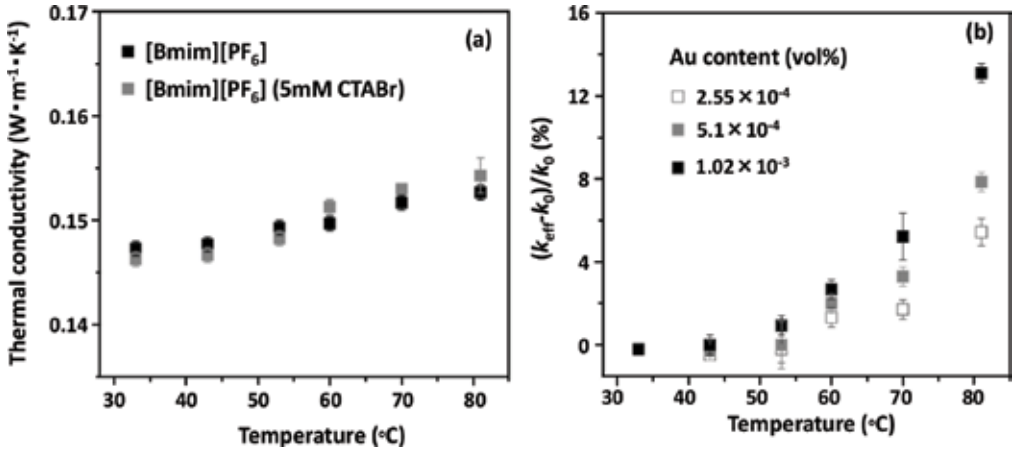

Figure 10. Thermal conductivity of [BMIM][PF_6] over a range of temperatures (a) with and without 5 mmol CTABr and (b) the thermal conductivity enhancement in Au/[BMIM][PF_6] nanofluids due to various Au concentrations [46].

Wang et al. measured the thermal conductivity of Au/[BMIM][PF_6] nanofluids of Au nanoparticles dispersed in a typical IL 1-butyl-3-methylimidazolium hexafluorophosphate medium ([BMIM][PF_6]) [46]. The thermal conductivities of the Au/[Bmim][PF_6] nanofluids stabilized by cetyltrimethylammonium bromide (CTABr) increases with an increase in the temperature and the rate of the increase also increases with an increase in the temperature (**Figure 10**). However, it was also seen that the thermal conductivity of [BMIM][PF_6] increases with an increase in the temperature (**Figure 10(a)**). In the thermal conductivity values of [BMIM][PF_6] reported by other researchers [13, 40], the thermal conductivity gradually decreases as the temperature increases; thus, the thermal conductivity measured by Wang et al. likely contains the influence of convection.

Adriana et al. reported the thermal conductivities of IoNano fluids, such as Al_2O_3/[C_4 mpyrr][NTf_2] and MWCNT/[C_4 mim][$(CF_3SO_2)_2N$]. The results showed that the enhancement rate of the thermal conductivity is almost the same as that predicted based on the Hamilton-Crosser equation; no significant enhancement in thermal conductivity has been confirmed in these systems [47].

França et al. reported that the thermal conductivity improved from 4 to 26% between MWCNT/[C_4mim][CF_3SO_2]$_2$N] and MWCNT/[C_2mim][$EtSO_4$] [48]. Although the measurements were obtained by commercial equipment, KD2 Pro, which introduces a large measurement uncertainty, the thermal conductivity was found to gradually decrease with an increase in the temperature in the pure IL component and IoNano fluid; this indicates that the measured values were almost not affected by convection.

4. Summary

In this study, the thermal conductivities of ILs and IoNano fluids were reviewed. The thermal conductivity is one of the physical properties of ILs for which few studies have been reported. The thermal conductivity of an IL is difficult to measure and the observed data are often

influenced by convection. Although the prediction and the correlation method have been proposed and examined, the results are not useful unless they are based on precisely measured values. Therefore, it is necessary to precisely measure and publish more data regarding the thermal conductivities of ILs and IoNano fluids.

Author details

Daisuke Tomida

Address all correspondence to: daisuke.tomida.e4@tohoku.ac.jp

Institute of Multidisciplinary Research for Advanced Materials, Tohoku University, Sendai, Japan

References

[1] Wilkes JS, Zaworotko MJ. Air and water stable 1-ethyl-3-methylimidazolium based ionic liquids. Journal of the Chemical Society, Chemical Communications. 1992;965-967

[2] Valkenburg MEV, Vaughn RL, Williams M, Wilkes JS. Thermochemistry of ionic liquid heat-transfer fluids. Thermochimica Acta. 2005;**425**:181-188

[3] Ionic Liquids Database—ILThermo (National Institute of Standards and Technology, 2006). http://ILThermo.boulder.nist.gov/ILThermo/ [Accessed: January 2018]

[4] Ge R, Hardacre C, Nancarrow P, Rooney DW. Thermal conductivities of ionic liquids over the temperature range from 293 K to 353 K. Journal of Chemical & Engineering Data. 2007;**52**:1819-1823

[5] Tomida D, Kenmochi S, Tsukada T, Qiao K, Yokoyama C. Thermal conductivities of imidazolium-based ionic liquid + CO_2 mixtures. International Journal of Thermophysics. 2010;**31**:1888-1895

[6] Chen Q-L, Wu K-J, He C-H. Thermal conductivities of [EMIM][$EtSO_4$], [EMIM][$EtSO_4$] + C_2H_5OH, [EMIM][$EtSO_4$] + H_2O, and [EMIM][$EtSO_4$] + C_2H_5OH + H_2O at T = (283.15 to 343.15) K. Journal of Chemical and Engineering Data. 2013;**58**:2058-2064

[7] Chen W, Qiu L, Liang S, Zheng X, Tang D. Measurement of thermal conductivities of [mmim]DMP/CH_3OH and [mmim]DMP/H_2O by freestanding sensor-based 3ω technique. Thermochimica Acta. 2013;**560**:1-6

[8] Yusoff R, Shamiri A, Aroua MK, Ahmady A, Shafeeyan MS, Lee WS, Lim SL, Burhanuddin SNM. Physical properties of aqueous mixtures of N-methyldiethanolamine (MDEA) and ionic liquids. Journal of Industrial and Engineering Chemistry. 2014;**20**:3349-3355

[9] Japan Society of Thermophysical Properties. Thermophysical Properties Handbook. Tokyo: Yokendo; 2008

[10] Seddon KR, Stark A, Torres MJ. Influence of chloride, water, and organic solvents on the thermophysical properties of ionic liquids. Pure and Applied Chemistry. 2000;**72**: 2275-2287

[11] Widegren JA, Laesecke A, Magee JW. The effect of dissolved water on the viscosities of hydrophobic room-temperature ionic liquids. Chemical Communications. 2005; 1610-1612

[12] Tomida D, Kenmochi S, Tsukada T, Yokoyama C. Measurements of thermal conductivity of 1-butyl-3-methylimidazolium tetrafluoroborate at high pressure. Heat Transfer—Asian Research. 2007;**36**:361-372

[13] Tomida D, Kenmochi S, Tsukada T, Qiao K, Yokoyama C. Thermal conductivities of [bmim][PF_6], [hmim][PF_6], and [omim][PF_6] from 294 to 335 K at pressures up to 20 MPa. International Journal of Thermophysics. 2007;**28**:1147-1160

[14] Tomida D, Kenmochi S, Tsukada T, Qiao K, Bao Q, Yokoyama C. Viscosity and thermal conductivity of 1-hexyl-3-methylimidazolium tetrafluoroborate and 1-octyl-3-methylimidazolium tetrafluoroborate at pressures up to 20 MPa. International Journal of Thermophysics. 2012;**33**:959-969

[15] Tomida D, Kenmochi S, Qiao K, Tsukada T, Yokoyama C. Densities and thermal conductivities of *N*-alkylpyridinium tetrafluoroborates at high pressure. Fluid Phase Equilibria. 2013;**340**:31-36

[16] Tomida D, Kanno S, Qiao K, Yokoyama C. Viscosities at pressures up to 20 MPa and thermal conductivities at 0.1 MPa of 1-alkyl-3-methylimidazolium bis[(trifluoromethyl) sulfonyl]amides. High Temperatures—High Pressures. 2017;**46**:231-245

[17] Lemmon EW, Huber ML, McLinden MO. NIST Standard Reference Data 23. REFPROP Version 9.1. CO: NIST; 2013

[18] Watanabe H, Seong DJ. The thermal conductivity and thermal diffusivity of liquid *n*-alkanes: C_nH_{2n+2} (n=5 to 10) and toluene. International Journal of Thermophysics. 2002;**23**:337-356

[19] Seddon KR, Stark A, Torres MJ. Viscosity and density of 1-alkyl-3-methylimidazolium ionic liquids. ACS Symposium Series. 2002;**819**:34-49

[20] Fröba AP, Rausch MH, Krzeminski K, Assenbaum D, Wasserscheid P, Leipertz A. Thermal conductivity of ionic liquids: Measurement and prediction. International Journal of Thermophysics. 2010;**31**:2059-2077

[21] Koller TM, Schmid SR, Sachnov SJ, Rausch MH, Wasserscheid P, Fröba AP. Measurement and prediction of the thermal conductivity of tricyanomethanide- and tetracyanoborate-based imidazolium ionic liquids. International Journal of Thermophysics. 2014;**35**:195-217

[22] Gardas RL, Coutinho JAP. Group contribution methods for the prediction of thermophysical and transport properties of ionic liquids. AICHE Journal. 2009;**55**:1274-1290

[23] Lazzus JA. A group contribution method to predict the thermal conductivity λ(T,P) of ionic liquids. Fluid Phase Equilibria. 2015;**405**:141-149

[24] Wu KJ, Zhao CX, He CH. Development of a group contribution method for determination of thermal conductivity of ionic liquids. Fluid Phase Equilibria. 2016;**339**:10-14

[25] Lazzús JA, Pulgar-Villarroel G. Estimation of thermal conductivity of ionic liquids using quantitative structure-property relationship calculations. Journal of Molecular Liquids. 2015;**211**:981-985

[26] Hezave AZ, Raeissi S, Lashkarbolooki M. Estimation of thermal conductivity of ionic liquids using a perceptron neural network. Industrial and Engineering Chemistry Research. 2012;**51**:9886-9893

[27] Lazzús JA. Estimation of the thermal conductivity $\lambda(T,P)$ of ionic liquids using a neural network optimized with genetic algorithms. Comptes Rendus Chimie. 2016;**19**:333-341

[28] Carrete J, Méndez-Morales T, García M, Vila J, Cabeza O, Gallego LJ, Varela LM. Thermal conductivity of ionic liquids: A pseudolattice approach. Journal of Physical Chemistry C. 2012;**116**:1265-1273

[29] Shojaee SA, Farzam S, Hezave AZ, Lashkarbolooki M, Ayatollahi S. A new correlation for estimating thermal conductivity of pure ionic liquids. Fluid Phase Equilibria. 2013;**354**:199-206

[30] Chen QL, Wu KJ, He CH. Thermal conductivity of ionic liquids at atmospheric pressure: Database, analysis, and prediction using a topological index method. Industrial and Engineering Chemistry Research. 2014;**53**:7224-7232

[31] Wu KJ, Chen QL, He CH. Speed of sound of ionic liquids: Database, estimation, and its application for thermal conductivity prediction. AICHE Journal. 2014;**60**:1120-1131

[32] Albert J, Müller K. Thermal conductivity of ionic liquids: An estimation approach. Chemical Engineering Science. 2014;**119**:109-113

[33] Atashrouz S, Mozaffarian M, Pazuki G. Modeling the thermal conductivity of ionic liquids and ionanofluids based on a group method of data handling and modified Maxwell model. Industrial and Engineering Chemistry Research. 2015;**54**:8600-8610

[34] Haghbakhsh R, Raeissi S. A novel correlative approach for ionic liquid thermal conductivities. Journal of Molecular Liquids. 2017;**236**:214-219

[35] Oster K, Jacquemin J, Hardacre C, Ribeiro APC, Elsinawi A. Further development of the predictive models for physical properties of pure ionic liquids: Thermal conductivity and heat capacity. The Journal of Chemical Thermodynamics. 2018;**118**:1-15

[36] Mohanty SR. A relationship between heat conductivity and viscosity of liquids. Nature. 1951;**168**:42

[37] Valderrama JO, Forero LA, Rojas RE. Critical properties and normal boiling temperature of ionic liquids. Update and a new consistency test. Industrial and Engineering Chemistry Research. 2012;**51**:7838-7844

[38] Choi SUS. Enhancing thermal conductivity of fluids with nanoparticles. ASME Fluids Engineering Division. 1995;**231**:99-105

[39] Eastman JA, Choi SUS, Li S, Yu W, Thompson LJ. Anomalously increased effective thermal conductivities of ethylene glycol-based nanofluids containing copper nanoparticles. Applied Physics Letters. 2001;**78**:718-720

[40] Nieto de Castro CA, Lourenco MJV, Ribeiro APC, Langa E, Vieira SIC. Thermal conductivity of $[C_{4\,m}im][(CF_3SO_2)_2N]$ and $[C_{2\,m}im][EtSO_4]$ and their IoNanofluids with carbon nanotubes: Experiment and theory. Journal of Chemical & Engineering Data. 2010; **55**:653-661

[41] Nieto de Castro CA, Murshed SMS, Lourenço MJV, Santos FJV, Lopes MLM, França JMP. Enhanced thermal conductivity and specific heat capacity of carbon nanotubes ionanofluids. International Journal of Thermal Sciences. 2012;**62**:34-39

[42] Hamilton R, Crosser OK. Thermal conductivity of heterogeneous two-component systems. Industrial and Engineering Chemistry Fundamentals. 1962;**1**:187-191

[43] Wang F, Han L, Zhang Z, Fang X, Shi J, Ma W. Surfactant-free ionic liquid-based nanofluids with remarkable thermal conductivity enhancement at very low loading of graphene. Nanoscale Research Letters. 2012;**7**:314

[44] Tertsinidou G, Assael MJ, Wakeham WA. The apparent thermal conductivity of liquids containing solid particles of nanometer dimensions: A critique. International Journal of Thermophysics. 2015;**36**:1367-1395

[45] Antoniadis KD, Tertsinidou GJ, Assael MJ, Wakeham WA. Necessary conditions for accurate, transient hot-wire measurements of the apparent thermal conductivity of nanofluids are seldom satisfied. International Journal of Thermophysics. 2015;**37**:78

[46] Wang B, Wang X, Lou W, Hao J. Gold-ionic liquid nanofluids with preferably tribological properties and thermal conductivity. Nanoscale Research Letters. 2011;**6**:259

[47] Adriana MA, Georgiana MM, Oana D. Thermal conductivity enhancement by adding nanoparticles to ionic liquids. Solid State Phenomena. 2017;**261**:121-126

[48] França JMP, Vieira SIC, Lourenço MJV, Murshed SMS, Nieto de Castro CA. Thermal conductivity of $[C_{4\,m}im][(CF_3SO_2)_2N]$ and $[C_{2\,m}im][EtSO_4]$ and their IoNanofluids with carbon nanotubes: Experiment and theory. Journal of Chemical & Engineering Data. 2013;**58**:467-476

Chapter 3

Thermal Conductivity in the Boundary Layer of Non-Newtonian Fluid with Particle Suspension

Rudraswamy N.G., Ganeshkumar K.,
Krishnamurthy M.R., Gireesha B.J. and Venkatesh P.

Additional information is available at the end of the chapter

http://dx.doi.org/10.5772/intechopen.76345

Abstract

The present chapter is focused on studies concerned with three-dimensional flow and heat transfer analysis of Carreau fluid with nanoparticle suspension. The heat transfer analysis in the boundary was carried out with the fluid flow over a stretching surface under the influence of nonlinear thermal radiation, mixed convection and convective boundary condition. Suitable similarity transformations are employed to reduce the governing partial differential equations into coupled nonlinear ordinary differential equations. The equations in non-linear form are then solved numerically using Runge-Kutta-Fehlberg fourth fifth-order method with the help of symbolic algebraic software MAPLE. The results so extracted are well tabulated and adequate discussions on the parameters affecting flow and heat transfer analysis were carried out with the help of plotted graphs.

Keywords: Carreau nano fluid, nonlinear thermal radiation, mixed convection, stretching sheet, convective boundary condition, numerical method

1. Introduction

Thermal radiation, the fundamental mechanism of heat transfer is an indispensable activity in rocket propulsion, plume dynamics, solar collector performance, materials processing, combustion systems, fire propagation and other industrial and technological processes at high temperatures. With the developments in computational dynamics, increasing attention has been diverted towards thermal convection flows with the significant radiative flux. Rayleigh initiated the theory of thermal convection, by deriving critical temperature gradient (Critical Rayleigh number). Importance of such radiations is intensified with absolute temperatures at

higher level. Thus a substantial interest is driven towards thermal boundary layer flows with a strong radiation. Governing equation of radiative heat transfer with its integro-differential nature makes numerical solutions of coupled radiative-convective flows even more challenging. Multiple studies were conducted employing several models to investigate heat and mass transfer in boundary layer and fully-developed laminar convection flows. As a consequence several simultaneous multi-physical effects in addition to radiative heat transfer including gravity and pressure gradient effects [1], mhd flow of nanofluids [2], buoyancy effects [3, 4], ferrofluid dynamics [5], stretching surface flow [6, 7], time-dependent, wall injection and Soret/Dufour effects [8–11].

These studies have however been confined to Newtonian flows. But industries related with fabrication of polymers and plastics at high temperatures show greater importance towards radiative flows of non-Newtonian fluids. The potential of non-Newtonian flows in ducts with radiative transfer were significantly developed after the studies on novel propellants for spacecraft [12]. The developments are extant and diversified the application of non-Newtonian fluid models. Most studies in this regard have employed the Rosseland model which is generally valid for optically-thick boundary layers. Recently, Kumar et al. [13] used such model to study melting heat transfer of hyperbolic tangent fluid over a stretching sheet with suspended dust particles. Cortell [14] and Batalle [15] have shown their earlier contribution towards radiative heat transfer of non-Newtonian fluids past stretching sheet under various circumstances. Relating to the studies Khan et al. [16] developed a numerical studies correlating MHD flow of Carreau fluid over a convectively heated surface with non-linear radiation. Appending to this studies Khan et al. [17] provided his results on hydromagnetic nonlinear thermally radiative nanoliquid flow with Newtonian heat along with mass conditions. Meanwhile, Rana and Bhargava [18] provided a numerical elucidation to study of heat transfer enhancement in mixed convection flow along a vertical plate with heat source/sink utilizing nanofluids. Hayat et al. [19] investigated the mixed convection stagnation-point flow of an incompressible non-Newtonian fluid over a stretching sheet under convective boundary conditions. Many diverse -physical simulations with and without convective and/or radiative heat transfer have been studied. Representative studies in this regard include [20–23] with analogous to the property of radiation flow.

Endeavoring the complications in three dimensional flow analysis, Shehzad et al. [24] studied the effect of thermal radiation in Jeffrey nanofluid by considering the characteristics of thermophoresis and Brownian motion for a solar energy model. Hayat et al. [25] analyzed the effect non-linear thermal radiation over MHD three-dimensional flow of couple stress nanofluid in the presence of thermophoresis and Brownian motion. Rudraswamy et al. [26] observations on Soret and Dufour effects in three-dimensional flow of Jeffery nanofluid in the presence of nonlinear thermal radiation clearly showed that concentration and associated boundary layer thickness are enhanced by increasing Soret and Dufour numbers. Many such problems [27–29] were considered disclosing the feature of thermal radiation in three dimensional flow of non-Newtonian fluids.

Inspired by the above works, we put forth the studies on the effect of non-linear thermal radiation on three dimensional flow of Carreau fluid with suspended nanoparticles. Present

studies even include the phenomenon of mixed convection and convective boundary conditions. A numerical approach is provided for the above flow problem by employing Runge-Kutta-fourth-fifth order method.

2. Mathematical formulation

A steady three-dimensional flow of an incompressible Carreau fluid with suspended nano particles induced by bidirectional stretching surface at $z = 0$ has been considered. The sheet is aligned with the $xy-$ plane $(z = 0)$ and the flow takes place in the domain $z > 0$. Let $u = u_w(x) = ax$ and $v = v_w(y) = by$ be the velocities of the stretching sheet along x and y directions respectively. A constant magnetic field of strength B is applied in the $z-$ direction. Heat and mass transfer characteristics are taken in to account in the presence of Brownian motion and Thermophoresis effect. The thermo physical properties of fluid are taken to be constant.

Extra stress tensor for Carreau fluid is.

$$\overline{\tau}_{ij} = \mu_0 \left[1 + \frac{n-1}{2}\left(\Gamma\overline{\dot{\gamma}}\right)^2\right]\overline{\dot{\gamma}}_{ij}$$

In which $\overline{\tau}_{ij}$ is the extra stress tensor, μ_0 is the zero shear rate viscosity, Γ is the time constant, $\overline{\dot{\gamma}}$ is the power law index and is defined as.

$$\overline{\dot{\gamma}} = \sqrt{\frac{1}{2}\sum\sum \overline{\dot{\gamma}}_{ij}\overline{\dot{\gamma}}_{ji}} = \sqrt{\frac{1}{2}\Pi}$$

Here Π is the second invariant strain tensor.

The governing boundary layer equations of momentum, energy and concentration for three-dimensional flow of Carreau nanofluid can be written as,

$$\frac{\partial u}{\partial x} + \frac{\partial v}{\partial y} + \frac{\partial w}{\partial z} = 0, \tag{1}$$

$$u\frac{\partial u}{\partial x} + v\frac{\partial u}{\partial y} + w\frac{\partial u}{\partial z} = \nu\frac{\partial^2 u}{\partial z^2} + 3\frac{(n-1)}{2}\Gamma\left(\frac{\partial u}{\partial z}\right)^2\frac{\partial^2 u}{\partial z^2} + g\beta_T(T - T_\infty) - \frac{\sigma B^2}{\rho}u, \tag{2}$$

$$u\frac{\partial v}{\partial x} + v\frac{\partial v}{\partial y} + w\frac{\partial v}{\partial z} = \nu\frac{\partial^2 v}{\partial z^2} + 3\frac{(n-1)}{2}\Gamma\left(\frac{\partial v}{\partial z}\right)^2\frac{\partial^2 v}{\partial z^2} - \frac{\sigma B^2}{\rho}v, \tag{3}$$

$$u\frac{\partial T}{\partial x} + v\frac{\partial T}{\partial y} + w\frac{\partial T}{\partial z} = \alpha\frac{\partial^2 T}{\partial z^2} + \tau\left[D_B\frac{\partial T}{\partial z}\frac{\partial C}{\partial z} + \frac{D_T}{T_\infty}\left(\frac{\partial T}{\partial z}\right)^2\right] - \frac{1}{(\rho c)_f}\frac{\partial q_r}{\partial z}, \tag{4}$$

$$u\frac{\partial C}{\partial x} + v\frac{\partial C}{\partial y} + w\frac{\partial C}{\partial z} = D_B\frac{\partial^2 C}{\partial z^2} + \frac{D_T}{T_\infty}\frac{\partial^2 T}{\partial z^2}. \tag{5}$$

The boundary conditions for the present flow analysis are,

$$u = ax, v = by, w = 0, k\frac{\partial T}{\partial z} = -h_f\left(T_f - T_\infty\right), C = C_w \text{ at } z = 0 \tag{6}$$

$$u \to 0, v \to 0, T \to T_\infty, C \to C_\infty \text{ as } z \to \infty, \tag{7}$$

where ν is the kinematic viscosity of the fluid, μ is the coefficient of fluid viscosity, ρ is the fluid density, B is the magnetic field, σ is the electrical conductivity of the fluid, T is the fluid temperature, α is the thermal diffusivity of the fluid, k is the thermal conductivity. τ is the ratio of effective heat capacity of the nanoparticle material to heat capacity of the fluid, q_r is the radiative heat flux, g is the gravitational acceleration, β_T is thermal expansion coefficient of temperature, D_B is the Brownian diffusion coefficient, h_f is the heat transfer coefficient, D_T is the thermophoretic diffusion coefficient, c_p is the specific heat at constant pressure, T_f is the temperature at the wall, T_∞ is the temperatures far away from the surface. C is the concentration and C_∞ is the concentration far away from the surface. The subscript w denotes the wall condition.

Using the Rosseland approximation radiation heat flux q_r is simplified as,

$$q_r = -\frac{4\sigma^*}{3k^*}\frac{\partial T^4}{\partial z} = -\frac{16\sigma^*}{3k^*}T^3\frac{dT}{dz}, \tag{8}$$

where σ^* and k^* are the Stefan-Boltzmann constant and the mean absorption coefficient respectively.

In view to Eq. (8), Eq. (4) reduces to.

$$u\frac{\partial T}{\partial x} + v\frac{\partial T}{\partial y} + w\frac{\partial T}{\partial z} = \frac{\partial}{\partial z}\left[\left(\alpha + \frac{16\sigma^* T^3}{3k^*(\rho c)_f}\right)\frac{dT}{dz}\right] + \tau\left[D_B\frac{\partial T}{\partial z}\frac{\partial C}{\partial z} + \frac{D_T}{T_\infty}\left(\frac{\partial T}{\partial z}\right)^2\right]. \tag{9}$$

The momentum, energy and concentration equations can be transformed into the corresponding ordinary differential equations by the following similarity variables,

$$u = axf'(\eta), v = byg'(\eta), w = -\sqrt{a\nu}(f(\eta) + g(\eta)),$$

$$\theta(\eta) = \frac{T - T_\infty}{T_w - T_\infty}, \phi(\eta) = \frac{C - C_\infty}{C_w - C_\infty}, \eta = \sqrt{\frac{a}{\nu}} \tag{10}$$

where $T = T_\infty(1 + (\theta_w - 1)\theta(\eta))$, $\theta_w = \frac{T_f}{T_\infty}$, $(\theta_w > 1)$ being the temperature ratio parameter.

Then, we can see that Eq. (1) is automatically satisfied, and Eqs. (2)–(7)are reduced to:

$$f''' + (f + g)f'' - f'^2 + 3\frac{n-1}{2}Wef''^2 f''' + \lambda\theta - Mf' = 0 \tag{11}$$

$$g''' + (f + g)g'' - g'^2 + 3\frac{n-1}{2}Weg''^2 g''' - Mg' = 0 \tag{12}$$

$$\frac{1}{\mathrm{Pr}}\left((1+R(\theta_w-1)\theta)^3\theta''\right)+(f+g)\theta'+Nb\theta'\varphi'+Nt\theta'^2=0, \tag{13}$$

$$\phi''+Le\mathrm{Pr}(f+g)\phi'+\frac{Nt}{Nb}\theta''=0 \tag{14}$$

With the boundary conditions,

$$f=0, g=0, f'=1, g'=c, \theta'=-Bi(1-\theta(0)),\ \ \phi=1,\ \ \text{at}\ \ \eta=0,$$
$$f'\to 0, g'\to 0, \theta\to 0, \phi\to 0\ \ \text{as}\ \ \eta\to\infty. \tag{15}$$

$We=\frac{cU_w^2\lambda^2}{\nu}$ is the Weissenberg number, $M=\frac{\sigma B^2}{\rho a}$ is the magnetic parameter, $c=\frac{b}{a}$ is the ratio of stretching rates, $\mathrm{Pr}=\frac{\nu}{\alpha}$ is Prandtl number, $R=\frac{16\sigma^* T_\infty^3}{3kk^*}$ is the radiation parameter, $Nb=\frac{\tau D_B(C_w-C_\infty)}{\nu}$ is the Brownian motion parameter, $Nt=\frac{\tau D_T\left(T_f-T_\infty\right)}{\nu T_\infty}$ is the Thermophoresis parameter, $\lambda=\frac{g\beta_T\left(T_f-T_\infty\right)}{\mathrm{Re}_x}$ is the mixed convection parameter, $Bi=\frac{h_f}{k}\sqrt{\frac{\nu}{a}}$ is the Biot number, $Le=\frac{\alpha}{D_B}$ is the Lewis number.

The local skin friction $\left(C_f\right)$, local Nusselt number (Nu_x) and local number Sherwood (Sh_x) are defined as,

$$C_{fx}=\frac{\tau_w}{\rho u_w(x)^2}, C_{fy}=\frac{\tau_w}{\rho v_w(y)^2}, Nu_x=\frac{u_w q_w}{ka\left(T_f-T_\infty\right)}\ \ \text{and}\ Sh_x=\frac{u_w q_m}{D_B a(C_w-C_\infty)}$$

The local skin friction, local Nusselt number and Sherwood number is given by,

$$\sqrt{\mathrm{Re}_x}C_{fx}=\left[f''(0)+\frac{(n-1)We^2}{2}\left(f''(0)\right)^3\right],\quad \sqrt{\mathrm{Re}_x}C_{fy}=\left[g''(0)+\frac{(n-1)We^2}{2}\left(g''(0)\right)^3\right],$$

$$\frac{Nu_x}{\sqrt{\mathrm{Re}_x}}=-\left(1++R\theta_w^3\right)\theta'(0),\qquad \frac{Sh_x}{\sqrt{\mathrm{Re}_x}}=-\phi'(0).$$

where $\mathrm{Re}_x=\frac{u_w x}{\nu}$ is the local Reynolds number based on the stretching velocity. $u_w(x)$.

3. Numerical method

The non-linear ordinary differential Eqs. (11)–(14) subjected to boundary conditions (15) has been solved using the Runge-Kutta-Fehlberg fourth-fifth order method with the help of symbolic algebraic software MAPLE. The boundary conditions for $\eta=\infty$ are replaced by $f'\left(\eta_{\max}\right)=1, \theta\left(\eta_{\max}\right)=0$ and $\phi\left(\eta_{\max}\right)=0$, where $\eta_{\max}$ is a sufficiently large value of η at which the boundary conditions (15) are satisfied. Thus, the values of $\eta=\eta_{\max}$ are taken to be 6. To validate the employed method, the authors have compared the results of $f''(0)$ and $g''(0)$

c	Wang [27]		Hayat et al. [30]		Present result	
	$-f''(0)$	$-g''(0)$	$-f''(0)$	$-g''(0)$	$-f''(0)$	$-g''(0)$
0	1	0	1	0	1	0
0.25	1.0488	0.1945	1.048810	0.19457	1.04881	0.19457
0.5	1.0930	0.4652	1.093095	0.465205	1.09309	0.46522
0.75	1.1344	0.7946	1.134500	0.794620	1.13450	0.79462
1.0	1.1737	1.1737	1.173721	1.173721	1.17372	1.17372

Table 1. Comparison of different values of c with Wang [27] and Hayat et al. [30].

with the that of published works by Wang [27] and Hayat [30] for the different values stretching parameter. These comparisons are given in **Table 1** and it shows that the results are in very good agreement.

4. Result and discussion

The purpose of this section is to analyze the effects of various physical parameters on the velocities, temperature and concentration fields. Therefore, for such objective, **Figures 1–11** has been plotted. Observations over these data with plotted graphs are discussed below.

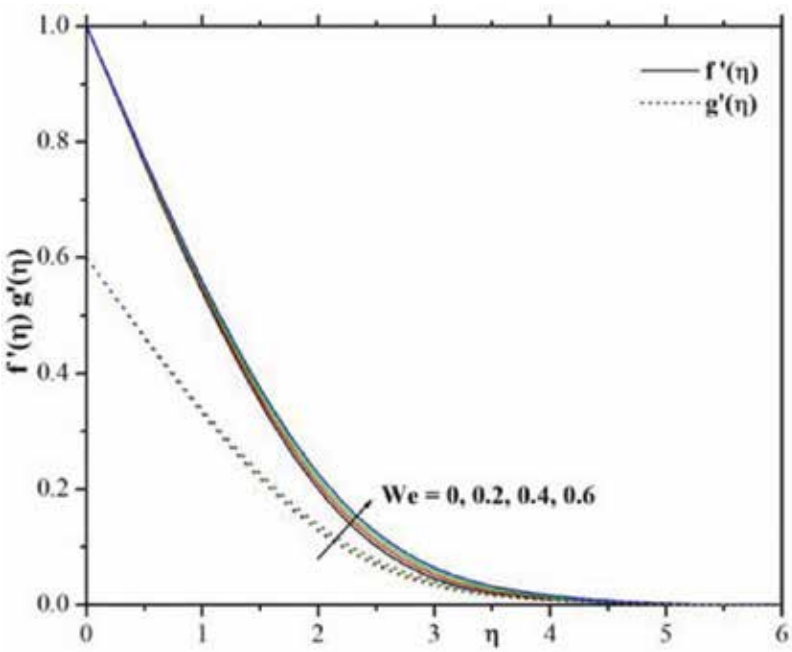

Figure 1. Influence of *We* on velocity profiles of both $f'(\eta)$ and $g'(\eta)$.

http://dx.doi.org/10.5772/intechopen.76345

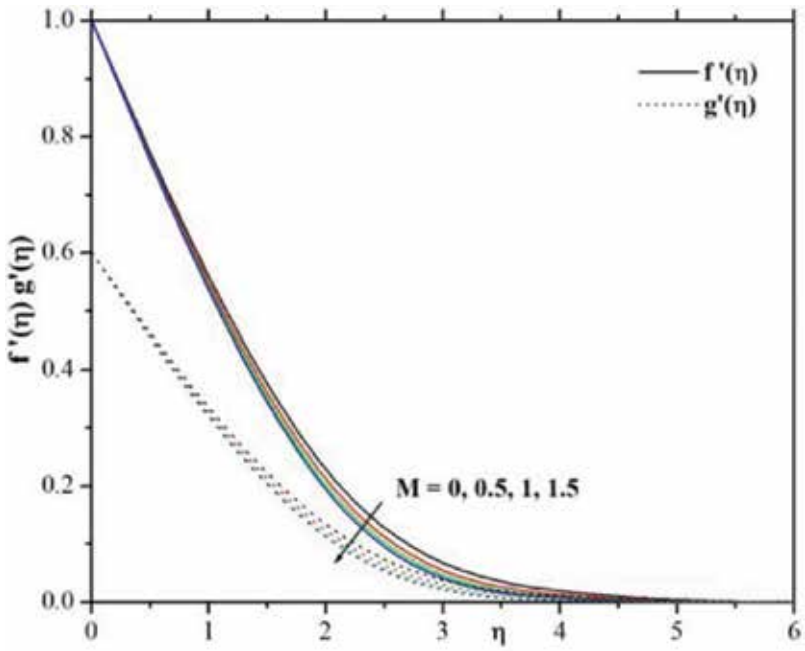

Figure 2. Influence of M on velocity profiles $f'(\eta)$ and $g'(\eta)$.

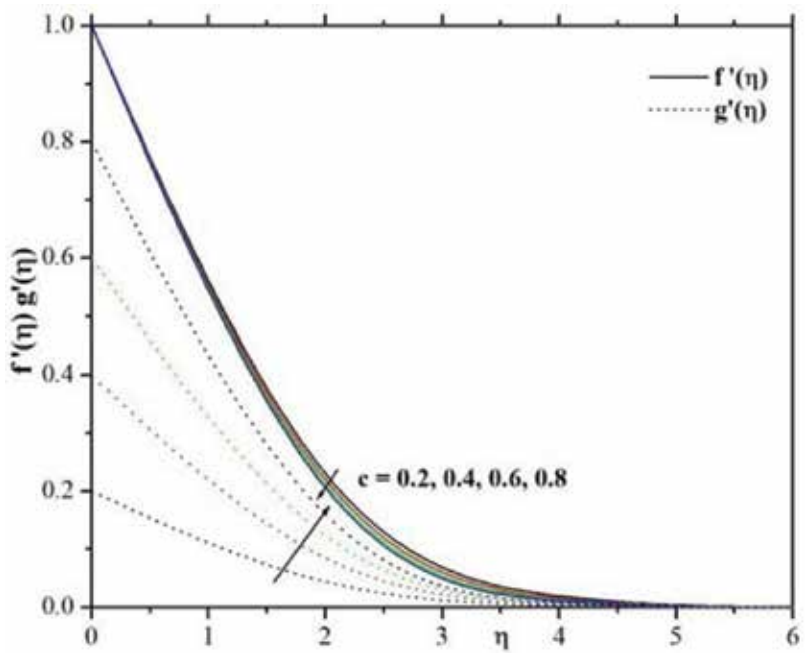

Figure 3. Influence of c on velocity profiles $f'(\eta)$ and $g'(\eta)$.

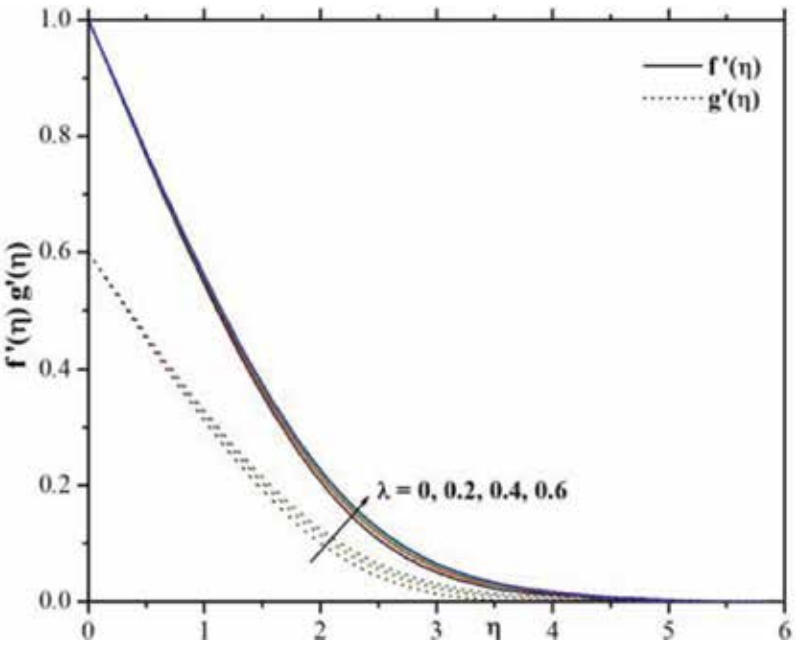

Figure 4. Influence of λ on velocity profiles $f'(\eta)$ and $g'(\eta)$.

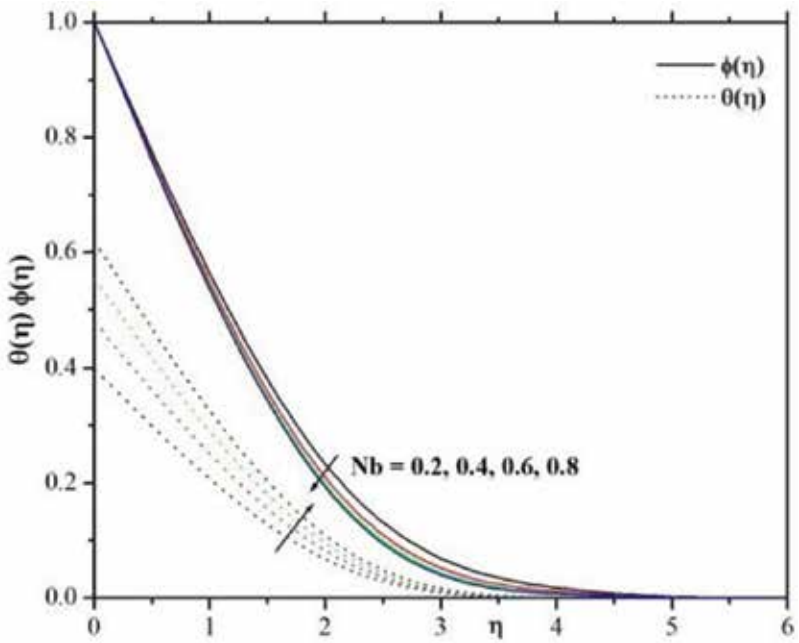

Figure 5. Influence of Nb on $\theta(\eta)$ and $\phi(\eta)$ profiles.

http://dx.doi.org/10.5772/intechopen.76345

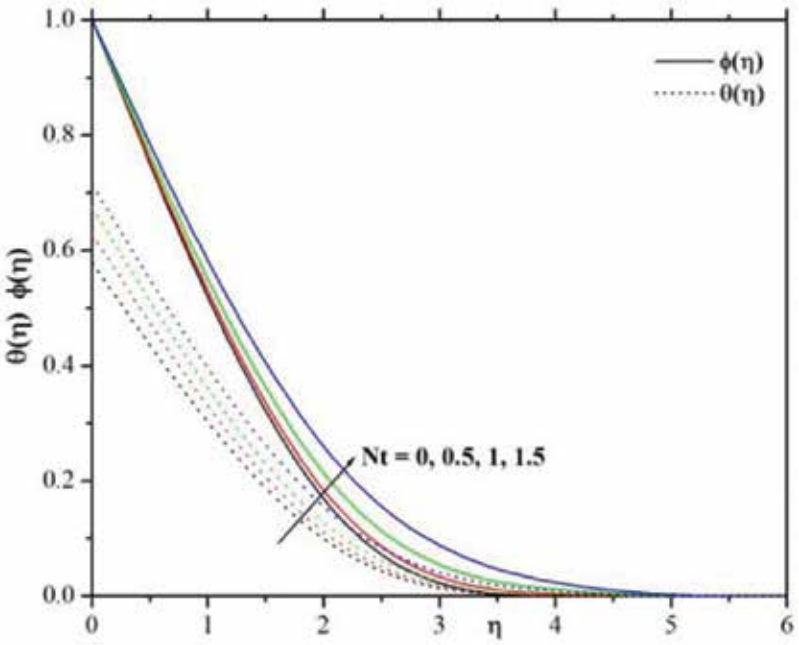

Figure 6. Influence of Nt on $\theta(\eta)$ and $\phi(\eta)$ profiles.

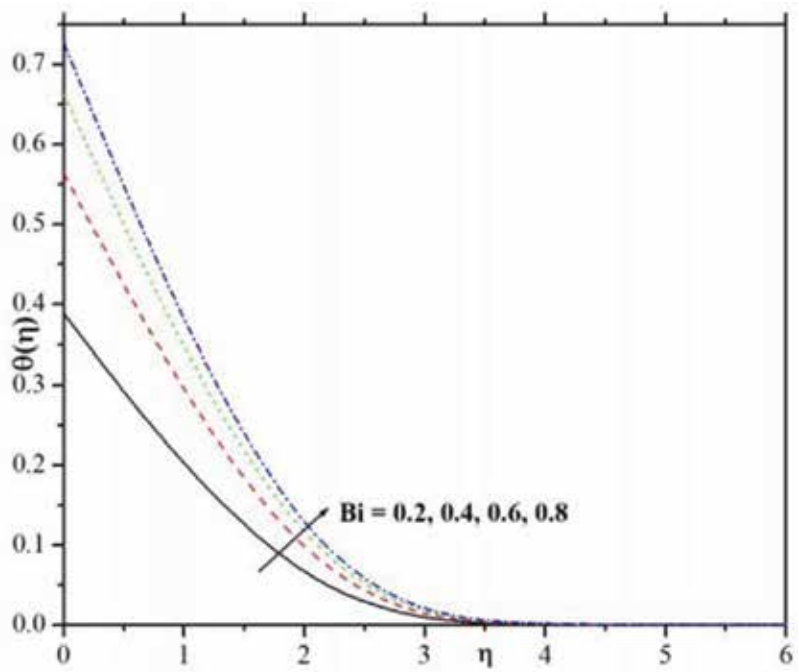

Figure 7. Influence of Bi on temperature profile.

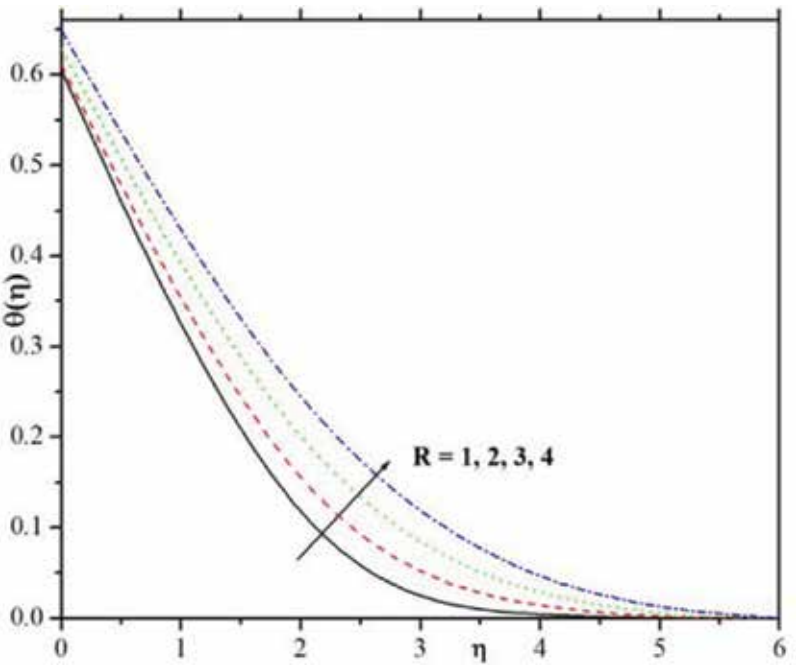

Figure 8. Influence of R on temperature profile.

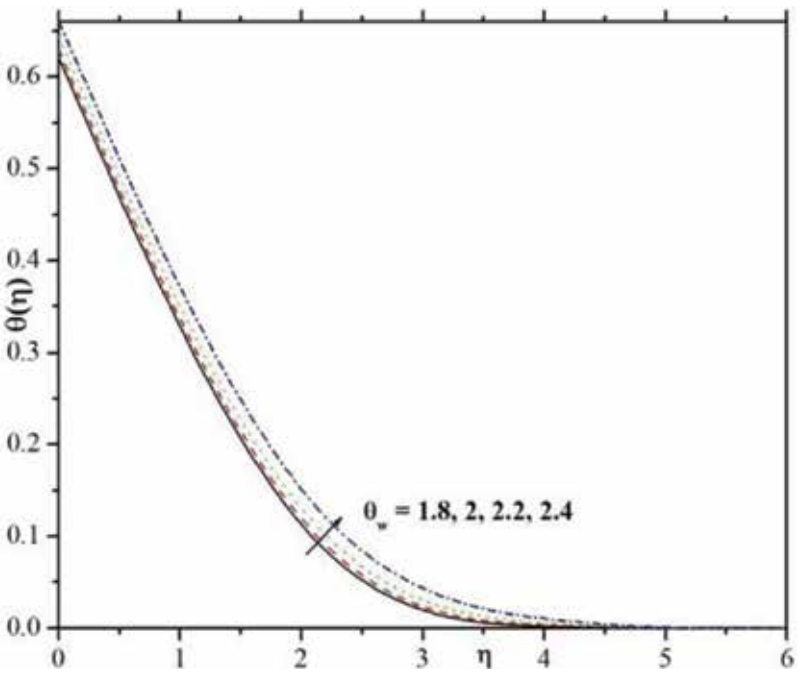

Figure 9. Influence of θ_w on temperature profile.

http://dx.doi.org/10.5772/intechopen.76345

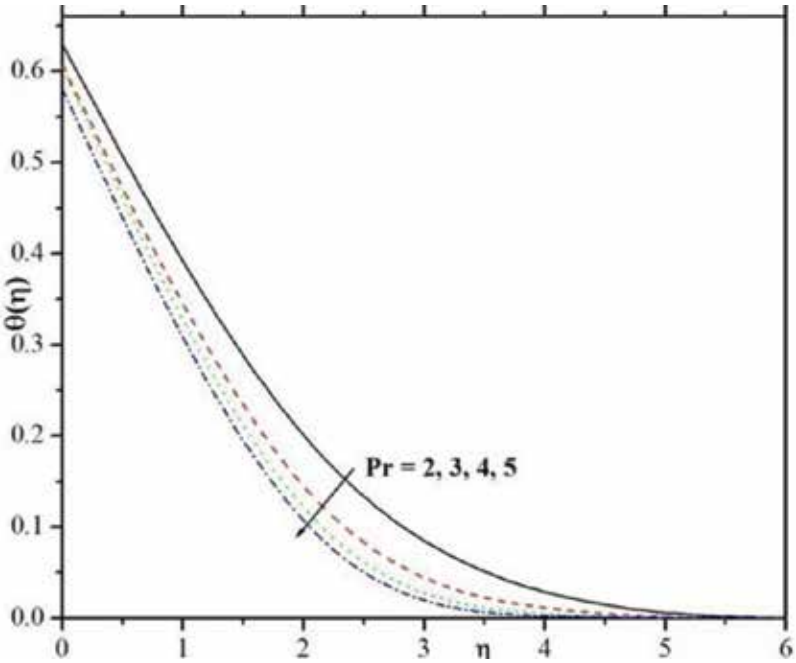

Figure 10. Influence of Pr on temperature profile.

Figure 1 characterizes the influence of Weissenberg number (We) on velocity profiles for both x and y direction. It is found that increasing values of the Weissenberg number increases the momentum boundary layers in both directions. Physically, Weissenberg number is directly proportional to the time constant and reciprocally proportional to the body. The time constant to body magnitude relation is higher for larger values of Weissenberg number. Hence, higher Weissenberg number causes to enhance the momentum boundary layer thickness.

The developments of a magnetic field (M) on velocity profiles are circulated in **Figure 2**. We tend to discover depreciation within the velocity profile for ascent values of magnetic field parameter. Physically, the drag force will increase with a rise within the magnetic flux and as a result, depreciation happens within the velocity field.

Figure 3 designed the velocity profiles of f' and g' for various values of stretching parameter(c). The velocity profiles and associated momentum boundary layer thickness decrease, once the stretching parameter will increase whereas velocity profile g', exhibits the opposite behavior of f'. **Figure 4** shows the velocity profiles for different values of mixed convection parameter(λ). It depicts that the velocity field and momentum boundary layer thickness increases in both x and y direction by increasing mixed convection parameter.

Figure 5 portraits the consequences of Brownian motion parameter on temperature and concentration profile. The Brownian motion parameter (Nb) will increase the random motion of the fluid particles and thermal boundary layer thickness conjointly will increase which ends up

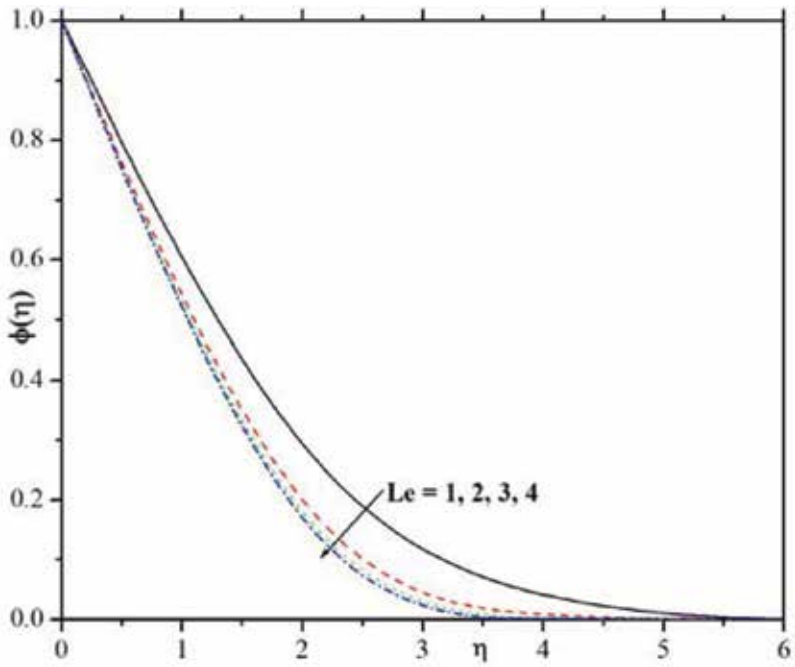

Figure 11. Influence of *Le* on concentration profile.

in an additional heat to provide. Therefore, temperature profile will increase however concentration profiles show opposite behavior.

The development of the thermophoresis parameter (Nt) on temperature and concentration profiles is inspecting in **Figure 6**. Form this figure we observed that, the higher values of thermophoresis parameter is to increases both $\theta(\eta)$ and $\phi(\eta)$ profiles. Further, the thermal boundary layer thickness is higher for larger values of thermophoresis parameter. This is because, it's a mechanism within which little particles area unit force off from the new surface to a chilly one. As a result, it maximizes the temperature and concentration of the fluid.

Figure 7 describe the influences of Biot number (Bi) on temperature profile. One can observe form the figure, the larger values of Biot number cause an enhancing the temperature profile. This is because, the stronger convection leads to the maximum surface temperatures which appreciably enhance the thermal boundary layer thickness.

Figures 8 and **9** are sketched to analyze the effect of radiation parameter (R) and temperature ratio (θ_w) parameter on temperature profile. The above graphs elucidate that, the temperature profile and thermal boundary layer thickness area unit increased by ascent values of radiation parameter and temperature ratio. Larger values of thermal radiation parameter provide more heat to working fluid that shows an enhancement in the temperature and thermal boundary layer thickness.

The effect of the Prandtl number (Pr) on $\theta(\eta)$ is seen in **Figure 10**. Since Pr is that the magnitude relation of the viscous diffusion rate to the thermal diffusion rate, the upper worth

Bi	*Le*	*R*	*c*	*λ*	*M*	**Absence**		**Presence**	
						C_{fx}	C_{fy}	C_{fx}	C_{fy}
0.2						1.2240	0.7261	1.3030	0.7836
0.4						1.1795	0.7280	1.2642	0.7847
0.6						1.1532	0.7289	1.2412	0.7854
	2					1.1719	0.7283	1.2575	0.7850
	3					1.1648	0.7285	1.2514	0.7851
	4					1.1619	0.7285	1.2489	0.7851
		1				1.1598	0.7289	1.2466	0.7855
		2				1.1420	0.7301	1.2300	0.7866
		3				1.1220	0.7314	1.2113	0.7878
			0.2			1.0852	0.2066	1.1657	0.2083
			0.4			1.1265	0.4509	1.2096	0.4657
			0.6			1.1648	0.7285	1.2514	0.7851
				0		1.3122	0.7242	1.3787	0.7816
				0.2		1.2523	0.7259	1.3143	0.7834
				0.4		1.1936	0.7276	1.2514	0.7851
					0	0.9611	0.5965	1.0281	0.6293
					0.5	1.1648	0.7285	1.2514	0.7851
					1	1.3441	0.8413	1.4521	0.9248

Table 2. Numerical result of skin friction coefficient for different physical parameter values for present and absence non Newtonian fluid.

of Prandtl number causes to scale back the thermal diffusivity. Consequently, for increasing values ofPr, the temperature profile gets decreases. The impact of Lewis number (Le) on nanoparticle concentration is plotted in **Figure 11**. It is evident that the larger values of Lewis number cause a reduction in nanoparticles concentration distribution. Lewis number depends on the Brownian diffusion coefficient. Higher Lewis number leads to the lower Brownian diffusion coefficient, which shows a weaker nanoparticle concentration.

Table 2 presents the numerical values of skin friction for various physical values in the presence and absence $(We = n = 0)$ of non-Newtonian fluid. It is observed that skin friction increase in both directions with increasing c for both presence and absence of non-Newtonian fluid. In the other hand, the skin friction coefficient decreases in both directions by increasingBi. The skin friction is higher in the presence of non-Newtonian fluid than in the absence of non-Newtonian fluid.

Table 3 also elucidates that, the wall temperature for different physical parameter for linear as well as nonlinear radiation. It reveals that, the wall temperature increases for increasing values of Bi, R and c for both linear and nonlinear radiation but the wall temperature decreases by

Bi	*Le*	*M*	*Nb*	*R*	*Nt*	Pr	*c*	Linear	Nonlinear
								$-\boldsymbol{Nu_x}(\mathbf{Re_x})^{-1/2}$	$-Nu_x(\mathbf{Re}_x)^{-1/2}$
0.2								0.1060	0.3289
0.4								0.1356	0.4683
0.6								0.1479	0.5421
	2							0.1825	0.5501
	3							0.1428	0.5102
	4							0.1200	0.4886
		0						0.1440	0.5206
		0.5						0.1428	0.5102
		1						0.1418	0.5011
			0.2					0.3354	0.8074
			0.4					0.2771	0.6974
			0.6					0.2091	0.5974
				1				0.1768	0.8621
				2				0.2059	1.5030
				3				0.2150	2.0523
					0			0.1834	0.5641
					0.5			0.1331	0.4971
					1			0.0913	0.4351
						2		0.2165	0.4958
						3		0.2059	0.5260
						4		0.1875	0.5307
							0.2	0.1268	0.4606
							0.4	0.1352	0.4870
							0.6	0.1428	0.5102

Table 3. Numerical result of Nusselt number for different physical parameter values for linear and non nonlinear radiation.

increasing Le, Nb, Nt and Pr. Further, it is noticed that the wall temperature is higher for nonlinear radiation than that linear radiation.

Table 4 clearly shows the numerical values of skin friction, Nusselt number and Sherwood number for various physical parameters values. It reveals that, numerical values of wall temperature $\theta(0)$ increase by increasing Bi, θ_w, R and c. In the other hand Nusselt number decreases by increasing. Le, M, Nb, Nt and Pr. From this table, the skin friction coefficient increases by increasing Bi and m. Further, the Sherwood number increases by increasing $Bi, \theta_w, R,$ Pr and We.

Bi	θ_w	Le	M	Nb	R	Nt	Pr	We	c	λ	$-C_{fx}$	$-C_{fy}$	$-Sh_x(\mathrm{Re}_x)^{-1/2}$	$-Nu_x(\mathrm{Re}_x)^{-1/2}$
0.2											1.3030	0.7836	1.4859	0.3289
0.4											1.2642	0.7847	1.4877	0.4683
0.6											1.2412	0.7854	1.4886	0.5421
	1.8										1.2434	0.7856	1.4825	0.7398
	2										1.2353	0.7860	1.4812	0.9218
	2.2										1.2250	0.7865	1.4814	1.1226
		2									1.2575	0.7850	1.1427	0.5501
		3									1.2514	0.7851	1.4882	0.5102
		4									1.2489	0.7851	1.7744	0.4886
			0								1.0281	0.6293	1.5340	0.5206
			0.5								1.2514	0.7851	1.4882	0.5102
			1								1.4521	0.9248	1.4493	0.5011
				0.2							1.3140	0.7831	1.2408	0.8074
				0.4							1.2926	0.7837	1.4118	0.6974
				0.6							1.2713	0.7844	1.4647	0.5974
					1						1.2466	0.7855	1.4781	0.8621
					2						1.2300	0.7866	1.4727	1.5030
					3						1.2113	0.7878	1.4740	2.0523
						0					1.2674	0.7845	1.4869	0.5641
						0.5					1.2472	0.7853	1.4901	0.4971
						1					1.2255	0.7863	1.5060	0.4351
							2				1.2113	0.7878	1.4740	0.4958
							3				1.2345	0.7863	1.4731	0.5260
							4				1.2449	0.7857	1.4767	0.5307
								0			1.1936	0.7276	1.4746	0.5070
								1			1.2974	0.8329	1.4985	0.5127
								2			1.3712	0.9109	1.5141	0.5164
									0.2		1.1657	0.2083	1.2770	0.4606
									0.4		1.2096	0.4657	1.3862	0.4870
									0.6		1.2514	0.7851	1.4882	0.5102
										0	1.3787	0.7816	1.4738	0.5068
										0.2	1.3143	0.7834	1.4811	0.5085
										0.4	1.2514	0.7851	1.4882	0.5102

Table 4. Numerical result of local skin friction coefficient, Sherwood number and Nusselt number for different physical parameter.

5. Conclusions

In the present study, influence of nonlinear radiation on three dimensional flow of an incompressible non-Newtonian Carreau nanofluid has been obtained. The obtained results are presented in tabulated and graphical form with relevant discussion and the Major findings from this study are:

The velocity profiles increase in $x-$ directions and decrease in the $y-$ direction by increasing the stretching parameter.

Concentration profile increase by increasing the values *Nb* but in case of *Nt* concentration profile decreases.

Nb and *Nt* parameter shows the increasing behavior for temperature profile.

Effects of *Le* nanoparticle fraction $\phi(\eta)$ show the decreasing behavior.

Magnetic parameter reduces the velocity profiles in both x and $y-$ directions.

Temperature and thermal boundary layer thickness are decreased when the Pr and tl number increases.

Nonlinear thermal radiation should be kept low to use it as a coolant factor.

The rate of heat transfer increases with the increases in parameters *Rd* and θ_w.

We also noticed that the velocity profile and its associated boundary layer thickness are increases by increasing the values of *We*.

Author details

Rudraswamy N.G.[1]*, Ganeshkumar K.[2], Krishnamurthy M.R.[3], Gireesha B.J.[2] and Venkatesh P.[1]

*Address all correspondence to: ngrudraswamy@gmail.com

1 Department of Mathematics, Sahyadri Science College (Autonomous), Kuvempu University, Shimoga, India

2 Department of P.G. Studies and Research in Mathematics, Kuvempu University, Shankaraghatta, India

3 Department of Mathematics, JNN College of Engineering, Shivamogga, India

References

[1] Anwar Bég O, Ghosh SK, Narahari M, Bég TA. Mathematical modelling of thermal radiation effects on transient gravity-driven optically-thick gray convection flow along

an inclined plate with pressure gradient. Chemical Engineering Communications. 2011; **198**:1-15

[2] Rahman MM, Eltayeb IA. Radiative heat transfer in a hydromagnetic nanofluid past a non-linear stretching surface with convective boundary condition. Meccanica. 2013;**48**: 601-615

[3] Rashidi MM, Ganesh NV, Abdul Hakeem AK, Ganga B. Buoyancy effect on MHD flow of nanofluid over a stretching sheet in the presence of thermal radiation. Journal of Molecular Liquids. October 2014;**198**:234-238

[4] Srinivas S, Muthuraj R. Effects of thermal radiation and space porosity on MHD mixed convection flow in a vertical channel using homotopy analysis method. Communications in Nonlinear Science and Numerical Simulation. 2010;**15**:2098-2108

[5] Zeeshan A, Majeed A, Ellahi R. Effect of magnetic dipole on viscous ferro-fluid past a stretching surface with thermal radiation. Journal of Molecular Liquids. 2016;**215**:549-554

[6] Cortell R. Fluid flow and radiative nonlinear heat transfer over stretching sheet. Journal of King Saud University Science. 2013;**26**:161-167

[7] Ferdows M, Khan MS, Anwar Bég O, Azad MAK, Alam MM. Numerical study of transient magnetohydrodynamic radiative free convection nanofluid flow from a stretching permeable surface. Proceedings of Institution of Mechanical E-Part E: Journal of Process Mechanical Engineering. 2014;**228**(3):181-196

[8] Anwar Bég O, Ferdows M, Bég A, Tasveer T, Ahmed MW, Alam MM. Radiative optically-dense magnetized transient reactive transport phenomena with cross diffusion and dissipation effects. Numer. Simul. Journal of Taiwan Institute of Chemical Engineers. 2016:15

[9] Pal D, Mondal H. Effects of Soret Dufour, chemical reaction and thermal radiation on MHD non-Darcy unsteady mixed convective heat and mass transfer over a stretching sheet. Communications in Nonlinear Science and Numerical Simulation. 2011;**16**(4):1942-1958

[10] Murthy PVSN, Mukherjee S, Srinivasacharya D. Combined radiation and mixed convection from a vertical wall with suction/injection in a non–Darcy porous medium. Acta Mechanica. 2004;**168**(3–4):145

[11] Sheikholeslami M, Ganji DD, Javed MY, Ellahi R. Effect of thermal radiation on magnetohydrodynamics nanofluid flow and heat transfer by means of two phase model. Journal of Magnetism and Magnetic Materials. 2015;**374**:36-43

[12] S. Snyder, N. Arockiam, P.E. Sojka, Secondary Atomization of Elastic Non-Newtonian Liquid Drops, In: AIAA Joint Propulsion Conference, Nashville, Tennessee, USA, 2010

[13] Kumar KG, Gireesha BJ, Rudraswamy NG, Gorla RSR. Melting heat transfer of hyperbolic tangent fluid over a stretching sheet with fluid particle suspension and thermal radiation. Communications in Numerical Analysis. 2017;**2017**(2):125-140

[14] Cortell R. Effects of viscous dissipation and radiation on the thermal boundary layer over a nonlinearly stretching sheet. Physical Letters A. 2008;**372**(5):631-636

[15] Batalle RC. Viscoelastic fluid flow and heat transfer over a stretching sheet under the effects of a non-uniform heat source, viscous dissipation and thermal radiation. International Journal of Heat and Mass Transfer. 2007;**50**(15–16):3152-3162

[16] Khan M, Hussain M, Azam M. Magnetohydrodynamic flow of Carreau fluid over a convectively heated surface in the presence of non-linear radiation. JMMM. 2016;**412**:63-68

[17] Khan MI, Alsaedi A, Shehzad SA, Hayat T. Hydromagnetic nonlinear thermally radiative nanoliquid flow with Newtonian heat and mass conditions. Results Physics. 2017;**7**:2255-2260

[18] Rana P, Bhargava R. Numerical study of heat transfer enhancement in mixed convection flow along a vertical plate with heat source/sink utilizing nanofluids. Communication in Nonlinear Science Numerical Simulation. 2011;**16**(11):4318-4334

[19] Hayat T, Shehzad SA, Alsaedi A, Alhothuali MS. Mixed convection stagnation point flow of Casson fluid with convective boundary conditions. Chinese Physics Letters. 2012; **29**(11):114704. https://doi.org/10.1088/0256-307X/29/11/114704

[20] Laxmi T, Shankar B. Effect of nonlinear thermal radiation on boundary layer flow of viscous fluid over nonlinear stretching sheet with injection/suction. Journal of Applied Mathematical Physics. 2016;**4**:307-319

[21] Kumar KG, Rudraswamy NG, Gireesha BJ, Manjunatha S. Non-linear thermal radiation effect on Williamson fluid with particle-liquid suspension past a stretching surface. Results in Physics. 2017;**7**:3196-3202

[22] Kumar KG, Gireesha BJ, Manjunatha S, Rudraswamy NG. Effect of nonlinear thermal radiation on double-diffusive mixed convection boundary layer flow of viscoelastic nanofluid over a stretching sheet. International Journal of Mechanical Material Engineering. 2017;**12**(1):18

[23] Mabood F, Imtiaz M, Alsaedi A, Hayat T. Unsteady convective boundary layer flow of Maxwell fluid with nonlinear thermal radiation: A numerical study. International Journal of Nonlinear Science Numerical Simulation. 2016;**17**(5):221-229

[24] Shehzad SA, Hayat T, Alsaedi A, Obid MA. Nonlinear thermal radiation in three-dimensional flow of Jeffrey nanofluid: A model for solar energy. Applied Mathematics and Computation. 2016;**248**:273-286

[25] Hayat T, Muhammad T, Alsaedi A, Alhuthali MS. Magnetohydrodynamic three-dimensional flow of viscoelastic nanofluid in the presence of nonlinear thermal radiation. JMMM. 2015;**385**:222-229

[26] Rudraswamy NG, Kumar KG, Gireesha BJ, Gorla RSR. Soret and Dufour effects in three-dimensional flow of Jeffery nanofluid in the presence of nonlinear thermal radiation. Journal of Nanoengineering Nanomanufacturing. 2016;**6**(4):278-287

[27] Wang CY. The three-dimensional flow due to a stretching sheet. Physics of Fluids. 1984;**27**: 1915-1917

[28] Hayat T, Muhammad T, Shehzad SA, Alsaedi A. Similarity solution to three dimensional boundary layer flow of second grade nanofluid past a stretching surface with thermal radiation and heat source/sink. AIP Advances. 2015;**5**:017107. https://doi.org/10.1063/1.4905780

[29] Shehzad SA, Hayat T, Alsaedi A. MHD three dimensional flow of viscoelastic fluid with thermal radiation and variable thermal conductivity. A Journal of Central South University. 2014;**21**(10):3911-3917

[30] Hayat T, Shehzad SA, Alsaedi A. Three-dimensional stretched flow of Jeffrey fluid with variable thermal conductivity and thermal radiation. Applied Mathematics and Mechanics. 2013;**34**:823-832

Chapter 4

Effective Thermal Conductivity of Cupra and Polyester Fiber Assemblies in Low Fiber Volume Fraction

Morihiro Yoneda

Additional information is available at the end of the chapter

http://dx.doi.org/10.5772/intechopen.75604

Abstract

In this study, the effective thermal conductivity of staple fiber assembly for wadding use is measured using KES-F7 II Thermo Labo II apparatus. Sample used are cupra, polyester (with round and heteromorphic section), and polytrimethylene terephthalate (PTT) fibers. Heat flux to calculate thermal conductivity is measured including heat leakage from sidewall and is calibrated in the analysis. Results are analyzed by nonlinear regression method. Results are obtained as follows. Thermal conductivity curve is convex downward in low fiber volume fraction (<3%). Thermal conductivity, λ, is expressed as following equation, $\lambda = A\phi + B/\phi + C$, where ϕ is fiber volume fraction, A and B are coefficients, and C is constant determined by nonlinear regression analysis. Based on this equation, the effective thermal conductivity is divided into three parts: $A\phi$, heat conduction in fiber; B/ϕ, radiative heat transfer; and C, heat conduction within air. By calibration, C component is divided into thermal conductivity of air, λ_{air} and heat leakage from sidewall of the sample frame. λ_{air} plays the most important role in thermal insulation property of fiber assembly, and component of heat conduction in fiber, $A\phi$, follows in higher fiber volume fraction. Component of radiative heat transfer, B/ϕ, is negligible small.

Keywords: effective thermal conductivity, fiber assembly, cupra fiber, polyester fiber, nonlinear regression

1. Introduction

In this chapter, a method to evaluate thermal insulation properties of staple fiber assembly for wadding use is proposed. Fiber assembly in low fiber volume fraction is a system which consists of a lot of air and a small amount of fiber, and its heat transfer mechanism is supposed to include convective and radiative heat transfer in addition to conductive heat transfer.

Therefore, it is not suitable to use thermal conductivity to evaluate thermophysical properties of fiber assembly. Instead, a concept of effective thermal conductivity is suitable to evaluate thermophysical properties of fiber assembly which can include different types of heat transfer mechanisms such as conduction, convection, and radiation. In this chapter, the effective thermal conductivity is used to evaluate thermal insulation properties of fiber assembly in low Fiber volume fraction, Φ for wadding use. In addition, a model to explain heat transfer mechanism within fiber assembly is proposed.

Effective thermal conductivity is measured based on guarded hot plate (GHP) method using KES-F7II Thermo Labo II apparatus (Kato Tech Ltd.). Fiber sample is put uniformly into sample frame made of polystyrene foam. In the measurement, sample system made of fiber assembly and sample frame is placed between heat source plate and heat sink, and heat flow to keep heat source temperature constant is measured.

Samples used are polyethylene terephthalate and cupra staple fiber assembly. Effective thermal conductivity is measured under various sample thickness and fiber volume fraction. The results are analyzed based on nonlinear regression method, and heat transfer mechanism within fiber assembly is discussed based on the result of analysis. Finally, designing of fiber assembly-based thermal insulation materials is investigated.

2. Background

Studies on heat conduction of fiber assembly have been conducted by Nogai et al. [1, 2], Fujimoto et al. [3], and Ohmura et al. [4] in Japan. Nogai et al. carried out theoretical and experimental study of heat transfer mechanism of polyester fiber assembly [1, 2]. Fujimoto et al. investigated the effective thermal conductivity of clothing materials for protection against cold [3]. Ohmura et al. studied the effective thermal conductivity of fibrous thermal insulation materials for building [4].

In all papers, it is confirmed that effective thermal conductivity- fiber volume fraction curve in low fiber volume fraction (<10%) shows the shape of convex downward. The fact that effective thermal conductivity curve has a minimum value gives a reason that fiber assembly have been widely used for thermal insulation materials. The minimum value in effective thermal conductivity curve was explained by increasing radiative heat transfer through pore space with increasing porosity based on their experimental and theoretical results and heat transfer model. Nogai et al. [1, 2] derived these facts based on uniaxial-oriented fiber assembly model considering conduction in fiber and radiative heat transfer. Fujimoto et al. [3] derived these facts based on serial-parallel model of heat transfer which is composed of fiber and pore part including radiative heat transfer.

In this study, effective thermal conductivity of fiber assembly in low fiber volume fraction is analyzed using empirical equation by nonlinear regression method [4–7]. The reason that fiber assembly has been used for thermal insulation materials is further investigated through the separation of heat transfer component of effective thermal conductivity.

3. Method

3.1. Materials

Four kinds of fiber materials used in this experiment such as cupra fiber (CU), polyester fiber with round section (RPE), polyester fiber with heteromorphic (W-shape) section (WPE), and polytrimethylene terephthalate fiber (PTT) of which fineness and fiber length are almost the same. The web after opening and carding process is conditioned under the environment of 20°C and 65% RH for 24 h. Fiber assembly is served as sample after conditioning. The details of fiber samples are shown in **Table 1**.

Main parameter for the measurement of effective thermal conductivity is fiber volume fraction in this experiment. Thermophysical properties for different fiber materials which have different specific gravity are compared under the same fiber volume fraction. Fiber volume fraction is defined as the ratio of fiber volume to apparent volume of fiber assembly. Fiber volume fraction Φ is calculated using following equation.

$$\Phi = \frac{W}{\rho_f d h^2} \tag{1}$$

where W is sample weight (g), ρf is specific gravity of fiber (n.d.), h is side length of heat plate (cm), and d is thickness of sample (cm). Staple fiber sample (W g) is filled uniformly into the space surrounded by wall of polystyrene foam of which inner size is 5 cm square and constant height (2, 3, and 5 cm). **Figure 1** shows sample frame filled with fiber assembly. **Figure 2** shows a plan of sample frame.

In this experiment, the effect of fiber volume fraction and sample thickness on effective thermal conductivity of fiber assembly is investigated. Fiber volume fraction is changed by five

Sample code	Detail of sample	Fineness (dtex)	Fiber length (mm)	Fiber diameter (μm)	Specific gravity (n.d.)	Percentage of crimp (%)
CU	Cupra-ammonium (Cupra) staple fiber	1.4	38	11.84	1.50	8.79
RPE	Polyester staple fiber with round section	1.3	38	12.76	1.38	26.70
WPE	Polyester staple fiber with w-shaped heteromorphic section	1.4	38	24.22*1 6.27*2	1.38	14.80
PTT	Polytrimethyleneterephtalate staple fiber	1.7	51	15.02	1.34	15.43

*1: a longer axis, *2: a minor axis

Table 1. Details of fiber samples for wadding use.

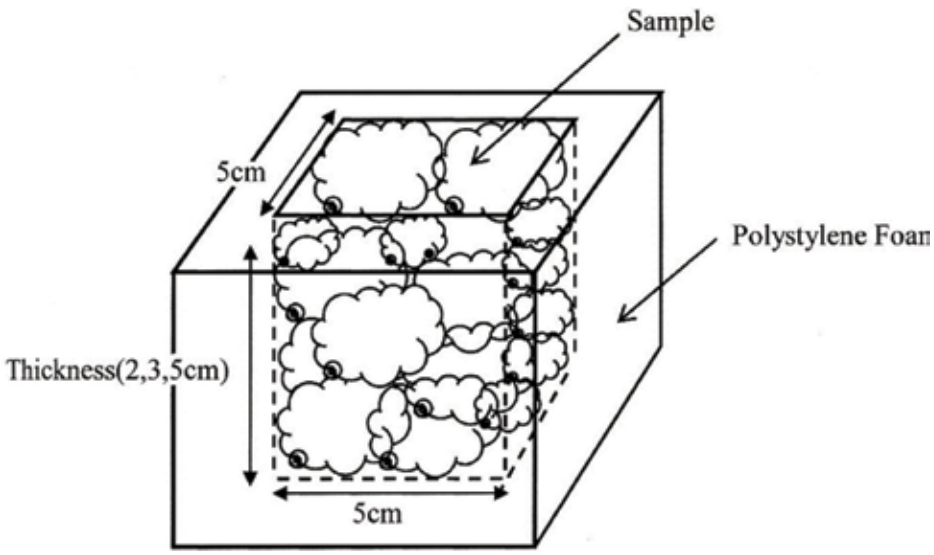

Figure 1. Schematic diagram of filling fiber sample into frame made of polystyrene foam.

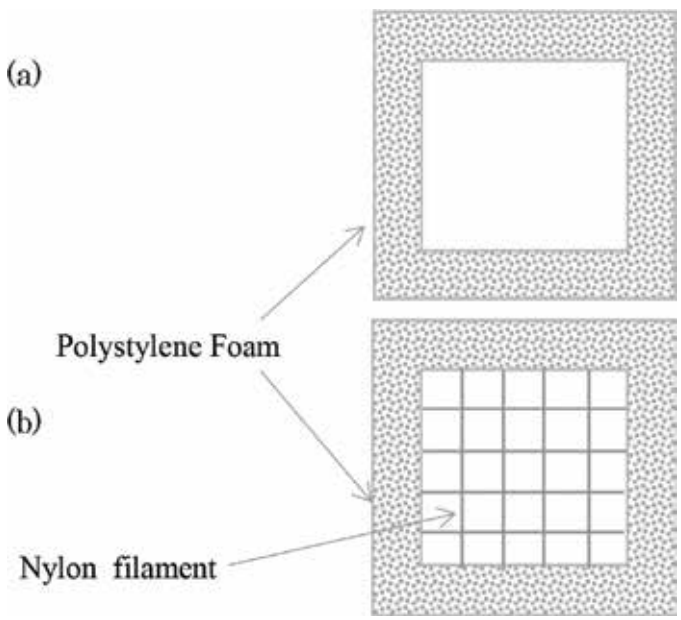

Figure 2. Frame made of polystyrene foam (a) top view and (b) bottom view.

stages such as 0.001, 0.005, 0.010, 0.025, and 0.030. Sample thickness is changed by three stages such as 2, 3, and 5 cm. One kind of fiber is, therefore, measured under 15 conditions. Sample weight for each fiber under different condition is shown in **Table 2**.

http://dx.doi.org/10.5772/intechopen.75604

3.2. Measurement method

Effective thermal conductivity is measured using KES-F7II Thermo Labo II apparatus (Kato Tech Ltd.) [8]. Heat flux which flows through fabric sample from heat source plate (BT-Box) to heat sink is measured based on guarded hot plate (GHP) method. Schematic diagram of measurement part (section) is shown in **Figure 3**. Fiber sample is put uniformly into frame made of polystyrene foam of which inner size is 5 cm square and constant thickness. Fiber assembly with sample frame is placed between heat source plate and heat sink and measurement of heat flow is carried out. The experiment is conducted in a controlled environment room of which temperature is 20°C and humidity is 65% RH.

Heat source temperature (BT-Box) is set at 30°C and temperature of heat sink is set at 20°C, and thus, temperature difference is 10°C. Heat source plate is placed on upper side of sample and heat sink is placed on lower side, and thus the direction of heat flow agrees with the direction of acceleration of gravity. Upper side of heat sink is made of metal plate and temperature of heat sink is controlled at 20°C by cooling device driven by Peltier element.

Sample	Volume fraction	Thickness of a sample		
		2cm	3cm	5cm
Cupra	0.001	0.075	0.113	0.188
	0.005	0.375	0.563	0.938
	0.010	0.750	1.125	1.875
	0.025	1.875	2.813	4.688
	0.030	2.250	3.375	5.625
Polyester	0.001	0.069	0.104	0.173
	0.005	0.345	0.518	0.863
	0.010	0.690	1.035	1.725
	0.025	1.725	2.588	4.313
	0.030	2.070	3.105	5.175
PTT	0.001	0.067	0.101	0.168
	0.005	0.335	0.503	0.838
	0.010	0.670	1.005	1.675
	0.025	1.675	2.513	4.188
	0.030	2.010	3.015	5.025

Table 2. Sample weight for each measurement condition (unit: G).

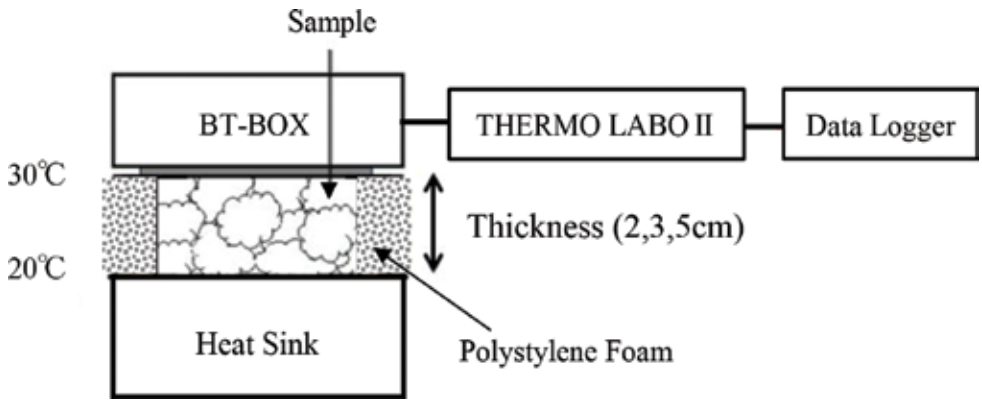

Figure 3. Measurement of thermal conductivity.

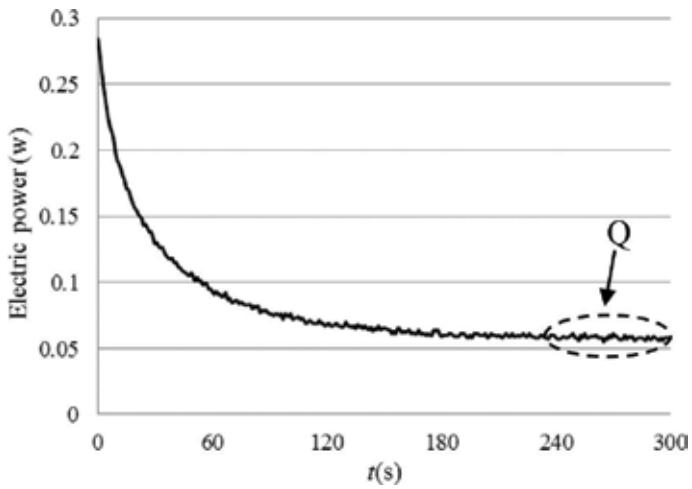

Figure 4. Method to obtain heat flux in steady state.

In the measurement, fiber assembly with sample frame is placed between heat source plate and heat sink, and electric power (W) is measured to keep heat source temperature steady state. Output signal of electric power is recorded with data logger which is connected to output terminal. Output signal is recorded at intervals of 1 s with time elapsed. An example of measurement is shown in **Figure 4**. Electric power is recorded against time from the contact between heat source and sample to the steady sate. Electric power, Q (W), is obtained from mean value between 4 and 5 min. Effective thermal conductivity, λ (W/mK), is calculated from the following equation:

$$\lambda = \frac{Qd}{A\Delta T} \tag{2}$$

where Q is electric power to keep steady state (W), d is sample thickness (m), A is area of heat source plate, and ΔT is temperature difference between heat source plate and heat sink (K).

In this experiment, a small amount of heat flow through insulation material is measured. Therefore, care must be taken so that measurement part (BT-Box and heat sink) is not affected by unexpected influence of heat caused by convective and radiative heat transfer. As for radiative heat transfer, board made of polystyrene foam is set up in the front, right, and left side of measurement part to block radiative heat transfer from operator. As for convective heat transfer, it is desirable that a device which may cause convection should be removed from the place where experiment is conducted.

4. Results

Effective thermal conductivity of staple fiber assembly is measured under three different thickness and five different fiber volume fractions. Results obtained from the measurement are investigated in connection with fiber volume fraction, sample thickness, fiber materials, and so on. In this experiment, three times of measurement were carried out for each condition, and mean value and standard deviation were obtained.

In the first place, the relation between effective thermal conductivity and fiber volume fraction is investigated in relation to fiber material. **Figures 5–7** show the results between effective thermal conductivity and fiber volume fraction. **Figures 5–7** show the results of 2, 3, and 5 cm thickness, respectively. In each graph, the ordinate denotes effective thermal conductivity (W/mK) and the abscissa denotes fiber volume fraction (n.d.). The fact that the level of the magnitude of thermal conductivity increases with increasing thickness is observed and this will be discussed later. Here, we concentrate on the relation between effective thermal conductivity and fiber

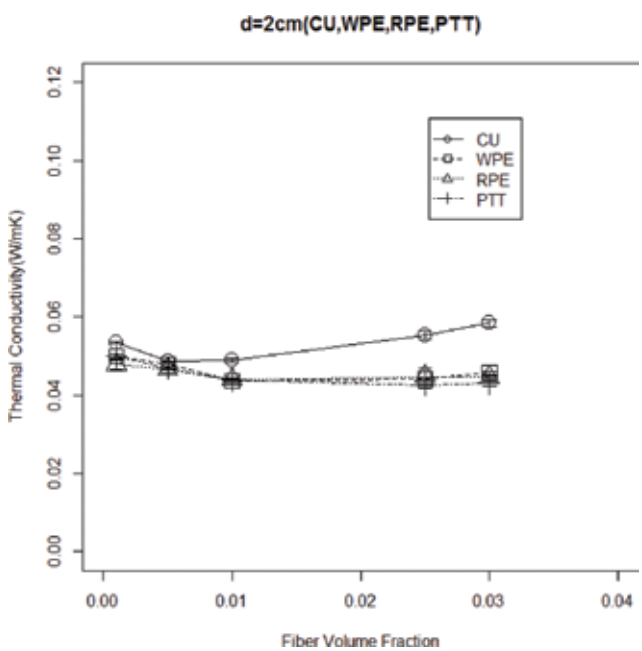

Figure 5. Thermal conductivity plotted against fiber volume fraction when thickness of sample is 2 cm.

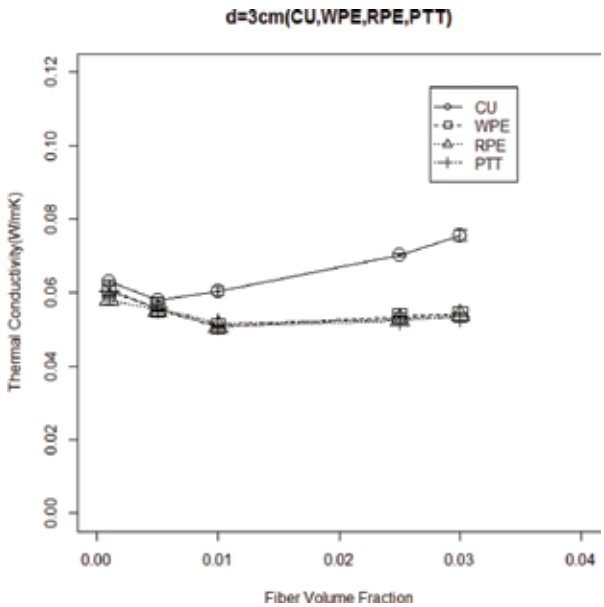

Figure 6. Thermal conductivity plotted against fiber volume fraction when thickness of sample is 3 cm.

volume fraction for the result of 5-cm thickness. Magnitude of effective thermal conductivity is compared under constant thickness. CU is the largest and polyester fiber group (RPE, WPE, PTT) follows. There is no significant difference among RPE, WPE, and PTT within the range of this method.

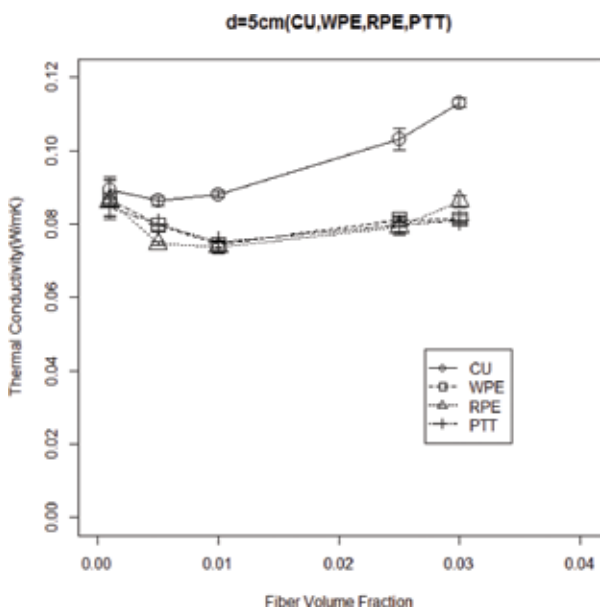

Figure 7. Thermal conductivity plotted against fiber volume fraction when thickness of sample is 5 cm.

http://dx.doi.org/10.5772/intechopen.75604

Next, the effect of fiber material on the relation between effective thermal conductivity and fiber volume fraction is investigated. For each material, the shape of thermal conductivity curve is convex downward. The feature of the curve for each fiber material is as follows.

For CU, the minimum value of thermal conductivity lies around $\phi = 0.005$ and thermal conductivity increases with increasing ϕ. For RPE, WPE, and PTT, the minimum value of thermal conductivity lies around $\phi = 0.01$ and thermal conductivity increases a little to $\phi = 0.03$. For CU, thermal conductivity increases a little when ϕ decreases from 0.005 to 0.001. For RPE, WPE, and PTT, thermal conductivity increases a little when ϕ decreases from 0.01 to 0.001. With decreasing thickness from 3 to 2 cm, the level of thermal conductivity decreases and the shape of curve becomes flattened.

Figure 8 shows the relationship between effective thermal conductivity and sample thickness for $\phi = 0.01$. The ordinate denotes effective thermal conductivity and the abscissa denotes sample thickness. Clearly, thermal conductivity increases linearly against thickness for all samples.

Effective thermal conductivity obtained in this section is tentative value including leakage of heat from sidewall. In the following section, the separation of effective thermal conductivity into elemental process of heat transfer will be discussed. The thickness dependence of effective thermal conductivity shown in **Figure 8** will be investigated after the discussion about the separation heat transfer component.

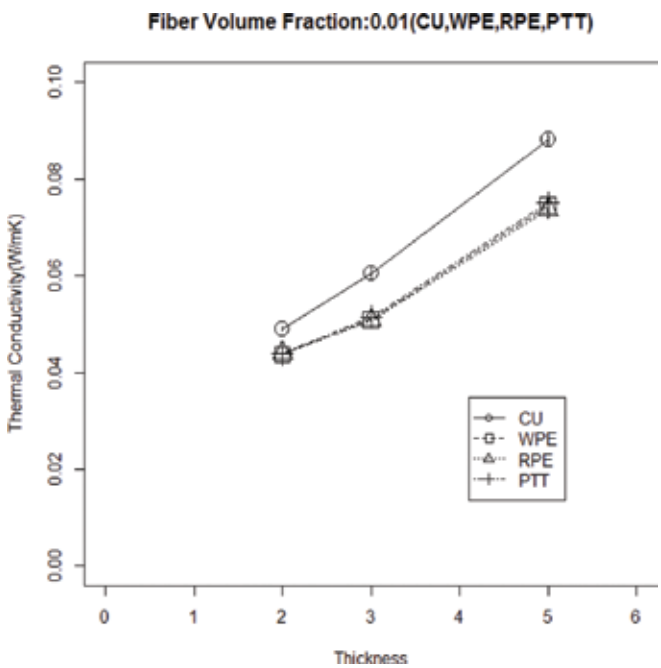

Figure 8. Thermal conductivity plotted against thickness when volume fraction of sample is 0.01.

5. Analysis

5.1. Analysis by nonlinear regression model

Because porosity of fiber assembly in this study is very large (97–99%), it is conjectured that the mechanism of heat transfer within fiber assembly is very much influenced by the effect originated from pore structure. The mechanism of heat transfer in fiber assembly consists of conduction in fiber, radiation in pore between fibers, and gas conduction (air), when forced convection does not occur. Here, it is supposed that heat flows through parallel model which is made of three components of heat transfer mentioned above. Measured value of effective thermal conductivity, λ (W/mK), is expressed by the following equation as a function of bulk density ρ(kg/m^3) [4–7]:

$$\lambda = A\rho + B/\rho + C. \tag{3}$$

where A (Wm^2/Kkg) and B (Wkg/m^{4}K) are constant coefficients and C (W/mK) is constant. The first term at the right side denotes conductive heat transfer in fiber, the second term

Parameter	Sample code	Thickness of a sample		
		2cm	3cm	5cm
A	CU	4.51×10^{-1}	7.51×10^{-1}	1.04
	RPE	-2.45×10^{-2}	3.76×10^{-1}	5.54×10^{-1}
	WPE	-1.68×10^{-2}	7.68×10^{-2}	2.51×10^{-1}
	PTT	-1.04×10^{-1}	5.25×10^{-3}	1.83×10^{-1}
B	CU	9.03×10^{-6}	1.04×10^{-5}	1.05×10^{-5}
	RPE	2.73×10^{-6}	6.42×10^{-6}	1.89×10^{-5}
	WPE	5.20×10^{-6}	9.62×10^{-6}	1.30×10^{-5}
	PTT	4.68×10^{-6}	8.10×10^{-6}	9.75×10^{-6}
C	CU	4.41×10^{-2}	5.20×10^{-2}	7.78×10^{-2}
	RPE	4.52×10^{-2}	5.18×10^{-2}	6.70×10^{-2}
	WPE	4.51×10^{-2}	5.13×10^{-2}	7.36×10^{-2}
	PTT	4.54×10^{-2}	5.25×10^{-2}	7.48×10^{-2}
Air		2.62×10^{-2}	2.62×10^{-2}	2.62×10^{-2}

Table 3. List of coefficients A, B, and constant C.

denotes radiative heat transfer, and the third term denotes conductive heat transfer through gas (air) in pore. (The details of parameters A, B, and C are shown in the Appendix.)

In this study, bulk density, ρ in Eq. (3) is replaced by fiber volume fraction, ϕ as follows,

$$\lambda = A\phi + B/\phi + C. \tag{4}$$

This is because ϕ plays an equivalent role of ρ which expresses quantity of fiber. Results of the effective thermal conductivity of fiber assembly are analyzed by nonlinear regression method based on Eq. (4). Nonlinear regression analysis is carried out using **R** (ver. 3.1.1).

Estimated values of parameters A, B, and C obtained by nonlinear regression analysis are shown in **Table 3**, where A is coefficient of conduction in fiber, B is coefficient of radiative heat transfer, and C is conductive heat transfer in gas (constant). Calculated values of effective thermal conductivity using estimated values of A, B, and C are shown in **Figures 9–12**. **Figures 9–12** show the results of thickness of 2, 3, and 5 cm for CU, RPE, WPE, and PTT fiber, respectively. In each graph, the ordinate denotes effective thermal conductivity, λ(W/mK),

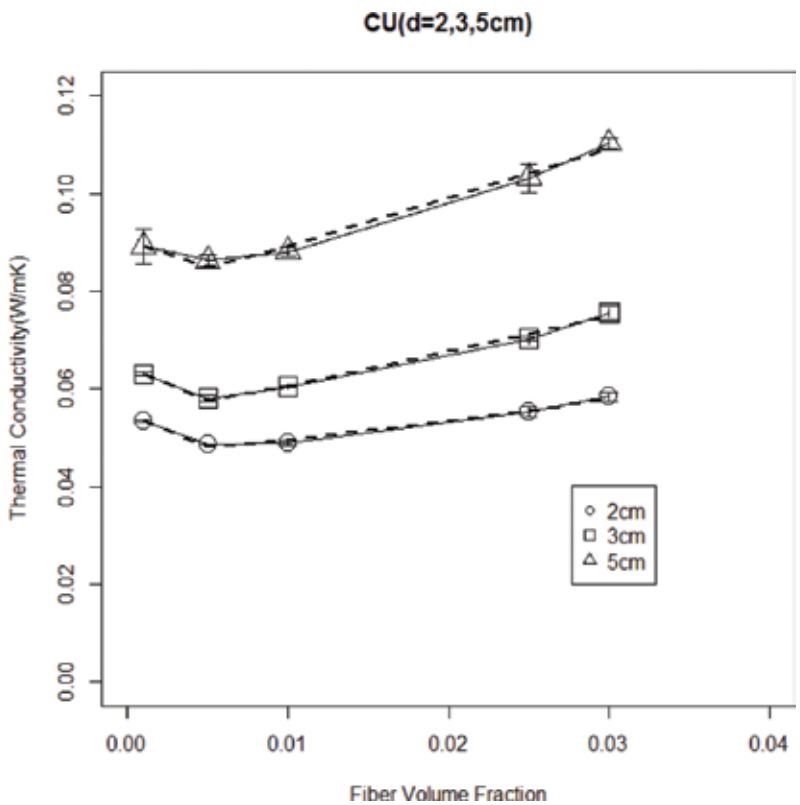

Figure 9. Comparison between calculated and measured values for CU. Symbols ○, □, △, and straight line: Measured values; broken line: Calculated values obtained by nonlinear regression analysis.

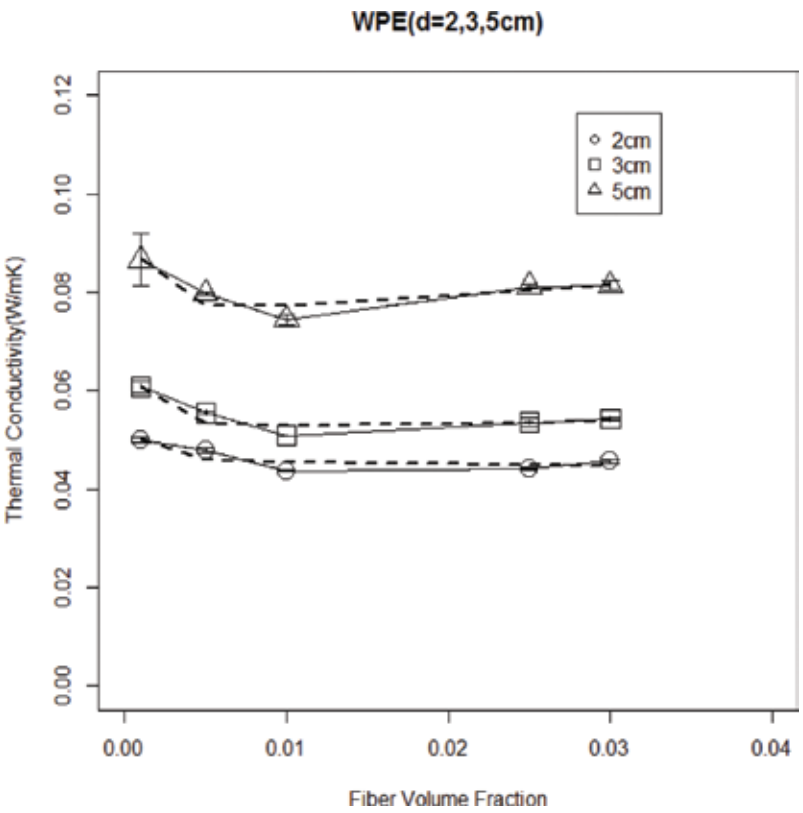

Figure 10. Comparison between calculated and measured values for WPE. Symbols ○, □, △, and straight line: Measured values; broken line: Calculated values obtained by nonlinear regression analysis.

and the abscissa denotes fiber volume fraction (n.d.). Symbols (○, △, □) and solid line show measured values, and broken line shows regression curve using estimated values of A, B, and C. As shown in figures, agreement between measured and calculated curves of effective thermal conductivity is very good.

5.2. Analysis of heat transfer components

Calculated curves of separation of components using estimated values of A, B, and C are shown in **Figures 13–16**. **Figures 13–16** show the results of 3-cm thickness for CU, RPE, WPE, and PTT fiber, respectively. The ordinate denotes effective thermal conductivity, λ(W/mK), and the abscissa denotes fiber volume fraction, ϕ(n.d.). Dashed line shows component of conduction in fiber, Aϕ, dash-dotted line shows component of radiative heat transfer, B/ϕ, two-dot chain line shows component of gas conduction, C, and solid line shows the measured value of effective thermal conductivity. Based on these graphs, the ratio of each component to effective thermal conductivity and the effect of pore in fiber assembly can be discussed for each fiber materials. It is clear that the ratio among Aϕ, B/ϕ, and C is different for different fiber materials.

http://dx.doi.org/10.5772/intechopen.75604

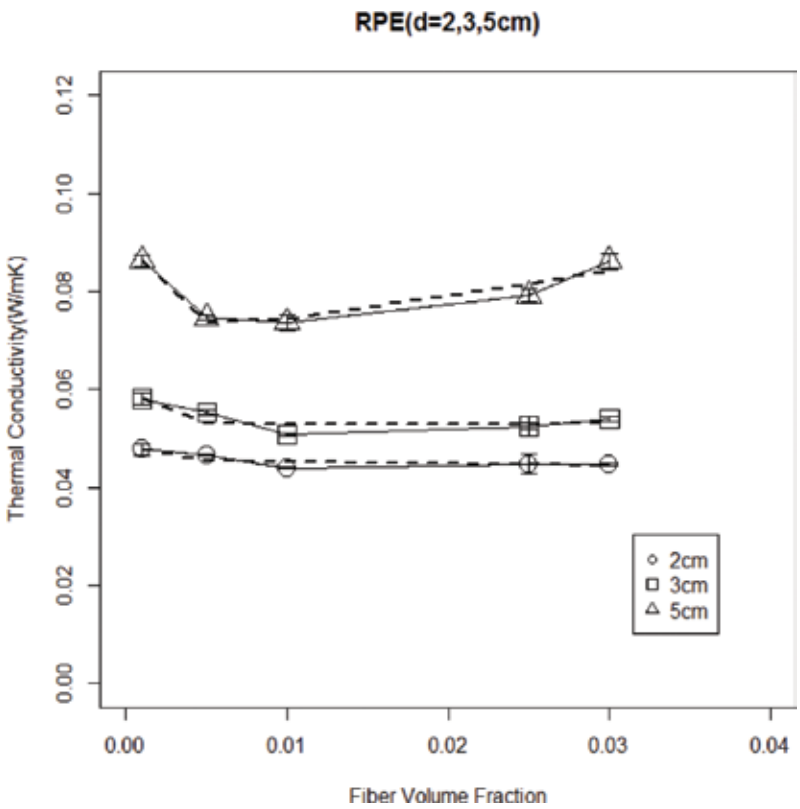

Figure 11. Comparison between calculated and measured values for RPE. Symbols ○, □, ∆, and straight line: Measured values; broken line: Calculated values obtained by nonlinear regression analysis.

First, component of conduction in fiber, Aϕ is investigated. Physical meaning of A is increasing rate of conduction in fiber against ϕ. As shown in **Table 3**, coefficient A varies with fiber materials. CU has large A value compared to polyester fibers (RPE, WPE, PTT), and increasing rate of conduction in fiber is also large. As a result, the ratio of Aϕ to effective thermal conductivity of CU is 30 percent at ϕ = 0.03. In contrast, the ratio of Aϕ of WPE is less than 20% at ϕ = 0.03. Large ratio of conduction in fiber and large increasing ratio to ϕ is the feature of CU fiber compared to polyester fibers.

Second, component of radiative heat transfer, B/ϕ, is investigated. Generally, the ratio of B/ϕ to effective thermal conductivity is negligibly small for all samples. Contribution of B/ϕ is slightly recognized below ϕ = 0.005. It is observed that component of radiative heat transfer increases with decreasing fiber volume fraction, ϕ, from 0.005 to 0.001. In this study, the ratio of radiative heat transfer is very small compared to the previous results obtained by Nogai and Fujimoto [1–3]. This may arise from the difference in the degree of fiber orientation in fiber assembly. While Nogai and Fujimoto [1–3] cover fiber assembly with high degree of fiber orientation, we concentrate on fiber assembly with random orientation. Because frequency of collision between radiant heat and fiber is very large for randomly oriented fiber assembly, decay of radiation energy by absorption may become large.

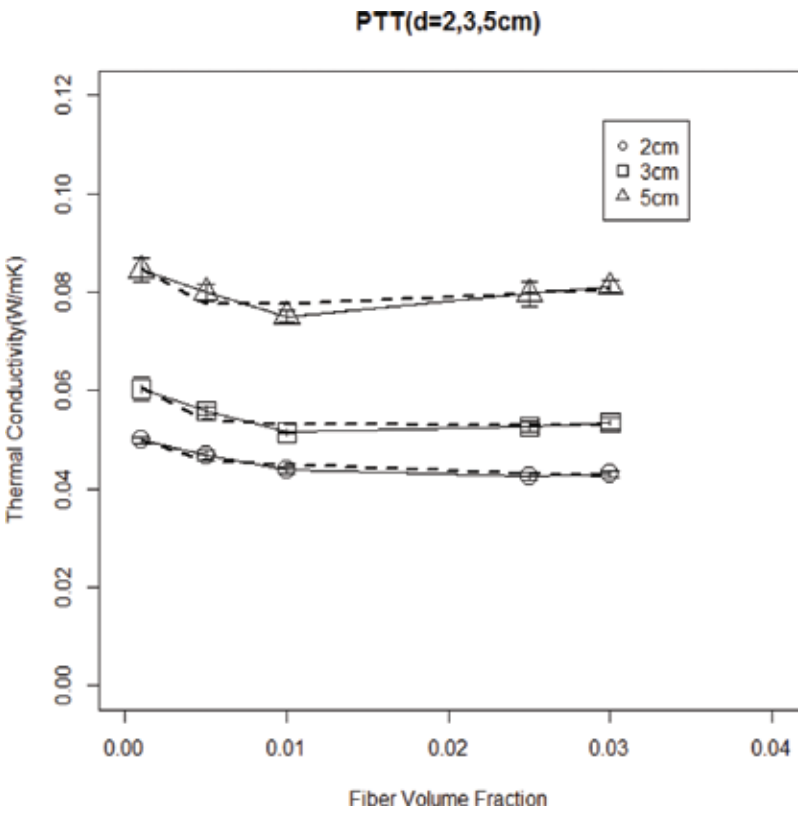

Figure 12. Comparison between calculated and measured values for PTT. Symbols ○, □, △, and straight line: Measured values; broken line: Calculated values obtained by using nonlinear regression analysis method.

5.3. Analysis of gas conduction

In this section, component of gas conduction, C, is investigated. Looking over **Figures 13–16**, it seems that component of gas conduction, C, occupies the dominant part in effective thermal conductivity in many cases. Therefore, physical meaning of gas conduction C is discussed, hereafter. Estimated values of C for samples of 2-, 3-, and 5-cm thickness are shown in the lower part of **Table 3**. It seems that C values for each thickness have almost constant value despite different samples. On the other hand, the value of thermal conductivity of air, λ_{air}, in this measurement condition (25°C, 1 atm) is 2.62×10^{-4} (W/mK) in Ref. [9]. Taking into consideration that parameter C has same value for same thickness and C must include thermal conductivity of air, λ_{air}, let us suppose that following relation holds:

$$C = \lambda_{air} + C' \tag{5}$$

where C′ is constant independent of fiber volume fraction, ϕ. Mean values of each thickness, C_{mean}, thermal conductivity of air, λ_{air} and C′ are shown in **Table 4** for the discussion in this section. It seems that C′ increases with increasing thickness. Relation between C′ and thickness

http://dx.doi.org/10.5772/intechopen.75604

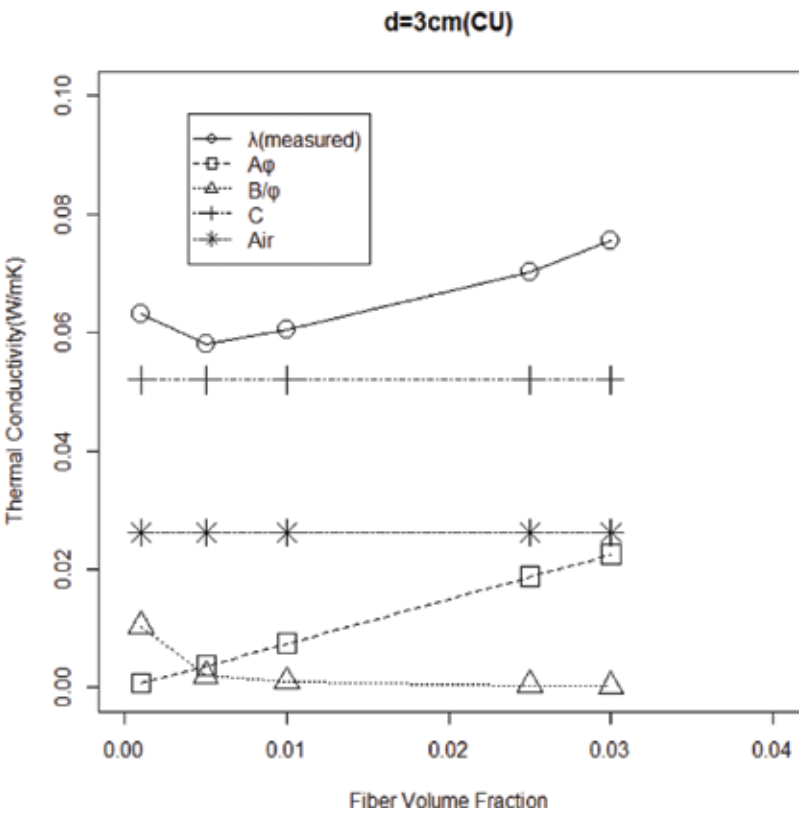

Figure 13. Separation of heat transfer component by nonlinear regression analysis for CU.

is analyzed by linear regression method. The results are shown in **Figure 17**. C′ and thickness, d, have good correlation, and the regression equation is given as follows,

$$C' = 0.9325\,d - 0.0425\ (R^2 = 0.996). \tag{6}$$

Because intercept is almost 0, C′ can be expressed approximately as linear function of d:

$$C' = k\,d\ (k\text{:constant}) \tag{7}$$

On the other hand, a function which expresses leakage of heat from sidewall of the frame is derived from another point of view. As inner side length of sample frame is 5 cm, total area of sidewall, A is expressed as following equation:

$$A = 4 \times 5 \times d\ (cm^2). \tag{8}$$

Here, temperature gradient along thickness direction is ignored for the simplification. Thus, leakage of heat per unit area along horizontal direction is assumed to be constant. Total leakage of heat from sidewall, Q′, is proportional to total area of sidewall which is expressed as follows:

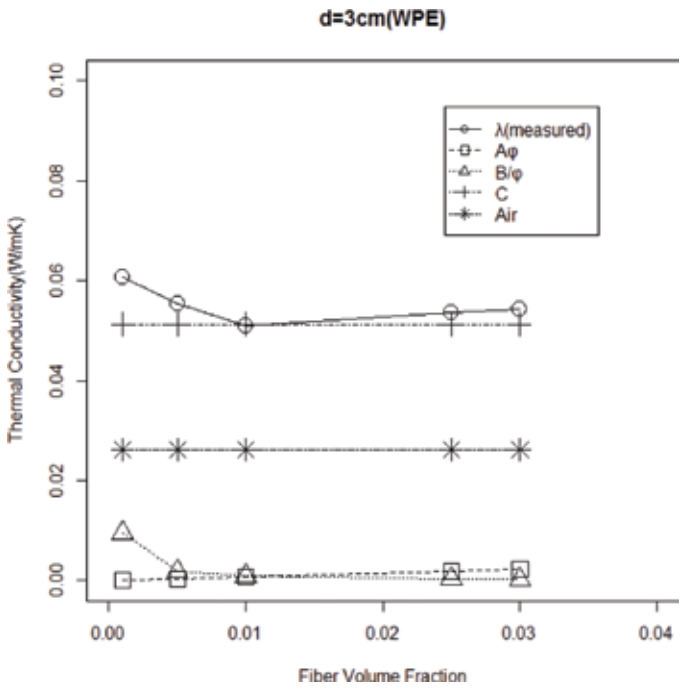

Figure 14. Separation of heat transfer component by nonlinear regression analysis for WPE.

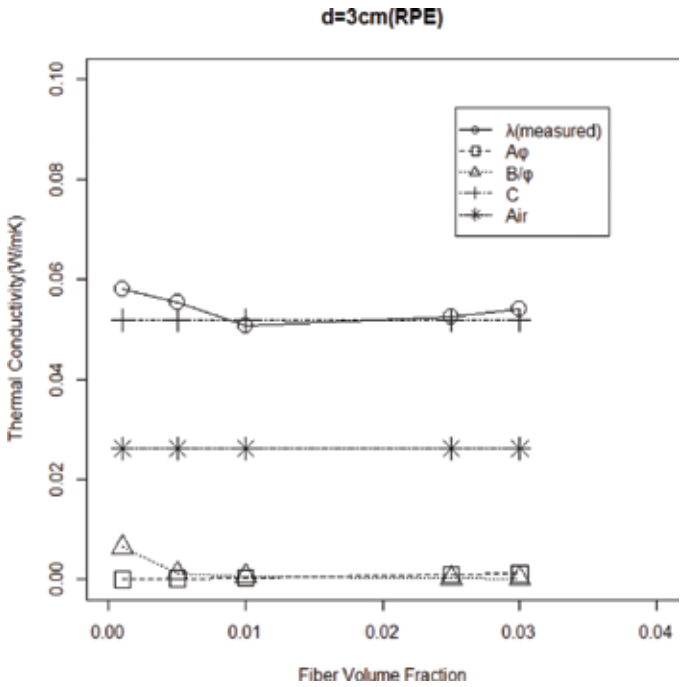

Figure 15. Separation of heat transfer component by nonlinear regression analysis for RPE.

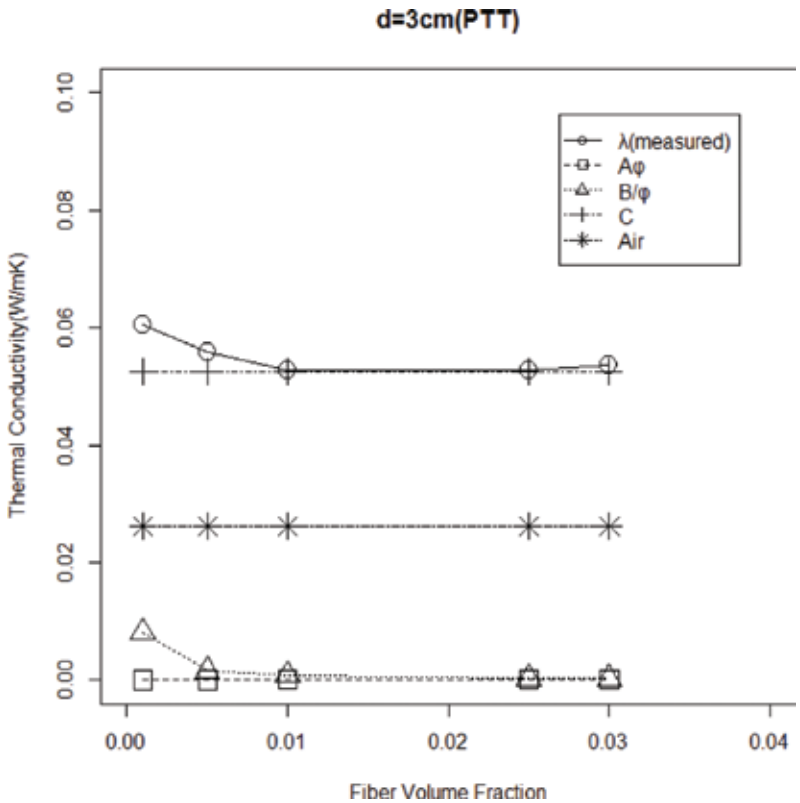

Figure 16. Separation of heat transfer component by nonlinear regression analysis for PTT.

$$Q' \propto A \propto d \tag{9}$$

This equation predicts that total leakage of heat from sidewall is proportional to thickness, d, and equals 0 at d = 0. This property coincides with the expression, C′ = k d in Eq. (7). Summarizing the discussion above, C′ can be regarded as total leakage of heat from sidewall.

Based on the discussion above, total leakage of heat, C′, can be eliminated from C value. Here, C values in **Figures 13–16** can be replaced by λ_{air} (=C-C′). The results are shown in **Figures 18–21**, where the abscissa denotes true effective thermal conductivity. It is concluded that large part

Thickness (cm)	C_{mean}	λ_{air}	C′
2	4.495×10^{-2}	2.62×10^{-2}	1.875×10^{-2}
3	5.19×10^{-2}	2.62×10^{-2}	2.57×10^{-2}
5	7.33×10^{-2}	2.62×10^{-2}	4.71×10^{-2}

Unit: W/mK

Table 4. Figures for calibration of leakage of heat.

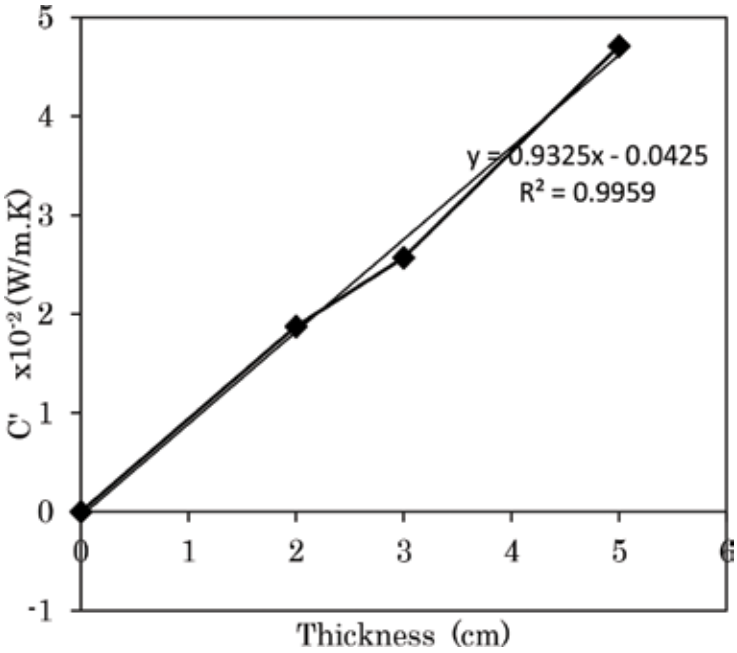

Figure 17. Function for the calibration of leakage of heat.

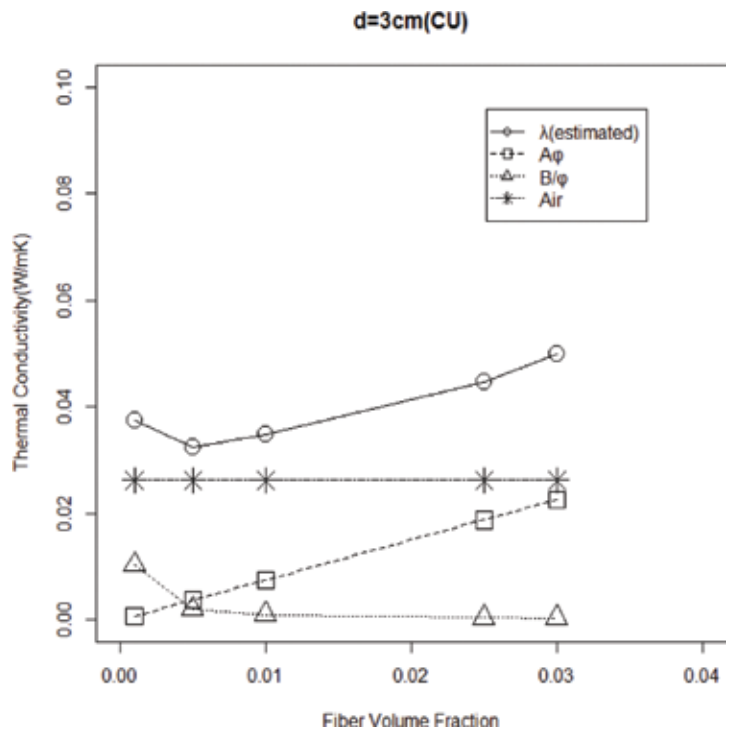

Figure 18. Estimated values of effective thermal conductivity and its component (sample: CU, d = 3 cm).

http://dx.doi.org/10.5772/intechopen.75604

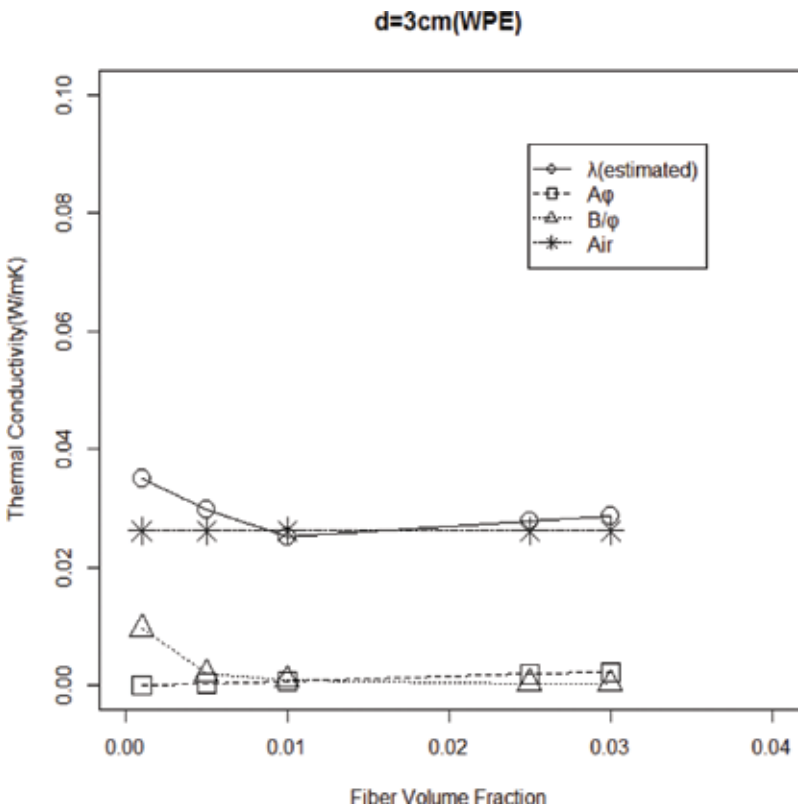

Figure 19. Estimated values of effective thermal conductivity and its component (sample: WPE, d = 3 cm).

of effective thermal conductivity of fiber assembly consists of thermal conductivity of air (still air), λ_{air}. It should be noted that the air is trapped by small amount of fiber ($\phi < 0.03$). (Explanation of this effect is given in the Appendix.)

Contribution of fiber material to the effective thermal conductivity is expressed by A, coefficient of conduction in fiber. Physical meaning of A is increasing rate of conduction in fiber and it consists of two parts, that is, heat conduction through fiber and heat conduction at contact point between fibers. It is conjectured that magnitude of A depends on contact effect between fibers compared to conduction through fiber. In this measurement, $A\phi$ component of cupra fiber (CU) is relatively large and that of polyester fibers (RPE, WPE, PTT) is relatively small. Polyester fibers have advantage in thermal insulation material because $A\phi$ component is small over the wide range of fiber volume fraction.

Based on nonlinear regression model, measured value of effective thermal conductivity can be separated into three components, such as conduction in fiber, radiative heat transfer, and gas conduction. Schematic diagram of the model is shown in **Figure 22**. Gas conduction plays the most important role in thermal insulation properties, which originates from immovable air trapped by fibrous network. Component of conduction in fiber has secondary contribution to thermal insulation properties, especially in the range of higher fiber volume fraction. Although radiative heat transfer slightly appears in low range of fiber volume fraction,

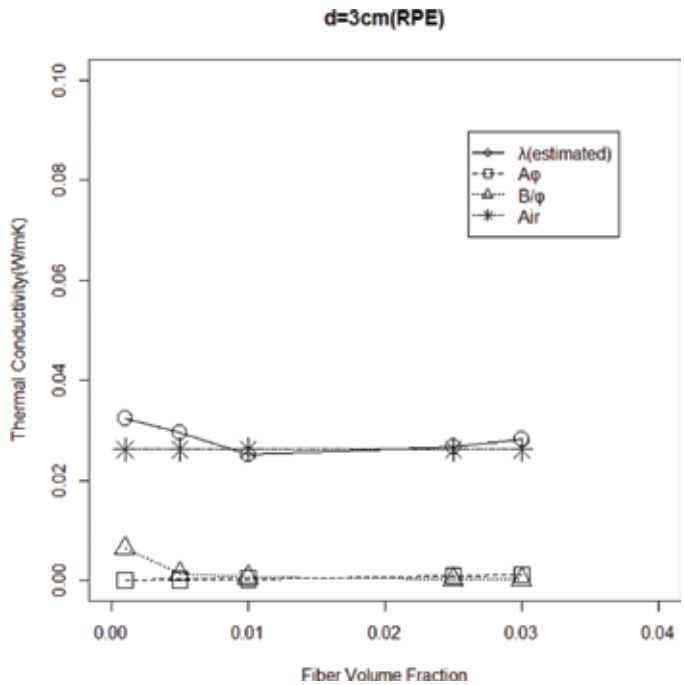

Figure 20. Estimated values of effective thermal conductivity and its component (sample: RPE, d = 3 cm).

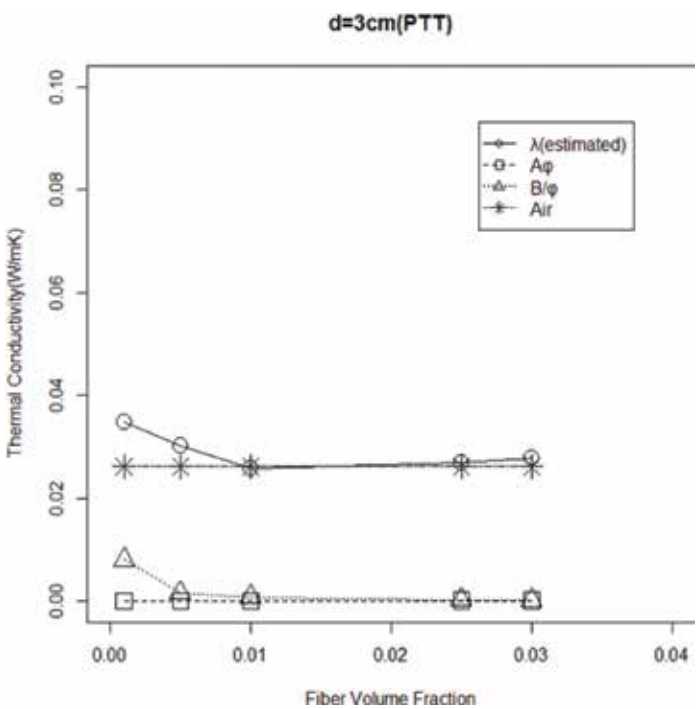

Figure 21. Estimated values of effective thermal conductivity and its component (sample: PTT, d = 3 cm).

http://dx.doi.org/10.5772/intechopen.75604

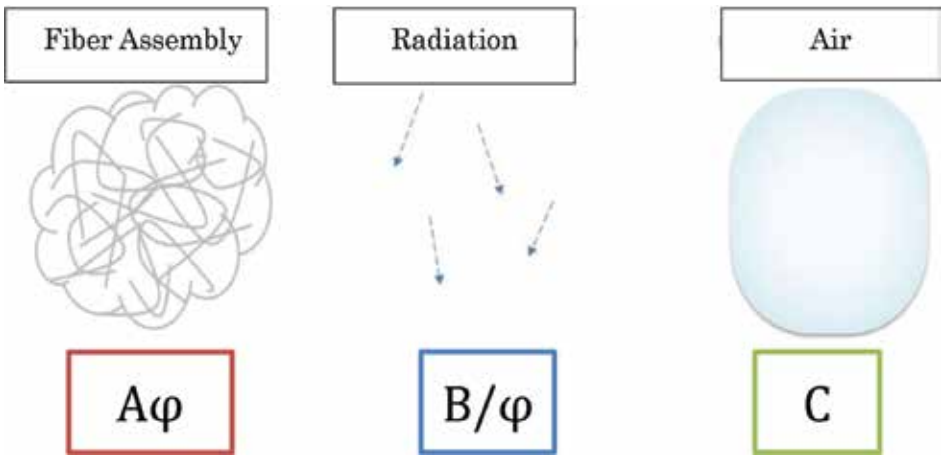

Figure 22. Mechanism of heat transfer in fiber assembly.

contribution of radiative heat transfer is negligible small to effective thermal conductivity of fiber assembly with random orientation. It is conjectured that relative ratio of each heat transfer component depends on fiber material and the effect of pore structure. These findings will be basic information for designing fiber assembly-based thermal insulation material.

6. Conclusion

In this study, the effective thermal conductivity of staple fiber assembly for wadding use is measured. Samples used are four kinds of fiber materials such as cupra fiber (CU), polyester fiber with round section (RPE), polyester fiber with heteromorphic section (WPE), and polytrimethylene terephthalate fiber (PTT).

Effective thermal conductivity is measured under five different fiber volume fractions, and effective thermal conductivity curve is obtained. Effective thermal conductivity curve is analyzed using empirical equation considering separation of heat transfer component. The results are analyzed by nonlinear regression method. Measurement is carried out including leakage of heat from sidewall of the sample frame. Calibration of leakage of heat is accomplished after the separation of heat transfer component by nonlinear regression analysis. Care must be taken so that the measurement system is not disturbed by radiative and convective heat transfer from outer environment. The results obtained are as follows.

1. The shape of effective thermal conductivity-fiber volume fraction curve is convex downward. For CU fiber, the minimum value of effective thermal conductivity lies around $\phi = 0.005$. For polyester fibers (RPE, WPE, PTT), the minimum value lies around $\phi = 0.01$.
2. Effective thermal conductivity can be separated into three components such as conduction in fiber, $A\phi$, radiative heat transfer, B/ϕ, and gas conduction, C.
3. Elimination of leakage of heat is accomplished after the separation of C component into thermal conductivity of air, λ_{air}, and leakage of heat from sidewall, C′.

4. Thermal conductivity of air, λ_{air}, has large contribution to total effective thermal conductivity, and conduction in fiber, Aϕ follows in the range of higher fiber volume fraction. Contribution of radiative heat transfer is negligible small through this measurement.
5. Effective thermal conductivity of CU is the largest, and those of polyester fibers (RPE, WPE, PTT) follows.
6. With decreasing thickness, the shape of effective thermal conductivity curve becomes flattened, and the difference between fiber materials becomes small.

Precise determination of C value is required for the precise measurement of effective thermal conductivity. These findings will be basic information for designing fiber assembly-based thermal insulation materials.

A. Appendix: Nonlinear regression model for effective thermal conductivity of fiber assembly

As porosity of fiber assembly in this study is very large (>97%), it is expected that heat transfer within fiber assembly is affected by the effect concerning pore as well as conduction in fiber. Mechanism of heat transfer consists of conduction in fiber, radiative heat transfer in pore, and gas conduction in air. If it is supposed that three components of heat transfer are arranged parallel to heat flux (parallel model), the effective thermal conductivity of fiber assembly, λ(W/mK), is expressed as a function of bulk density ρ(kg/m^3) as follows [4].

$$\lambda = \lambda_c + \lambda_r + \lambda_g. \tag{A1a}$$

$$= A\rho + B/\rho + C. \tag{A1b}$$

where λ_c is equivalent thermal conductivity of fiber, λ_r is equivalent thermal conductivity of radiative heat transfer, λ_g is equivalent thermal conductivity of gas conduction, A (Wm^2/Kkg) and B (Wkg/m^{4}K) are coefficients, and C (W/mK) is constant.

The first term in Eq. (A1b) denotes conduction in fiber, the second term denotes radiative heat transfer, and the third term denotes conductive heat transfer through gas. Here, the physical meaning of parameters A, B, and C are summarized based on literature [4] and other literatures concerning subjects in this study.

A.1. Conduction in fiber

Conduction in fiber consists of two components that is, conduction through fiber and conduction at contact point between fibers. The factors concerning conduction in fibers, therefore, are numbers of fiber and numbers of contact point per unit volume. These factors are expected to be increase with increasing bulk density. If the relation between these factors and bulk density is assumed to be proportional for the simplification, equivalent thermal conductivity for conduction in fiber, λ_c, is expressed using coefficient A as follows:

$$\lambda_c = A\rho. \tag{A2}$$

A.2. Radiative heat transfer in pore.

Equivalent thermal conductivity of radiative heat transfer in pore within fiber assembly is expressed as follows:

$$\lambda_r = 4C_0\, d\sigma\varepsilon T^3. \tag{A3}$$

where C_0 is constant coefficient (n.d.), d is distance between parallel plate (m), σ is Stefan-Boltzmann constant (W/m^2K^4), ε is emissivity (n.d.), and T is absolute temperature (K).

Let M be the mass of fiber assembly filled into cell and S be area of section, d = M/Sρ. Substituting M/Sρ for d in Eq. (A3), λ_r is expressed as,

$$\lambda_r = 4\,C_0 \frac{M}{S\rho}\sigma\varepsilon\, T^3 = \frac{B}{\rho} \tag{A4}$$

$$B = 4\,C_0 \frac{M}{S}\sigma\varepsilon\, T^3 \tag{A5}$$

Nogai et al. [1, 2] classifies contribution of total radiative heat transfer in fiber assembly into following four elements: between heat source and fibers, (2) between heat source and heat sink, (3) between fibers, and (4) between fibers and heat sink.

Equation (A3) expresses radiative heat transfer between heat source and heat sink (2).

A.3. Conductive heat transfer through gas

The third term, C (W/mK), is discussed in this section. It is confirmed that size of pore in this experiment is much larger than L, mean free path of air under atmospheric pressure. Therefore, it must be investigated that natural convection occurs or not by change of porosity.

To judge generation of natural convection in fiber assembly, it is not suitable to use Rayleigh number. Instead, modified Rayleigh number [10] to which shape factor of fiber assembly is added is used.

$$Ra = \frac{g\beta\Delta\theta\, d^3}{\nu\kappa}\frac{k}{d^2} \tag{A6}$$

where g is acceleration of gravity (=9.8 m/s^2), β is coefficient of body inflation (1/K), Δθ is temperature difference between heat source and heat sink (K), d is thickness of sample (m), ν is dynamic viscosity of air (m^2/s), κ is thermal diffusivity of air (m^2/s). k (m^2) is Darcy's transmission coefficient which depends on fiber diameter, t (m) and porosity, ϕ(n.d.).

$$k = \frac{t^2\varphi^3}{122\,(1-\varphi)^2} \tag{A7}$$

If Ra is larger than critical modified Rayleigh number, Ra_{cr} (=39.5), natural convection occurs in fiber assembly.

An example of calculation of Ra for sample RPE is shown. Parameters concerning sample RPE (ϕ = 0.03, T = 25°C) are as follows:

t = 1.276 × 10^{-5} (m), ϕ = 0.97, g = 9.8 (m^2/s), β = 1/373 (1/K), $\Delta\theta$ = 10 (K), ν = 1.579 x 10^{-5} (m^2/s), κ = 2.215 x 10^{-5} (m^2/s).

Ra is calculated as follows:

Ra = 0.0202 for d = 0.02

Ra = 0.0304 for d = 0.03

Ra = 0.0513 for d = 0.05

As Ra < Ra_{cr} (=39.5) for all cases, natural convection does not occur in fiber assembly in this case. Therefore, C is constant and λ_g = C. C is called as component of gas conduction.

Author details

Morihiro Yoneda

Address all correspondence to: gkdzd429@ybb.ne.jp

Nara Women's University, Kitauoya-Nishimachi, Nara, Japan

References

[1] Nogai T. Estimation of the effective thermal conductivity perpendicular to fiber axes of unidirectionally oriented fiber assembly. Sen' i-Gakkaishi. 1980;**36**:389-396

[2] Nogai T, Ihara M. An experimental study of the effective thermal conductivity perpendicular to fiber axes of unidirectionally oriented fiber assembly. Sen'i-Gakkaishi. 1980; **36**:427-434

[3] Fujimoto T, Niwa M. Experimental study of effective thermal conductivity of fiber assembly Part 1: Evaluation of anisotropic effective thermal conductivity and role of radiative heat transfer. Journal of Textile Machinery Society of Japan. 1989;**42**:27-35

[4] Ohmura T, Tsuboi M, Onodera M, Tomimura T. Study on effective thermal conductivity of fibrous insulation. In: Proceedings of the Institute for Functional Material Science (Kyusyu University). 2002;**16**:13-17

[5] Rennex B, Somers T. Apparent-thermal-conductivity characterization of low-density, glass-fiber insulation material, Journal of Thermal Insulation (predecessor journal of Journal of Building Physics). 1985;**8**:175-197

[6] Symons JG, Clarke RE, Peirce JV. The thermal performance of several Australian fibrous insulating materials. Journal of Thermal Insulation and Building Envelopes (predecessor journal of Journal of Building Physics). 1995;**19**:72-88

[7] Campanale M, Moro L. Simplified procedure for the determination of thermal resistance of thick specimens enclosing air only. Journal of Thermal Insulation and Building Envelopes (predecessor journal of Journal of Building Physics). 1997;**21**:153-170

[8] Kawabata S. Development of a device for measuring heat-moisture transfer properties of apparel fabrics. Journal of Textile Machinery Society of Japan. 1984;**37**:130-138

[9] Japan Society of Thermophysical Properties, editors. In: Thermophysical Properties Handbook. Thermophysical Properties of Air. Tokyo: Yokendo Ltd.; 1990. p.59. ch-B.5.6

[10] Natural convection heat transfer in porous materials. Ibid. p.178. ch-C.2.5.6

Section 2

Thermal Conductivity of Solid and Fluid Systems

Chapter 5

Thermal Conductivity of Liquid Metals

Peter Pichler and Gernot Pottlacher

Additional information is available at the end of the chapter

http://dx.doi.org/10.5772/intechopen.75431

Abstract

Over the last decades, many experimental methods have been developed and improved to measure thermophysical properties of matter. This chapter gives an overview over the most common techniques to obtain thermal conductivity λ as a function of temperature T. These methods can be divided into steady state and transient methods. At the Institute of Experimental Physics at Graz University of Technology, an ohmic pulse-heating apparatus was installed in the 1980s, and has been further improved over the years, which allows the investigation of thermal conductivity and thermal diffusivity for the end of the solid phase and especially for the liquid phase of metals and alloys. This apparatus will be described in more detail. To determine thermal conductivity and thermal diffusivity with the ohmic pulse-heating method, the Wiedemann-Franz law is used. There are electronic as well as lattice contributions to thermal conductivity. As the materials examined at Graz University of Technology, are mostly in the liquid phase, the lattice contribution to thermal conductivity is negligibly small in most cases. Uncertainties for thermal conductivity for aluminum have been estimated ±6% in the solid phase and ±5% in the liquid phase.

Keywords: thermal conductivity, ohmic pulse-heating, Wiedemann-Franz law, sub-second physics, high temperature, liquid phase

1. Introduction

Knowing thermophysical properties, i.e., properties that are influenced by temperature, of metals and alloys is not only of academic interest, but also profoundly important for industry and commerce. Casting of metal objects, made of, e.g., steel or aluminum, is prone to casting defects and imperfections. Therefore, in the majority of modern production procedures, computer simulations are performed to reduce defects and imperfections as well as generally

optimize manufacturing processes. The driven benefits from such simulations often are limited by an insufficient or lacking access to experimentally obtained data. It is especially the liquid phase of metals and alloys, that is of interest, as such production processes like, e.g., casting, naturally take place in the liquid phase.

The term thermophysical properties include various properties: thermal conductivity, thermal diffusivity, thermal volume expansion, heat capacity, density, viscosity and so on. Many of those properties are important in industrial processes; however, it is thermal conductivity, more precisely, thermal conductivity of liquid metals and alloys that will be discussed in this chapter.

Naturally, the numbers of experimental methods to measure the desired quantities that have been developed over the past decades are manifold. It is the goal of this work to give a brief overview of the most common or practical techniques in Section 2, but only few of these methods are suitable to conduct measurements in the liquid phase. These techniques will be highlighted in Section 2.

At the Thermo- and Metalphysics group at Graz University of Technology, fast pulse-heating experiments are performed to measure thermophysical properties of liquid metals and alloys. The Wiedemann-Franz law is applied to calculate thermal diffusivity and thermal conductivity from measured quantities. These mentioned calculations are briefly explained in Section 3, and the experimental apparatus used is described in Section 4.

2. An overview of methods to measure thermal conductivity of liquid metals

In principle, there are three different classes of measurement methods:

- Steady state methods
- Non-steady state methods
- Transient methods

However, it is not always as easy to classify a certain technique. Especially, distinguishing between non-steady state methods and transient methods can be challenging.

Steady state methods are defined as techniques, where the temperature gradient remains constant across the sample. Those methods require precise temperature control throughout the whole experiment to confine convection effects to a minimum, which is especially hard to achieve for metals with high melting points.

Transient methods and non-steady state methods make use of very short time frames in order to conclude measurements before convection plays a role. Non-steady state methods achieve those conditions due to very high heating rates of up to 1000 Ks^{-1}, with rather large temperature gradients of over 100 K.

The temperature gradient in transient methods is significantly lower (on the order of 5 K) than in non-steady state methods, which minimizes the possibility of convection-induced effects in the measurements. In recent history transient methods grew in importance and started to replace non-steady state methods.

2.1. Steady state methods

2.1.1. Axial heat flow method

A known heat flux q is applied to one end of a sample and dissipated on the other end by a heat sink. Thermal conductivity can be calculated by

$$\lambda = \frac{q}{A} \cdot \frac{\Delta z}{\Delta T} \tag{1}$$

where q is the applied heat flux, A is the specimen cross-section, and $\frac{\Delta z}{\Delta T}$ is the inverse temperature gradient across two points z_q and z_2.

Therefore, the conditions to determine thermal conductivity with this method is the determination of the geometry A and Δz, guarantee that the heat flow is unidirectional, measurement of the heat flux q, and measurement of temperature of at least two points z_q and z_2 (normally thermocouples).

While this technique is mostly targeted at solid materials, it can be used on a variety of liquid metals with low melting points such as mercury, lead, indium, and gallium [1].

The temperature range is 90–1300 K, and the accuracy in this range has been estimated to be ±0.5 to ±2% [2].

2.1.2. Radial heat flow method

Another method to measure thermal conductivity for both solid and liquid materials is the concentric cylinder method.

The solid sample is placed in-between two concentric cylinders, and a known heat flux is applied by leading a heater through the inner cylinder. The outer cylinder is water cooled to provide a temperature gradient between the two cylinders.

The temperature difference between temperature sensors (often thermocouples) in the two cylinders is determined when steady state is achieved. Knowing the radii of the two cylinders and their length, thermal conductivity can be calculated by

$$\lambda = \frac{q}{L} \cdot \frac{\ln\left(\frac{r_2}{r_1}\right)}{2 \cdot \pi \cdot \left(T_1 - T_2\right)} \tag{2}$$

with q being the applied heat flux, L as the length of the cylinders, r_1 as radius of the inner cylinder, r_2 as radius of the outer cylinder, and T_1 and T_2 as the respective temperatures.

A more in-depth explanation of this method can be found in [2].

The method can be adapted for liquid metals by providing a container for the liquid sample in-between the two concentric cylinders. Apart from this container, the measuring principle remains the same for liquid metal samples.

The radial heat flow method operates in a temperature range of 4–1000 K and the uncertainty of this method has been estimated to be about ±2% [3].

2.2. Direct heating methods

The term "direct electrical heating method" summarizes all those measurement techniques, where the sample is heated up, by running a current through it, without an additional furnace. An example of such a method, but in a dynamic way and not as a steady state method, is the ohmic pulse-heating method that will be discussed later in this chapter.

Direct electrical heating methods are therefore limited to samples which are decent electrical conductors. The shape of the samples can vary from wires, rods, sheets to tubes. The advantage of such techniques is for one, the lack of a furnace and, secondly, the possibility to measure a multitude of thermophysical properties simultaneously.

Direct heating methods are able to achieve high temperatures of about 4000 K and are therefore suitable for measuring thermal conductivity in the liquid phase of metals with high melting points.

2.2.1. Guarded hot plate

This steady state method utilizes two temperature-controlled plates that sandwich a solid disc-shaped sample. Heating one plate, while cooling the other one, generates a uniformly distributed heat flux through the sample, achieving a steady state temperature at each plate. The technique is considered as the steady state method with the highest accuracy.

The guarded hot plate apparatus can be constructed in single sided or double sided mode. When operated in double sided mode, there is a total amount of three plates as well as two samples: A central heater plate together with two cooling plates sandwiching the two samples. The temperature drop across the two specimens is measured with thermocouples, which are apart a distance L. Thermal conductivity can then be determined by

$$\lambda = \frac{q \cdot L}{2 \cdot A \cdot \Delta T} \tag{3}$$

where q is the heat flux through the specimen, A is the cross section, L is the spatial distance between the two thermocouples, and ΔT is the temperature difference.

In the single-sided mode, one of the cooling plates as well as the second specimen is removed. The temperature gradient in one direction therefore vanishes, which leads to the loss of a factor 2 in Eq. (3)

$$\lambda = \frac{q \cdot L}{A \cdot \Delta T} \tag{4}$$

The experimental setup and the calculation of the thermal conductivity are more thoroughly explained in [4].

Commercially available guarded hot plate (GHP) apparatus, like the NETZSCH GHP 456 Titan [5], operate in a temperature range of 110–520 K and provide an accuracy of ±2%.

It has to be noted that the GHP method is applicable only for solid samples and it is not a suitable method to determine thermal conductivity of high-melting metals.

2.2.2. Calorimeter method

The calorimeter technique is a direct measurement of Fourier's law. It consists of a heating source (typically SiC or $MoSi_2$ elements) and a SiC slab to distribute the temperature gradient. The specimen is enclosed by two insulating guard bricks, which are, like the specimen as well, in thermal contact with a water-cooled copper base. As the name gives away, the central part of the system is a calorimeter, which is surrounded by the guards. The apparatus is designed in a way that the heat flow into the calorimeter is one-dimensional.

Two thermocouples, which are apart a distance L and lie vertically to each other, are enclosed in the specimen and the temperature difference $T_2 - T_1$ between them is measured.

Thermal conductivity can be determined by

$$\lambda = \frac{\frac{dq}{dt} \cdot L}{A(T_2 - T_1)} \tag{5}$$

with A being the cross section of the calorimeter, L as the distance between the two thermocouples, $\frac{dq}{dt}$ as the rate of heat flow into the calorimeter, and $T_2 - T_1$ as the temperature difference between the two thermocouples.

2.3. Transient methods

2.3.1. Transient hot wire and transient hot strip method

Simple experimental arrangements and short measurement times are granted by the transient hot wire (THW) along with the transient hot strip (THS) method.

The transient hot wire technique is most commonly used for measuring thermal conductivity λ and thermal diffusivity a. An electrically heated wire, which acts as a self-heated thermometer is placed into a material and distributes a radial heat flow into the sample. The specimen itself acts as a heat sink for the system, while the wire functions as a heat source as well as providing a mechanism to measure the thermal transport properties, due to a temperature-dependent drop of the voltage along the wire. Solving the fundamental heat conduction equation yields

$$\Delta T(r, t) = \frac{q}{4 \cdot \pi \cdot \lambda} \cdot \ln\left(\frac{4 \cdot a \cdot t}{r^2 \cdot e^{\gamma}}\right), \tag{6}$$

with q the heat input per unit length of the wire, r the radius of the wire, a the thermal diffusivity, γ Euler's constant, t the time, and λ, of course, the thermal conductivity.

An in-depth explanation of this method to determine thermal conductivity is given in [6, 7].

The transient hot strip (THS) method further improves the THW method. Instead of a wire as the heat source and measuring device, a thin strip of metal foil is used. The metal foil provides a greater surface as well as a smaller thickness than the heated wire, leading to a lower density of heat flow and consequently, a smaller thermal contact resistance to the sample.

While the THW method is only applicable for liquids and some solids, which can be wrapped around the heating wire in a way the thermal resistance is low enough, the THS method is the go-to method to perform measurements on solids.

Note: this work focuses on the measurement techniques for thermal conductivity of liquids. THS measurements are also performed on gases (see [8]).

At Physikalisch-Technische Bundesanstalt (PTB), Braunschweig, an upgraded version of the THS and THW method, the transient hot bridge technique, has been developed. In this method, a total of eight strips are deployed in a way they form a Wheatstone bridge, allowing an effective thermal and electrical self-compensation [9].

Uncertainties of the THW technique have been reported (e.g., see [10]) to be ±5.8% for the determination of thermal conductivity. However, the method has also be described as even more accurate [11], with uncertainties of below ±1% for gases, liquids, and solids. With a maximum temperature of about 1000 K, this method is only suitable for low melting metals.

2.3.2. 3ω method

The 3ω method goes back to the work done by Cahill [12] in 1987. The method has similarities with the THS and THW technique, since it also uses a single element as heat source as well as thermometer. While both the THS and THW method measure temperature in dependence of time, the 3ω technique records the amplitude and phase of the resistance depending on the frequency of the excitation.

It is most commonly used as a technique to measure thermal conductivity of solids or liquids, but has been improved to also be applicable on thin films [12, 13]. A conducting wire is distributed onto a specimen and an AC voltage with a frequency ω is driven through it. Due to the electrical resistance, the sample is heated up, resulting in a temperature change. The frequency of the change in temperature is 2ω. The product of the resistance oscillation 2ω and the excitation frequency ω gives a voltage of frequency 3ω, which is measured and responsible for the name 3ω method.

Measuring the 3ω voltage at two frequencies f_1 and f_2, thermal conductivity is

$$\lambda = \frac{V^3 \ln f_2/f_1}{4 \cdot \pi \cdot l \cdot R^2 \left(V_{3,1} - V_{3,2}\right)} \frac{\mathrm{d}R}{\mathrm{d}T} \tag{7}$$

with $V_{3,1}$ the 3ω voltage at frequency f_1, $V_{3,2}$ the 3ω voltage at frequency f_2, and R the average resistance of the metal line of length l.

In the original work of Cahill [13], the temperature range of the 3ω method is 30–750 K, which is not suitable for high melting metals. This method often is applied on nanofluids and publications state an uncertainty of around ±2% [14].

2.3.3. Laser flash method

Under the laser flash method (LFM), the directly measured quantity is thermal diffusivity and not thermal conductivity. Thermal conductivity can, however, be determined with knowledge of specific heat as well as density of the sample.

$$\lambda(T) = a(T) \cdot \rho(T) \cdot c_p(T), \tag{8}$$

with $a(T)$ the thermal diffusivity, $\rho(T)$ the density, and $c_p(T)$ the specific heat.

In the LFM, the sample is exposed to a high intensity laser pulse at one face, which generates heat at said surface. On the back surface, which is not exposed to the laser pulse, an infrared sensor detects a rising temperature signal, due to heat transfer through the sample.

For adiabatic conditions, thermal diffusivity can be obtained by

$$a = 0.1388 \frac{l^2}{t_{0.5}}, \tag{9}$$

with l the sample thickness and $t_{0.5}$ the time at 50% of the temperature increase.

LFM, as introduced by Parker et al. [15], has been a convenient technique to determine thermal diffusivity a and thermal conductivity λ of solids at moderate temperatures. The method has been further improved since then and is applicable for a great temperature range, up to around 2500°C.

In 1972, Schriempf [16] applied LFM to determine thermal diffusivity for liquid metals at high temperatures. The liquid metal has to be placed in a suitable container in order to arrange a proper setup. Problems arise for liquids of low thermal conductivity. When the thermal conductivity of the sample is of the same order as of the container, this leads to an unneglectable heat current through the container. Therefore, it was proposed in [17] not to insert the liquid sample into a container, but have it placed between a metal disc, which is exposed to the laser pulse.

Commercially available laser flash apparatus like the NETZSCH LFA 427 [18] operate in a temperature range from −120 to 2800°C, depending on the furnace and are therefore applicable for higher melting metals as well.

Kaschnitz [19] estimates uncertainties of thermal conductivity for LFM to be between ±3 and ±5% in the solid phase and ±8 to ±15% in the liquid phase.

Hay [20] did an uncertainty assessment for their apparatus at Bureau national de métrologie (BNM) and claimed uncertainty estimations from ±3 to ±5%.

Hohenauer [21] did an uncertainty assessment of their laser flash apparatus and stated an expanded uncertainty with thermal diffusivity measurement in the temperature range from 20 to 900°C of 3.98%.

3. Calculations via Wiedemann-Franz law

In some cases, it is more applicable to measure electrical conductivity respectively electrical resistivity. Heat transport and thus thermal conductivity through a metal or an alloy needs carriers. One has to distinguish between the component λ_e of thermal conductivity due to electrons and λ_l, which is the lattice contribution, due to phonons. Naturally for liquid metals and alloys, thermal conductivity is dominated by the electronic contribution. The total thermal conductivity would then be the sum of the components $\lambda = \lambda_e + \lambda_l$.

Thermal conductivity of liquid aluminum was examined at Graz University of Technology. Here the sole consideration of the electronic contribution gave promising results for the liquid phase [22]. A detailed derivation of the lattice-contribution to thermal conductivity can be found in the paper of Klemens [23].

An example when the lattice contribution has to be considered in the calculation of thermal conductivity for the Inconel 718 alloy is given in [24].

The Wiedemann-Franz law states that for conducting metals the electronic component of the thermal conductivity λ_e is

$$\lambda_\mathrm{e} = L_0 \frac{T}{\rho(T)} \tag{10}$$

with $\rho(T)$ the temperature-dependent electrical resistivity and $L = \frac{\pi^2}{3} \cdot (k_\mathrm{B}/e)^2 = 2.45 \times 10^{-8}\,\mathrm{W} \cdot \Omega \cdot \mathrm{K}^{-2}$ the (theoretical) Lorenz number.

Considering thermal expansion, the temperature-dependent electrical resistivity is

$$\rho(T) = \rho_\mathrm{IG} \frac{d\,(T)^2}{d_0^2}, \tag{11}$$

with d_0 the diameter at reference temperature (room temperature), ρ_{IG} the electrical resistivity at initial geometry, and $d(T)$ the diameter at an elevated temperature T. To calculate thermal conductivity, it is therefore necessary to measure thermal volume expansion as well.

An estimation of thermal diffusivity $a(T)$ can be found by

http://dx.doi.org/10.5772/intechopen.75431

$$a(T) = \frac{L_0 \cdot T}{c_p(T) \cdot D(T) \cdot \rho(T)} \tag{12}$$

with $c_p(T)$ the heat-capacity and $D(T)$ the temperature-dependent density. With the ohmic pulse-heating setup at Graz University of Technology (as explained later in this work), radial over longitudinal expansion is ensured (see, e.g., [25]). Considering Eq. (12) and radial expansion yields

$$a(T) = \frac{L_0 \cdot T}{c_p(T) \cdot D(T) \cdot \rho(T)} = \frac{L_0 \cdot T}{c_p(T) \cdot D_0 \rho_{IG}} \tag{13}$$

with D_0 the density at room temperature.

Thus, Eqs. (10) and (12) enable us to determine thermal conductivity and thermal diffusivity from ohmic pulse-heating experiments, and deliver results that are in the same range as results from Laser flash measurements, as shown in the thermal diffusivity intercomparisons NPL – Report CBTLM S30 [26]. With a variation of only 3%, our results were significantly close to the average determined.

The experimental setup at Graz University of Technology is described in the following section.

4. Measurements at Graz University of Technology

In ohmic pulse-heating experiments, the electric conducting sample is heated up by passing a large current pulse through it. Due to the resistivity of the material, the sample is heated up from room temperature to the melting point and further up through the liquid phase to the boiling point in a period of about 50–70 μs.

The specimen typically is in the shape of a wire, with diameters ranging from a few hundred micrometers up to some millimeters, rectangular shape for materials that cannot be drawn into wires, foils or tubes. As a consequence of the narrow time frame under which these experiments are performed, the liquid phase does not collapse due to gravitational forces, enabling investigations of the entire liquid phase up to the boiling point. In addition, the specimen can be considered to not be in contact with the surrounding medium, rendering the experiment to being a container-less method.

4.1. Setup

A typical pulse heating experiment consists of the following parts: An energy storage (mostly a capacitor or battery bank) with a charging unit, a main switching unit (e.g., high-voltage mercury vapor ignition tubes) and an experimental chamber with windows for optical diagnostics and the ability to maintain a controlled ambient atmosphere. Pulse heating experiments are mostly performed under inert atmosphere, e.g., nitrogen or argon at ambient pressure,

or in vacuum. The setup of the pulse-heating apparatus at Graz University of Technology is presented in **Figure 1**.

The setup has been explained in detail in previous publications [27–29].

4.2. Current and voltage measurement

The current pulse, which the sample is subjected to, is measured using an induction coil (Pearson Electronics, Model Number 3025). To measure the voltage drop, two Molybdenum voltage-knives are attached to the specimen. The voltage drop relative to a common ground is measured for both of the voltage-knives, allowing the measurement of the voltage drop between the two contact points of the sample and the respective voltage-knives (**Figure 2**).

4.3. Temperature measurement

A fast pyrometer provides temperature determination. The pyrometer measures the spectral radiance of a sample surface from which the temperature can be calculated using Planck's law.

$$L_{\lambda,B}(\lambda, T) = \frac{c_1}{\pi \cdot \lambda^5} \cdot \frac{1}{e^{\frac{c_2}{\lambda \cdot T}} - 1}, \tag{14}$$

with $L_{\lambda,B}(\lambda, T)$ the radiance emitted by a black body at temperature T and wavelength λ and the two radiation constants $c_1 = 2\pi \cdot h \cdot c^2$ and $c_2 = \frac{h \cdot c}{k_B}$ (h is the Planck's constant, c the speed of light, and k_B the Boltzmann constant). It has to be considered that nearly no real material is a perfect black body. The deviation from black body radiation is taken into account by emissivity $\varepsilon(\lambda,T)$. The ratio of radiation emitted by a real material therefore is

$$L_\lambda(\lambda, T) = \varepsilon(\lambda, T) \cdot L_{\lambda,B}(\lambda, T). \tag{15}$$

It has to be noted as well that the measured quantity of the pyrometer is a voltage signal $U_{Pyro}(T)$, which is dependent on measuring geometry, transmission of the optical measuring setup, width of the spectral range and detector sensitivity. When summarizing the majority of the temperature-independent quantities in a constant C, the pyrometer signal is

$$U_{Pyro}(T) = C \cdot \varepsilon(\lambda, T) \cdot \left(e^{\frac{c_2}{\lambda \cdot T}} - 1\right)^{-1} \tag{16}$$

4.4. Thermal diffusivity and thermal conductivity

With the obtained values of the time-dependent current $I(t)$, the time-dependent voltage drop $U(t)$, the specimen radius $r(t)$ and the surface radiation $L(t)$ it is now possible to calculate the desired thermal properties, i.e., thermal conductivity $\lambda(T)$, thermal diffusivity $a(T)$ as well as specific heat capacity $c_p(T)$. This has been shown briefly in the second section of this chapter and is thoroughly discussed in [30, 31].

The solid phase as well as the liquid phase data are fitted linearly (for the solid phase) and quadratically (for the liquid phase). In our publications (e.g., [22]) we give the coefficients for the

http://dx.doi.org/10.5772/intechopen.75431

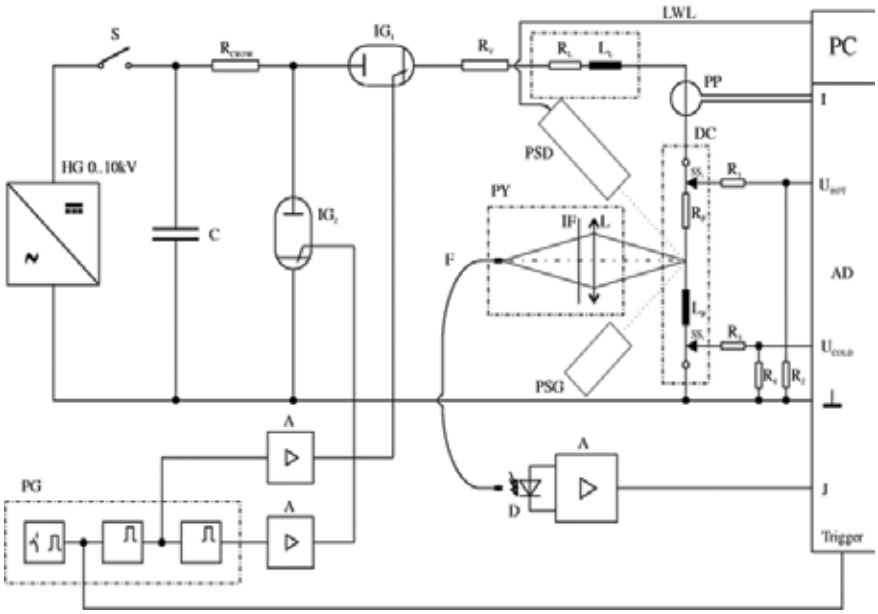

Figure 1. Schematic experimental setup. HG: high voltage power supply; S: switch for loading the capacitor bank C; R CROW: crowbar resistor; I G 1 : main ignitron; I G 2 : crowbar ignitron; R V : matching resistor; R C, L C, R S, L S : resistance and inductance of the circuit and/or the sample; R 1 – R 4 : voltage dividers; K E 1, K E 2 : knife-edge probes; PP: Pearson-probe; DC: discharge chamber; PY: Pyrometer; L: lens; IF: interference filter; F: fiber; D: photo-diode; A: amplifier; PG: pulse generator; AD: analog-to-digital converter; PC: personal computer; I, U HOT, U COLD, J : measurement signals of current, voltages and intensity of radiation; PSG: polarization state generator; PSD: polarization state detector; LWL: light wire line.

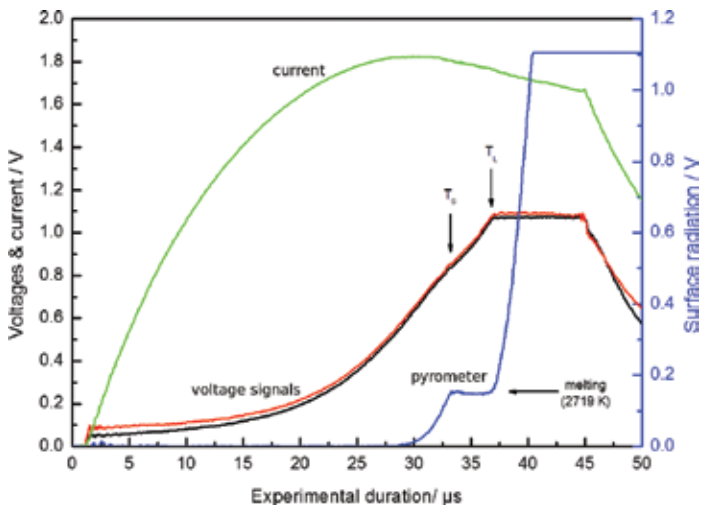

Figure 2. Typical raw measurement signals of the ohmic pulse-heating experiment performed on Iridium. The black line and red line are the voltage signals, the green line is the current signal and the blue line is the signal of the pyrometer. Note that solidus temperature (T_s) and liquidus temperature (T_l) are visible not only in the pyrometer signal, but also in the voltage signals.

linear fits as well as uncertainty assessments. The schematic data provided in this chapter are for aluminum; therefore, the temperature range is rather low. With the ohmic pulse-heating apparatus, it is also possible to examine high melting metals like tungsten, niobium and tantalum.

Figures 3 and **4** show typical results of thermal conductivity and thermal diffusivity determination with the ohmic pulse-heating apparatus for aluminum.

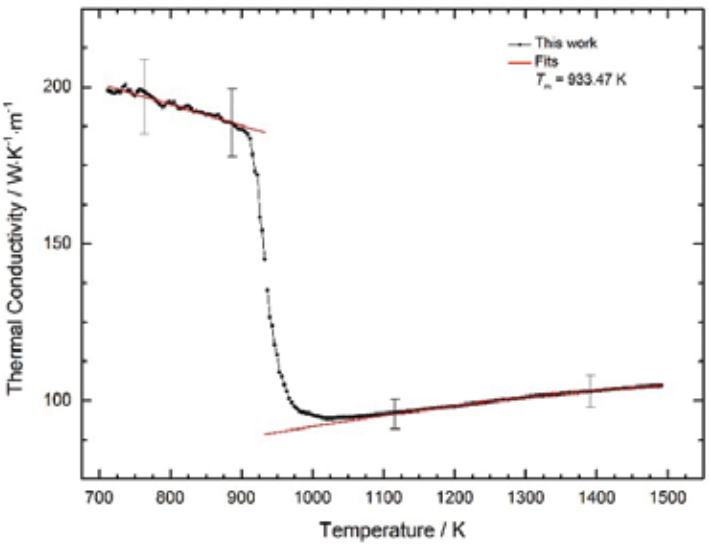

Figure 3. Results of thermal conductivity determination for aluminum. Data taken from [22].

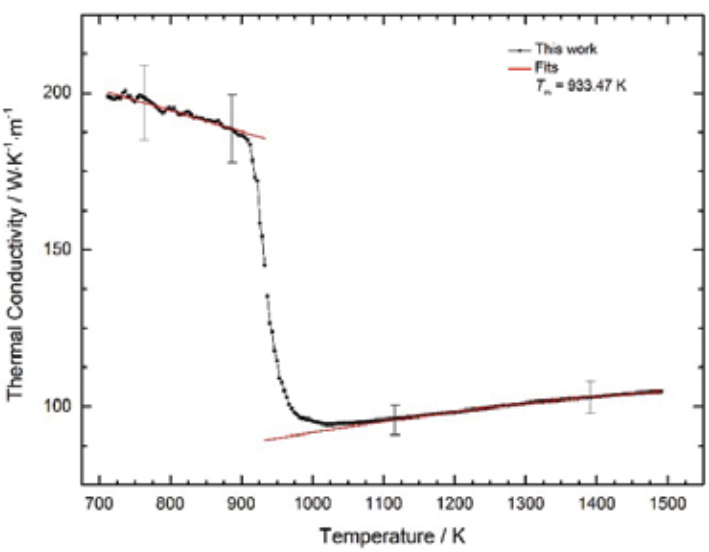

Figure 4. Results of thermal diffusivity determination for aluminum. Data taken from [22].

The data show the solid phase (up to about 900 K) and the liquid phase (up to 1500 K). Thermal conductivity in this case can be fitted quadratically with a positive slope in the liquid phase.

4.5. Uncertainty for the ohmic pulse-heating method

Uncertainties have been estimated according to GUM [32], with a coverage factor of $k = 2$ (95%).

Uncertainties for thermal conductivity $\lambda(T)$ for aluminum have been estimated ±6% in the solid phase and ±5% in the liquid phase. Uncertainties for thermal diffusivity $a(T)$ for aluminum have been estimated ±8% in the solid phase and ±5% in the liquid phase. See also [22].

5. Conclusions

A variety of common methods to determine thermal conductivity of liquid metals have been reviewed in this chapter. These methods can be classified into steady state, non-steady state, and transient techniques. However, not all of the reviewed methods are suitable for the liquid phase of high-melting metals.

To conclude this chapter, the methods that are suitable for the determination of thermal conductivity of high-melting metals in the liquid phase are summarized.

The laser flash method (LFM) is applicable also for high-melting metals, as the temperature range has been reported to be −120 to 2800°C. Uncertainties for this measurement technique range from ±3 to ±15% [16–19].

Another suitable method to determine thermal conductivity of even high-melting metals in the liquid phase is the ohmic pulse-heating method in combination with the Wiedemann-Franz law. This method can easily achieve temperatures of about 4000 K and higher and is therefore suitable for all high-melting metals (the metal with the highest melting point is tungsten with 3695 K). Uncertainties for thermal conductivity for aluminum have been estimated ±6% in the solid phase and ±5% in the liquid phase [22].

Especially in the liquid phase, where lattice contributions in the determination of thermal conductivity can be neglected, the ohmic pulse-heating method has been proven to be a very accurate method. This has been shown in an intercomparison with laser flash measurements in [26].

Author details

Peter Pichler and Gernot Pottlacher*

*Address all correspondence to: pottlacher@tugraz.at

Institute of Experimental Physics, Graz University of Technology, NAWI Graz, Austria

References

[1] Mills KC, Monaghan BJ, Keene BJ. Thermal conductivities of molten metals: Part 1. Pure metals. International Materials Review. 1996;**41**(6):209-242

[2] Maglic KD, Cezairliyan A, Peletsky VE. Compendium of Thermophysical Property Measurement Methods: Vol. 1. Survey of Measurement Techniques. New York, NY: Plenum Press; 1984

[3] Buck W, Rudtsch S. Thermal properties. In: Czichos H, Saito T, Smith L, editors. Springer Handbook of Materials Measurement Methods [Internet]. Berlin, Heidelberg: Springer Berlin Heidelberg; 2006. pp. 399-429. DOI: 10.1007/978-3-540-30300-8_8

[4] Salmon D. Thermal conductivity of insulations using guarded hot plates, including recent developments and sources of reference materials. Measurement Science and Technology. 2001;**12**(12):R89. Available from: http://stacks.iop.org/0957-0233/12/i=12/a=201

[5] [Internet] [cited 2018/01/20]. Available from: https://www.netzsch-thermal-analysis.com/en/products-solutions/thermal-diffusivityconductivity/ghp-456-titan/

[6] Assael MJ, Dix M, Gialou K, Vozar L, Wakeham WA. Application of the transient hot-wire technique to the measurement of the thermal conductivity of solids. International Journal of Thermophysics. 2002;**23**(3):615-633. DOI: 10.1023/A:1015494802462

[7] Hammerschmidt U. A quasi-steady state technique to measure the thermal conductivity. International Journal of Thermophysics. 2003;**24**(5):1291-1312. Available from: http://link.springer.com/article/10.1023/A:1026151101668

[8] Roder HM, Perkins RA, Laesecke A, de Castro CAN. Absolute steady-state thermal conductivity measurements by use of a transient hot-wire system. Journal of Research of the National Institute of Standards and Technology. 2000;**105**(2):221

[9] Hammerschmidt U, Meier V. New transient hot-bridge sensor to measure thermal conductivity, thermal diffusivity, and volumetric specific heat. International Journal of Thermophysics. 2006;**27**(3):840-865. DOI: 10.1007/s10765-006-0061-2

[10] Hammerschmidt U, Sabuga W. Transient hot wire (THW) method: Uncertainty assessment. International Journal of Thermophysics. 2000;**21**(6):1255-1278. Available from: http://link.springer.com/article/10.1023/A:1006649209044

[11] Assael MJ, Antoniadis KD, Wakeham WA. Historical evolution of the transient hot-wire technique. International Journal of Thermophysics. 2010 Jun 1;**31**(6):1051-1072. DOI: 10.1007/s10765-010-0814-9

[12] Cahill DG, Katiyar M, Abelson J. Thermal conductivity of a-Si: H thin films. Physical Review B. 1994;**50**(9):6077

[13] Cahill DG. Thermal conductivity measurement from 30 to 750 K: The 3ω method. Review of Scientific Instruments. 1990;**61**(2):802-808

[14] Choi TY, Maneshian MH, Kang B, Chang WS, Han CS, Poulikakos D. Measurement of the thermal conductivity of a water-based single-wall carbon nanotube colloidal suspension with a modified 3- ω method. Nanotechnology. 2009;**20**(31):315706. Available from: http://stacks.iop.org/0957-4484/20/i=31/a=315706

[15] Parker W, Jenkins R, Butler C, Abbott G. Flash method of determining thermal diffusivity, heat capacity, and thermal conductivity. Journal of Applied Physics. 1961;**32**(9):1679-1684. Available from: http://scitation.aip.org/content/aip/journal/jap/32/9/10.1063/1.1728417

[16] Schriempf JT. A Laser Flash Technique for Determining Thermal Diffusivity of Liquid Metals at Elevated Temperatures. Review of Scientific Instruments. 1972;**43**(5):781-786. DOI: 10.1063/1.1685757

[17] Tada Y, Harada M, Tanigaki M, Eguchi W. Laser flash method for measuring thermal conductivity of liquids—Application to low thermal conductivity liquids. Review of Scientific Instruments. 1978;**49**(9):1305-1314

[18] https://www.netzsch-thermal-analysis.com/en/products-solutions/thermal-diffusivity-conductivity/lfa-427/ [Internet]. Available from: https://www.netzsch-thermal-analysis.com/en/products-solutions/thermal-diffusivity-conductivity/lfa-427/

[19] Kaschnitz E. Private conversation

[20] Hay B, Filtz JR, Hameury J, Rongione L. Uncertainty of thermal diffusivity measurements by laser flash method. International Journal of Thermophysics. 2005 Nov 1;**26**(6):1883-1898. DOI: 10.1007/s10765-005-8603-6

[21] Vozár L, Hohenauer W. Uncertainty of thermal diffusivity measurements using the laser flash method. International Journal of Thermophysics. 2005 Nov 1;**26**(6):1899-1915. DOI: 10.1007/s10765-005-8604-5

[22] Leitner M, Leitner T, Schmon A, Aziz K, Pottlacher G. Thermophysical properties of liquid aluminum. Metallurgical and Materials Transactions A. 2017;**48**:3036-3045

[23] Klemens PG, Williams RK. Thermal conductivity of metals and alloys. International Metals Reviews. 1986;**31**(5):197-215

[24] Pottlacher G, Hosaeus H, Kaschnitz E, Seifter A. Thermophysical properties of Inconel 718 alloy up to 1800 celsius. Scandinavian Journal of Metallurgy. 2002;**31**:161-168

[25] Schmon A. Density Determination of Liquid Metals by Means of Containerless Techniques [Internet]. Graz University of Technology; 2016. Available from: https://www.tugraz.at/fileadmin/user_upload/Institute/IEP/Thermophysics_Group/Files/Diss-SchmonAlexander.pdf

[26] James M, Monaghan B, Cusco L, Redgrove JPQ. Intercomparison of measurements of the thermal diffusivity of molten metals. NPL Report CBTLM S30; 2000

[27] Cagran C, Huepf T, Wilthan B, Pottlacher G. Selected thermophysical properties of Hf-3% Zr from 2200K to 3500K obtained by a fast pulse-heating technique. High Temperatures-High Pressures. 2008;**37**:205-219

[28] Schmon A, Aziz K, Luckabauer M, Pottlacher G. Thermophysical properties of Manganin ($Cu_{86}Mn_{12}Ni_2$) in the solid and liquid state. International Journal of Thermophysics. 2015

[29] Wilthan B, Cagran C, Brunner C, Pottlacher G. Thermophysical properties of solid and liquid platinum. Thermochimica Acta. 2004;**415**:47-54

[30] Cagran C, Wilthan B, Pottlacher G, Roebuck B, Wickins M, Harding RA. Thermophysical properties of a Ti-44%Al-8%Nb-1%B alloy in the solid and molten states. Intermetallics. 2003;**11**:1327-1334

[31] Kaschnitz E, Pottlacher G, Jaeger H. A new microsecond pulse-heating system to investigate thermophysical properties of solid and liquid metals. International Journal of Thermophysics. 1992 Jul;**13**(4):699-710. Available from: http://www.springerlink.com/openurl.asp?genre=article&id=doi:10.1007/BF00501950

[32] Metrology (JCGM/WG 1) WG 1 of the Joint Committee for Guides. In: Guide to the Expression of Uncertainty in Measurement. BIPM; 1993

Chapter 6

Thermal Conductivity Measurement of the Molten Oxide System in High Temperature

Youngjae Kim, Youngjo Kang and Kazuki Morita

Additional information is available at the end of the chapter

http://dx.doi.org/10.5772/intechopen.76018

Abstract

In spite of practical importance in the pyro-metallurgy process, thermal conductivity of molten oxide system has not been sufficiently studied due to its notorious convection and radiation effects. By an aid of appropriate modification of measurement technique and evaluations for systematic errors, thermal conductivity measurement at high temperature becomes feasible. In this chapter, thermal conductivity measurement technique for high-temperature molten oxide system was discussed along with related experimental errors. In addition, thermal conduction mechanism by phonon was briefly introduced. The laser flash method and hot-wire method, which are representative measurement methods for high-temperature system, were compared. During the measurement by using hot-wire method, the convection and radiation effects on measurement results were evaluated. In the hot-wire method, both convection and radiation effects were found to be negligible within short measurement time. Finally, the effect of network structure of molten oxide system on thermal conductivity was discussed. The positive relationship between thermal conductivity and polymerization in the silicate and/or borate system was presented. In addition, the effect of cation expressed by function of ionization potential on thermal conductivity was also briefly introduced. This chapter is partially based on a dissertation submitted by Youngjae Kim in partial fulfillment of the requirements for the degree of Doctor of Philosophy at The University of Tokyo, September 2015.

Keywords: thermal conductivity, hot-wire method, transient method, molten oxide, network structure

1. Introduction

In the iron-making and steel-making field, understanding of thermal conductivity of the molten oxide system is significant because it is closely related with the operation conditions, quality of final products and recycling of slag.

For the recycle of blast furnace slag, the slag is slowly cooled down in the atmosphere or rapidly quenched by using rotary cup atomizer or air blast method. Highly crystallized slag can be recycled as cement concrete for road construction or fertilizer. On the other hand, noncrystalline blast furnace slag can be used as Portland cement for construction owing to its properties of cement when it is ground [1]. Therefore, in order to recycle the blast furnace slag as Portland cement, proper fineness and glass state should be achieved. Since the characteristic fine-granular shape and glass state are mainly determined by a cooling rate, understanding of thermal conductivity of blast furnace slag is important. For this reason, the thermal conductivity measurement in the molten $CaO\text{-}SiO_2\text{-}Al_2O_3$ system, which is the typical blast furnace slag system, has been carried out by using hot-wire method [2–4] and laser flash method [5].

During the steel-making process, understanding of thermal conductivity of the molten slag is closely related to the quality of final products and refractory lifetime. Recently, many works have been focused on the development of heat flow of the whole steel-making chain. However, due to the short information concerning about thermal conductivity of ladle slag, ladle slag is hardly considered during the simulation [6]. For the purpose of better understanding of heat flow, understanding of thermal conductivity of ladle slag is important. Glaser and Sichen [6] measured thermal conductivity of the conventional ladle slag system; $CaO\text{-}SiO_2\text{-}Al_2O_3\text{-}MgO$ system, using the hot-wire method. Their results show the negative temperature dependence of thermal conductivity within the experimental region between 1773 and 1923 K. They reported that the formation of solid state in the slag results in the significant increase of thermal conductivity. On the other hand, Kang et al. [7], who measured thermal conductivity in the steel-making slag system of $CaO\text{-}SiO_2\text{-}FeO_x$ system, reported that addition of FeO_x results in the decreasing of thermal conductivity due to the basic oxide behavior of FeO_x. Considering the structural information of FeO_x obtained by Mössbauer, they found the linear relationship between thermal conductivity and the NBO/T, which is the relative fraction of the number of nonbridging oxygen over total tetrahedral cation, implying the effect of network structure on thermal conductivity.

In addition, during the continuous casting process, irregular horizontal heat transfer through mold flux results in the "longitudinal cracking" and "star cracking" on the final product. Therefore, understanding of thermal conductivity of mold flux system is practically important in terms of quality control. Many studies [8–11] have been carried out in order to find out the relationship between structure of mold flux system and thermal conductivity at high temperature of molten state. These works [8–11] commonly observed the structure dependence of thermal conductivity. Addition of basic oxide, such as sodium oxide or calcium oxide, decreases thermal conductivity as a result of depolymerization of silicate network structure [8, 11]. Susa et al. [10] found that fluorides play a role of network modifier resulting in the lowering thermal conductivity. According to Mills [12], phonon transfer along silicate network

chain or ring has much lower thermal resistivity($1/\lambda$) than from chain to chain. Similarly, Susa et al. [10] observed that more ionic bonding has the greater thermal resistivity. Therefore, it can be concluded that the positive relationship between thermal conductivity and network structure is closely related to the formation of covalent bond which has low thermal resistivity.

Not only the steel-making process, but also other pyro-metallurgy process, understanding of thermal conductivity is significant. During the operation of submerged arc furnace (SAF) which is widely used in manganese ferroalloy producing, "freeze" lining is applied in order to insulate the refractory and prevent direct contact with molten metal and slag [13]. "Freeze" lining can enhance the refractory lifetime because it prevents the wear mechanism; such as alkali attack, thermal stress and dissolution of refractory. According to Steenkamp et al. [14], who measured thermal conductivity in the CaO-SiO_2-Al_2O_3-MgO-MnO system, "freeze" lining becomes thicker with higher thermal conductivity indicating that thermal conductivity is the major factor determining the thickness of "freeze" lining.

The observed thermal conductivity, called effective thermal conductivity (λ_{eff}), can be expressed by the summation of each different thermal conductivity such as lattice thermal conductivity (λ_L), radiation thermal conductivity (λ_R) and electronic thermal conductivity (λ_{el}) [15]

$$\lambda_{eff} = \lambda_L + \lambda_R + \lambda_{el} \tag{1}$$

The lattice thermal conductivity (λ_L) is based on the heat transfer by phonon. Because scattering of phonon results in the decrease in thermal conductivity, thermal conductivity by phonon is significantly influenced by the change of disordering of network structure in the glass and molten oxide system [16]. Over the 800 K, radiative heat transfer (λ_R) in the clear glass becomes dominant factor [17]. At higher temperature of the transparent molten oxide system, more than 90% of heat is transferred by the radiation conduction. On the other hand, thermal conductivity by electron is insignificant in the molten oxide system as long as the composition of transition metallic oxide does not exceed 70% [15, 18].

In the molten oxide system, the radiative heat conduction can be simply predicted by assuming the steady state along with grey-body conditions. The radiative heat transfer through an optically thick sample can be calculated by a function of absorption coefficient and refractive index in the Stefan-Boltzmann law [15]. However, due to its tremendous radiative and convection effect, precise measurement of thermal conductivity by phonon in the molten oxide system was challenging. Recently, owing to the appropriate modifications [2, 4, 19] and evaluations for systematic error by simulation [20], thermal conductivity measurement technique in the molten oxide system has been improved.

In this chapter, transient hot-wire method that is one of the major thermal conductivity measurement techniques for molten oxide system is introduced comparing with laser flash method. The measurement principle is simply dealt with, and experimental errors are considered. In addition, thermal conduction mechanism in the amorphous system by phonon is discussed. Since the lattice thermal conduction is mainly determined by the structure of oxide system, the effect of structure such as silicate network or ionic bonding, and type of cation is briefly discussed.

2. Thermal conduction in glass and molten oxide system

Ziman [21] explained the transport of heat in terms of collective model instead of individual particle vibration. Namely, thermal energy is the distribution of normal modes of vibration. Owing to the collective model, the excitations that can be considered as the movement of particles in a gas, and kinetic theory is possibly adopted. In the case of glass and ceramic system, determination of a single Brillouin zone is impossible since there is no regular lattice. For this reason, not Umklapp scattering but irregular structure determines the phonon scattering in the glass system. Kingery [22] reported that the phonon interaction by discrete lattice is equivalent to random scattering in the ceramic and glass system. For convenience, he adopted mean free path concept and expressed thermal conductivity by phonon as the transport of energy by particle. As a result, thermal conductivity has been simply explained by the phonon gas model in various glass and ceramic systems [16, 23, 24].

$$\lambda = \frac{1}{3} C \bar{v} l \tag{2}$$

where λ, C, $\bar{v}$ and l indicate thermal conductivity, heat capacity, mean particle velocity, and mean free path of collision.

However, the heat transfer mechanism in the liquid and molten oxide system is still controversial. In the liquid state, Zwanzig [25] proposed the collective dynamical variables having the similar characteristic of longitudinal and transverse phonon. The frequency of the elementary excitation is defined as approximate eigenvalue by an eigen function of the Liouville operator. In addition, he also calculated the lifetimes of elementary excitations reporting that it is determined by the elastic moduli and viscosities. As a result, in the molten oxide system which has enough viscosity coefficients, an elementary excitation has physical meaning. Recently, using *ab initio* molecular dynamics simulations, Iwashita et al. [26] showed that the local configurational excitations in the atomic connectivity network are the elementary excitations in molten metal at high temperature.

Turnbull [27] found that thermal conduction mechanism in the molten salts system is similar to the solid state. Due to the similar ionic spacing of salt system in the solid and liquid state along with the relatively small heat of fusion, he assumed that thermal motion would be similar in liquid and solid. In addition, according to his calculation, the diffusional contribution to thermal conductivity of liquids does not exceed 4%, indicating the major role of vibrational conduction in heat transfer. Similar to molten salt system, it can be inferred that heat is mainly transferred by vibrational excitations in the molten oxide system.

Recently, considering the similar thermal conduction mechanism in glass and molten oxide system, Kim and Morita [28] explained the effect of temperature on thermal conductivity following the same approach. Adopting the one-dimensional Debye temperature and phonon gas model, variables and effect of temperature on thermal conductivity were discussed. According to their work, thermal conductivity of glass initially increases with increasing temperature due to the increase of heat capacity. At one-dimensional Debye temperature where heat capacity becomes max, thermal conductivity reaches the maximum. Afterward, owing to the fluidity of molten state, mean particle velocity along with mean free path of collision decreases with increasing temperature. From physical viewpoint, as increasing

temperature, the required frequency of shear waves to propagate in molten oxide system increases. Since phonon is bosonic particle, the average number of particles follows Bose-Einstein distribution indicating that lower frequency modes have more phonons at a fixed temperature. As a result, negative temperature dependence of thermal conductivity can be found because lower number of shear wave with much higher frequency can propagate as temperature increases.

3. Thermal conductivity measurement technique and related experimental errors

3.1. Thermal conductivity measurement technique for high-temperature oxide melts

Although the understanding of thermal conductivity by phonon is significant for the process control in the iron-making and steel-making field, precise measurement of thermal conductivity by phonon is challenging due to the notorious radiation and convection effect at high temperature [29]. The measurement method of thermal conductivity by phonon can be classified into largely two groups: one is steady-state and another one is nonsteady-state method. In steady-state method, thermal conductivity is determined by the temperature profile across a sample contacting directly with a heat source [15]. However, steady-state method requires a relatively long measurement time in order to obtain the steady state of thermal profile across the sample [18]. In addition, during the measurement, contribution of radiation and convection becomes significant due to the long measurement time. For these reasons, at high temperature, thermal conductivity by phonon transfer cannot be precisely measured by using steady-state method.

In order to investigate the thermal conductivity of molten oxide system, nonsteady-state measurement method has been modified for the last few decades. For the measurement of molten oxide system, two measurement techniques have been widely adopted: one is laser flash method and another one is hot-wire method. Two techniques have in common that both two methods apply constant energy and monitor the temperature change with time. Because the thermal conductivity can be measured within approximately 10 s by nonsteady-state method, the effect of radiation and convection is insignificant as compared to the steady-state method.

Since the first introduction of laser flash method in 1961, this technique has been widely adopted for the purpose of measurement of thermal diffusivity and heat capacity in various materials [30]. During the measurement, the front surface is heated by a single pulse laser resulting in an increasing of temperature at the opposite surface. Then, thermal diffusivity is calculated from the increasing temperature. However, due to the leakage of heat from measurement sample, the sufficient accuracy cannot be achieved at high temperature. Several improvements of laser flash method have been introduced in order to overcome various problems occurred during the measurement. In the 1990s, Ogura et al. [31] developed three-layered laser flash method. Although it has the merit of relatively small heat leakage, calculation of thermal conductivity by phonon transfer requires various physical properties related with radiation such as absorption coefficient [32]. For this reason, recently, Ohta et al. [32, 33], revised the three-layered laser flash method and introduced new method,

called front heating-front-detection laser flash method. Distinct from previous laser flash methods, the laser pulse is irradiated on the bottom of platinum crucible during the front-heating front-detection technique. Assuming the one-dimensional heat flow along with semi-infinite thickness of liquid sample, [33] thermal conductivity is calculated by the measurement of the temperature decay at the bottom of surface. Since the thermal conductivity is measured within only 12 ms, front-heating front detection technique does not consider the additional process for distinguishing radiation effect from observed thermal conductivity data. However, although the front heating-front detection laser flash method has the merit of simple procedure and easy data processing, [34] the effect of radiation on thermal conductivity measurement is still controversial, especially at high temperature [18]. The three different laser flash methods, namely, conventional, three-layered and front heating-front detection laser flash method, have been adopted for the measurement of thermal conductivity, and more details can be found elsewhere [18].

Figure 1 shows the schematic diagram of the hot-wire method for molten oxide system. The hot-wire method, also known as line-source method, is a nonsteady-state method. Because the hot-wire method uses a very thin metal wire, the effect of radiation is relatively insignificant even at high temperature [35]. Since transient hot-wire technique firstly introduced in the 1780s, this method has been widely used for the precise measurement of thermal conductivity of solid, liquid and even gas phases [36]. During the thermal conductivity measurement of molten oxide system, a thin Pt-13%Rh wire is placed in the middle of molten oxide sample and heated up by the applied constant current. The generated heat is transferred from hot-wire

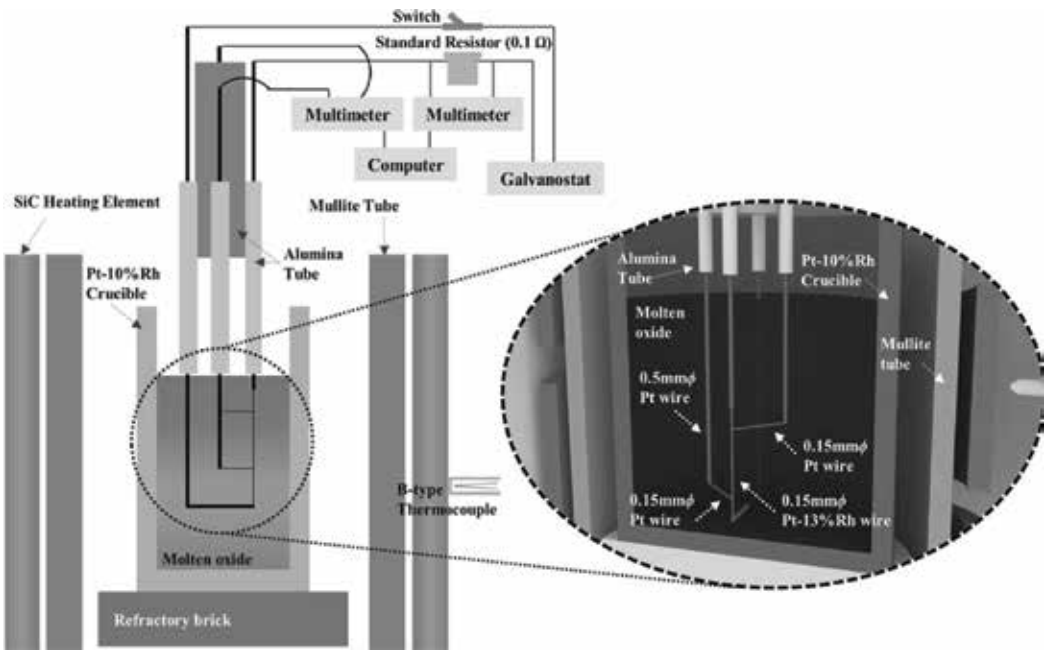

Figure 1. Schematic diagram of the transient hot-wire method for molten oxide system.

into molten oxide system resulting in increasing temperature. If the hot-wire is long enough, the temperature change of molten oxide system resulting from constant heat flux Q can be expressed by a continuous line heat source solution [37].

$$\Delta T = \frac{Q}{4\pi\lambda}\left(\ln\frac{4\kappa t}{r^2} - \gamma\right) = \frac{Q}{4\pi\lambda}\left(\ln t + \ln\frac{4\kappa}{r^2 e^{\gamma}}\right) \tag{3}$$

Here, ΔT is the temperature change of hot-wire, Q is the heat generation per unit length of hot-wire, λ is the thermal conductivity, κ is the thermal diffusivity, r is the radius of hot-wire, t is the time, and γ is the Euler's constant, 0.5772. The continuous line heat source solution can be adopted when the length and diameter ratio of hot-wire is larger than 30 [38]. Following the differentiation of Eq. (4), thermal conductivity can be expressed by Eq. (4).

$$\lambda = \left(\frac{Q}{4\pi}\right)/\left(\frac{dT}{d\ln t}\right) \tag{4}$$

Because a constant current is applied by galvanostat, heat generations per unit length of hot-wire (Q) can be calculated by the following equation.

$$Q = \frac{VI}{m} = I^2\frac{R_T}{m} \tag{5}$$

$$R_T = R_0(1 + AT + BT^2) \tag{6}$$

The abovementioned equation, V, I, m, R_T, and R_0 represents the voltage, current, length of hot-wire, resistance per unit length at T°C, and resistance per unit length at 0°C, respectively. Eq. (6) shows the empirical linear relationship between R_T and R_0. According to Kang and Morita [3], constant of A and B for Pt-13%Rh wire is $1.557\text{x}10^{-3}$ and $-1.441\text{x}10^{-7}$, respectively. During the measurement, R_T is obtained by applying infinitely small current which could not heat up the experimental sample.

From the Ohm's law, the following equation can be obtained at the given temperature T.

$$\frac{dV}{dT} = I\frac{dR_T}{dT} = IR_0(A + 2BT) \tag{7}$$

From the Eqs. (4), (5) and (7), the thermal conductivity can be expressed as the function of voltage and time.

$$\lambda = \left(\frac{I^3 R_T R_0(A + 2BT)}{4m\pi}\right)/\left(\frac{dV}{d\ln t}\right) \tag{8}$$

Using the four-terminal sensing, [11] the voltage change of hot-wire is recorded in real time. Therefore, thermal conductivity of the molten oxide system can be easily calculated by the slope of V versus ln t.

Recently, Mills et al. [39] found that thermal conductivity of molten slag system measured by laser flash method is approximately 10 times than by hot-wire method implying the effect of radiation in the laser flash method. Therefore, it would be inferred that thermal conductivity of molten oxide system is precisely measured at high temperature by using the hot-wire method rather than using the laser flash method.

3.2. Evaluation of the experimental errors occurred during the thermal conductivity measurement by hot-wire method

According to Kwon and Lee [40] and Healy et al. [41] who studied about the errors occurred during the thermal conductivity measurement, appropriately designed hot-wire method can measure thermal conductivity of liquid with the error of less than 0.31%. Although they considered low temperature, below 100°C, effect of other variables such as convection and current leakage seems insignificant during the thermal conductivity measurement even at high temperature.

As previously mentioned, in order to reduce the radiative heat transfer, a thin Pt-13%Rh wire of 0.15 mmφ is used in the hot-wire method during the thermal conductivity measurement. However, although a hot-wire method uses extremely thin wire, the heat can be transferred from the surface of hot-wire by radiation and it becomes significant as temperature increases during the thermal conductivity measurement.

Using the Stefan–Boltzmann law for grey-body radiation, the radiation heat at the surface of hot wire was estimated.

$$q = \varepsilon E_b = \varepsilon \sigma T_s^4 \tag{9}$$

where q is the radiated heat energy, ε is the emissivity, σ is the Stefan-Boltzmann constant, T_s is the surface temperature (K). During the calculation, emissivity of Pt-13%Rh wire was extrapolated on the basis of empirical equation of emissivity of Pt- 10%Rh wire [42]

$$\varepsilon = 0.751\,(T\rho)^{0.5} - 0.632(T\rho) + 0.670\,(T\rho)^{1.5} - 0.607\,(T\rho)^2 \tag{10}$$

where ρ is the resistivity, and T is the temperature of hot-wire (°C). The temperature change of hot-wire along with heat generation was evaluated by the voltage change. Considering the resistivity of hot-wire, the radiation heat during the measurement was evaluated. In **Figure 2**, change of radiation heat along with applied power at 1273 K is presented. After 5 s of experiment, the ratio of radiation heat to the applied power, which is the net heat flow, becomes approximately 0.69% at 1273 K. This value is accordance with the previously calculated value of 1% in the transparent slag at 1273 K after 5 s of experiment [2]. Especially, within the thermal conductivity measurement region, which is 0.8–2 s, radiation heat takes less than 0.51% over total heat flow. Therefore, it can be concluded that radiation effect is not significant during the thermal conductivity measurement using a hot-wire method.

The effect of free convection can be reduced by placing the upper level of the sample in the highest temperature zone [4]. However, during the measurement, the heating up of hot-wire

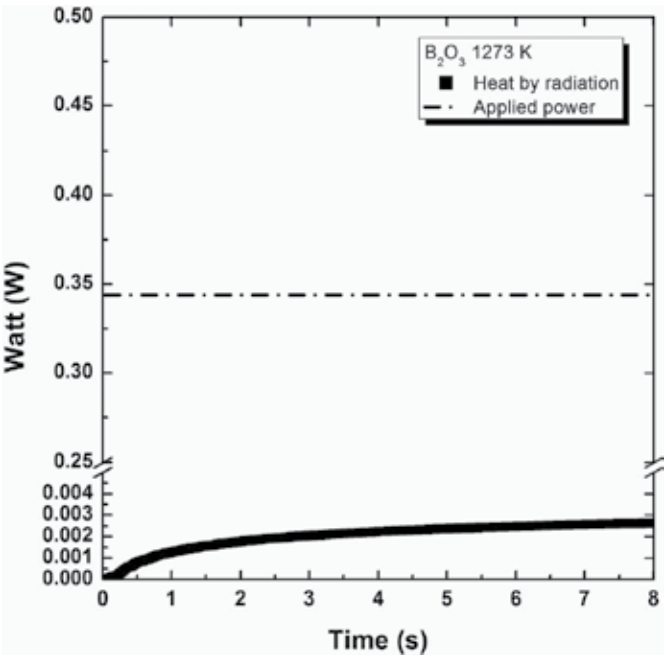

Figure 2. Change of radiation heat (black rectangular) with varying time at a fixed temperature of 1273 K. Dashed dot line indicates the applied power.

results in the increase in temperature of molten oxide system along with partial temperature difference. Such temperature gradient would lead to the convection. In order to determine the effect of convection, the change of Rayleigh number with varying time was considered. **Figure 3** shows the schematic diagram of heat penetration during a hot-wire measurement.

When a current is applied, heat is generated in a thin hot-wire; radius of r_0. Since it is a non-steady-state method, the heat penetration distance will be varying with time. δ is the penetration distance. T_0 and T_1 is the temperature at the surface of hot-wire and the temperature at δ, respectively. The heat penetration distance (δ) is a function of time (t). Tokura et al. [43] reported that heat penetration distance from the hot-wire can be expressed by the following equation.

$$\delta \approx \left(24\alpha r_0 t\right)^{1/3} + r_0 \tag{11}$$

The abovementioned Eq. (11) is valid when $(\delta - r_0) >> 4r_0$. α represents the thermal diffusivity.

It has been reported that free convection is occurred when Rayleigh number (Ra) is larger than 1000 [1]. Therefore, calculation of Rayleigh number in the present molten oxide system is significant in order to evaluate the effect of free convection during the experiment. Rayleigh number can be expressed by the following equation, which is the product of Grashof number and Prandtl number.

$$Ra = \frac{\beta \Delta T g L^3}{\nu \alpha} \tag{12}$$

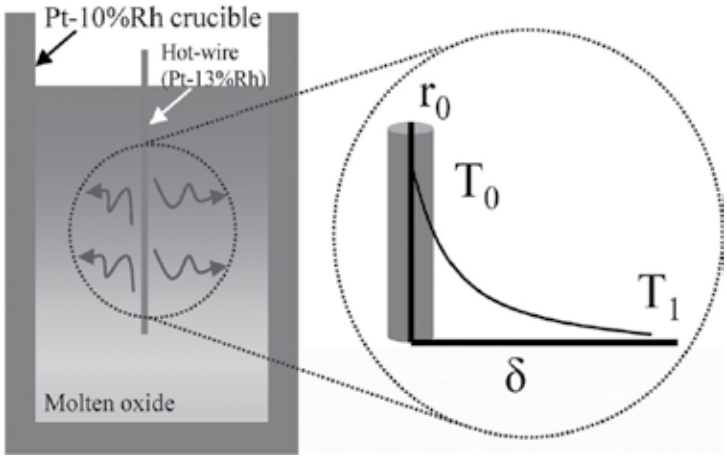

Figure 3. Schematic diagram of heat penetration during thermal conductivity measurement by hot-wire measurement.

where β is thermal expansion coefficient, ΔT is temperature difference, g is gravitational acceleration, L is characteristic length, v is kinetic viscosity. L can be substituted with heat penetration distance (δ). Combine the Eqs. (3), (11) and (12), Rayleigh number can be deduced by the following equation, where C is the exponential of Euler's constant; 1.78.

$$Ra = \frac{\beta g Q}{4\pi\lambda v\alpha}\left[(24\alpha r_0 t)^{1/3} + r_0\right]^3 \ln\left(\frac{4\alpha t}{r_0^2 C}\right) \tag{13}$$

Using Eq. (13) along with following physical properties of molten B_2O_3 system at 1273 K, Rayleigh number can be calculated. Thermal expansion coefficient (β) of molten B_2O_3 is 100 ppm/K at the temperature range between 1273 and 1473 K [44]. Thermal diffusivity (α) is 4.325 $cm^2\ s^{-1}$ at 1273 K [31]. Kinematic viscosity, that is, the ratio of dynamic viscosity to density is 0.0065 $m^2\ s^{-1}$ [45]. Rayleigh number is calculated, and it is shown in **Figure 4**. Compared to Rayleigh number of pure water at 298 K, molten B_2O_3 system shows much lower Rayleigh number. Due to much higher kinematic viscosity and thermal diffusivity, B_2O_3 shows much lower Rayleigh number even at high temperature of 1273 K. Therefore, it can be concluded that there is no free convection effect during the thermal conductivity measurement of molten oxide system within 10 s. In addition, if there is convection effect, the linearity between voltage and time could not be observed. As a result, the thermal conductivity by phonon transfer can be safely obtained within the region where the linear relationship between voltage and time exists.

Recently, several studies have evaluated the experimental conditions which affect precision of the measurement using hot-wire method [20, 46]. A computational fluid dynamics (CFD) calculation [20] revealed that determination of the resistivity and the temperature coefficient of resistance of the hot-wire is crucial in order to obtain precise thermal conductivity. In addition, Kang et al. [46] calculated the current leakage by semi-quantitative evaluation and reported that the current leakage is 2% (at most) in various silicate melts which contain less than 20 wt% FeO_x.

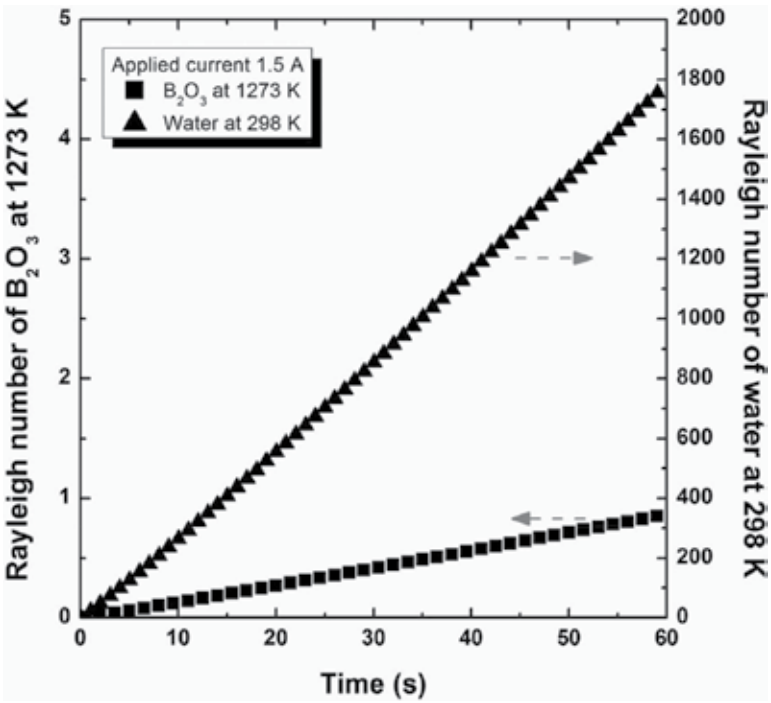

Figure 4. Calculated Rayleigh number of molten B_2O_3 at 1273 K (left) and water at 298 K (right) with varying time.

4. Effect of structure and cation on thermal conductivity of molten oxide system

Similar to other physical properties, such as density, thermal expansion, viscosity and electric conductivity, thermal conductivity of molten oxide system is affected by the network structure such as silicate, borate and aluminate network structures. It was known that formation of network structure in the glass and molten oxide system plays a role of limiting to the network randomness [47] resulting in the increase of thermal conductivity by reducing of phonon-phonon scattering. According to Kang and Morita [3], depolymerization of silicate network structure results in lowering thermal conductivity. In addition, amphoteric behavior of aluminum oxide related to aluminate structure leads to both increasing and decreasing of thermal conductivity depending on its compositions. Recently, Kim and Morita reported the effect of intermediate range order borate structure [48–52]. In case of borate structure, complicated super-structure units exist consisting of 3- and 4-coordinate boron ions associated with oxygen ions [53]. Depending on the compositions and oxide system, different borate superstructure can be formed resulting in different effects on thermal conductivity.

In **Figure 5**, thermal conductivity of molten Na_2O-B_2O_3-SiO_2 system is shown with varying SiO_2/B_2O_3 mole ratio [49]. At 1273 K, increasing of thermal conductivity with higher ratio of SiO_2/B_2O_3 can be found. Although these systems show similar silicate network structures with

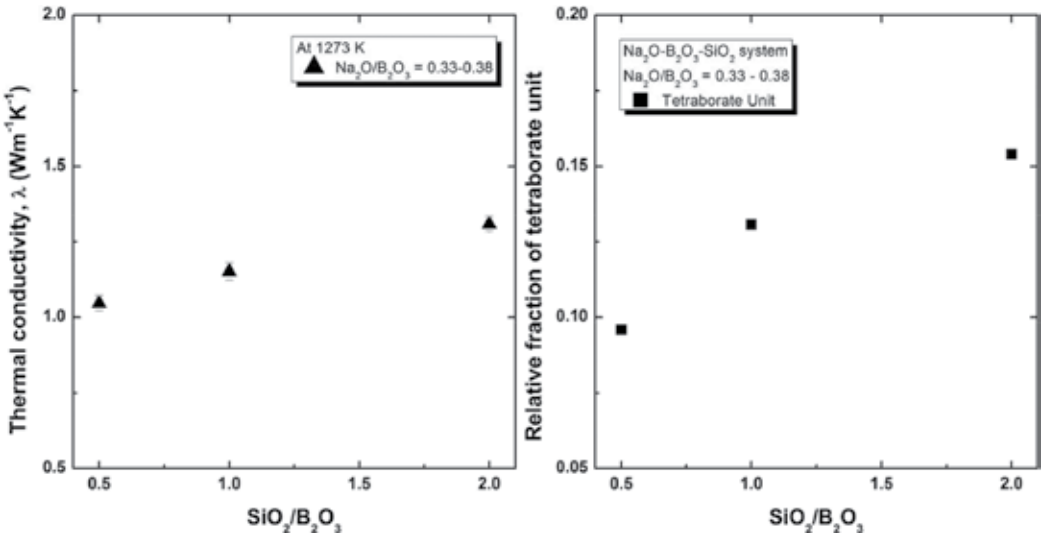

Figure 5. Relationship between SiO_2/B_2O_3 ratio and the thermal conductivity (left), SiO_2/B_2O_3 ratio and relative fraction of tetraborate unit (right).

analogous non-bridging oxygen (NBO) number [49]. On the right side of **Figure 5**, the effect of SiO_2/B_2O_3 ratio on borate super-structure obtained by Raman spectroscopy is shown. It should be noted that the Raman spectra were identified by using Gaussian deconvolution from appropriate references. According to area ratio, the relative fraction of associated structures was calculated. The increase of relative fraction of tetraborate unit can be found with higher concentration of SiO_2. Considering that tetraborate unit consisting of 3- and 4-coordinate boron forms three-dimensional network, thermal conductivity increases as a result of polymerization of the network structure. Similar effect can be found in another study reporting the increase of viscosity with formation of tetraborate unit in the $CaO\text{-}Al_2O_3\text{-}Na_2O\text{-}B_2O_3$ system [54].

Not only the polymerized network structure, but also cation affects thermal conductivity in the molten oxide system [8, 28, 51, 55]. The linear relationship between thermal conductivity and ionization potential (Z/r^2); the ratio of the charge of the cation (Z) to the square of the cation radius (r), was observed in the alkali-borate system [28, 51]. In addition, the effect of ionization potential of cation on thermal conductivity is similar in both glass and molten oxide system. Recently, Crupi et al. [56] reported that intermediate range order borate structure, that is borate super-structure, is affected by the type of cations. As increasing of the ionic radius of cation, larger radius of void can be found. Since larger void has high flexibility with high configurations, thermal conductivity decreases as increasing of ionic radius [28].

5. Conclusions

In this chapter, the thermal conductivity measurement technique for high-temperature molten oxide system was reviewed along with heat conduction. Although phonon cannot be

defined in the molten oxide system, phonon-like excitation is elementary excitation having similar characteristic of longitudinal and transverse phonon. Recent studies revealed that local configurational excitation is a origin of phonon-like excitation. In addition, the effect of temperature on thermal conductivity in both glass and molten oxide system was reviewed. The laser flash method and hot-wire method, typical thermal conductivity measurement techniques for high temperature, were briefly reviewed. Compared to laser flash method, hot-wire method is relatively precise for measurement of molten oxide system by reducing radiation effect through small surface of heating source. The systematic errors probably occurred were considered. The radiation and convection effects were reviewed based on the simple modeling and mathematical calculations in the molten oxide system. Results showed that radiation effect and convection effect on thermal conductivity are insignificant at 1273 K. Especially, since the measurement is terminated within 5 s, its effect would be negligible. Finally, the effect of network structure and cations on thermal conductivity was discussed. Due to limiting its randomness, polymerization of glass and molten oxide system results in the increase of thermal conductivity. In addition, the effect of cation type on thermal conductivity in the molten oxide system was discussed through the ionization potential.

Acknowledgements

Youngjae Kim is grateful for the financial support that was provided by the Basic Research Project (GP2017-025) of the Korea Institute of Geoscience and Mineral Resources (KIGAM), funded by the Ministry of Science and ICT.

Author details

Youngjae Kim[1]*, Youngjo Kang[2] and Kazuki Morita[3]

*Address all correspondence to: youngjae.kim@kigam.re.kr

1 Korea Institute of Geoscience and Mineral Resources, Republic of Korea

2 Dong-A University, Republic of Korea

3 The University of Tokyo, Japan

References

[1] Kang Y. Thermal Conductivity of Na_2O-SiO_2 and CaO-Al_2O_3-SiO_2 melt [thesis]. The University of Tokyo; 2004

[2] Nagata K, Goto KS. Heat conductivity and mean free path of phonons in metallurgical slags. In: Fine HA, Gaskell DR, editors. Second International Symposium on

Metallurgical Slags and Fluxes. Warrendale: The Metallurgical Society of AIME; 1984. pp. 875-889

[3] Kang Y, Morita K. Thermal conductivity of the $CaO-Al_2O_3-SiO_2$ system. ISIJ International. 2006;**46**(3):420-426

[4] Nagata K, Susa M, Goto KS. Thermal conductivities of slags for ironmaking and steelmaking. Tetsu-to-Hagane. 1983;**11**(11):1417-1424

[5] Hasegawa H, Hoshino Y, Kasamoto T, et al. Thermal conductivity measurements of some synthetic Al_2O_3-CaO-SiO_2 slags by means of a front-heating and front-detection laser-flash method. Metallurgical and Materials Transactions B. 2012;**43**(6):1405-1412. DOI: 10.1007/s11663-012-9702-y

[6] Glaser B, Sichen D. Thermal conductivity measurements of ladle slag using transient hot wire method. Metallurgical and Materials Transactions B. 2012;**44B**(1):1-4. DOI: 10.1007/s11663-012-9773-9

[7] Kang Y, Nomura K, Tokumitsu K, Tobo H, Morita K. Thermal conductivity of the molten $CaO-SiO_2-FeO_x$ system. Metallurgical and Materials Transactions B. 2012;**43**(6):1420-1426. DOI: 10.1007/s11663-012-9706-7

[8] Ozawa S, Susa M. Effect of Na_2O additions on thermal conductivities of $CaO–SiO_2$ slags. Ironmaking & Steelmaking. 2005;**32**(6):487-493

[9] Qiu X, Xie B, Qing X, Diao J, Huang Q, Wang S. Effects of transition metal oxides on thermal conductivity of mould fluxes. Journal of Iron and Steel Research, International. 2013;**20**(11):27-32. DOI: 10.1016/S1006-706X(13)60192-2

[10] Susa M, Kubota S, Hayashi M, Mills KC. Thermal conductivity and structure of alkali silicate melts containing fluorides. Ironmaking & Steelmaking. 2001;**28**(5):390-395. DOI: 10.1179/irs.2001.28.5.390

[11] Ozawa S, Endo R, Susa M. Thermal conductivity measurements and prediction for R_2O-CaO-SiO_2(R= Li, Na, K) slags. Tetsu-to-Hagane. 2007;**93**(6):416-423

[12] Mills KC. The influence of structure on the physico-chemical properties of slags. ISIJ International. 1993;**33**(1):148-155. DOI: 10.2355/isijinternational.33.148

[13] Duncanson PL, Toth JD. The truths and myths of freeze lining technology for submerged arc furnaces. In *INFACON X*: Transformation Through Technology, The South African Institute of Mining and Metallurgy: Cape Town, South Africa, 2004; 488-499

[14] Steenkamp JD, Tangstad M, Pistorius PC. Thermal conductivity of solidified manganese-bearing slags—a preliminary investigation. In: Jones RT, den Hoed P, editors. Southern African Pyrometallurgy 2011 International Conference. Johannesburg: The Southern African Institute of Mining and Metallurgy; 2011. pp. 327-344

[15] Mills KC. Slag Atlas, Verein Deutscher Eisenhüttenleute (VDEh). 2nd ed. Dusseldorf: Verlag Stahleisen GmbH; 1995

[16] Kittel C. Interpretation of the thermal conductivity of glasses. Physical Review. 1949; **75**(6):972-974

[17] De Jong BHWS, Beerkens RGC, van Nijnatten PA, Le Bourhis E. Glass, 1. Fundamentals. In: Ullmann's Encyclopedia of Industrial Chemistry. Weinheim: Wiley-VCH; 2000. DOI: 10.1002/14356007

[18] Kang Y, Lee J, Morita K. Thermal conductivity of molten slags: A review of measurement techniques and discussion based on microstructural analysis. ISIJ International. 2014;**54**(9):2008-2016. DOI: 10.2355/isijinternational.54.2008

[19] Ogino K, Nishiwaki J, Yamamoto Y. Suragu yuutai no netsudendoudo no sokutei [Thermal conductivity measurement in the molten slag]. Tetsu- to- Hagane. 1979;**65**(11):S683

[20] Glaser B, Ma L, Sichen D. Determination of experimental conditions for applying hot wire method to thermal conductivity of slag. Steel Research International. 2013;**84**(7):649-663. DOI: 10.1002/srin.201200206

[21] Ziman JM. Electrons and Phonons: The Theory of Transport Phenomena in Solids. London: Oxford University Press; 1960

[22] Kingery WD. Introduction to Ceramics. New York: Wiley; 1967

[23] Tohmori M, Sugawara T, Yoshida S, Matsuoka J. Thermal conductivity of sodium borate glasses at low temperature. Physics and Chemistry of Glasses - European Journal of Glass Science and Technology Part B. 2009;**50**(6):358-360

[24] Zeller RC, Pohl RO. Thermal conductivity and specific heat of noncrystalline solids. Physical Review B. 1971;**4**(6):2029-2041

[25] Zwanzig R. Elementary excitations in classical liquids. Physical Review. 1967;**156**(1):190-195. DOI: 10.1103/PhysRev.156.190

[26] Iwashita T, Nicholson DM, Egami T. Elementary excitations and crossover phenomenon in liquids. Physical Review Letters. 2013;**110**(20):205504. DOI: 10.1103/PhysRevLett.110.205504

[27] Turnbull AG. The thermal conductivity of molten salts II. Theory and results for pure salts. Australian Journal of Applied Science. 1961;**12**:324-329

[28] Kim Y, Morita K. Temperature dependence and cation effects in the thermal conductivity of glassy and molten alkali borates. Journal of Non-Crystalline Solids. 2017;**471**:187-194. DOI: 10.1016/j.jnoncrysol.2017.05.034

[29] Nagashima A. Viscosity, thermal conductivity, and surface tension of high-temperature melts. International Journal of Thermophysics. 1990;**11**(2):417-432. DOI: 10.1007/BF01133571

[30] Waseda Y, Ohta H. Current views on thermal conductivity and diffusivity measurements of oxide melts at high temperature. Solid State Ionics. 1987;**22**:263-284

[31] Ogura G, Suh I-K, Ohta H, Waseda Y. Thermal diffusivity measurement of boron oxide melts by laser flash method. Journal of the Ceramic Society of Japan. 1990;**98**(3):305-307

[32] Ohta H, Shibata H, Waseda Y. Recent progress in thermal diffusivity measurement of molten oxides by the laser flash method. In: Kongoli F, Itagaki K, Yamauchi C, Sohn HY,

editors. Yazawa International Symposium. San Diego: TMS (The Minerals, Metals & Materials Society); 2003. pp. 453-462

[33] Ohta H, Shibata H, Hasegawa H, et al. Thermal conductivity of R-Na_2O-SiO_2 (R = Al_2O_3, CaO) melts. Journal for Manufacturing Science & Production. 2013;**13**(1-2):115-119. DOI: 10.1515/jmsp-2012-0020

[34] Hasegawa H, Ohta H, Shibata H, Waseda Y. Recent development in the investigation on thermal conductivity of silicate melts. High Temperature Materials and Processes. 2012;**31**(4-5):491-499. DOI: 10.1515/htmp-2012-0085

[35] Mills KC, Yuan L, Li Z, Zhang G. Estimating viscosities, electrical & thermal conductivities of slags. High Temperatures – High Pressures. 2013;**42**:237-256

[36] Assael MJ, Antoniadis KD, Wakeham WA. Historical evolution of the transient hot-wire technique. International Journal of Thermophysics. 2010;**31**(6):1051-1072. DOI: 10.1007/s10765-010-0814-9

[37] Carslaw HS, Jaeger JC. Conduction of Heat in Solids. 2nd ed. London: Oxford University Press; 1959

[38] Blackwell J. The axial-flow error in the thermal-conductivity probe. Canadian Journal of Physics. 1956;**34**(4):412-417

[39] Mills KC, Yuan L, Jones RT. Estimating the physical properties of slags. Journal of the Southern African Institute of Mining and Metallurgy. 2011;**111**(10):649-658

[40] Kwon SY, Lee S. Precise measurement of thermal conductivity of liquid over a wide temperature range using a transient hot-wire technique by uncertainty analysis. Thermochimica Acta. 2012;**542**:18-23. DOI: 10.1016/j.tca.2011.12.015

[41] Healy JJ, de Groot JJ, Kestin J. The theory of the transient hot-wire method for measuring thermal conductivity. Physica B+C. 1976;**82**(2):392-408. DOI: 10.1016/0378-4363(76)90203-5

[42] Bradley D, Entwistle AG. Determination of the emissivity, for total radiation, of small diameter platinum-10% rhodium wires in the temperature range 600-1450 C. British Journal of Applied Physics. 1961;**12**(12):708-711. DOI: 10.1088/0508-3443/12/12/328

[43] Tokura I, Saito H, Kishinami K, Takekawa Y. Application of the transient hot-wire method on thermal conductivity measurement of solid-liquid mixtures. Memoirs of the Muroran Institute of Technology. Science and Engineering. 1990;**40**:63-73

[44] Shartsis L, Capps W, Spinner S. Density and expansivity of alkali borates and density characteristics of some other binary glasses. Journal of the American Ceramic Society. 1953;**36**(2):35-43. DOI: 10.1111/j.1151-2916.1953.tb12833.x

[45] Napolitano A, Macedo PB, Hawkins EG. Viscosity and density of boron trioxide. Journal of the American Ceramic Society. 1965;**48**(12):613-616. DOI: 10.1111/j.1151-2916.1965.tb14690.x

[46] Kang Y, Lee J, Morita K. Comment on "thermal conductivity measurements of some synthetic Al_2O_3-CaO-SiO_2 slags by means of a front-heating and front-detection laser-flash method". Metallurgical and Materials Transactions B. 2013;**44**(6):1321-1323. DOI: 10.1007/s11663-013-9933-6

[47] Kingery WD. Thermal conductivity: XIV, conductivity of multicomponent systems. Journal of the American Ceramic Society. 1959;**42**(12):617-627

[48] Kim Y, Morita K. Relationship between molten oxide structure and thermal conductivity in the CaO–SiO_2–B_2O_3 system. ISIJ International. 2014;**54**(9):2077-2083. DOI: 10.2355/isijinternational.54.2077

[49] Kim Y, Yanaba Y, Morita K. The effect of borate and silicate structure on thermal conductivity in the molten Na_2O–B_2O_3–SiO_2 system. Journal of Non-Crystalline Solids. 2015;**415**:1-8. DOI: 10.1016/j.jnoncrysol.2015.02.008

[50] Kim Y, Morita K. Thermal conductivity of molten B_2O_3, B_2O_3-SiO_2, Na_2O-B_2O_3, and Na_2O-SiO_2 systems. Journal of the American Ceramic Society. 2015;**98**(5):1588-1595. DOI: 10.1111/jace.13490

[51] Kim Y, Morita K. Thermal conductivity of molten Li_2O-B_2O_3 and K_2O-B_2O_3 systems. Smith D (ed). Journal of the American Ceramic Society. 2015;**98**(12):3996-4002. DOI: 10.1111/jace.13820

[52] Kim Y, Yanaba Y, Morita K. Influence of structure and temperature on the thermal conductivity of molten CaO-B_2O_3. Journal of the American Ceramic Society. 2017;**100**(12):5746-5754. DOI: 10.1111/jace.15123

[53] Wright AC. Borate structures: crystalline and vitreous. Physics and Chemistry of Glasses – European Journal of Glass Science and Technology Part B. 2010;**51**(1):1-39

[54] Kim GH, Sohn I. Role of B_2O_3 on the viscosity and structure in the CaO-Al_2O_3-Na_2O-based system. Metallurgical and Materials Transactions B. 2013;**45**:86-95. DOI: 10.1007/s11663-013-9953-2

[55] Hayashi M, Ishii H, Susa M, Fukuyama H, Nagata K. Effect of ionicity of nonbridging oxygen ions on thermal conductivity of molten alkali silicates. Physics and Chemistry of Glasses. 2001;**42**(1):6-11

[56] Crupi C, Carini G, González M, D'Angelo G. Origin of the first sharp diffraction peak in glasses. Physical Review B. 2015;**92**(13):134206. DOI: 10.1103/PhysRevB.92.134206

Chapter 7

Effect of Ice and Hydrate Formation on Thermal Conductivity of Sediments

Evgeny Chuvilin, Boris Bukhanov, Viktor Cheverev, Rimma Motenko and Erika Grechishcheva

Additional information is available at the end of the chapter

http://dx.doi.org/10.5772/intechopen.75383

Abstract

Thermal conductivity of ice- and hydrate-bearing fine-grained porous sediments (soils) has multiple controls: mineralogy, particle size, and physical properties of soil matrix; type, saturation, thermal state, and salinity of pore fluids; and pressure and temperature. Experiments show that sediments generally increase in thermal conductivity upon freezing. The increase is primarily due to fourfold difference between thermal conductivity of ice and water (~2.23 against ~0.6 W/(m·K)) and is controlled by physicochemical processes in freezing sediments. Thermal conductivity of frozen soils mainly depends on lithology, salinity, organic matter content, and absolute negative temperature, which affect the amount of residual liquid phase (unfrozen water). It commonly decreases as soil contains more unfrozen water, in the fining series 'fine sand – silty sand – sandy clay – clay', as well as at increasing temperatures, salinity, or organic carbon contents. According to experimental evidence, the behavior of thermal conductivity in hydrate-bearing sediments strongly depends on conditions of pore hydrate formation. It is higher when pore hydrates form at positive temperatures ($t > 0^{o}C$) than in the case of hydrate formation in frozen samples. Freezing and thawing of hydrate-bearing sediments above the equilibrium pressure reduces their thermal conductivity due to additional hydrate formation.

Keywords: thermal conductivity, sediments, temperature, ice, gas hydrate, freezing, permafrost, unfrozen water, salinity, hydrate saturation, organic matter

1. Introduction

Thermal conductivity of rocks depends on their origin and deposition environments and related lithology, mineralogy, structure and texture, as well as on thermal state and

thermodynamic conditions [1–13]. There is a wealth of published evidence on thermal conductivity control by mineralogy, particle size, pore space structure, and pore fluid state and composition: whether it is fresh or saline water, ice, gas, organic compounds, and so on [14–21]. However, the effect of some pore filling materials on thermal properties of sediments remains poorly investigated, especially that of pore hydrates [22, 23]. Natural gas hydrates share much physical similarity with ice (heat capacity, density, and acoustic properties) and thus pore hydrates in permafrost, though being known since the 1970s [24], are hard to identify and study with conventional geophysical methods, mainly seismic. Meanwhile, pore gas hydrate and ice differ markedly in thermal conductivity, which is 2.23 W/(m·K) in hydrate, 0.54–0.65 W/(m·K) in ice, and 0.6 W/(m·K) in liquid water [25–27].

Knowledge of thermal properties, especially thermal conductivity, of frozen and freezing porous sediments is valuable in geocryological predictions for reducing geological engineering risks during construction and operation of buildings and utilities in regions of Arctic and highland permafrost [28, 29]. True thermal conductivity values of frozen soils are also indispensable to choose optimal strategies of mitigating risks from permafrost thawing as a result of global warming or local manmade impacts.

The development of hydrate-bearing gas and oil reservoirs likewise requires knowing their thermal properties [30]. Methane production from these reservoirs is most often simulated with reference to thermal conductivity of pure methane hydrates [31], but this simplistic assumption can entrain serious errors during methane recovery, especially for permafrost containing hydrates and ice.

The marked thermal conductivity difference between hydrate and ice is a prerequisite for creating a method of identifying and mapping intra-permafrost gas hydrates.

2. Thermal conductivity of sediments in unfrozen and frozen state and freezing effect

Thermal properties of rocks, soils, water, and air vary as a function of their composition, structure and state, as well as thermodynamic conditions. Thermal conductivity values of different materials are quoted in **Table 1** per unit volume of rocks, sediments, water, ice, snow and air. Note that it linearly depends on temperature for water, ice and air.

Comparative analysis of experimental data shows that thermal conductivity of igneous (granite, basalt), metamorphic (quartzite, schists), and sedimentary (sandstone, limestone, dolomite) rocks can vary from 1.0 to 5.0 W/(m·K) as a function of different factors. The mineralogy dependence is associated with the presence of thermally conductive minerals, such as SiO_2 quartz (~7.0 W/(m·K)) or iron-bearing phases (e.g., pyrite). Density and porosity effects appear as greater thermal conductivity in denser and less porous rocks, that is, it is lower in sediments than in igneous or metamorphic rocks. Experiments show that 15–20% densening of skeleton in sand leads to about twice higher thermal conductivity. The variations result from more or less close packing of particles. Manmade compaction likewise leads to thermal conductivity increase in sediments, which is often used in civil engineering.

Cemented porous sediments fall into three thermal conductivity groups: (1) coarse clastics (conglomerates, gritstones, and sandstones); (2) fine clastics (silt and clay); (3) chemogenic and biogenic carbonates and silicates (dolomite, anhydrite, limestone, diatomite, etc.). Thermal conductivity of coarse clastics is from 1.5 to 4.5 W/(m·K), estimated separately for matrix and cement, and reaches 5.8 W/(m·K) in low-porosity monomineral sediments (dolomite, limestone). Thermal conductivity is anizotropic in many sedimentary and metamorphic rocks: it is on average 10–30% higher along than across the bedding, especially in shale and gneiss [32]. The reason is that interactions of mineral particles and heat transfer are more active along the bedding controlled by the origin and deposition environments of rocks.

Thermal conductivity variations in sediments and soils, which are multicomponent and multiphase systems, depend on relative percentages of solid, liquid, and gas phases; soil chemistry and mineralogy; structure and texture (particle size, porosity, layering, etc.); moisture contents; and temperature. Saturation of sediments affects significantly their thermal properties: thermal conductivity reaches its maximum at full water saturation [11] as water with λ = 0.54 (W/(m·K) supplants gas with λ = 0.024 (W/(m·K).

The dependence on particle size composition shows up in higher thermal conductivity of coarse and very coarse soils (of boulder, pebble, gravel, and sand particles) compared to finer-grained varieties, the moisture content, density, and other parameters being equal. The upper limit for coarse sediments (up to 3–9 W/(m·K)) corresponds to hard components while the lower limit (0.3–0.5 W/(m·K)) represents dry fine-grained material. Thermal conductivity decreases with fining, in a descending series of sand – silt – clay – peat (**Table 1**), because of a greater number of loose contacts between particles [33].

Saturated frozen sediments and soils with medium or high moisture contents have higher thermal conductivity than their unfrozen counterparts because pore ice is four times more conductive than water (**Table 1**): 2.22 W/(m·K) against 0.54 W/(m·K). However, the temperature dependence of thermal conductivity in wet porous sediments is rather controlled by relative percentages of pore ice and water and conditions of heat transfer at their contacts. Within the range of positive temperatures, thermal conductivity decreases slowly from 25 to 0°C, in accordance with linear dependence on water temperature, but rises abruptly at the transition from 0 to –1°C when pore water rapidly converts to ice (**Figure 1**). Note that thermal conductivity of ice-rich soil depends more on the conditions of cooling and heating than on absolute temperature. Of special importance is the direction of heat transfer at alternating pressures and temperatures, when pore water converts to ice and back, and changes in their relative amounts [15]. **Figure 2** shows qualitative variations of thermal conductivity in frozen sediments subject to further freezing and subsequent thawing. The curves comprise several segments corresponding to different temperature intervals. Thermal conductivity decreases linearly within the range of positive temperatures till the onset of freezing (segment A-B) and then increases dramatically in the region of rapid water-to-ice transition (segment B-C), when ice, with its thermal conductivity four times that of water, appears as a new pore filling component, while the amount of unfrozen pore water reduces. Further freezing to –15°C and colder (segment C-D) corresponds to notable (30–40%) decrease in thermal conductivity. The reason is that increasing crystallization of unfrozen bound water and related thermomechanic stress, as well as thermal expansion variations, cause rapid growth of cracks. Saline

Material	Thermal conductivity λ (W/(m·K))
Water	
At +4.1°C	0.54
At +20°C	0.60
Ice	2.22–2.35
Air	
At 0°C	0.024
At −23°C	0.022
Snow	
Loose	0.1
Dense	0.3–0.4
Granite	2.3–4.1
Basalt	1.74–2.91
Quartzite	2.9–6.4
Shale	1.74–2.33
Sandstone	0.7–5.8
Limestone	0.8–4.1
Dolomite	1.1–5.2
Sand	
Dry	0.3–0.35
Unfrozen, water-saturated	1.7–2.6
Frozen, ice-saturated	1.5–3.0
Silty clay	
Dry	0.19–0.22
Unfrozen, water-saturated	0.6–1.0
Frozen, ice-saturated	1.2–1.4
Clay	
Air-dry	0.8–1.0
Unfrozen, water-saturated	1.2–1.4
Frozen, ice-saturated	1.4–1.8
Peat	
Dry	0.012–0.14
Unfrozen, water-saturated	0.7–0.9
Frozen, ice-saturated	1.1–1.2

Table 1. Thermal conductivity of different materials [19].

http://dx.doi.org/10.5772/intechopen.75383

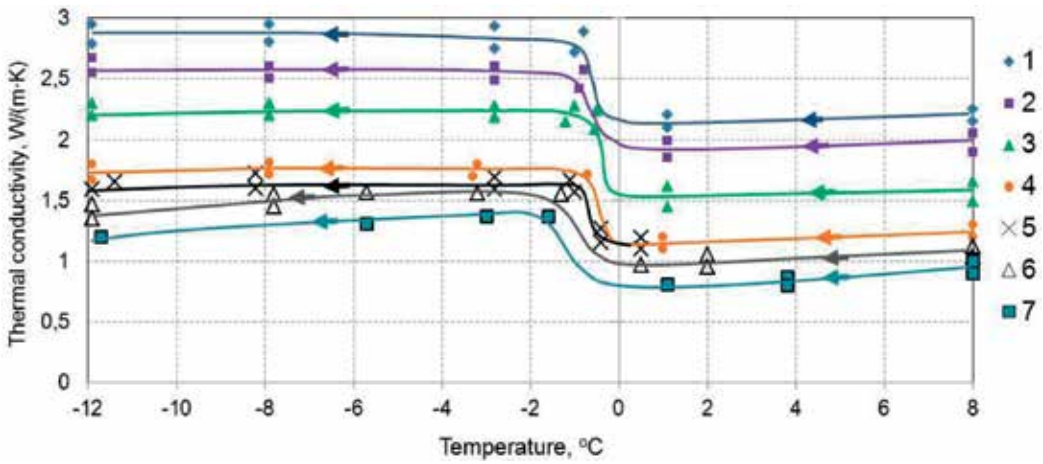

Figure 1. Effect of temperature on thermal conductivity in different types of sediments: 1—coarse crushed stone filled with silt, 2—fine sand, 3—silty sand, 4—loess-like silty clay, 5—silty clay, 6—clay, and 7—degraded peat [15, 19]. Data points are experimental measurements; lines are approximation trends. The arrows show the direction of temperature change.

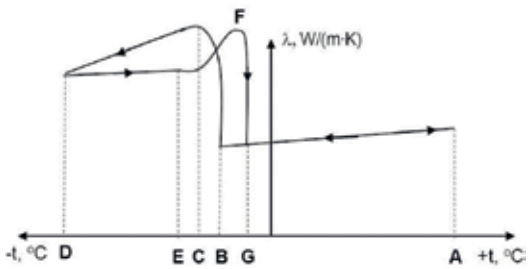

Figure 2. Variations of thermal conductivity in frozen sediments subject to freezing and subsequent thawing. The arrows show the direction of temperature change.

peat-bearing fine-grained porous soil contains much unfrozen water even at low negative temperatures, till -15°C [16, 19, 34]. The thermal conductivity reduction is especially large in ice-rich peat subject to further cooling and related brittle deformation when internal stress in soil releases through microcracks.

Subsequent warming (segment E-F) leads to notable increase in thermal conductivity as the cracks heal up because ice, and soil as a whole, become more plastic. The highest thermal conductivity values in the warming-thawing cycle of frozen soil approach those in the freezing-cooling cycle, but correspond to higher negative temperatures because of hysteretic behavior of moisture phases. Thermal conductivity decreases dramatically till the thawing temperature within the segment F-G, as pore ice melting increases the contents of liquid water.

The thermal conductivity decreases with grain sizes in the series 'coarse sand – fine sand – silty sand – silt – silty clay – clay' was observed in both frozen and unfrozen sediments with

different degrees of water or ice saturation [15, 17–21], over the range of temperatures from +20 to -20 °C, including the region of rapid water-ice phase transitions. Finer sediments have more thermal resistance contacts and are more hydrophilic and ultraporous, which increases relative contents of low-conductive liquid unfrozen water.

Thermal conductivity of frozen sediments increases systematically with ice saturation as low-conductivity gas gives way to high-conductivity ice. Sediments with high contents of ice, which swells out the mineral skeleton, have thermal conductivity about that of ice.

Salinity, or the presence of soluble salts in pore water, is another important control of thermal conductivity in frozen sediments. Namely, Na+ and Cl- ions lead to changes in the phase state of pore moisture in permafrost. Frozen soils with higher salinity (Z, %), that is, salt-to-dry sediment weight ratio, contain more unfrozen pore water and, correspondingly, have lower thermal conductivity (**Figure 3**). Thermal conductivity of saline sand and silty sand containing liquid pore water is much lower than that in non-saline sediments: only 1% increase of salinity in frozen sand may cause twofold thermal conductivity decrease. Unlike sand, more or less water-saturated low saline (0 to 0.5-0.7%) clay silt and clay have thermal conductivity slightly (within 10%) higher than in their non-saline counterparts, but more saline varieties are less conductive. Namely, at Z > 1%, thermal conductivity shows a weak decreasing trend traceable until the system reaches the eutectic point. This behavior is related primarily with changes in relative contents of water phases (ratio of unfrozen water content to total moisture content) as salinity increases. The amount of liquid water depends on concentration as well as on chemistry of salts: it increases progressively in the series Na_2SO_4-Na_2CO_3-$NaNO_3$-NaCl, while thermal conductivity decreases correspondingly. Note that further cooling of frozen soils reduces the amount of unfrozen pore water [34]. As the pore fluid reaches eutectic concentration and temperature, salts form cryohydrates, whereby the content of unfrozen water decreases dramatically. The formation of thermally conductive cryohydrates in the pore space and the respective reduction of the liquid water content leads to thermal conductivity increase in frozen soils. Experiments show that thermal conductivity of saline soils tends to that of non-saline soils at temperatures below eutectics [35].

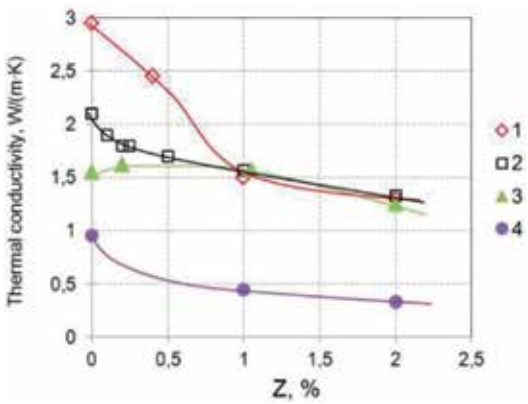

Figure 3. Salinity (Z,%) dependence of thermal conductivity for different types of NaCl-bearing soil: 1—fine sand, 2—silty sand, 3—sandy clay, and 4—kaolin clay (W = 15–30% for 1–3 and W = 50–70% for 4) [18]. Data points are experimental measurements; lines are approximation trends.

http://dx.doi.org/10.5772/intechopen.75383

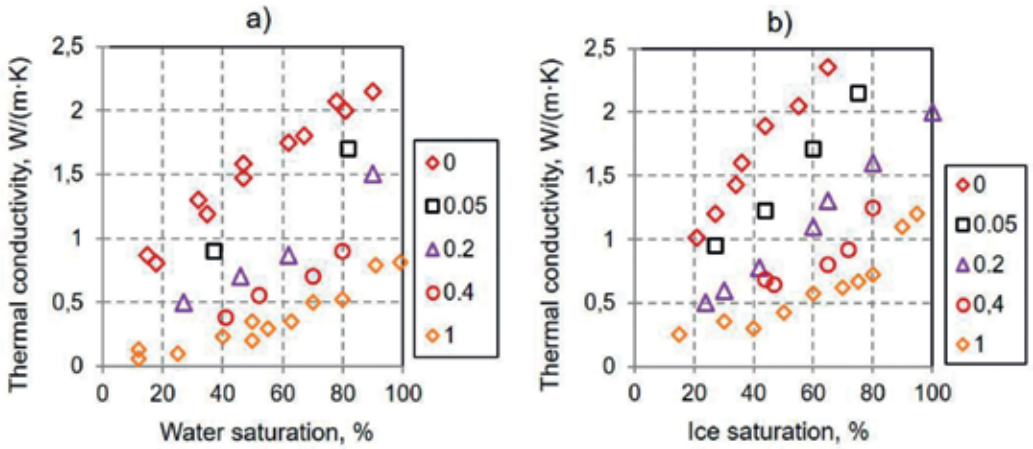

Figure 4. Water (a) and ice (b) saturation dependence of thermal conductivity in unfrozen and frozen peat-bearing sandy soils with different peat contents [36] (found as organic component to total sediment dry weight ratio).

Thermal conductivity is lower in frozen sediments containing organic matter (especially, peat) (**Figure 4**). This is because the presence of peat increases specific surface activity and the contents of unfrozen pore water, and the organic component itself (peat, oil, etc.) most often has lower thermal conductivity than mineral particles and ice. Therefore, unfrozen water-saturated soils with organic-filled porosity likewise have low thermal conductivity.

Unlike heat capacity, thermal conductivity is not an additive value but depends on sediment structure and texture. As shown by experiments, massive frozen clay is more conductive than that with ice lenses at similar water contents and density. Note that thermal conductivity of sediments with lenticular cryostructure is anisotropic: it is 20–30% higher at heat flux along than across ice lenses. The reason is in higher thermal conductivity of ice and lower thermal resistance at contacts between mineral layers and ice lenses.

3. Thermal conductivity of gas hydrate-bearing sediments and hydrate-accumulation effect

Thermal conductivity has been worse studied in hydrate-bearing sediments than in frozen (ice-bearing) sediments: the available data are limited to sporadic estimates for manmade hydrate-bearing materials [37–41]. The first experimental evidence on thermal conductivity of sediments containing natural gas hydrates was obtained from well Malik 5L-38 (Mackenzie Delta, Canada). Ice-bearing soils were found to have thermal conductivity generally higher than their hydrate-bearing counterparts [42]. On the other hand, frozen hydrate-saturated sediments are often more thermally conductive than those in the unfrozen state. New experimental data on thermal conductivity of natural gas hydrate-bearing sediments from the Nankai Trough published a few years ago were used to predict thermal conductivity from the known particle size distribution, porosity, and hydrate saturation [43]. The most successful prediction for natural sediments with hydrate saturation within 14% was achieved with a model of

complex distribution (geometric mean), but the proposed equations were poorly applicable to sediment samples containing greater percentages of hydrates (up to 30%) [44]. This is because hydrate-bearing sediments are actually complex systems and their thermal conductivity is not a sum of values for the system constituents but rather depends on the pore space structure.

According to experimental evidence, hydrate formation conditions influence largely the thermal conductivity of hydrate-bearing sediments [45]. Its variations were studied at different conditions of hydrate formation: (1) low positive temperatures (t ≈ +2 ± 1°C), (2) negative temperatures (t ≈−5 ± 1°C), (3) cooling from +2 ± 1 to −5 and −8°C, where residual pore water (not converted to hydrate at positive temperatures) froze and induced additional hydrate formation, and (4) warming from −5 ± 1 to +2 ± 1°C, where residual pore ice (not converted to hydrate at negative temperatures) thawed and induced additional hydrate formation.

3.1. Hydrate formation at t > 0°C

First, the effect of gas hydrate formation at t > 0°C on thermal conductivity of hydrate-bearing sediments was studied at low positive temperatures (t = +2 ± 1°C). The typical pattern of pore hydrate formation, under favorable conditions, is evident in time-dependent variations in the fraction of pore space occupied by hydrates or hydrate saturation (S_h, %) (**Figure 5**). This fraction decreases with time as a result of changes in the hydrate formation mechanism. Hydrate formation is rapid early during the process, and most of hydrate forms within the first 45–50 h, while S_h (**Figure 5**) reaches 67%. Then hydrate formation decelerates, while S_h remains almost invariable (about 67%). The observed kinetics of hydrate formation at low positive temperatures can be explained as follows. Rapid formation of hydrates in the beginning is due to direct gas-water contacts. Later, a gas hydrate film forms at the pore water-gas interface and impedes gas access to pore water, whereby the hydrate formation rate slows down, being limited by the permeability of the gas hydrate film. The thickening of the hydrate film makes it much less permeable, and hydrate formation almost stops at a certain film thickness, despite the fact that the residual pore water content exceeds its equilibrium content at the given temperatures and pressures.

The time-dependent behavior of thermal conductivity during hydrate accumulation in gas-saturated silty sand (W = 18%) at positive temperatures is irregular (**Figure 6**). The curve

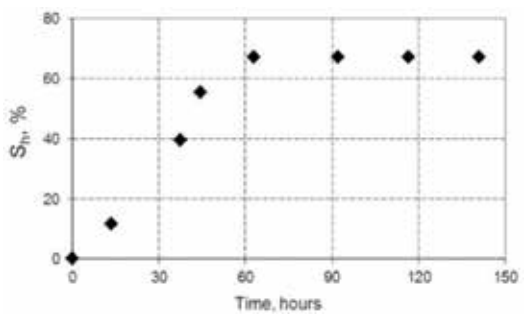

Figure 5. Pore hydrate formation in gas-saturated silty sand (W = 18%; n = 0.40), at t = +2 ± 1°C: time-dependent hydrate saturation (S_h, %) [45].

comprises three characteristic segments: (1) thermal conductivity (λ) changes little (1.77–1.78 W/(m·K) or within a measurement accuracy of 3%) for the first 40 h, but (2) becomes 13% higher (1.78–2.01 W/(m·K)) for the following 20 h, and (3) remains almost invariable about 2.01 W/(m·K), with 3–4% variations (within a measurement accuracy) till 60 h after the run start. While thermal conductivity almost does not change for the first 40 h, saturation (S_h) becomes 40% higher than at the run onset; then both parameters increase for the following 20 h, peak concurrently, and remain invariable within 100 h afterward.

At gas saturation S_h within 45%, thermal conductivity does not change (**Figure 7**), as reported previously [42–44]. The variations become notable when hydrates occupy more than 45% of the pore space. For instance, thermal conductivity became 14% higher, while Sh reached 61% in silty sand (W = 18%) and 9% higher as S_h increased to 57% in fine sand.

3.2. Hydrate formation at t < 0°C

Hydrate formation at t < 0°C was studied in frozen methane-bearing samples in a pressure cell, at temperatures of −5 ± 1°C (**Figure 8**). Unlike the tests at low positive temperatures, methane hydrates form more slowly at negative temperatures. As a result, the rate of hydrate formation in frozen samples is commensurate with that at positive temperatures for quite a long time. The reason is that, at negative temperatures, gas hydrates form directly on the surface of ice particles, as demonstrated by special studies of interaction between ice particles and CO_2 and CH_4 gases [46, 47]. Hydrate that forms during this interaction has a low density, and, hence, a high permeability and does not impede much the conversion of ice particles to hydrate. The same mechanism apparently works during transition of pore ice into hydrate, judging by the dynamics of gas hydrate formation in frozen sediments. Unlike the case of t > 0°C, the thermal conductivity of frozen samples decreases nonuniformly with time during hydrate formation (**Figure 9**). The decrease is to 1.81 W/(m·K) (8%) for the first 50 h of hydrate growth and then as small as 3% for the subsequent 125 h. In general, this decrease is observed in the S_h range from 0 to 50–60% (**Figure 10**). The thermal conductivity decrease most likely results from reduction in the amount of ice, with its thermal conductivity as high as 2.23 W/(m·K), and the related growth in the share of the less conductive hydrate (0.6 W/(m·K)).

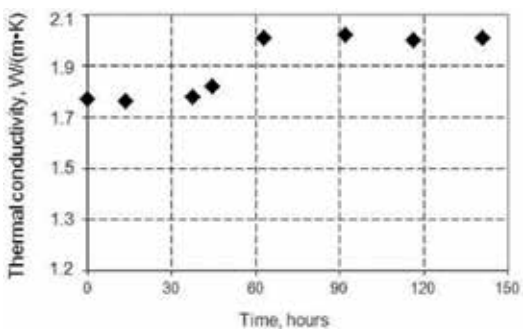

Figure 6. Time-dependent thermal conductivity of gas-saturated silty sand (W = 18%; n = 0.40) during hydrate formation at t = +2 ± 1°C [45].

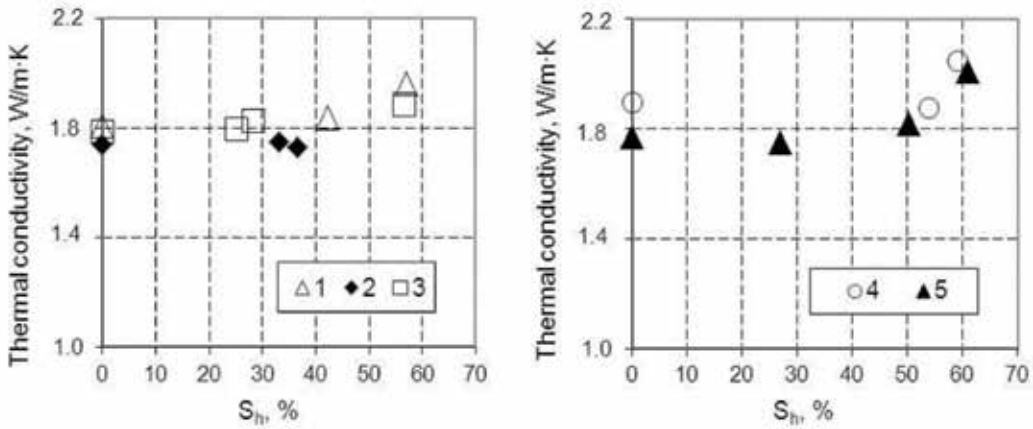

Figure 7. Thermal conductivity of sediments as a function of hydrate saturation (S_h, %) at t = +2 ± 1°C: (1) fine sand, W = 16%; (2) fine sand, W = 10%; (3) fine sand, W = 15%; (4) fine sand +14% kaolin clay, W = 15%; and (5) silty sand, W = 18% [45].

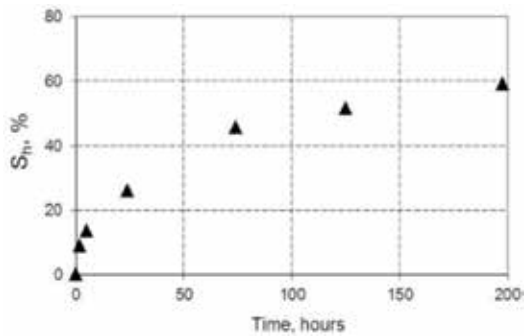

Figure 8. Pore methane hydrate formation in frozen fine sand (W = 22%; n = 0.60) at t = −5 ± 1°C: time-dependent hydrate saturation (S_h, %) [45].

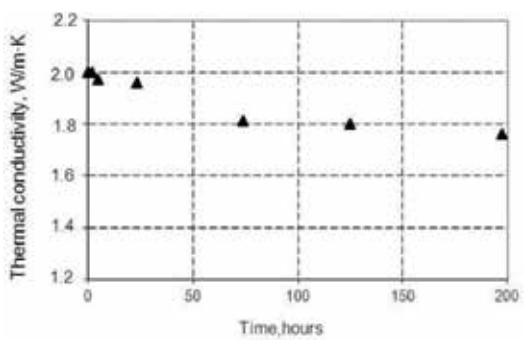

Figure 9. Time-dependent thermal conductivity of gas-saturated fine sand (W = 22%; n = 0.60) during hydrate formation at t = −5 ± 1°C [45].

http://dx.doi.org/10.5772/intechopen.75383

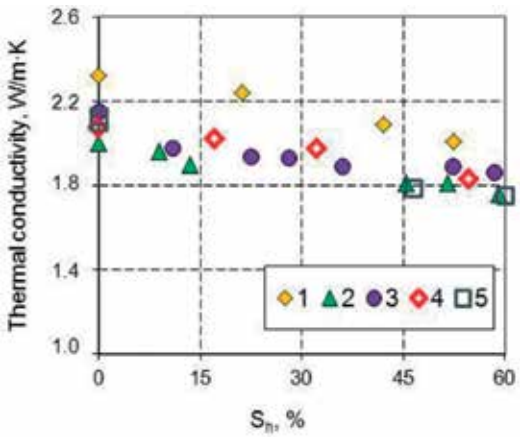

Figure 10. Thermal conductivity of sediments as a function of hydrate saturation (S_h, %), at t = −5 ± 1°C: (1) fine sand, W = 19% and n = 0.40; (2) fine sand, W = 22% and n = 0.60; (3) fine sand, W = 15% and n = 0.38; (4) silty sand, W = 24% and n = 0.60; and (5) silty sand, W = 16% and n = 0.38 [45].

3.3. Effect of freezing

To study the effects of freezing on thermal conductivity, the samples saturated with hydrate at t > 0°C were cooled from −5 to −8°C. Although hydrate had already saturated 50–60% of the pore space before freezing and the hydrate formation almost ceased, the samples produced additional pore hydrate upon further cooling, in all runs (**Table 2**), more in silty sand than in fine sand. Thus, a large portion of residual water that survived conversion to hydrate at positive temperatures became consumed during cooling and freezing. Hydrate formation became more active as the survived pore water froze up because cryogenic deformation of the soil skeleton and release of dissolved gas produced new water-gas interfaces. The amount of hydrate additionally formed as a result of freezing mainly depends upon soil mineralogy, clay content, and water saturation.

Thermal conductivity decreased dramatically in freezing hydrate-saturated sediments (**Figure 11** A) but became 15–20% higher in hydrate-barren samples (**Figure 11** B). The freezing-induced thermal conductivity reduction was 10% in fine sand (from 1.96 to 1.77 W/(m·K)) but reached 50% in silty sand with W = 16% (2.01–0.96 W/(m·K)) [45].

Type of soil	W (%)	S_h (%)	
		Before freezing	After freezing
Fine sand	16	58	71
Fine sand +14% kaolin	15	62	79
Silty sand	18	61	85
Silty sand	16	52	79

Table 2. Methane hydrate formation upon freezing of residual pore water [45].

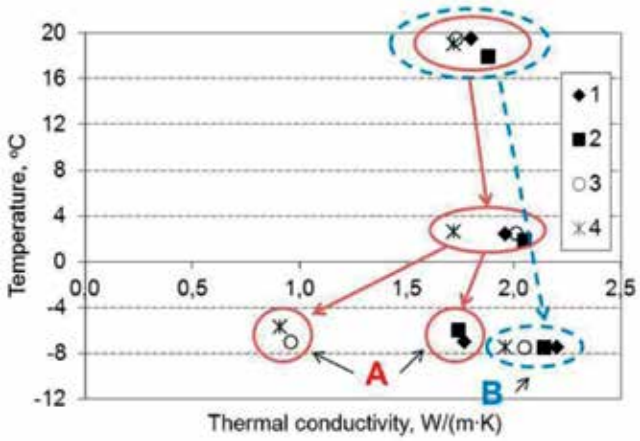

Figure 11. Variations in thermal conductivity of gas-saturated sediments upon cooling (to +2°C) and freezing: (A) hydrate-bearing samples after freezing and (B) frozen hydrate-barren samples. Solid (red) and dash (blue) lines correspond to samples saturated with gases that can and cannot form hydrates (methane and nitrogen, respectively): (1) fine sand, W = 16%; (2) fine sand +14% kaolin, W = 15%; (3) silty sand, W = 18%; and (4) silty sand, W = 16%.

Thus, thermal conductivity may decrease dramatically in hydrate-saturated sediments exposed to further freezing, whereby the survived pore water freezes up, as a result of additional hydrate formation. This behavior may be due to structure and texture changes in freezing gas- and hydrate-bearing sediments. These are especially the effects of heaving or cracking of hydrate-saturated soil or the formation of highly porous hydrate at grain boundaries, with thermal conductivity as low as ~0.35 W/(m·K).

3.4. Effect of thawing

To study the effect of thawing on the behavior of thermal conductivity, the frozen sand samples that were saturated with hydrate at t < 0°C were heated to +2 ± 1°C. The tests showed additional hydrate formation in fine sand (**Table 3**), as in the case of freezing, but unlike the latter case, it did not exceed 10% [45]. Faster hydrate generation upon thawing was attributed to deformation of soil skeleton and formation of new water-gas interfaces. Additional hydrate formation upon thawing of hydrate-saturated sand was more intense in the initially water-saturated samples: 10 and 7% of additional hydrate formed in sandy samples with W = 19 and 15%, respectively. As the frozen hydrate-bearing samples thawed, their thermal conductivity

Type of sediment	W (%)	S_h (%)		Thermal conductivity (W/(m·K))	
		Before thawing	After thawing	Before thawing	After thawing
Fine sand	19	0.64	0.71	1.80	1.70
Fine sand	15	0.57	0.61	1.86	1.76

Table 3. Thermal conductivity and hydrate saturation of frozen hydrate-bearing sand upon thawing (to +2 ± 1°C) at above-equilibrium methane pressure [45].

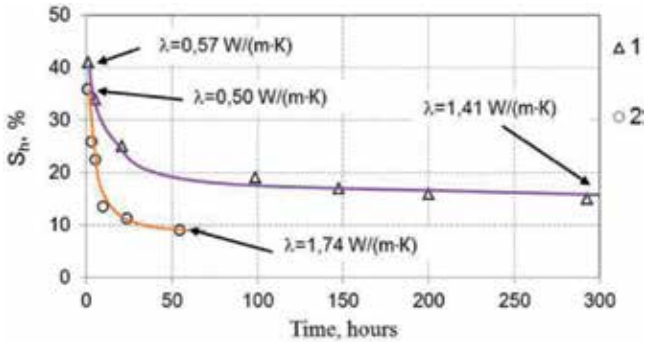

Figure 12. Thermal conductivity variations of frozen hydrate-contain sands during methane hydrate dissociations at t = −5 to −6°C and pressure 0.1 MPa: Data points (triangles and circles) are experimental measurements; lines are approximation trends: (1) fine sand, W = 17% and n = 0.40; (2) silty sand, W = 17% and n = 0.40.

decreased (from 1.86 to 1.72 W/(m·K) or for 8%). Two main reasons of such reduction are (1) thermal conductivity difference between pore ice and water and (2) hydrate saturation increase.

Thus, both freezing and thawing cause thermal conductivity reduction in frozen soils saturated with methane hydrate at above-equilibrium pressures.

The observed thermal conductivity variations associated with hydrate formation at different conditions (low positive and negative temperatures, freezing and thawing) indicate that this behavior is mostly controlled by phase transitions in pore fluids and by structure and texture changes in main sample constituents, which were explained by Chuvilin and Bukhanov [45] in two models of structure and texture changes in gas-saturated sediment during hydrate formation. These models can be used for reference in geomechanical and thermal simulations of gas hydrate reservoirs, taking into account the conditions of pore hydrate formation, with implications for methane recovery.

3.5. Effect of hydrate dissociation

The effect of hydrate dissociation on thermal conductivity of frozen hydrate-bearing soils at below-equilibrium pressure was investigated in manmade sand samples at temperatures about −5 to −6°C and atmospheric pressure [48]. Pore hydrates in the frozen sand samples failed to reach complete decomposition in the experiments due to their self-preservation [49–52], with residual hydrate saturation (S_h, %) up to 10% or more (**Figure 12**). The hydrate dissociation was attendant with notable increase in thermal conductivity; it became 2.5 times higher (from 0.57 W/(m·K) to 1.41 W/(m·K) as S_h reduced from 40 to 15%) in fine sand and more than three times higher as S_h became 10% in silty sand. Thermal conductivity increase in the end of the experiment was due to decrease in the amount of pore hydrate and increase in pore ice, with residual hydrate saturation (Sh, %) of 10% (**Figure 11**). Low thermal conductivity of frozen hydrate-bearing samples (0.5–0.6 W/(m·K)) for first few minutes after the equilibrium pressure drop to the atmospheric value (0.1 MPa) may result from both high contents of pore hydrate and formation of microcracks in this hydrate which heal up afterward during its dissociation [53].

4. Conclusions

Thermal conductivity of wet porous fine-grained soils depends on particle size, mineralogy, pore space structure, and moisture contents, as well as on the phase state and phase change of pore fluids. The effects of water→ice, water→gas hydrate, and ice→gas hydrate transitions were studied in experiments, which show the phase change direction and relative contents of water phases in the pore space to be principal controls of thermal conductivity. It increases in wet porous sediments subject to freezing and subsequent cooling, primarily, due to pore water-to-ice conversion at a wide range of negative temperatures. However, the process may induce microcracking, which may reduce thermal conductivity.

Thermal conductivity of frozen sediments mainly depends on lithology, salinity, organic matter content, and absolute negative temperature, which affect the amount of residual liquid phase (unfrozen water) in frozen soils. Namely, thermal conductivity commonly decreases as soil contains more unfrozen water, in the series 'fine sand – silty sand – sandy clay – clay', as well as at increasing salinity or organic (e.g., peat) contents.

As demonstrated by our experiments, thermal conductivity can either increase or decrease depending on hydrate formation conditions. Namely, it increases if gas hydrates form at positive temperatures ($t > 0^{o}C$) but decreases during hydrate formation in frozen samples. Freezing and thawing of hydrate-bearing sediments above the equilibrium pressure reduces their thermal conductivity due to additional hydrate formation. On the other hand, thermal conductivity of hydrate-bearing frozen sediments may increase during dissociation of pore hydrates due to their self-preservation. It increases as the pore space contains smaller amounts of hydrates but more ice which is four times more thermally conductive.

Acknowledgements

This research is supported by the Russian Science Foundation (grant no. 16-17-00051).

Author details

Evgeny Chuvilin[1,2]*, Boris Bukhanov[1], Viktor Cheverev[2], Rimma Motenko[2] and Erika Grechishcheva[3]

*Address all correspondence to: chuviline@msn.com

1 Skolkovo Institute of Science and Technology (Skoltech), Skolkovo Innovation Center, Moscow, Russia

2 Geology Faculty, Moscow State University (MSU), Moscow, Russia

3 OJSC Fundamentproekt, Moscow, Russia

References

[1] Von-Herzen RP, Maxwell AE. The measurement of thermal conductivity of deep-sea sediments by a needle probe method. Journal of Geophysical Research. 1959;**84**:1629-1634

[2] Ivanov NS, Gavriliev RI. Thermal Properties of Frozen Rocks. Nauka: Moscow; 1965. 74 pp. (in Russian)

[3] Ivanov NS. Heat and Mass Transfers in Frozen Rocks. Novosibirsk: Nauka; 1969. 240 p. (in Russian)

[4] Sass JH, Lachenbruch AH, Munroe RJ. Thermal conductivity of rocks from measurements on fragments and its application to heat-flow determinations. Journal of Geophysical Research. 1971;**76**(14):3391-3401

[5] Farouki OT. Thermal Properties of Soils. CRREL: Hanover; 1981. 151 p

[6] Balobaev VT, Pavlov AV, Perl'shtein GZ. Thermal Study of Permafrost in Siberia. Novosibirsk: Nauka; 1983. 214 p. (in Russian)

[7] Blackwell DD, Steele JL. Thermal conductivity of sedimentary rocks: Measurement and significance. In: Naeser ND, McCulloch TH, editors. Thermal History of Sedimentary Basins. New York: Springer-Verlag; 1989. pp. 45-96

[8] Clauser C, Huenges E. Thermal conductivity of rocks and minerals. In: Ahrens TJ, editor. Rock Physics and Phase Relations: A handbook of physical constants. Washington: American Geophysical Union; 1995. pp. 105-126

[9] Beck AE. Methods for determining thermal conductivity and thermal diffusivity. In: Haenel R, Rybach L, Stegena L, editors. Handbook of Terrestrial Heat-Flow Density Determination. Dordrecht: Kluwer Academic Publisher; 1998. pp. 87-124

[10] Gavriliev RI. Thermal Properties of Rocks and Soils in Permafrost Regions. Novosibirsk: SO RAN; 1998. 208 p. (in Russian)

[11] Côté J, Konrad J-M. Thermal conductivity of base-course materials. Canadian Geotechnical Journal. 2005;**42**:61-78. DOI: 10.1139/T04-081

[12] Côté J, Konrad J-M. A generalized thermal conductivity model for soils and construction materials. Canadian Geotechnical Journal. 2005;**42**:443-458. DOI: 10.1139/T04-106

[13] Côté J, Grosjean V, Konrad J-M. Thermal conductivity of bitumen concrete. Canadian Journal of Civil Engineering. 2013;**40**:172-180. DOI: 10.1139/cjce-2012-0159

[14] Penner E. Thermal conductivity of frozen soils. Canadian Journal of Earth Sciences. 1970;**7**:982-987

[15] Ershov ED, Danilov ID, Cheverev VG. Petrography of Frozen Soils. Moscow: MSU; 1987. 311 p. (in Russian)

[16] Williams PJ, Smith MW. The Frozen Earth: Fundamentals of Geocryology. Cambridge: Cambridge University Press; 1989. 306 p

[17] Ershov ED, Komarov IA, Cheverev VG, Barkovskaya EN, Shesternev DM. Heat and mass transfer properties. In: Ershov ED, editor. Fundamentals of Geocryology. Part 2. Lithogenetic Geocryology. Moscow: MSU; 1996. pp. 118-133. (in Russian)

[18] Motenko RG. Thermal properties and phase composition of frozen saline soils [PhD thesis] Moscow: MSU; 1997. 195 p. (in Russian)

[19] Yershov ED. General Geocryology. Cambridge: Cambridge University Press; 1998. 580 p

[20] Komarov IA. Thermodynamics and Mass Transfer in Frozen Sediments. Moscow: Nauchniy Mir; 2003. 608 p. (in Russian)

[21] Cheverev VG. The Nature of Cryogenic Properties of Soils. Moscow: Nauchniy Mir; 2004. 234 p. (in Russian)

[22] Sloan ED. Clathrate Hydrates of Natural Gases. 2nd ed. New York: Marcel Dekker; 1998. 757 p

[23] Max MD, editor. Natural Gas Hydrate in Oceanic and Permafrost Environments. Boston: Kluwer Academic Publishers; 2000. 414 p

[24] Cherskiy NV, Tsarev VP, Nikitin SP. Investigation and prediction of conditions of accumulation of gas resources in gas-hydrate pools. Petroleum Geology. 1985;**21**:65-89

[25] Stoll RD, Bryan GM. Physical properties of sediments containing gas hydrates. Journal of Geophysical Research. 1979;**84**:1629-1634

[26] Rosenbaum EJ, English NJ, Johnson JK, Shaw DW, Warzinski RP. Thermal conductivity of methane hydrate from experiment and molecular simulation. The Journal of Physical Chemistry. B. 2007;**111**:13193-13205

[27] Waite WF, Stern LA, Kirby SH, Winters WJ, Mason DH. Simultaneous determination of thermal conductivity, thermal diffusivity and specific heat in sI methane hydrate. Geophysical Journal International. 2007;**169**:767-774

[28] Andersland OB, Ladanyi B. An Introduction to Frozen Ground Engineering. Dordrecht: Springer-Science + Business Media; 1994. DOI: 10.1007/978-1-4757-2290-1

[29] Muller SW. Frozen in Time: Permafrost and Engineering Problems. Virginia: ASCE; 2008. 280 p

[30] Ye Y, Liu C. Natural Gas Hydrates. Experimental Techniques and their Applications. New York: Springer; 2013. 402 p

[31] Warzinski RP, Gamwo IK, Rosenbaum EJ, Myshakin EM, Jiang H, Jordan KD, English NJ, Shaw DW. Thermal properties of methane hydrate by experiment and modeling and impacts upon technology. In: Proceeding of the 6th International Conference on Gas Hydrates; 6-10 July 2008; Vancouver; 2008

[32] Popov Y, Beardsmore G, Clauser C, Roy S. ISRM suggested methods for determining thermal properties of rocks from laboratory tests at atmospheric pressure. Rock Mechanics and Rock Engineering. 2016;**49**:4179-4207. DOI: 10.1007/s00603-016-1070-5

[33] Das BM. Advanced Soil Mechanics. 3rd ed. New York: Taylor & Francis; 2008. 567 p

[34] Istomin V, Chuvilin E, Bukhanov B, Uchida T. Pore water content in equilibrium with ice or gas hydrate in sediments. Cold Regions Science and Technology. 2017;**137**:60-67. DOI: 10.1016/j.coldregions.2017.02.005

[35] Grechishcheva E, Motenko R. Experimental study of freezing point and water phase composition of saline soils contaminated with hydrocarbons. In: Proceedings of the 7th Canadian Permafrost Conference; 21-23 September 2015; Quebec City; 2015: ABS_ 316

[36] Roman LT. Frozen Peat Soils as Foundations of Constructions. Novosibirsk: Nauka; 1987. 222 p. (in Russian)

[37] Groysman AG. Thermal Properties of Gas Hydrates. Novosibirsk: Nauka; 1985. 94 p. (in Russian)

[38] Asher GB. Development of computerized thermal conductivity measurement system utilizing the transient needle probe technique: An application to hydrates in porous media [PhD thesis]. Colorado: Colorado School of Mines, Golden; 1987. 179 p

[39] Huang D, Fan S. Measuring and modeling thermal conductivity of gas hydrate-bearing sand. Journal of Geophysical Research. 2005;**110**:B01311. DOI: 10.1029/2004JB003314

[40] Duchkov AD, Manakov AY, Kazantsev SA, Permyakov ME, Ogienko AG. Thermal conductivity measurement of the synthetic samples of bottom sediments containing methane hydrates. Izvestiya, Physics of the Solid Earth. 2009;**45**:661-669. DOI: 10.1134/S1069351309080060

[41] Yang L, Zhao J, Wang B, Liu W, Yang M, Song Y. Effective thermal conductivity of methane hydrate-bearing sediments: Experiments and correlations. Fuel. 2016;**179**:87-96. DOI: 10.1016/j.fuel.2016.03.075

[42] Wright JF, Nixon FM, Dallimore SR, Henninges J, Cote MM. Thermal conductivity of sediments within the gas-hydrate-bearing interval at the JAPEX/JNOC/GSC et al. In: Dallimore SR, Collett TS, editors. Mallik 5L-38 Gas Hydrate Production Research Well. Bulletin 585. Ottawa: Geological Survey of Canada; 2005. pp. 1-5

[43] Muraoka M, Ohtake M, Susuki N, Yamamoto Y, Suzuki K, Tsuji T. Thermal properties of methane hydrate-bearing sediments and surrounding mud recovered from Nankai trough wells. Journal of Geophysical Research - Solid Earth. 2014;**119**:8021-8033. DOI: 10.1002/2014JB011324

[44] Muraoka M, Susuki N, Yamaguchi H, Tsuji T, Yamamoto Y. Thermal properties of a supercooled synthetic sand−water−gas−methane hydrate sample. Energy & Fuels. 2015; **29**(3):1345-1351. DOI: 10.1021/ef502350n

[45] Chuvilin E, Bukhanov B. Effect of hydrate formation conditions on thermal conductivity of gas-saturated sediments. Energy & Fuels. 2017;**31**(5):5246-5254. DOI: 10.1021/acs.energyfuels.6b02726

[46] Kuhs WF, Klapproth A, Gotthardt F, Techmer K, Heinrichs T. The formation of meso- and macroporous gas hydrates. Geophysical Research Letters. 2000;**27**(18):2929-2932

[47] Staykova DK, Kuhs WF, Salamatin A, Hansen T. Formation of porous gas hydrates from ice powder: Diffraction experiments and multi-stage model. Journal of Physical Chemistry B. 2003;**107**:10299-10311

[48] Bukhanov BA, Chuvilin EM, Guryeva OM, Kotov PI. Experimental study of the thermal conductivity of the frozen sediments containing gas hydrate. In: Proceedings of the 9th International Conference on Permafrost (9-ICOP); 23 June-03 July 2008; Fairbanks; 2008. pp. 205-209

[49] Chuvilin EM, Kozlova EV. Experimental estimation of hydrate-containing sediments stability. In: Proceedings of the 5th International Conference on Gas Hydrate (ICGH-5); 12-16 June 2005; Trondheim; 2005. pp. 1540-1547

[50] Chuvilin EM, Guryggeva OM. Experimental study of self-preservation effect of gas hydrates in frozen sediments. In: Proceedings of the 9th International Conference on Permafrost (9-ICOP); 23 June-03 July 2008; Fairbanks; 2008. pp. 263-267

[51] Hachikubo A, Takeya S, Chuvilin E, Istomin V. Preservation phenomena of methane hydrate in pore spaces. Physical Chemistry Chemical Physics. 2011;**13**:17449-17452. DOI: 10.1039/c1cp22353d

[52] Takeya S, Fujihisa H, Gotoh Y, Istomin V, Chuvilin E, Sakagami H, Hachikubo A. Methane clathrate hydrates formed within hydrophilic and hydrophobic porous media: Kinetics of dissociation and distortion of host structure. Journal of Physical Chemistry C. 2013;**117**:7081-7085. DOI: 10.1021/jp312297h

[53] Ershov ED, Lebedenko YP, Chuvilin EM, Yakushev VS. Experimental investigations of microstructure of ice—Methane hydrate agglomerate. Engineering Geology. 1990;**3**: 38-44 (in Russian)

Chapter 8

Thermal Conductivity Measurement of Vacuum Tight Dual-Edge Seal for the Thermal Performance Analysis of Triple Vacuum Glazing

Saim Memon

Additional information is available at the end of the chapter

http://dx.doi.org/10.5772/intechopen.74255

Abstract

A vacuum tight glass edge seal's thermal conductivity is one of the principal factor in determining the heat distribution towards the centre of pane, ultimately influences the thermal transmittance (U-value) of a triple vacuum glazing. So far indium and solder glass have proven to be vacuum tight edge sealing materials but both have certain limitations. In this chapter, a new low-temperature vacuum tight glass edge seal composite's thermal conductivity, Cerasolzer CS186 alloy and J-B Weld epoxy-steel resin, were measured and validated with the mild-steel and indium using transient plane source method with a sensor element of double spiral and resistance thermometer in a hot disk thermal constants analyser TPS2500s are reported. The thermal conductivity data of Cerasolzer CS186 alloy and J-B Weld epoxy steel resin were measured to be 46.49 and 7.47 Wm^{-1} K^{-1}, with the deviations (using analytical method) of ±4 and ±7% respectively. These values were utilised to predict the thermal transmittance value of triple vacuum glazing using 3D finite element model. The simulated results show the centre-of-glass and total U-value of 300 × 300 mm triple vacuum glazing to be 0.33 and 1.05 Wm^{-2} K^{-1}, respectively. The influence of such a wide edge seal on the temperature loss spreading from the edge to the central glazing area is analysed, in which the predictions show wider edge seal has affected the centre-of-glass U-value to 0.043 Wm^{-2} K^{-1} due to the temperature gradient loss spread to 54 and 84 mm on the cold and warm side respectively.

Keywords: thermal conductivity, transient plane source, triple vacuum glazing, thermal performance, vacuum seal

1. Introduction

Carbon reduction and energy efficiency of domestic buildings have been one of the major global concerns due to limits with climate change [1]. Energy efficiency can be improved by high performance smart windows, high levels of wall insulation, efficient appliances and effectiveness of renewable energy results in saving financial cost to consumers and carbon dioxide emissions [2, 3]. One of the main functions of a smart triple vacuum glazed windows is to reduce heat flow between indoors and outdoors, i.e. to provide preeminent thermal insulation so called thermal transmittance (U-value) [4]. It depends on the number of glass panes, the space between glass panes, emissivity of the coatings on glass pane, frame in which the glass is installed, the type of spacers that separate the panes of glass and the type of window frame. The total U-value includes the effect of the frame and the glazing edge area. An influence of the glazing edge area is dependent on the width and the type of edge sealing material.

The hermetic edge seal of a triple vacuum glazing must be capable of maintaining vacuum pressure of less than 0.1 Pa in order to suppress gaseous conduction for long term duration [5]. Sealing of two glass panes edges using high power laser through quartz window in vacuum chamber was developed by Benson et al. [6]. This achieves hermetic seal but the level of vacuum was not less than 0.1 Pa, due to gases and vapour particles caused by lasering remain in the cavity [7]. High temperature edge sealing technique developed by the Collins group at the University of Sydney is based on material solder glass sealed at high temperature around 450°C [8–10]. This technique achieved significant centre of pane U value of 0.8 $Wm^{-2}\,K^{-1}$ and considered at commercial level. The problems with high temperature method of sealing is degradation of low emittance coatings only hard coatings can be used, if using toughened glass then loss of toughness, and require more amount of heat energy for fabrication due to heat require for several hours. Low temperature solder glass material was investigated to form a hermetic edge seal, but durability was a problem due to the absorption of moisture. Polymers have problems of gas permeability and out gassing [7]. Low temperature edge sealing technique developed at the University of Ulster is based on Indium alloy sealed at low temperature process about 160°C. It requires secondary adhesive seal to prevent access from moisture [11, 12]. A low temperature sealing process allows the use of low emittance soft coatings reduces radiative heat transfer between glass panes and toughened glass allows to increase support pillar spacing reduces conductive heat transfer. The problem with low temperature edge sealing material is indium alloy is high-priced and for long term cost effective vacuum glazing, this method is not encouraged at commercial level [13, 14].

A new low-temperature composite materials and methods of fabrication was reported in Memon et al. [15]. In which CS-186 type of Cerasolzer and steel reinforced epoxy by J-B resin were used for the development of triple vacuum glazing as shown in **Figure 1**. In this chapter, the experimental measurements of thermal conductivity of this composite material are reported. The significance of this study is to analyse the influence of edge area on the thermal transmittance of the composite edge seal for the fabrication of triple vacuum glazing. This value of the thermal conductivity was then used to develop model using finite element method to predict the influence of its wider edge seal and due to its thermal conductivity on the thermal performance.

http://dx.doi.org/10.5772/intechopen.74255

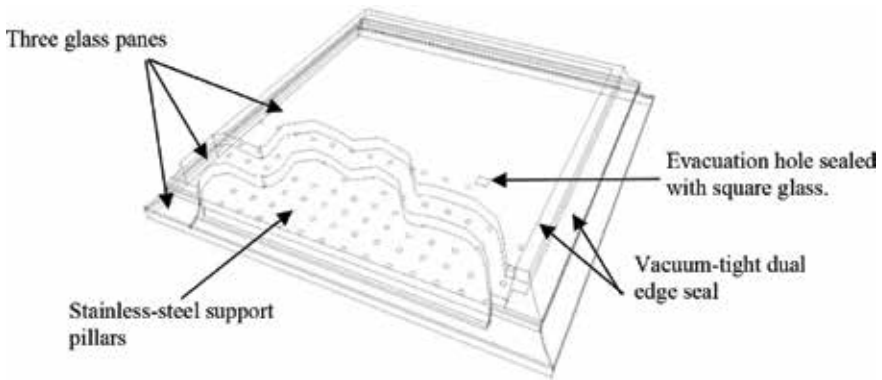

Figure 1. A schematic diagram of vacuum tight dual edge sealed triple vacuum glazing.

2. Methodology

A number of different instruments are available for the measurement of the thermal properties of materials [16]. There are two main methods, steady state method and transient. The steady state approach is further divided into one dimensional heat flow and radial heat flow techniques. One dimensional heat flow technique include the guarded hot plate method which is the ASTM standard based measurement system used for highly insulating materials. The radial heat flow technique includes cylindrical, spherical and ellipsoidal methods. There are a number of transient methods, which can be used for the measurement of thermal conductivity such as hot wire, transient hot strip and transient plane source methods. The experimental measurements of thermal conductivity performed in this study were undertaken using a Hot Disk thermal constants analyser TPS 2500 s. This system is based on the transient plane source (TPS) method. The TPS method consists of a sensor element in the shape of a double spiral which acts both as a heat source to increase the temperature of the sample and a resistance thermometer to record the time dependent temperature increase [17]. In the current experiments, a sensor of design 7577 was used which is made of a 10 μm thick Nickel-metal double spiral. The radius of the sensor was chosen to be 2.001 mm in order to reduce the size of the sample. It is advised [18] that the diameter of the sample should not be less than twice that of the sensor diameter and the thickness of the sample should not be less than the radius of the sensor. The sensor element is usually insulated with a material to provide electrical insulation. The material used is dependent on the operating temperatures. A thin polyamide (Kapton) insulating material was chosen for the sensor insulation which is suitable from cryogenic temperatures to about 500 K [19].

A sensor is placed between two flat cylindrical samples, as shown in **Figure 2**. Passage of a constant electric power through the spiral produces heat, increases the temperature and therefore the resistance of the spiral sensor as a function of time which can be expressed according to Gustavsson et al. [16] as,

$$R(t) = R_o\{1 + \varphi[\Delta T_i + \Delta T_{ave}(\tau)]\} \quad (1)$$

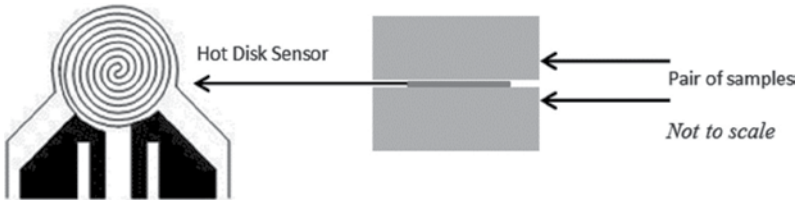

Figure 2. A schematic diagram of the pair of samples and the hot disk sensor placed in between two flat cylindrical samples.

where R_o is the resistance in ohms before the sensor is heated or at time t = 0 s, φ is the temperature coefficient of the resistivity (TCR) of the sensor 7577 i.e. 46.93×10^{-4} K^{-1}, ΔT_i is the initial temperature difference that develops momentarily over the thin insulating layers which cover the two sides of the sensor. The thermal conductivity of the sample can be expressed according to Bohac et al. [19] as,

$$k = \frac{P_o}{\pi^{\frac{3}{2}}.a.\Delta T_{ave}(\tau)}.D(\tau) \tag{2}$$

$$\tau = \sqrt{\frac{t}{t_c}} \tag{3}$$

$$t_c = \frac{a^2}{\alpha} \tag{4}$$

Where α is the thermal diffusivity of the sample in mm^2 s^{-1}. From the experimentally recorded temperature increase over $D(\tau)$ a straight line can be plotted which intercepts ΔT_i, and slope of $\frac{P_o}{\pi^{\frac{3}{2}}.a.\Delta T_{ave}(\tau)}$ which allows the thermal conductivity to be determined. The final straight line from which the thermal conductivity measured is obtained through a process of iteration [17]. During a pre-set time, 200 resistance recordings are taken and from these a relation between temperature and time is established.

3. Results and discussions

3.1. Experimental measurements of the thermal conductivity of the hermetic edge seal

In order to validate the measurements of Cerasolzer allow and J-B Weld epoxy the results were compared with several measurements of the samples of Mild Steel (MSteel) and Indium in four repetitive experiments, combined the cut faces flatten to reduce the experimental errors. The experimental data are plotted in **Figure 3**. As can be seen this work is verified by the reported data of Mild steel and Indium. An increase of temperature with respect to reporting time interval have similar deviations and the highest increase of temperature was recorded for JB-Weld which gives a good agreement with the experimental data. The average

http://dx.doi.org/10.5772/intechopen.74255

temperature increase measured by the TPS sensor type 7577 of the mild steel, indium, J-B Weld epoxy steel resin and Cerasolzer CS186 samples are shown in **Figure 4**. It can be seen that the increase in temperature in the epoxy J-B Weld is greater than the mild steel. This is due to the fact that heat flow in semi-polymeric materials is low compared to metallic materials. The temperature increase in the sample made from Cerasolzer alloy was higher than the indium sample [20, 21].

An average thermal conductivity of a mild steel type SIS2343 sample was measured to be 13.76 Wm^{-1} K^{-1}. The reliability of the measured thermal conductivity is compared with the standard measurement value given in the standard data sheet i.e.13.62 Wm^{-1} K^{-1}. An average thermal conductivity of the indium sample was measured to be 77.84 Wm^{-1} K^{-1} with a repeatability of four times. The thermal conductivity measurement for Cerasolzer alloy and J-B Weld epoxy steel resin, as detailed in **Table 1**, with the deviations were calculated to be ±4 and ±7% in the experimental measurements as compared with the analytical methods as detailed in the Section 2.

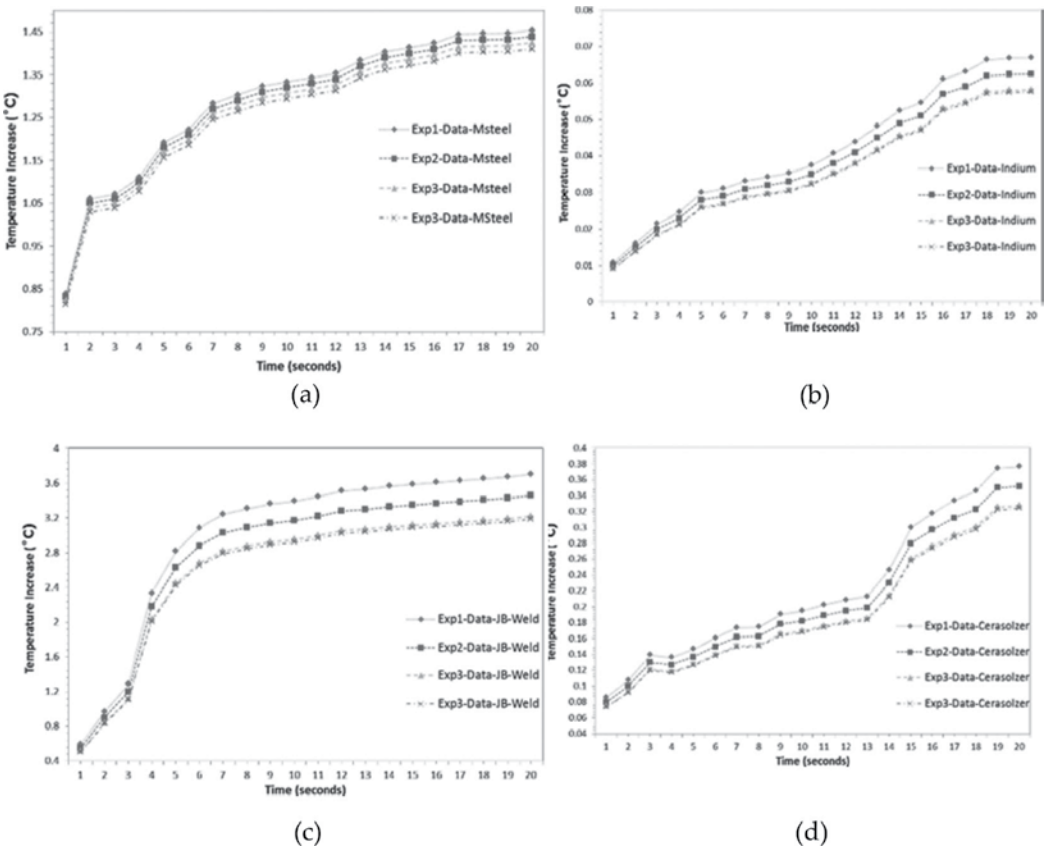

Figure 3. Experimental results as function of temperature increase for JB-weld and Cerasolzer in comparison to the verified mild steel and indium.

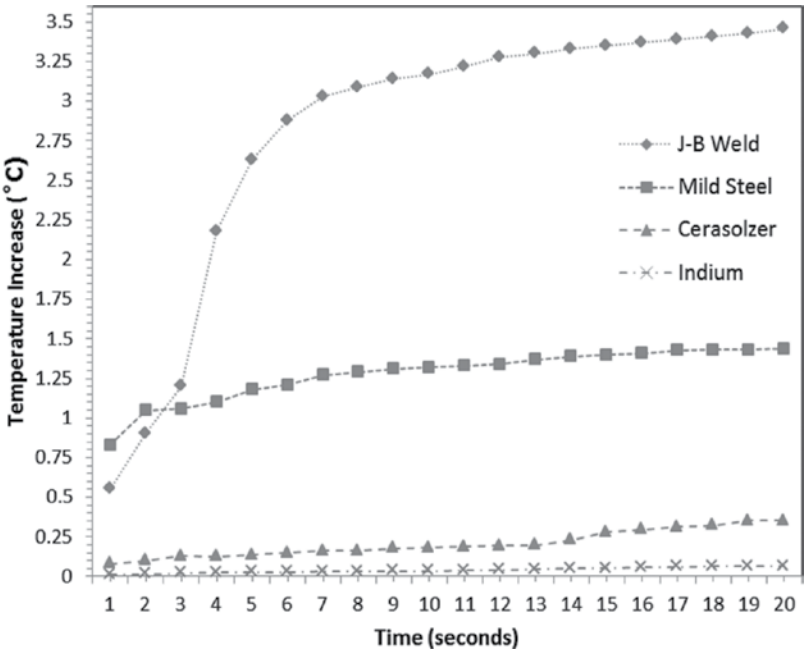

Figure 4. The average recorded temperature increase using the TPS sensor type 7577 for the samples made from mild steel, indium, J-B weld epoxy steel resin and Cerasolzer CS186.

Sample	Thermal conductivity at 21°C (Wm^{-1} K^{-1}) (Deviation)	Measuring time (second)	Power output from sensor (watts)
Mild Steel	13.76 (1%)	20	1
Indium	77.84 (7%)	20	1
Cerasolzer CS186	46.49 (±4%)	20	1
J-B Weld	7.47 (±7%)	20	1

Table 1. Measured thermal conductivities of Cerasolzer alloy CS186 and J-B weld epoxy steel resin and measurements of mild steel and indium.

3.2. Thermal performance analysis of hermetic edge sealed triple vacuum glazing

By utilising the measured thermal conductivities of Cerasolzer alloy as primary seal and JB-Weld as secondary seal, as detailed in **Table 1**, a 3D FE (finite element) model based on a commercial software package MSC Marc was employed to analyse the heat transfer and predict the thermal performance of the triple vacuum glazing. The symmetry of the model was exploited to simulate the heat transfer process in computationally efficient way; only one quarter (150 × 150 mm) of the triple vacuum glazing of dimensions 300 × 300 mm was modelled and simulated using ASTM boundary conditions [22]. Three k glass sheets having thermal conductivity of 1 Wm^{-1} K^{-1} with SnO_2 coatings on inner surfaces with the emissivity

http://dx.doi.org/10.5772/intechopen.74255

of 0.15 were used. The support pillars were incorporated into the model explicitly [23]. This is based on the actual stainless steel pillar array having 16.2 Wm^{-1} K^{-1} of thermal conductivity. The number of support pillars was employed in the triple vacuum glazing that represented by the same number of pillars in the developed finite-element model. Since modelling the pillars with circular cross-section would lead to non-uniform mesh with distorted elements around the pillar, they were modelled using square cross-section (considered the diameter of 0.3 mm, height of 0.15 mm and pillar separation of 24 mm). Additionally, it is already established in the literature that the heat transfer through the pillar does not depend upon its shape but its cross-sectional area under certain boundary conditions [24, 25]. In order to keep the cross-sectional area similar to circular pillar with radius *r,* the side length of each square used is 1.78 *r*. The FE model implemented eight-node iso-parametric elements, with a total of 170,455 elements and 201,660 nodes to represent a quarter of the fabricated triple vacuum glazing. In FE model, the evacuated gap between glasses was represented with as a material with almost zero thermal conductivity to represent triple vacuum glazing. For sake of simplicity, the influence of residual gas among glasses was neglected in the model. In order to achieve realistic results from the simulation, a graded mesh with large number of elements was employed in the pillar. In addition to this, a convergence study was performed on the pillar to ensure the accuracy of the thermal performance predicted using the model. The material properties of the glass sheets applied to the models are those found in [22] and summarised in **Table 2**. The ASTM weather indoor/outdoor boundary conditions were employed in which the indoor and outdoor surface air temperatures were set to be at 21.1°C and −17.8°C respectively in winter conditions [23].

Type	Details	Value
TVG size	Top	284 by 284 by 4 mm
	Middle	292 by 292 by 4 mm
	Bottom	300 by 300 by 4 mm
Glass sheet	Thermal conductivity	1 Wm^{-1} K^{-1}
Surface coating	Three low-e coatings	ε of 0.15 (SnO_2)
Glass sheet support-pillar	Thermal conductivity	16.2 Wm^{-1} K^{-1}
	Material	Stainless steel 304
	Diameter	0.3 mm
	Height	0.15 mm
	Spacing	24 mm
Hermetic edge seal (Primary)	Measured thermal conductivity	46.49 Wm^{-1} K^{-1}
	Material	Cerasolzer CS-186
	Width (wideness)	10 mm
Support seal (Secondary)	Measured thermal conductivity	7.47 Wm^{-1} K^{-1}
	Epoxy steel resin	J-B Weld
	Width (wideness)	4 mm

Table 2. Parameters employed in FEM of the fabricated sample of triple vacuum glazing.

The internal and external surface heat transfer coefficients were set to 8.3 and 30 $Wm^{-2}\ K^{-1}$ respectively [26].

The finite element 3D modelling results show a centre of glass and overall U-value of 0.33 and 1.05 $Wm^{-2}\ K^{-1}$, respectively, this is compared to the predictions of [26] i.e. 0.2 $Wm^{-2}\ K^{-1}$ and [27] i.e. 0.26 $Wm^{-2}\ K^{-1}$ as follows.

The U value (centre of glass) 0.2 $Wm^{-2}\ K^{-1}$ [13] was based on the parametric model of triple vacuum glazing without frame focused on the central glazing area. This value was achieved with 6 mm (top), 4 mm (middle) and 6 mm (bottom) thick untampered soda lime glass sheets having four layers (1-top, 2-middle and 1-bottom) of low-e coatings (ε of 0.03). It is compared with the results of this paper, it is found that an increase of U value (centre-of-glass) 0.13 $Wm^{-2}\ K^{-1}$. Such deviation is due to the design of the fabricated sample reported in this paper which is made of 4 mm(top), 4 mm (middle) and 4 mm(bottom) untampered soda lime glass sheets having three layers of low-e SnO_2 coatings (ε = 0.15). The reason, to use such dimensions and SnO_2 coatings, is the conventional availability of glass sheets from Pilkington Glass and its use in the UK dwelling.

The influence of edge effects is well-detailed in Fang et al. [27, 28] and reported predicted the U values (centre-of-glass and overall) to be 0.26 and 0.65 $Wm^{-2}\ K^{-1}$, respectively. These values were reported for a TVG sample size of 500 × 500 mm with 4 mm (top), 4 mm(middle) and 4 mm (bottom) un-tempered soda lime glass sheets having four layers (1-top, 2-middle and 1-bottom) of low-e coatings (ε of 0.03) with a frame rebate depth of 10 mm and the width of indium-alloy edge seal 6 mm (k of 83.7 $Wm^{-1}\ K^{-1}$). It can be compared, considering all factors, with the results of this paper. It is found that an increase of 0.07 $Wm^{-2}\ K^{-1}$ (deviation of 26.9%) and 0.4 $Wm^{-2}\ K^{-1}$ (deviation of 61.54%) of centre of glass and overall U value, respectively. Such deviations, as per FEM calculations, are due to: the sample size influences to a small extent as the TVG fabricated sample size was of the size 300 × 300 mm, the width of the edge seal influences to a large extent because the TVG fabricated sample width of edge seal used was total 14 mm (10 mm wide Cerasolzer seal and 4 mm wide J-B Weld supportive seal), the use of three SnO_2 low-e coatings (ε of 0.15) in the fabricated sample instead of four Ag low-e coatings (ε of 0.03), and there is no frame rebate depth utilised in the fabricated sample of TVG that has an influence to a small extent on the overall U value of the TVG because the purpose of this paper is focused on the hermetic sealing materials thermal conductivities and triple vacuum glazing area thermal performance only. By accounting all these factors and including the thermal conductivity of the sealing materials, the FEM model predictions are in good agreement.

The simulated isotherms of the triple vacuum glazing for the outdoor and indoor surfaces are shown in **Figure 5**. The mean glass surface temperatures were simulated to be −12.55 and 6.71°C for the outdoor and indoor surfaces of the total glazing area. The mean surface temperatures for the centre of glass area were simulated to be 16.43 and −16.60°C for the outdoor and indoor surfaces respectively. It can be seen the temperature discrepancies on the outdoor side are smaller than the indoor side. This is, however, due to the use of 14 mm composite edge seal as compared to the edge seal thickness of 6 mm [28]. Thus, the edge effects need to be reduced by narrowing the width of edge-seal to 9 mm (6 mm and 3 mm for primary and secondary respectively) which reduces the centre-of-glass U-value of 0.043 $Wm^{-2}\ K^{-1}$.

http://dx.doi.org/10.5772/intechopen.74255

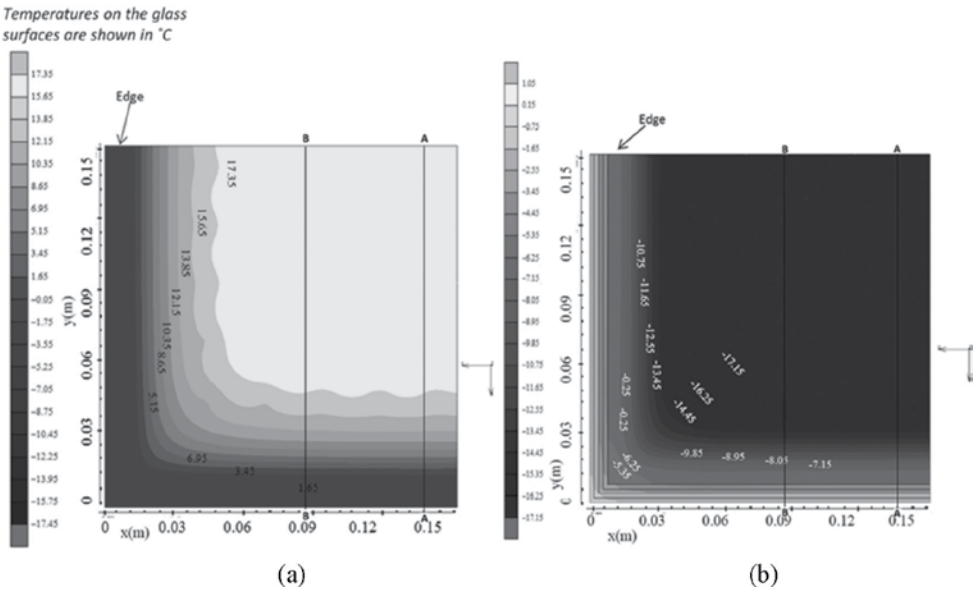

Figure 5. The FEM based isotherms on (a) the indoor (b) the outdoor glass surface showing the temperature variations from the edge area towards the central glazing area.

A finite element calculations of the temperature loss due to a wider edge seal are analysed, along the outer surface lines AA and BB (as shown in **Figure 5**), showing the temperature gradient from the glazing edge to the central area of the glazing as illustrated in **Figure 6**. An

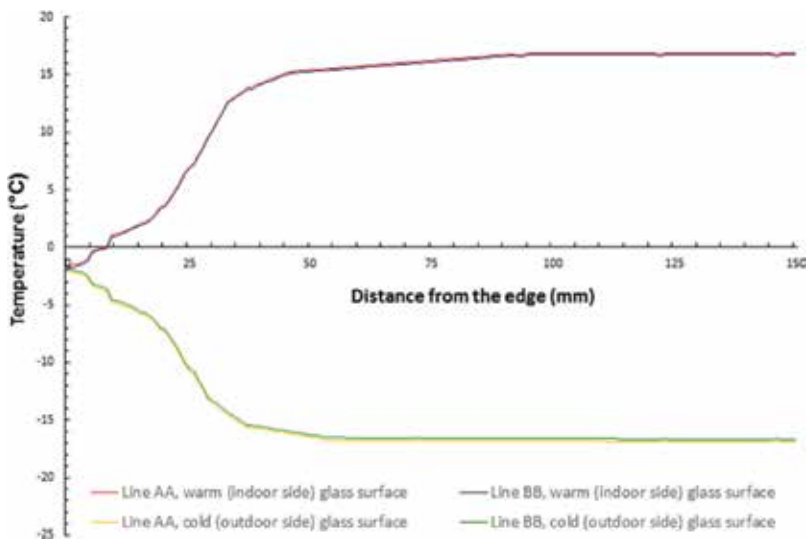

Figure 6. The temperature loss, due to a wider edge seal, along the glazing surface lines AA and BB showing the temperature gradient from the glazing edge to the central area of the glazing of the one quarter of total sample of 300 × 300 mm using ASTM boundary conditions.

influence of wider edge seal on temperature loss around the edge area has affected the centre-of-pane U value. **Figure 6** shows there are smaller temperature gradients on the cold surface as compared to the warm surface of the glazing which is due to the periodic shape of the edge sealing area of triple vacuum glazing as shown in **Figure 1(b)**. It can be seen the influence of temperature gradient loss spread to 54 and 84 mm on the cold and warm side respectively. When comparing with the temperature gradient profiles of [26, 27] the results are in good agreement with the results presented in this paper.

4. Conclusions

In this study, a hot disk thermal constants analyser TPS 2500s using transient plane source technique with a sensor element in the shape of double spiral and resistance thermometer is proved to be an adequate in measuring and analysing the thermal conductivity of hermetic edge sealing materials (i.e. Cersolzer CS186 and J-B Weld). The technique was validated by measuring the thermal conductivity for Mild Steel and Indium and comparing these results with those available in literature. This validated technique based on hot disk thermal constants analyser was then used to measure thermal conductivity of Cerasolzer CS186 alloy and J-B Weld epoxy steel resin and found to be 46.49 and 7.47 Wm^{-1} K^{-1}, respectively. It has been shown that an increase in temperature has direct relation with respect to reporting time with highest increase in temperature was recorded for JB-Weld for a given time period, which is in agreement with the experimental data. It has also been shown that the increase in temperature in the epoxy J-B Weld is greater than that of mild steel. This observation is linked to the fact that the heat flow in semi-polymeric materials is less as compared to that of metallic materials. The temperature increase in the sample made from Cerasolzer alloy was higher than that of indium sample. These values were utilised for the numerical prediction of thermal performance of triple vacuum glazing using 3D FE model. The simulated resulted showed that the centre-of-glass and total U-value of 300 $\times$ 300 mm triple vacuum glazing are 0.33 and 1.05 Wm^{-2} K^{-1}, respectively. The thermal transmittance values can be reduced by using soft low emittance coatings and by reducing the width of the hermetic edge seal to 9 mm. An influence of wider edge seal on temperature loss spreading from the edge to the central glazing area was further analysed with the FEM model calculations. In which it is concluded that the wider edge seal has affected the U-value to 0.043 Wm^{-2} K^{-1} because of the temperature gradient loss spread to 54 and 84 mm on the cold and warm side respectively.

Acknowledgements

The author acknowledge the valuable advice and guidance received from Prof P. C. Eames during the course of this research work. This work was supported by the EPSRC funded project CALEBRE (Consumer Appealing Low energy Technologies for Building Retrofitting) [EP/G000387/1].

http://dx.doi.org/10.5772/intechopen.74255

Nomenclature

a	overall radius of the sensor [m]
d	thickness of the glass sheet [mm]
D	dimensionless time dependent variable
k	thermal conductivity [$Wm^{-1}\ K^{-1}$]
P_o	total output power from the sensor [W]
R	resistance [ohms]
t	time [s]
ΔT_i	initial temperature difference [K]
$\Delta T_{ave}(\tau)$	average temperature increase of the sample surface on the other side of the sensor [K]
T	temperature [°C]
U	thermal transmittance [$Wm^{-2}\ K^{-1}$]

Abbreviations

ASTM	American Society for Testing and Materials
CALEBRE	consumer appealing low energy technologies for building retrofitting
CIBSE	chartered institution of building services engineers
FEM	finite element model
TPS	transient plane source
TVG	triple vacuum glazing

Subscripts

ave.	average
o	before the sensor is heated at
c	t = 0 s characteristic

Greek letters

ρ	density [kgm^{-3}]
α	thermal diffusivity of the sample [$mm^2\ s^{-1}$]

τ	dimensionless time dependent function
φ	temperature coefficient of the resistivity [K^{-1}]
ϕ	heat loss [W]
ε	emittance

Author details

Saim Memon

Address all correspondence to: s.memon@lsbu.ac.uk

Centre for Advanced Materials, Division of Electrical and Electronic Engineering, School of Engineering, London South Bank University, London, UK

References

[1] Memon S, Eames PC. Heat load and solar gain prediction for solid wall dwellings retrofitted with triple vacuum glazing for selected window to wall area ratios, World Renewable Energy Forum, WREF 2012, Including World Renewable Energy Congress XII and Colorado Renewable Energy Society (CRES) Annual Conference, Colorado, USA. 6, 2012. pp. 4636-4643. ISBN: 9781622760923

[2] Memon S, Eames PC. Predicting the solar energy and space-heating energy performance for solid-wall detached house retrofitted with the composite edge-sealed triple vacuum glazing. Energy Procedia. 2017;**122**:565-570. DOI: 10.1016/j.egypro.2017.07.419

[3] Memon S. Analysing the potential of retrofitting ultra-low heat loss triple vacuum glazed windows to an existing UK solid wall dwelling. International Journal of Renewable Energy Development. 2014;**3**(3):161. DOI: 10.14710/ijred.3.3.161-174

[4] Memon S. Design, fabrication and performance analysis of vacuum glazing units fabricated with low and high temperature hermetic glass edge sealing materials. [PhD Thesis]. UK: Loughborough University Institutional Repository; 2013. DOI: https://dspace.lboro.ac.uk/2134/14562

[5] Fang F, Eames PC, Norton B, Hyde TJ. Experimental validation of a numerical model for heat transfer in vacuum glazing. Solar Energy. 2006;**80**:564-577. DOI: 10.1016/j.solener.2005.04.002

[6] Benson DK, Tracy CE. Evacuated window glazings for energy efficient buildings. Proceedings of SPIE 0562, Optical Materials Technology for Energy Efficiency and Solar Energy Conversion IV. San Diego, CA; 1985. p. 250

[7] Eames PC. Vacuum glazing: Current performance and future prospects. Vacuum. 2008; **82**:717-722. DOI: https://doi.org/10.1016/j.vacuum.2007.10.017

[8] Robinson SJ, Collins RE. Evacuated windows—theory and practice. ISES Solar World Congress, International Solar Energy Society, Kobe, Japan; 1989

[9] Collins RE, Simko TM. Current status of the science and technology of vacuum glazing. Solar Energy. 1998;**62**:189-213. DOI: 10.1016/S0038-092X(98)00007-3

[10] Collins RE, Tang JZ, Merrylands. Design improvements to vacuum glazing. 1999. US Patent No. 5891536

[11] Griffiths PW, Di Leo M, Cartwright P, Eames PC, Yianoulis P, Leftheriotis G, Norton B. Fabrication of evacuated glazing at low temperature. Solar Energy. 1998;**63**:243-249. DOI: 10.1016/S0038-092X(98)00019-X

[12] Zhao JF, Eames PC, Hyde TJ, Fang Y, Wang J. A modified pump-out technique used for fabrication of low temperature metal sealed vacuum glazing. Solar Energy. 2007;**81**:1072-1077. DOI: 10.1016/j.solener.2007.03.006

[13] Manz H, Brunner S, Wullschleger L. Triple vacuum glazing: Heat transfer and basic mechanical design constraints. Solar Energy. 2006 Dec 31;**80**(12):1632-1642. DOI: https://doi.org/10.1016/j.solener.2005.11.003

[14] Memon, S. Investigating energy saving performance interdependencies with retrofit triple vacuum glazing for use in UK dwelling with solid walls, Sustainable Development on Building and Environment: Proceedings of the 7th International Conference, Reading, UK; 2015. ISBN-13: 978–0993120701

[15] Memon S, Farukh F, Eames PC, Silberschmidt VV. A new low-temperature hermetic composite edge seal for the fabrication of triple vacuum glazing. Vacuum. 2015;**120**:73-82. DOI: 10.1016/j.vacuum.2015.06.024

[16] Gustavsson M, Karawacki E, Gustafsson SE. Thermal conductivity, thermal diffusivity, and specific heat of thin samples from transient measurements with hot disk sensors. Review of Scientific Instruments. 1994 Dec;**65**(12):3856-3859. DOI: https://doi.org/10.1063/1.1145178

[17] Gustafsson SE. Transient plane source techniques for thermal conductivity and thermal diffusivity measurements of solid materials. The Review of Scientific Instruments. 1991 Mar;**62**(3):797-804. DOI: 10.1063/1.1142087

[18] Hot Disk Thermal Constants Analyzer. 2013. TPS 2500s Instruction Manual, Mathis Instruments. [Accessed: 05–07-2013]

[19] Bohac V, Gustavsson MK, Kubicar L, Gustafsson SE. Parameter estimations for measurements of thermal transport properties with the hot disk thermal constants analyzer. The Review of Scientific Instruments. 2000 Jun;**71**(6):2452-2455. DOI: 10.1063/1.1150635

[20] Memon S, Eames PC. An investigation on edge sealing materials for the fabrication of vacuum glazing, 3rd School of Electrical, Electronic and Systems Engineering (EESE) Research conference, 2013 Mar 21–22, Loughborough University, UK

[21] Memon S. Experimental measurement of hermetic edge seal's thermal conductivity for the thermal transmittance prediction of triple vacuum glazing. Case Studies in Thermal Engineering. 2017;**10**:169-178. ISSN 2214-157X. DOI: 10.1016/j.csite.2017.06.002

[22] ASTM, Standard procedures for determining the steady state thermal transmittance of fenestration systems, ASTM Standard E 1423-91, in: 1994 Annual Book of ASTM Standard 04.07, American Society of Testing and Materials; 1991. pp. 1160-1165

[23] Memon S, Farukh F, Eames PC, Silberschmidt VV. A new low-temperature hermetic composite edge seal for the fabrication of triple vacuum glazing. Vacuum. 2015;**120**:73-82. DOI: 10.1016/j.vacuum.2015.06.024

[24] Collins RE, Robinson SJ. Evacuated glazing. Solar Energy. 1991 Jan;**47**(1):27-38. DOI: 10.1016/0038-092X(91)90060-A

[25] Wang J, Eames PC, Zhao JF, Hyde T, Fang Y. Stresses in vacuum glazing fabricated at low temperature. Solar Energy Materials & Solar Cells. 2007;**91**(4):290-303. DOI: 10.1016/j.solmat.2006.10.007

[26] Fang Y, Hyde T, Hewitt N, Eames PC, Norton B. Comparison of vacuum glazing thermal performance predicted using two-and three-dimensional models and their experimental validation. Solar Energy Materials & Solar Cells. 2009;**93**(9):1492-1498. DOI: https://doi.org/10.1016/j.solmat.2009.03.025

[27] Fang Y, Hyde TJ, Hewitt N. Predicted thermal performance of triple vacuum glazing. Solar Energy. 2010;**84**(12):2132-2139. DOI: 10.1016/j.solener.2010.09.002

[28] Fang Y, Hyde TJ, Arya F, Hewitt N, Wang R, Dai Y. Enhancing the thermal performance of triple vacuum glazing with low-emittance coatings. Energy and Buildings. 2015;**97**:186-195. DOI: 10.1016/j.enbuild.2015.04.006

Section 3

Thermal Conductivity of Nano Systems

Chapter 9

Structural and Thermoelectric Properties Characterization of Individual Single-Crystalline Nanowire

Dedi, Indah Primadona, Ping-Chung Lee, Chi-Hua Chien and Yang-Yuan Chen

Additional information is available at the end of the chapter

http://dx.doi.org/10.5772/intechopen.76635

Abstract

Herein, we report a method for structural characterization as well as TE properties measurements of individual single-crystalline Lead telluride (PbTe) NWs by employing a new microchip design. In this work, the single PbTe NW was characterized in four different types of measurement: structural characterization, Seebeck coefficient S, electrical conductivity σ, and thermal conductivity κ. The structural characterization by transmission electron microscope (TEM) revealed that the PbTe NWs were high-quality single crystals with a growth along the [100] direction. The TE properties S, σ, and κ measurement results of individual 75 nm PbTe NW at room temperature were −54.76 μV K^{-1}, 1526.19 S m^{-1}, and 0.96 W m^{-1} K^{-1}, respectively. Refer to the result of S, σ and κ; the figure of merit ZT values of a 75 nm PbTe NW at the temperature range of 300–350 K were 1.4–4.3 x 10^{-3}. Furthermore, it was observed that the κ value is size-dependent compared to previous reported, which indicates that thermal transport through the individual PbTe NWs is limited by boundary scattering of both electrons and phonons. The results show that this new technique measurement provided a reliable ZT value of individual NW yielded high accuracy for size-dependent studies.

Keywords: lead telluride, nanowires, thermal conductivity, size-dependent, figure of merit

1. Introduction

Recently, nano-engineered thermoelectric (TE) materials used for converting waste heat into electricity have become an interesting research topic. TE energy converters are devices that

can harvest renewable energy for power generation and thermal sensing application [1–3]. The efficiency of TE materials is evaluated based on the dimensionless figure of merit ZT, which is written as $S^2\sigma T/(\kappa_e + \kappa_l)$, where S, σ, κ_e, and κ_l denotes the thermal power or Seebeck coefficient, the electrical conductivity, the electronic thermal conductivity, and the lattice thermal conductivity, respectively. The quantity of $S^2\sigma$ is defined as the power factor (PF). Theoretically, a reduction in dimensionality from three dimensions to one dimension yields a dramatically increased electronic density of states (DOS) at the energy band edges and a decreased thermal conductivity. As a result, the thermoelectric PF and assuredly ZT value enhances [4, 5]. Numerous studies have reported that the enhancement of ZT value in nanomaterials is the result of quantum confinement effects and increased surface phonon scattering [3, 6, 7].

Due to the nanometer scale effect, it is believed that in NWs comprising TE materials, such as PbTe, the value of S is higher than its bulk counterpart [8, 9]. According to the certain carrier-scattering assumptions, the enhancement of S value occurs because of the sharp increase in the local DOS around the Fermi level, which also can be interpreted as an increased local DOS effective mass (m_d^*). However, with the overall benefit of such an improvement in S, nanosize will cause a declining in carrier mobility (μ) and thus affect to the decreasing the ZT value. This is occurs because the increased local DOS usually leads to a heavier transport-effective mass of carriers. In the most well-known high-temperature TE, the carriers are predominantly scattered by phonons. [10] Increasing the S is an obvious goal for obtaining a high efficiency TE materials. Nevertheless, other changes in transport properties often sacrifice the σ correlated with an increase in the S and thus do not ultimately lead to an improvement in ZT.

In order to unveil the size effect on the intrinsic physical properties of TE materials, the measurement of nanowire without interference from either the matrix or external contacts is imperative. Furthermore, the TE properties measurement as well as structural characterization on single nanowire is also crucial in terms of the accuracy and reliability of the resulting ZT value. The low accuracy may occur because every single nanowire, although in the same batch synthesis process, may have a different structure or TE properties. However, measuring all properties on single nanowire is still challenging due to the unavailability of NW microchip which is compatible for all type measurements.

In this chapter, the synthesis and structural characterization of PbTe NWs as well as the preparation of newly design NW's microchip to resolve the above mentioned problem will be described in the first section. For synthesizing the NW, an alternative free-catalyst technique, the stress-induced growth method will be introduced. In the second section, we will discuss about their TE properties (S, σ, and κ).

Type of TE NW used in this chapter was single-crystalline PbTe NW. PbTe is a semiconductor with an energy band gap of 0.31 eV at 300 K [11–14]. In recent years, it has been found that PbTe is one of the superior TE materials in the temperature range of 400–900 K. This material has a large Seebeck coefficient, a very low κ_l (2.2 W m^{-1} K^{-1} at 300 K) [15] and a good electrical conductivity when appropriately chemical doped [16]. The synthesis of low-dimensional PbTe NWs has been

http://dx.doi.org/10.5772/intechopen.76635

intensively explored in the past decades [17–27]. Besides that, there have also been some studies on the TE properties of PbTe-based nanostructures such as PbTe/PbSeTe quantum dot superlattice [28] and PbTe NWs [20] with room temperature ZT value 0.75 and 0.0054, respectively.

2. Synthesis and structural characterization of PbTe NWs

2.1. Synthesis of PbTe NWs

In this work, the synthesis of single-crystalline PbTe NWs via a stress-induced method is described elsewhere [27], in a way similar to the on-film formation (ON–OFF) growth of other semiconductor NWs. [29] Briefly, the PbTe was made by mixing elemental Pb (Alfa Aesar, −200 mesh, 99.9%) and Te (Alfa Aesar, −325 mesh, 99.999%) inside a carbon-coated silica tube. After that, the resulting mixtures inside the tube was vacuumed up to 10^{-6} Torr, sealed, and slowly heated to 1000°C over a period of 12 hours. On the top of the heating process, the temperature was held for 4 hours, and then cooled down to room temperature. The resulted ingot was then cut by a diamond saw into a disc shape with a diameter of 10 mm. Before fabricating the PbTe films, the disc target and substrates were both ultrasonically cleaned in acetone, isopropanol, and then rinsed with deionized water. The PbTe films were prepared by depositing the synthesized PbTe ingot on single-crystal SiO_2/Si (100) substrates in a pulsed laser deposition (PLD) system (LPX Pro 210). The base pressure of the vacuum system was 5.0×10^{-7} Torr. The excimer laser was applied for 15 min at room temperature with energy and frequency of 140 mJ and 10 Hz, respectively. The substrate rotation speed was approximately 10 rpm. With the all mentioned set up, the total thickness of the PbTe films was about 20 nm. To synthesis PbTe NWs, the PbTe films were sealed in a vacuumed quartz tube below 5×10^{-6} Torr, annealed at 450°C for 5 days, and then cooled slowly to room temperature. During the annealing process, the NWs grew from the film to release the compressive stress caused by the difference in thermal expansion coefficients between the PbTe film (19.8×10^{-6}/°C) and the SiO_2/Si substrate (0.5×10^{-6}/°C)/(2.4×10^{-6}/°C).

2.2. Microchip preparation

As mentioned above, the challenge in working with TE NW was the measurement of thermoelectric properties as well as structural analysis on specific single-crystalline nanowire, to get a high accuracy of ZT value. Here, in order to solve that problem, a novel design of microchip was discussed. The preparation processes of the measurement platform are shown in **Figure 1**. First, the silicon (Si) wafer with Si_3N_4 layer (**Figure 1a**) on both sides was covered with the photoresist by using spin coating method (**Figure 1b**), followed by standard photolithography processes. After that the exposure soluble photoresist can be developed by the developer. The Si wafer was then put into the reactive ion etching system (RIE, Model: ANELA DEM-451T) for dry etching. The unprotected Si_3N_4 will be etched by the reactive ion. Then, the wafer is immersed into potassium hydroxide (KOH) solution for wet etching. The silicon which is exposed to KOH will be etched and leaving a thin Si_3N_4 membrane for further processes.

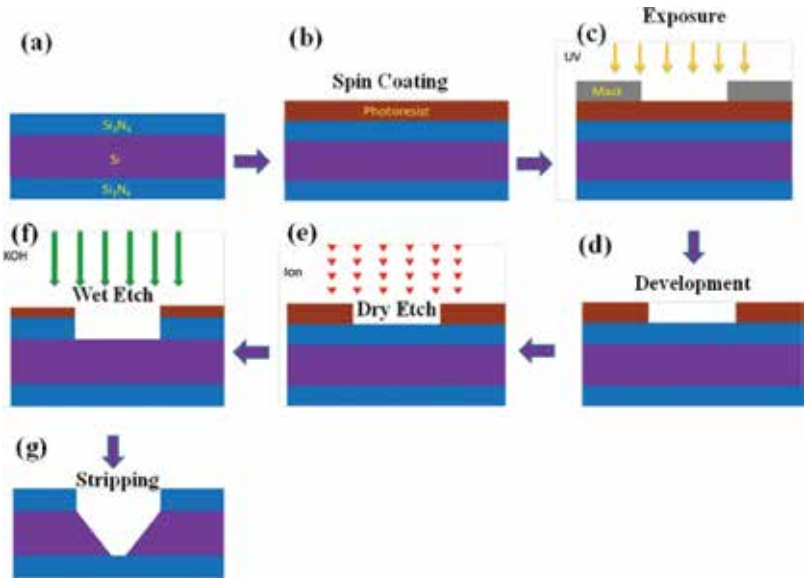

Figure 1. Schematic Si_3N_4 membrane template preparation: (a) the silicon wafer with Si_3N_4 on the both sides, (b) substrate is spin coated with photoresist, (c) Photoresist is exposed to a rectangular pattern with ultraviolet light, (d) soluble photoresist can be developed by the developer, (e) removing Si_3N_4 layer by reactive ion etching system (RIE), (f) dip the wafer into a bath of KOH for wet etching to create a cavity and leave a suspended Si_3N_4 membrane, and (g) strip the photoresist.

The standard photolithography processes were used to define the contact pads of the measurement platform. As shown in **Figure 2**, first, Si wafer with Si_3N_4 membrane is covered with photoresist material by spin coating, followed by exposure, evaporation, and lift-off process. The developed primary measurement platform is then ready to be used.

The flow chart of the suspending process of a nanowire on the measurement platform (microchip) was shown in **Figure 3**. Resistance temperature detectors (RTDs) and current leads were fabricated on the primary measurement platform by electron beam lithography [E-Beam Writer System, Model: Elionix ELS-7000 (100 keV)]. The Si_3N_4 membrane was removed by inductively coupled plasma etching system (ICP, Model: Elionix EIS-700) to open the window. After that, the single nanowire from the PbTe thin film was picked up by a tungsten needle (dw = 100 nm) under a binocular optical microscope and placed across on two RTDs of a Si_3N_4 microchip, where both ends of the nanowire attached to the current leads. In order to improve thermal and electrical contacts between the nanowire and the contact pads, the contacts of the nanowire on thermometers and current leads were covered with a thin layer of Platinum (Pt) using a focused ion beam (FIB) [DBFIB-SEM, FEI NOVA-600].

To examine how good the prepared contact, the contact resistance of all four points (point 1, 2, 3, and 4) as depicted in **Figure 4** were measured. First, the known direct current (DC) was applied between contacts 1 and 4 (4 probes) and then the voltage drop across contact 2 and 3 (2 probes, see **Figure 4**) was measured. The total resistance of two-point probe configuration is expressed as $R_{2point} = R_{lead} + 2R_{contact} + R_{nw}$. Wherein, R_{2point}, R_{lead}, $R_{contact}$, and

http://dx.doi.org/10.5772/intechopen.76635

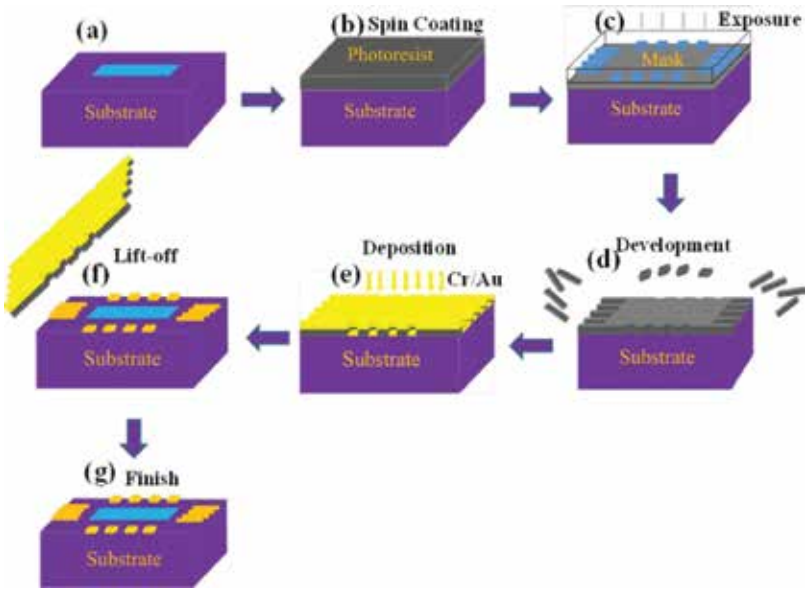

Figure 2. Schematic of depositing outer electrodes of the template: (a) silicon wafer with Si_3N_4 membrane, (b) substrate is spin coated with photoresist, (c) photoresist can be exposed to a pattern by ultraviolet light, (d) soluble photoresist will be developed by the developer, (e) the Cr/Au electrodes are deposited by thermal evaporator, (f) lift-off the photoresist by acetone, and (g) measurement platform is ready to be used.

R_{nw} represents resistance between point 2 and 3, resistance of Cr/Au electrodes, resistance of contacted NW to electrode, and NW resistance, respectively. The resistance of R_{2point} and R_{nw} were measured by two and four-point probes. Whilst, in order to obtain the contact resistance as $R_{cont} = (R_{2point} - R_{nw})/2$, R_{lead} (~10 Ω) was neglected. The measurement result of R_{2point} was about 6–7% from R_{nw} value. Since the power dissipation at the contacts is much smaller than the minimum power for 3ω signal, the resultant contact resistance supposedly does not affect the third harmonic signal. Furthermore, the contact metal pads act as large thermal reservoirs where the temperature is kept constant at the initial temperature during the experiment.

In addition, the prepared nanowire exhibited a linear current–voltage (I-V) curve wherein indicated the Ohmic contact response; the current range within 0 to 100 μA indicating the resistivity of NW follows the Ohm's law. An Ohmic contact is an electrical junction between two conductors which has a linear current–voltage (I-V) curve following the Ohm's law. Low resistance Ohmic contacts are applied to facilitate the flow of charge in both directions between the two conductors, without blocking from the excess power dissipation due to voltage thresholds. The contact quality has a contribution to both an electrical and a thermal effect, such as, if the electrical contact resistance is too high, the third harmonics measurement will be influenced by the heat dissipation occurred at the contacts due to Joule heating. Furthermore, incorrect selection of a working frequency will develop an error experiment results. Therefore, the AC impedance measurements with no electrical artifacts involved were utilized to choose a correct working frequency.

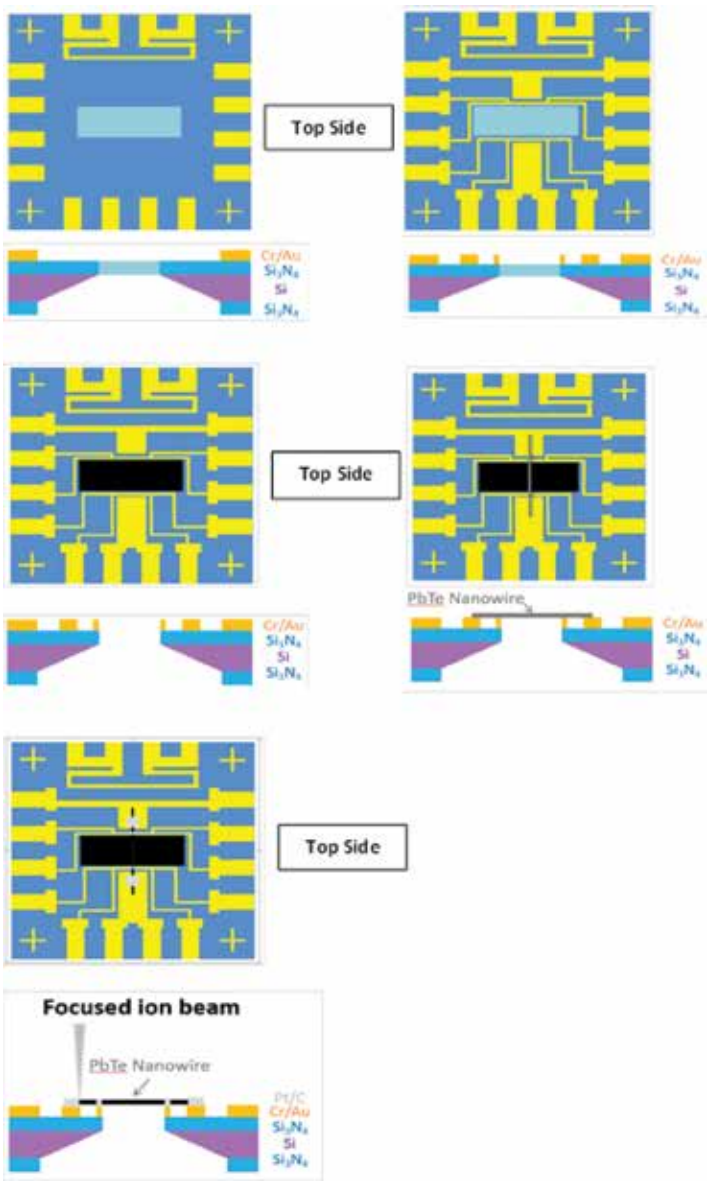

Figure 3. Flow charts of the suspending process of a nanowire on the measurement platform.

2.3. Structural characterization of PbTe NWs

The size and crystalline structure of PbTe NWs were characterized by scanning electron microscope (SEM) and transmission electron microscope (TEM). The SEM image of grew PbTe NWs on the substrate (**Figure 5a**) reveals that the length and the diameter of NWs were ranging from 5 to 70 μm and 50 to 300 nm, respectively. The NWs with length about 70 μm was picked up, placed, and contacted on the microchip as shown in **Figure 5b**. The prepared contacts have a

http://dx.doi.org/10.5772/intechopen.76635

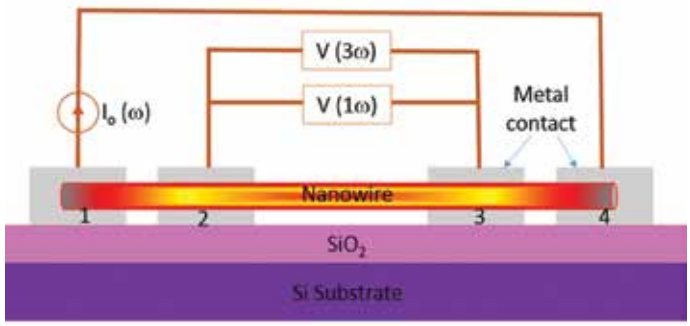

Figure 4. A schematic setup of four-point probe for measurement of electrical resistance (*R*), Seebeck coefficient (*S*) and the thermal conductivity (κ) by 3ω method.

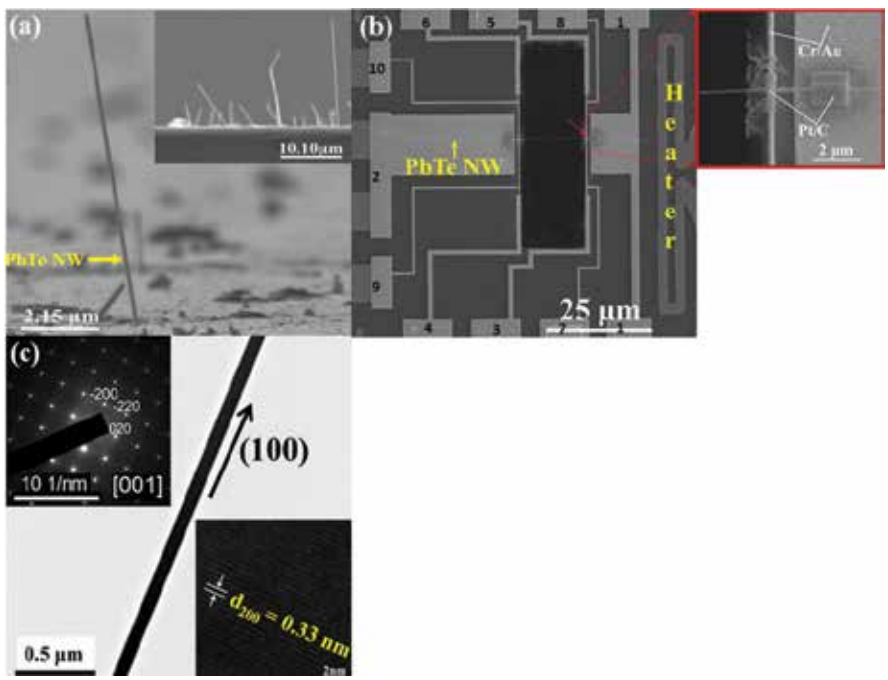

Figure 5. (a) SEM image of PbTe NWs grew on the surface of the PbTe thin film, (b) SEM images of a PbTe NW suspended on a Si_3N_4 template, inset: the Pt/C thermal contact between the PbTe NW and 10-nm Cr/50-nm Au electrodes on a Si_3N_4 microchip, (c) low-magnification TEM images of a PbTe NW, inset of the top left of figure: the SAED pattern (at the [001] zone axis), inset of the bottom right of figure: a high-resolution TEM image of a PbTe NW.

resistance about 425–430 Ω, wherein showed nearly Ohmic contacts. The microchip consisting of PbTe NW displayed in **Figure 5b** was used for complete structural analysis and TE properties measurements. The representative TEM image showed that the employed PbTe NWs has a diameter of 75 nm (**Figure 5c**) and this size was further convinced by the scanning transmission electron microscope (STEM) result (**Figure 6a**). In addition, the TEM image and a corresponding selected-area electron diffraction (SAED) pattern (inset of the top left of **Figure 5c**) revealed

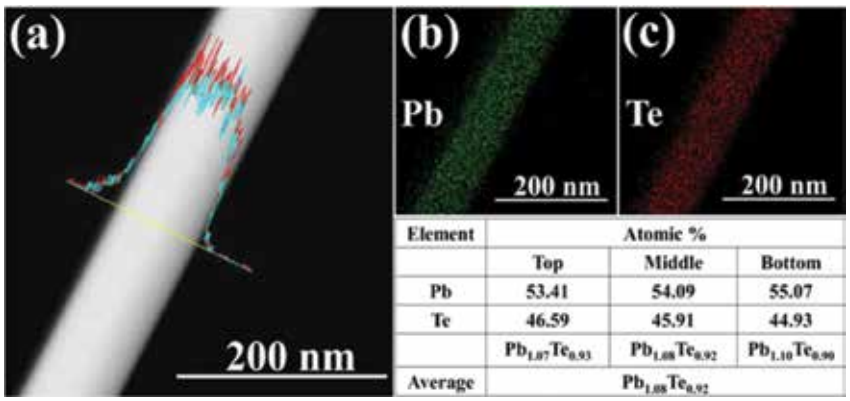

Element	Atomic %		
	Top	Middle	Bottom
Pb	53.41	54.09	55.07
Te	46.59	45.91	44.93
	$Pb_{1.07}Te_{0.93}$	$Pb_{1.08}Te_{0.92}$	$Pb_{1.10}Te_{0.90}$
Average	$Pb_{1.08}Te_{0.92}$		

Figure 6. (a) STEM images of a PbTe NW. The line profiles show that the Pb (blue line) and Te (red line) are homogeneously distributed throughout the NW, (b) and (c) elemental mapping showing the uniform distribution of Pb and Te along the NW, respectively.

that the PbTe NWs were high-quality single crystals with a growth along the [100] direction. While, the lattice fringes of the smooth PbTe were separated by 0.33 nm (inset of the bottom right of **Figure 5c**). This is consistent with a periodicity along the [200] direction with lattice constants of approximately 6.549 Å, which are approximately 1.2% higher than the bulk counterpart (a = 6.47 Å).

The chemical composition of the PbTe NWs was studied by using energy dispersive X-ray spectroscopy (EDS). The EDS line scan profile, shown in **Figure 6a**, revealed the uniform spatial distribution of the Pb and Te elements throughout the NW. This was further confirmed by using a STEM to map elements across the NW [**Figure 6b** and **c**]. The EDS point scanning experiments of the NWs quantitatively confirmed that Pb and Te are present in an average atomic ratio of 54.19 and 45.81% (Table in **Figure 6**), respectively. In addition, the EDS data also revealed that the atomic ratio of Pb/Te ≈ 1.18, with no impurities. As a result, the stoichiometric composition of the individual NW was $Pb_{1.08}Te_{0.92}$.

3. Thermoelectric properties

As mentioned before that the microchip with a rectangular window which shown in **Figure 5b** was employed to measure the TE properties of NW, i.e. electrical resistivity (ρ) and Seebeck coefficient (S). In this experiment, the PbTe NW was placed across two resistance thermometers, hot side thermometer Th (a gold wire parallel line to the heater between contact electrodes 7 and 8 which is marked as red arrows in **Figure 5b**) and cold side thermometer Tc (a gold wire between the contact electrode 9 and 10, **Figure 5b**) with both ends of the NW attach to the current leads (electrode 1 and 2, **Figure 5b**). To measure the V1ω and V3ω signal, electrodes 3 and 4 (voltage leads) were connected to lock-in amplifier. The thermal conduction

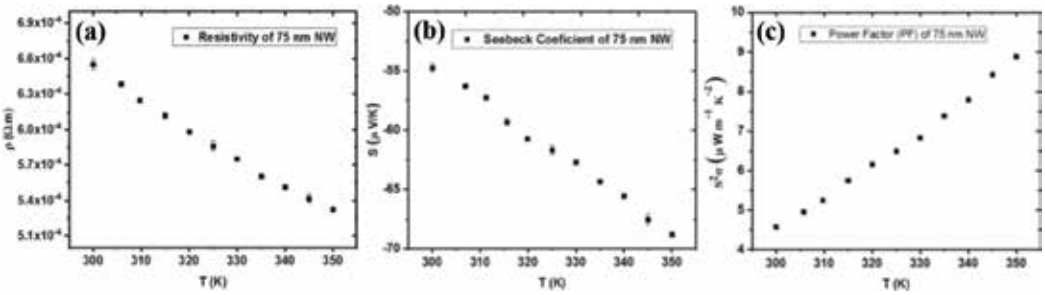

Figure 7. Temperature dependence of (a) electrical resistivity, (b) Seebeck coefficient, and (c) power factor of a 75 nm PbTe NW.

from NW to the microchip substrate that affects the S and ρ measurement was assured zero. Furthermore, in order to eliminate convectional heat loss, all measurements were carried out in a high vacuum of at least lower than 2×10^{-6} Torr.

Four-point probe method was applied for ρ measurement. In this work, an AC current flowed to the NW via electrode 1. The voltage (V) and current (I) difference between electrode 1 and 2 was measured through the voltage leads. A pair of current leads into the NW to determine the root mean square of the voltage difference of a pair of voltage leads. By substituting the obtained V and I value to the V = I•R formula, the resistance (R) value is obtained. We get the R of NW, the ρ value could be attained by applying the formula of ρ = R•A / L where A and L are cross-section area of the wire and length between a pair of voltage leads, respectively. **Figure 7a** showed the measurement results of NW resistivity ρ at temperatures range 300–350 K. This figure demonstrated that the resistivity ρ of a 75-nm PbTe NW was temperature dependence which indicated a semiconducting behavior. The resistivity of a PbTe NW at near room temperature was 6.55×10^{-4} Ω m, which 43 times greater than the bulk counterpart (1.52×10^{-5} Ω m) [14]. This is probably due to the surface scattering of charge carriers [30].

For the Seebeck effect measurement, the characterization was based on the voltage and temperature difference generated between electrodes 3 and 4 (**Figure 5b**). To generate the temperature gradient between those two electrodes, the heater with frequency 1ω and magnitude equals to $I \bullet Sin(\omega t)$ was applied at one end of the NW. In this experiment, the sample was employed as the sensor of the thermometer as well, thus, temperature coefficient of electrical resistance of them are needed to be calibrated at first. By applying a DC current to the sensor and measuring the change of the voltage difference at frequency 2ω between the two ends of the sensor, the resistance change of the sensor would be known. After obtaining the temperature coefficient of electrical resistance, the temperature gradient created between two ends of the NW would be gained, because the observed heat is proportional to the square of the current multiplied by the electrical resistance of the NW, $Q \propto I^2 \bullet \sin^2(\omega t) \bullet R$, where Q and R denote the observed heat and the electrical resistance of the NW, respectively. Mathematically, $\sin^2\alpha = [(1-\cos 2\alpha)/2]$, it means that the frequency of 2ω was applied to heat the heater. As the heater is heated at frequency 2ω, the sample temperature and sensor resistance would fluctuated at frequency 2ω as well. By

knowing the temperature gradient and also measuring the thermoelectric voltage of two ends of the sample, S can be calculated by implementing the formula: $S = (\triangle V) / (\triangle T)$.

The experiment results of Seebeck effect of a 75-nm PbTe NW shown in **Figure 7b** revealed that the S value was temperature dependence. The S value increased with increasing the temperature. In addition, as depicted in **Figure 7b** that the S of PbTe NWs at various temperature measurements has a negative sign which indicated for n-type semiconductor material. Those negative sign appears because their electrons have a much higher μ than holes and dominate the electronic transport properties [31, 32]. At temperature of 300 K, the S value for the 75-nm NW was −54.76 μV K^{-1}, which is about 69% lower compare to the bulk counterpart [14]. This result may due to the consequences of structural imperfections, such as antisite defects inside PbTe NW (i.e., the creation of one vacancy at the tellurium site) [14, 33].

Theoretically, for almost all materials, the trend of ρ was closely correlated with the S. It was consistent with our experimental resultts (**Figure 7a** and **b**) which showed that the smaller ρ had a higher S value. Conversely, due to $s = 1/\rho$, thus s value increases when S is increased. The PF ($S^2\sigma$) calculation results of PbTe NWs as a function of temperature are plotted in **Figure 7c**. The PF increased gradually when the temperature increased, and this result was mainly due to the influence of ρ trends. At the temperature about 300 K the $S^2\sigma$ values were 4.58 μW m^{-1} K^{-2}.

Comparing the S value as a function of carrier density of various PbTe bulk obtained by Harman et al., **Figure 8** show that the S was closely correlated with the carrier concentration (n), Our results was consistent with the other previous experiments [14, 34] in which a smaller n had a higher S value.

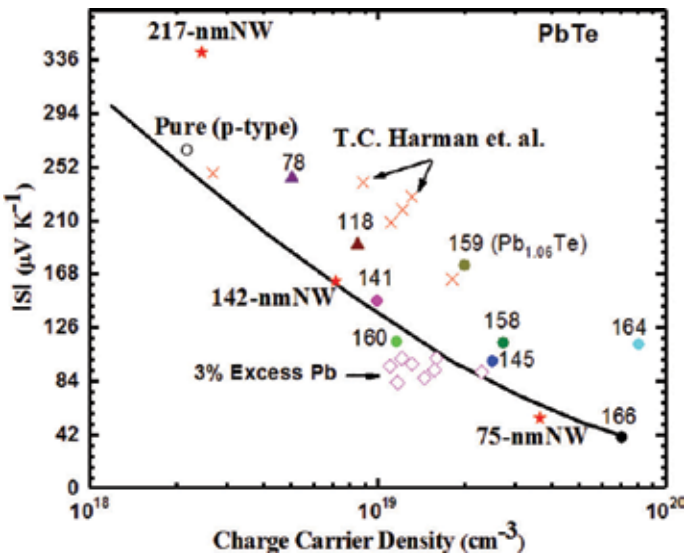

Figure 8. Absolute value of the thermoelectric power or Seebeck coefficient (S) of various PbTe samples [14] as a function of carrier density; electrons (n) or holes (h) at room temperature. The solid red stars denote the $Pb_{1.08}Te_{0.92}$ samples with 75, 142, and 217 nm diameter wires [27, 34].

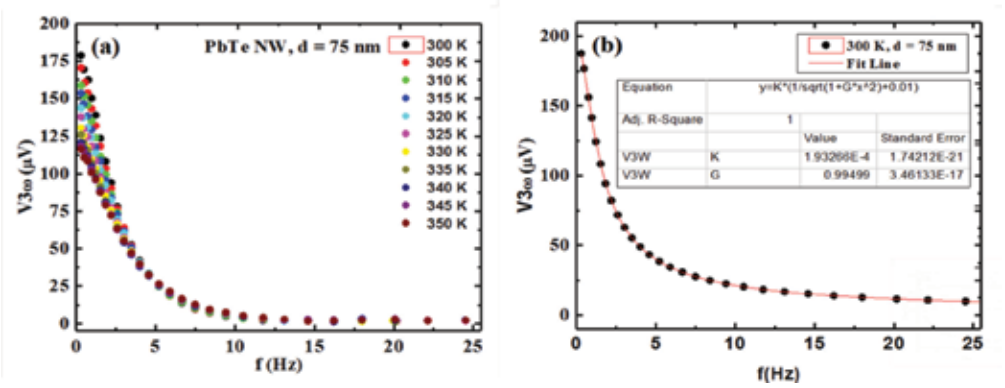

Figure 9. (a) Frequency dependence of $V_{3\omega}$ at 300–350 K for 75 nm PbTe NW and (b) the solid line is predicted relation $V_{3\omega} \alpha 1/\sqrt{(1 + (2\omega\gamma)^2)}$ at 300 K for a 75 nm PbTe NW.

The thermal conductivity of the 75 nm PbTe nanowire was measured by the self-heating 3ω method [35] in the temperature range of 300–350 K. In the experiment, the $V_{3\omega}$ as a function of frequency will be attained. As shown in **Figure 9a**, the $V_{3\omega}$ was dependent on the frequency. The $V_{3\omega}$ reduce significantly by increasing the frequency, however, the reduction become slightly at a frequency above 10 Hz. The relation between thermal conductivity, $V_{3\omega}$ and frequency is described in the Eq. (1).

$$V_{3\omega} = \frac{4 I_0^3 R R' L}{\pi^4 \kappa S \sqrt{1 + (2\omega\gamma)^2}} \tag{1}$$

which simplified as:

$$y = \frac{K}{\sqrt{1 + Gx^2}} \tag{2}$$

where I and ω denote the amplitude and frequency of the alternating current applied on nanowire, R and R′ are the resistance and derivative of resistance at corresponding temperature, κ is the thermal conductivity, S is the cross section, and γ is the characteristic thermal time constant.

Figure 9b shows the fitting result of $V_{3\omega}$ to frequency of a 75 nm PbTe NW at 300 K. The thermal conductivity κ of the nanowire can be derived from the intercept of the fitting value at a certain temperature $V_{3\omega} = (4I_0^3 LRR')/(\pi^4 \kappa S)$ ($\omega\gamma \rightarrow 0$). To further validate the extraction of thermal conductivity by 3ω method, the variation of 3ω signals toward the input current amplitude I_0 and frequency was studied. The result shows that $V_3\omega$ versus I_0 follows the I_0^3, as exhibited in the equation of **Figure 10**, which mean it agree with the Eq. (1).

By substituting all acquired data from self-heating 3ω experiment to Eq. (1), the thermal conductivity, κ of a 75 nm PbTe NW at range temperature of 300–350 K were 0.96–0.72 $Wm^{-1} K^{-1}$ (**Figure 11a** and **b**), which is approximately 2.40–3.19 times lower than the bulk counterpart (κ = 2.3 $W m^{-1} K^{-1}$). Likewise, the κ value at room temperature was 0.96 $W m^{-1} K^{-1}$, which is

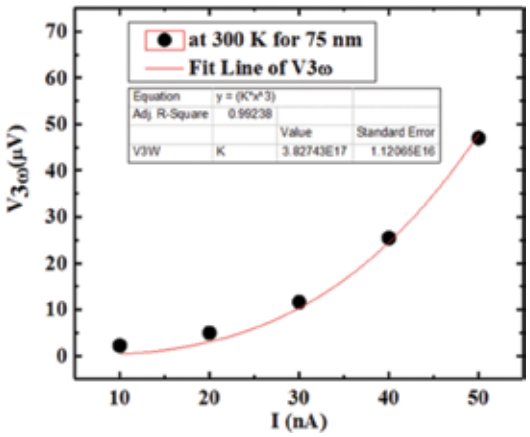

Figure 10. The 3rd harmonic voltage signal $V_{3\omega}$ as function of the extraction current amplitude I_0 for a 75 nm PbTe NW at 300 K. Red solid line represents the cubic relationship of $V_{3\omega}$ and I_0.

approximately 58% lower than the typical reported value of $\kappa = 2.3$ W m^{-1} K^{-1} for bulk PbTe. This decline mainly due to the carrier concentration difference or size effect. [36]

For the purpose of calculating the κ_l value, the electron thermal conductivity κ_e need to be determined. The κ_e value is calculated by using Eq. (3) (Wiederman-Franz law, where the Lorenz number $L = 2.44 \times 10^{-8}$ W.Ω.K^{-2}), while the κ_l is gained from subtracting the κ with κ_e value. The values of κ_l of a 75 nm PbTe NW at 300 K was 0.95 W m^{-1} K^{-1}, which is 57% lower than the PbTe bulk ($\kappa_l = 2.2$ W m^{-1} K^{-1}). [16] As reference, the lattice contribution (κ_l) of superlattice thin films $PbSe_{0.98}Te_{0.02}$/PbTe at room temperature was 0.35 W m^{-1} K^{-1} [28].

$$\kappa_e = L.\sigma.T \tag{3}$$

The lattice thermal conductivity has a lower limit wherein the phonon mean free path becomes comparable to the lattice spacing of the atoms [37]. Alternatively, the lattice thermal conductivity of a material can be determined by using Eq. (4), where C, ν, andι represent the heat capacity per unit volume, the speed of sound in the material, and the mean free path of the phonons, respectively. By applying the atom spacing of PbTe as the minimum ι and substituting the values of the ν and C to Eq. (4), the κ_l of PbTe is around 0.2 W m^{-1} K^{-1}. Repeating this calculation for a variety of compounds, the lowest possible value of κ_l are in the range of 0.1–0.2 W m^{-1} K^{-1} [38].

$$\kappa_l = 1/3.C.\nu.\iota \tag{4}$$

As the size of the nanowire approaches the ι (the median phonon free path in PbTe is about 42 nm) [39], the κ value will drop due to the increased phonon scattering. According to the reported κ of individual PbTe NW with various diameters (d = 182, 277, and

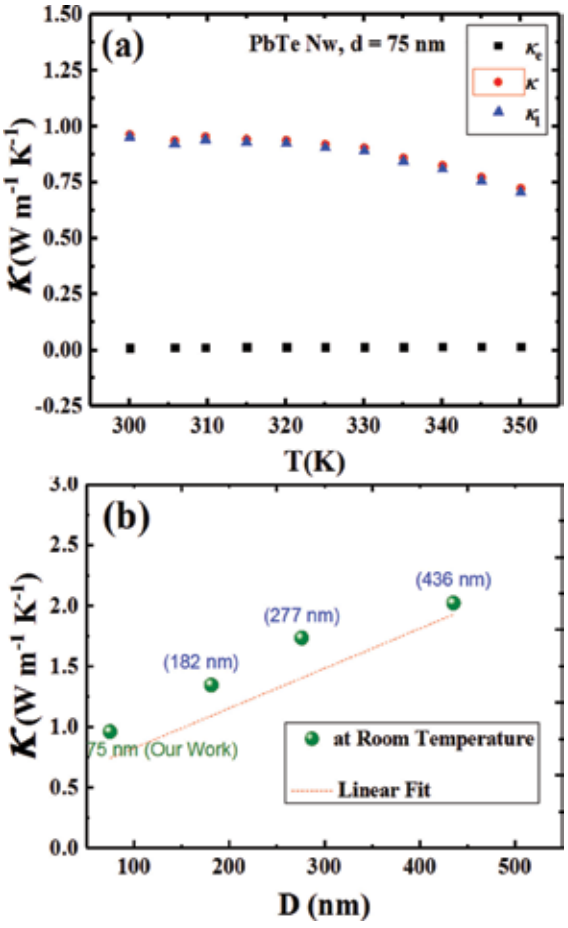

Figure 11. (a) Measured thermal conductivity κ( ), electron thermal conductivity κ_e ( ) and lattice thermal conductivity κ_l ( ) of a 75 nm PbTe NW and (b) size-dependent κ properties of individual 75 nm PbTe NW (compared to the reported 182 nm, 277 nm and 436 nm [19].

436 nm) [19] including our recent work (d = 75 nm) which were plotted in **Figure 11b**, the κ value decreases gradually as its diameter shrinks. The enhanced phonon boundary scattering has a considerable effect in reducing the κ value of NW. Hence, it is suggested to have an effect on suppressing the phonon transport through the NWs as well [40, 41]. Theoretically, those phenomena would cause the *ZT* value of NW higher than the bulk counterpart, provided that the electronic properties were not degraded by the nanostructure. However, based upon all the above measurement results, i.e. S (−54.76 – –68.80 μV K^{-1}) [27], σ (1526.19–1878.68 S m^{-1}) [27] and κ (0.96–0.72 W m^{-1} K^{-1}), the obtained *ZT* value of a 75 nm PbTe NW at 300–350 K are in the range of ~1.4–4.3 x 10^{-3} (**Figure 12**) and it is still much lower than the ZT of PbTe bulk which is approximately ~ 0.25 at 300 K and maximal ~ 0.8 at 700 K [42].

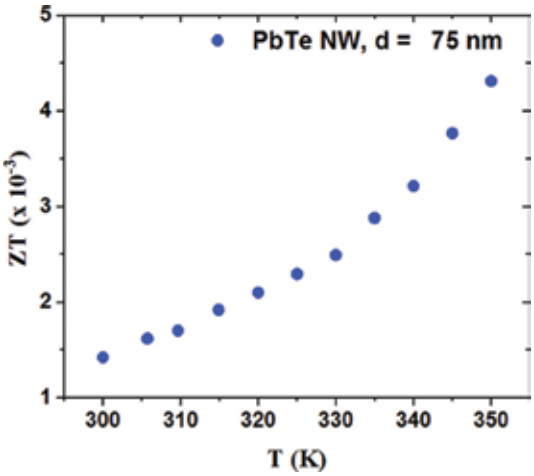

Figure 12. Figure of merit *ZT* for a n-type 75 nm PbTe NW.

4. Conclusions

In summary, we have demonstrated a new technique for structural characterization and TE properties measurement of individual single-crystalline PbTe NW by using a novel design of microchip. In this work, the single PbTe NW grown by the stress-induced method was employed for four different type of characterization simultaneously: structural characterization, Seebeck coefficient, electrical conductivity, and thermal conductivity. The structural characterization revealed that the synthesized PbTe NWs were single crystals with a growth along the [100] direction. While the TE properties (S, σ, and κ) of a 75 nm single-crystalline PbTe NW at room temperature are −54.76 μV K^{-1}, 1526.19 S m^{-1}, and 0.96 W m^{-1} K^{-1}, respectively. Based on those results, the experimental calculation of *ZT* value of its NW was ~1.4–4.3 x 10^{-3} at 300–350 K range. This technique provided high accuracy and reliable ZT value of individual single-crystalline TE NW. Thus, the size-dependent study of TE properties is very feasible. In this study, the κ value in growth [100] direction PbTe NW is size-dependent, wherein indicates that thermal transport through the individual PbTe nanowires is limited by boundary scattering of both electrons and phonons.

Acknowledgements

Technical support was provided by the Core Facilities for Nanoscience and Nanotechnology at the Institute of Physics of the Academia Sinica in Taiwan. This study was funded by the National Science Council of Taiwan (grant NSC 100-2112-M-001-019-MY3).

Conflict of interest

The authors declare no competing conflict of interests.

Author details

Dedi[1,3]*, Indah Primadona[2], Ping-Chung Lee[3], Chi-Hua Chien[3] and Yang-Yuan Chen[3]

*Address all correspondence to: dediamada@yahoo.com

1 Research Center for Electronics and Telecommunication, Indonesian Institute of Sciences, Bandung, Indonesia

2 Research Unit for Clean Technology, Indonesian Institute of Sciences, Bandung, Indonesia

3 Institute of Physics, Academia Sinica, Taipei, Taiwan

References

[1] DiSalvo FJ. Thermoelectric cooling and power generation. Science. 1999;**285**:703-706. DOI: 10.1126/science.285.5428.703

[2] Tritt TM. Thermoelectric materials: Holey and unholey semiconductors. Science. 1999;**283**:804-805. DOI: 10.1126/science.283.5403.804

[3] Dresselhaus MS, Chen G, Tang MY, Yang RG, Lee H, Wang DZ, Ren ZF, Fleurial JP, Gogna P. New directions for low-dimensional thermoelectric materials. Advanced Materials. 2007;**19**:1043-1053. DOI: 10.1002/adma.200600527

[4] Mahan GD. Good thermoelectrics solid state physics. Advances in Research and Applications. 1998;**51**:81-157. DOI: 10.1016/S0081-1947(08)60190-3

[5] Lin YM, Sun X, Dresselhaus MS. Theoretical investigation of thermoelectric transport properties of cylindrical bi nanowires. Physical Review B. 2000;**62**:4610-4623. DOI: 10.1103/PhysRevB.62.4610

[6] Bassi AL, Bailini A, Casari CS, Donati F, Mantegazza A, Passoni M, Russo V, Bottani CE. Thermoelectric properties of Bi–Te films with controlled structure and morphology. Journal of Applied Physics. 2009;**105**:124307(1-9). DOI: 10.1063/1.3147870

[7] Szczech JR, Higgins JM, Jin S. Enhancement of the thermoelectric properties in nanoscale and nanostructured materials. Journal of Materials Chemistry. 2011;**21**:4037-4055. DOI: 10.1039/C0JM02755C

[8] Hicks LD, Dresselhaus MS. Effect of quantum-well structures on the thermoelectric figure of merit. Physical Review B. 1993;**47**:12727-12731. DOI: 10.1103/PhysRevB.47.12727

[9] Hicks LD, Dresselhaus MS. Thermoelectric figure of merit of a one-dimensional conductor. Physical Review B. 1993;**47**:16631-16634. DOI: 10.1103/PhysRevB.47.16631

[10] Pei Y, Wang H, Gibbs ZM, LaLonde AD, Snyder GJ. Thermopower enhancement in Pb1−xMnxTe alloys and its effect on thermoelectric efficiency. NPG Asia Materials. 2012;**4**:e28. DOI: 10.1038/am.2012.52

[11] Rowe DM. CRC Handbook of Thermoelectrics. Boca Raton, FL, USA: CRC Press; 1995. p. 441

[12] Dughaish ZH. Lead telluride as a thermoelectric material for thermoelectric power generation. Physica B: Condensed Matter. 2002;**322**:205-223. DOI: 10.1016/S0921-4526(02)01187-0

[13] Heremans JP, Thrush CM, Morelli DT. Thermopower enhancement in lead telluride nanostructures. Physical Review B. 2004;**70**:115334(1-5). DOI: 10.1103/PhysRevB.70.115334

[14] Heremans JP, Thrush CM, Morelli DT. Thermopower enhancement in PbTe with Pb precipitates. Journal of Applied Physics. 2005;**98**:063703(1-6). DOI: 10.1063/1.2037209

[15] Orihashi M, Noda Y, Chen LD, Goto T, Hirai T. Effect of tin content on thermoelectric properties of p-type lead tin telluride. Journal of Physics and Chemistry of Solids. 2000;**61**:919-923. DOI: 10.1016/S0022-3697(99)00384-4

[16] LaLonde AD, Pei Y, Wang H, Snyder GJ. Lead telluride alloy thermoelectrics. Materials Today. 2011;**14**:526-532. DOI: 10.1016/S1369-7021(11)70278-4

[17] Wei Q, Lieber CM. Synthesis of single crystal bismuth-telluride and lead-telluride nanowires for new thermoelectric materials. Materials Research Society Symposium Proceedings. 2000;**581**:219-223. DOI: 10.1557/PROC-581-219

[18] Fardy M, Hochbaum AI, Goldberger J, Zhang MM, Yang P. Synthesis and thermoelectrical characterization of lead chalcogenide nanowires. Advanced Materials. 2007;**19**:3047-3051. DOI: 10.1002/adma.200602674

[19] Roh JW, Jang SY, Kang J, Lee S, Noh JS, Kim W, Park J, Lee W. Size-dependent thermal conductivity of individual single-crystalline PbTe nanowires. Applied Physics Letters. 2010;**96**:103101(1-3). DOI: 10.1063/1.3352049

[20] Lee SH, Shim W, Jang SY, Roh JW, Kim P, Park J, Lee W. Thermoelectric properties of individual single-crystalline PbTe nanowires grown by a vapor transport method. Nanotech. 2011;**22**:295707(1-6). DOI: https://doi.org/10.1088/0957-4484/22/29/295707

[21] Yang Y, Taggart DK, Cheng MH, Hemminger JC, Penner RM. High-throughput measurement of the seebeck coefficient and the electrical conductivity of lithographically patterned polycrystalline PbTe nanowires. Journal of Physical Chemistry Letters. 2010;**1**:3004-3011. DOI: 10.1021/jz101128d

[22] Yang Y, Kung SC, Taggart DK, Xiang C, Yang F, Brown MA, Guell AG, Kruse TJ, Hemminger JC, Penner RM. Synthesis of PbTe nanowire arrays using lithographically

patterned nanowire electrodeposition. Nano Letters. 2008;**8**:2447-2451. DOI: 10.1021/nl801442c

[23] Jung H, Park DY, Xiao F, Lee KH, Choa LH, Yoo B, Myung NV. Electrodeposited single crystalline PbTe nanowires and their transport properties. Journal of Physical Chemistry C. 2011;**115**:2993-2998. DOI: 10.1021/jp110739v

[24] Tai G, Zhou B, Guo W. Structural characterization and thermoelectric transport properties of uniform single-crystalline lead telluride nanowires. Journal of Physical Chemistry C. 2008;**112**:11314-11318. DOI: 10.1021/jp8041318

[25] Tai G, Guo W, Zhang Z. Hydrothermal synthesis and thermoelectric transport properties of uniform single-crystalline pearl-necklace-shaped PbTe nanowires. Crystal Growth & Design. 2008;**8**:2906-2911. DOI: 10.1021/cg701262x

[26] Yan Q, Chen H, Zhou W, Hng HH, Boey FYC, Ma J. A simple chemical approach for PbTe nanowires with enhanced thermoelectric properties. Chemistry of Materials. 2008;**20**:6298-6300. DOI: 10.1021/cm802104u

[27] Dedi, Lee PC, Chien CH, Dong GP, Huang WC, Chen CL, Tseng CM, Harutyunyan SR, Lee CH, Chen YY. Stress-induced growth of single-crystalline lead telluride nanowires and their thermoelectric transport properties. Applied Physics Letters. 2013;**103**:023115(1-5). DOI: 10.1063/1.4813606

[28] Caylor JC, Coonley K, Stuart J, Colpitts T, Venkatasubramanian R. Enhanced thermoelectric performance in PbTe-based superlattice structures from reduction of lattice thermal conductivity. Applied Physics Letters. 2005;**87**:023105(1-3). DOI: 10.1063/1.1992662

[29] Shim W, Ham J, Lee KI, Jeung WY, Johnson M, Lee W. On-film formation of bi nanowires with extraordinary electron mobility. Nano Letters. 2009;**9**:18-22. DOI: 10.1021/nl8016829

[30] Wang D, Sheriff BA, Heath JR. Complementary symmetry silicon nanowire logic: Power-efficient inverters with gain. Small. 2006;**2**:1153-1158. DOI: 10.1002/smll.200600249

[31] Partin DL, Heremans J, Morelli DT, Thrush CM, Olk CH, Perry TA. Growth and characterization of epitaxial bismuth films. Physical Review B: Condensed Matter. 1988;**38**:3818-3824. DOI: 10.1103/PhysRevB.38.3818

[32] Dekuijper AH, Bisschop J. Temperature dependence of concentrations and mobilities in thin bismuth films. Thin Solid Films. 1983;**110**:99-106. DOI: 10.1016/0040-6090(83)90214-6

[33] Horak J, Navratil J, Stary Z. Lattice point defects and free-carrier concentration in $Bi_{2+x}Te_3$ and $Bi_{2+x}Se_3$ crystals. Journal of Physics and Chemistry of Solids. 1992;**53**:1067-1072. DOI: 10.1016/0022-3697(92)90079-S

[34] Dedi, Idayanti N, Lee PC, Lee CH, Chen YY. Thermoelectric power of single crystalline lead telluride nanowire. Journal of Physics Conference Series. 2016;**776**:012046. DOI: 10.1088/1742-6596/776/1/012046

[35] Lu L, Yi W, Zhang D.L. 3ω method for specific heat and thermal conductivity measurements. The Review of Scientific Instruments. 2001;**72**:2996-3003. DOI: 10.1063/1.1378340

[36] Ioffe AF. Semiconductor Thermoelements and Thermoelectric Cooling. London: Infosearch; 1957

[37] Slack GA. The thermal conductivity of nonmetallic crystals. In: Ehreneich H, Seitz F, Turnbull D, editors. Solid State Physics. Vol. 34. New York: Academic Press; 1979. pp. 1-71. DOI: 10.1016/S0081-1947(08)60359-8

[38] Goldsmid HJ. A New Upper Limit to the Thermoelectric Figure-of-Merit. In: Rowe DM, editor. Thermoelectrics Handbook: Macro to Nano. CRC Taylor & Francis; 2006. p. 10.1-10.8

[39] Dames C, Chen G. Thermal Conductivity of Nanostructured Thermoelectric Material. In: Rowe DM, editor. Thermoelectrics Handbook: Macro to Nano. CRC Taylor & Francis; 2006. p. 42.1-42.11

[40] Li D, Wu Y, Kim P, Yang P, Majumdar A. Thermal conductivity of individual silicon nanowires. Applied Physics Letters. 2003;**83**:2934-2936. DOI: 10.1063/1.1616981

[41] Abouelaoualim D. Size effects on nanowire phonon thermal conductivity: A numerical investigation using the Boltzmann equation. Acta Physica Polonica A. 2007;**112**:49-54

[42] Tritt TM, Subramanian MA. Thermoelectric materials, phenomena, and applications: A bird's eye view. MRS Bulletin. 2006;**31**:188-198. DOI: 10.1557/mrs2006.44

Chapter 10

Nonlinear Radiative Heat Transfer of Cu-Water Nanoparticles over an Unsteady Rotating Flow under the Influence of Particle Shape

K. Ganesh Kumar, B.J. Gireesha and S. Manjunatha

Additional information is available at the end of the chapter

http://dx.doi.org/10.5772/intechopen.74807

Abstract

A 3D study on Cu-water-rotating nanofluid over a permeable surface in the presence of nonlinear radiation is presented. Particle shape and thermophysical properties are considered in this study. The governing equations in partial forms are reduced to a system of nonlinear ordinary differential equations using suitable similarity transformations. An effective Runge-Kutta-Fehlberg fourth-fifth order method along with shooting technique is applied to attain the solution. The effects of flow parameters on the flow field and heat transfer characteristics were obtained and are tabulated. Useful discussions were carried out with the help of plotted graphs and tables. It is found that the rate of heat transfer is more enhanced in column-shaped nanoparticles when compared to tetrahedron- and sphere-shaped nanoparticles. Higher values of rotating parameter enhance the velocity profile and corresponding boundary layer thickness. It has quite the opposite behavior in angular velocity profile. Further, unsteady parameter increases the velocity profile and corresponding boundary layer thickness.

Keywords: particle shape effect, nonlinear radiation, Cu-water nanoparticles, unsteady rotating flow

1. Introduction

The interaction of thermal radiation has increased greatly during the last decade due to its importance in many practical applications. We know that the radiation effect is important under many isothermal and nonisothermal situations. If the entire system involving the polymer extrusion process is placed in a thermally controlled environment, then radiation

could become important. The knowledge of radiation heat transfer in the system can, perhaps, lead to a desired product with a sought characteristic. Magnetohydrodynamic 3D flow of viscoelastic nanofluid in the presence of nonlinear thermal radiation has been examined by Hayat et al. [1]. Shehzad et al. [2] proposed the nonlinear thermal radiation in 3D flow of Jeffrey nanofluid. Refs. [3–11] are some of the works associated with stretching sheet problem of thermal radiation.

Nanotechnology has been widely utilized in the industries since materials with the size of nanometers possess distinctive physical and chemical properties. Nanofluids are literally a homogeneous mixture of base fluid and the nanoparticles. Common base fluids embody water, organic liquids, oil and lubricants, biofluids, polymeric solution and other common liquids. Nanoparticles are created from totally different materials, like oxides, nitrides, carbide, ceramics metals, carbons in varied (e.g., diamond, graphite, carbon nanotubes, fullerene) and functionalized nanoparticles. Nanofluids have novel properties that are potentially helpful in several applications in heat transfer, as well as microelectronics, pharmaceutical processes, heat exchanger, hybrid-powered engines, domestic refrigerator, fuel cells, cooling/vehicle thermal management, nuclear reactor agent, in grinding, in space technology, ships and in boiler flue gas temperature reduction. Choi [12] was the first who composed the analysis on nanoparticles in 1995. Later, Maiga et al. [13] initiated the heat transfer enhancement by using nanofluids in forced convective flows. The laminar fluid flow which results from the stretching of a flat surface in a nanofluid has been investigated by Khan and Pop [14]. Recently, a number of researchers are concentrating on nanofluid with different geometries; see [15–19].

Experimental studies have shown that the thermal conductivity of nanofluids is determined by the parameters related to: nanoparticles, concentration, size, spherical and nonspherical shapes, agglomeration (fractal-like shapes), surface charge and thermal conductivity, base fluids (e.g., thermal conductivity and viscosity), nanofluids (e.g., temperature), the interfacial chemical/physical effect or interaction between the particles and base fluid and others. For more details, readers are referred to the studies [20–25].

Impact of nonlinear thermal radiation on 3D flow and heat transfer of Cu-water nanoliquid over unsteady rotating flow have been considered. The heat transfer characteristics are studied in the presence of different particle shapes, thermophysical properties and nonlinear thermal radiation. The principal equations of continuity, momentum, energy and mass equations are transferred into a set of nonlinear similarity equalities by applying the appropriate transformations. The condensed equalities are solved numerically, and the impacts of relevant parameters are discussed through plotted graphs and tables.

2. Mathematical formulation

An unsteady laminar flow over a permeable surface in a rotating nanofluid is considered in this study. The copper-water motion is 3D due to Coriolis force in the present problem. The Cartesian coordinates are x, y and z where the rotation of the nanofluid is at an angular velocity $\overline{\Omega}(t)$ about the z-axis, and time is denoted as t. Let $u_w(x,t) = \frac{bx}{1-\delta t}$ and $v_w(x,t)$ represent

the surface velocity in x and y directions, respectively, and $w_w(x,t)$ is the wall mass flux velocity in the z-direction as represented in **Figure 1**. Under these conditions, the governing equations can be written as:

$$\frac{\partial u}{\partial x}+\frac{\partial v}{\partial y}+\frac{\partial w}{\partial z}=0, \tag{1}$$

$$\frac{\partial u}{\partial t}+u\frac{\partial u}{\partial x}+v\frac{\partial u}{\partial y}+w\frac{\partial u}{\partial z}-2\overline{\Omega}v=-\frac{1}{\rho}\frac{\partial p}{\partial x}+\frac{\mu_{nf}}{\rho_{nf}}\frac{\partial^2 u}{\partial z^2}, \tag{2}$$

$$\frac{\partial v}{\partial t}+u\frac{\partial v}{\partial x}+v\frac{\partial v}{\partial y}+w\frac{\partial v}{\partial z}+2\overline{\Omega}v=-\frac{1}{\rho}\frac{\partial p}{\partial y}+\frac{\mu_{nf}}{\rho_{nf}}\frac{\partial^2 v}{\partial z^2}, \tag{3}$$

$$\frac{\partial w}{\partial t}+u\frac{\partial w}{\partial x}+v\frac{\partial w}{\partial y}+w\frac{\partial w}{\partial z}=-\frac{1}{\rho}\frac{\partial p}{\partial z}+\frac{\mu_{nf}}{\rho_{nf}}\frac{\partial^2 v}{\partial z^2}, \tag{4}$$

$$\frac{\partial T}{\partial t}+u\frac{\partial T}{\partial x}+v\frac{\partial T}{\partial y}+w\frac{\partial T}{\partial z}=\alpha_{nf}\frac{\partial^2 T}{\partial z^2}+\frac{1}{(\rho c_p)_{nf}}\frac{\partial q_r}{\partial z}. \tag{5}$$

Boundary conditions for the problem are,

$$\begin{aligned} &u=u_w(x,t)=v=0, w=0, T=T_w \ \text{ at } \ z=0,\\ &u\to 0, v\to 0, w=0, T\to T_\infty \ \text{ as } \ z\to\infty \end{aligned} \tag{6}$$

where velocity components in x, y and z directions are u, v and w, constant angular velocity of the Nano fluid is Ω, dynamic viscosity of the Nano fluid is μ_{nf}, density of the nanofluid is ρ_{nf}, thermal diffusivity of the nanofluid is α_{nf}, T is temperature of nanofluid and wall temperature is T_w, T_∞ denotes temperature outside the surface (**Table 1**).

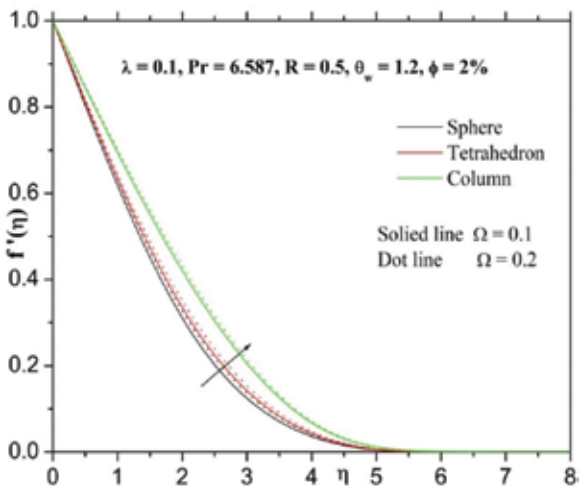

Figure 1. Influence of Ω on $f'(\eta)$.

The radiative heat flux expression in Eq. (5) is given by:

$$q_r = -\frac{16\sigma^*}{3k^*}T_\infty^3\frac{\partial T}{\partial z} \tag{7}$$

where σ^* and k^* are the Stefan-Boltzmann constant and the mean absorption coefficient, respectively, and in view to Eq. (7), Eq. (4) reduces to:

$$\frac{\partial T}{\partial t}+u\frac{\partial T}{\partial x}+v\frac{\partial T}{\partial y}+w\frac{\partial T}{\partial z}=\frac{\partial}{\partial y}\left[\left(\alpha_{nf}+\frac{16\sigma^*T_\infty^3}{3(\rho c_p)_{nf}k^*}\frac{\partial T}{\partial Z}\right)\right]\frac{\partial T}{\partial y}. \tag{8}$$

Parameters μ_{nf}, ρ_{nf} and α_{nf} are interrelated with nanoparticle volume fraction; ϕ and can be defined as:

$$\begin{aligned}&\rho_{nf}=\rho_f\left(1-\phi+\phi\left(\frac{\rho_s}{\rho_f}\right)\right),\mu_{nf}=\frac{\mu_f}{(1-\phi)^{2.5}},\alpha_{nf}=\frac{k_{nf}}{(\rho c_p)_{nf}}\\&(\rho c_p)_{nf}=(\rho c_p)_f\left(1-\phi+\phi\left(\frac{(\rho c_p)_s}{(\rho c_p)_f}\right)\right),\frac{k_{nf}}{k_f}=\frac{[k_s+(m-1)k_f]-(m-1)\phi(k_f-k_s)}{[k_s+(m-1)k_f]+\phi(k_f-k_s)}\end{aligned} \tag{9}$$

where volumetric heat capacity of the solid nanoparticles is $(\rho c_p)_s$, volumetric heat capacity of the base fluid is $(\rho c_p)_f$, volumetric heat capacity of the nanofluid is $(\rho c_p)_{nf}$, thermal conductivity of the nanofluid is k_{nf}, thermal conductivity of the base fluid is k_f, thermal conductivity of the solid nanoparticles is k_s, nanoparticle volume fraction is ϕ, density viscosity of the base fluid is ρ_f and dynamic viscosity of the base fluid is μ_f (**Table 2**).

Now, we introduce similarity transformations:

$$u=\frac{bx}{1-\delta t}f'(\eta),\ v=\frac{bx}{1-\delta t}g(\eta),\ w=-\sqrt{\frac{bx}{1-\delta t}}f(\eta),\ \eta=\sqrt{\frac{bx}{\upsilon(1-\delta t)}}z,\ \theta(\eta)=\frac{T-T_\infty}{T_w-T_\infty} \tag{10}$$

with $T=T_\infty(1+(\theta_w-1)\theta)$ and $\theta_w=\frac{T_w}{T_\infty}$, $\theta_w>1$ is the temperature ratio parameter.

	ρ	c_p	k
Copper (Cu)	385	8933	400
Water	997.1	4179	0.613

Table 1. Thermophysical properties of water and nanoparticles.

Particle shapes	**Sphere**	**Tetrahedron**	**Column**
m	3	4.0613	6.3698

Table 2. Values of the empirical shape factor for different particle shapes.

Using Eqs. (2)–(6) and (10), we can have

$$\frac{1}{(1-\phi)^{2.5}\left(1-\phi+\phi\left(\frac{\rho_s}{\rho_f}\right)\right)}f''' - \left[f'^2 - ff' - 2\Omega g + \lambda\left(\frac{\eta}{2}f'' + f'\right)\right] = 0, \tag{11}$$

$$\frac{1}{(1-\phi)^{2.5}\left(1-\phi+\phi\left(\frac{\rho_s}{\rho_f}\right)\right)}g'' - \left[f'g - fg' - 2\Omega f + \lambda\left(\frac{\eta}{2}g' + g\right)\right] = 0, \tag{12}$$

$$\frac{k_{nf}}{k_f\left(1-\phi+\phi\left(\frac{(\rho c_p)_s}{(\rho c_p)_f}\right)\right)}\left[1+R(1+(\theta_w-1)\theta)^3\theta\right] - \Pr\left[\lambda\frac{\eta}{2}\theta' - f\theta'\right] = 0, \tag{13}$$

The transformed boundary conditions are as follows:

$$\begin{aligned} &f(0) = 0, f'(0) = 1, g(0) = 0, \theta(0) = 1 \text{ at } \eta = 0 \\ &f'(\eta) \to 0, g(\eta) \to 0, \theta(\eta) \to 0 \text{ as } \eta \to \infty \end{aligned} \tag{14}$$

where $\Omega = \frac{\omega}{b}$ is rotation rate, $\lambda = \frac{\delta}{b}$ is unsteadiness parameter $R = \frac{16\sigma^* T_\infty^3}{3k_f k^*}$ is radiation parameter, $\Pr = \frac{\alpha_{nf}}{\upsilon_{nf}}$ is Prandtl number and primes denote the differentiation with respect to η.

Rosca et al. [11] mentioned that the pressure term (p) can be integrated from Eq. (4); thus, we obtain:

$$p = \upsilon\rho\frac{\partial w}{\partial z} - \frac{\rho w^2}{2} + c \tag{15}$$

The physical quantities of interest in this problem are the skin friction coefficients in x and y directions, C_{fx} and C_{fy} as well as the local Nusselt number Nu_x which are defined as:

$$C_{fx} = \frac{\tau_{wx}}{\rho u_w^2(xt)},\ C_{fy} = \frac{\tau_{wy}}{\rho u_w^2(yt)},\ Nu_x = \frac{xq_w}{k_f(T_w - T_\infty)}, \tag{16}$$

Surface shear stress τ_{wx}, τ_{wy} and surface heat flux q_w are defined as:

$$\tau_{wx} = \mu_{nf}\left(\frac{\partial u}{\partial z}\right)_{z=0}, \tau_{wy} = \mu_{nf}\left(\frac{\partial v}{\partial z}\right)_{z=0} \text{ and } q_w = -k_{nf}\left(\frac{\partial T}{\partial z}\right) + qr_{z=0} \tag{17}$$

Using Eqs. (16) and (17), we obtain

$$\sqrt{\mathrm{Re}_x}C_{fx} = \frac{1}{(1-\phi)^{2.5}}f''(0),\ \sqrt{\mathrm{Re}_x}C_{fy} = \frac{1}{(1-\phi)^{2.5}}g'(0) \text{ and } \frac{Nu_x}{\sqrt{\mathrm{Re}_x}} = \frac{k_{nf}}{k_f}\left(-\left[1+R\theta_w^3\right]\theta'(0)\right), \tag{18}$$

where $\mathrm{Re}_x = \frac{u_w x}{\upsilon}$ is local Reynolds number.

3. Numerical method

Numerical solutions of nonlinear coupled differential Eqs. (11)–(13) subject to the boundary conditions (14) constitute a two-point boundary value problem. Due to coupled and highly nonlinear nature, which are not amenable to closed-form solutions; therefore, we resorted to numerical solutions. In order to solve these equations numerically, we follow most efficient fourth-fifth order Runge-Kutta-Fehlberg integration scheme along with shooting technique. In this method, it is most important to choose the appropriate finite values of η_∞. The asymptotic boundary conditions at η_∞ were replaced by those at η_8 in accordance with standard practice in the boundary layer analysis.

4. Result and discussion

To get a clear insight into the physical situation of the present problem, numerical values for velocity and temperature profile are computed for different values of dimensionless parameters using the method described in the previous section. The numerical results for the local Nusselt number are presented for different values of the governing parameters in **Table 3**.

λ	Ω	Pr	R	θ_w	ϕ.	Nusselt number		
						$m = 3$	$m = 4.0613$	$m = 6.3698$
0.2						0.36722	0.35144	0.32983
0.3						0.29671	0.29256	0.28353
0.4						0.21897	0.22635	0.23028
	0.01					0.33069	0.32112	0.30611
	0.02					0.29005	0.28739	0.27973
	0.03					0.24936	0.25364	0.25333
		5.776				0.35865	0.34247	0.32053
		6.587				0.36722	0.35151	0.32990
		7.578				0.37598	0.36090	0.33978
			0.5			0.36722	0.35144	0.32983
			1			0.33266	0.31642	0.29491
			1.5			0.30957	0.29332	0.27217
				1.2		0.36722	0.35144	0.32983
				1.4		0.32565	0.31078	0.29076
				1.6		0.28807	0.27416	0.25572
					1%	0.43665	0.42492	0.40752
					2%	0.36722	0.35144	0.32983
					3%	0.30841	0.29212	0.27084

Table 3. Numerical values of Nusselt number for different physical parameters.

Figure 1 portrays the effect of Ω on velocity profile $f'(\eta)$. The velocity profile and corresponding thickness of the boundary layer enhance with larger values of Ω. This is because the larger value of Ω parameter leads to higher rotation rate as compared to stretching rate. Therefore, the larger rotation effect enhances velocity field. **Figure 2** shows the impact of Ω on angular profile $g(\eta)$. From this figure, one can see that $g(\eta)$ reduces for larger values of Ω. Further, it is noticed that rate of heat transfer is larger in column-shaped nanoparticles when compared to tetrahedron- and sphere-shaped nanoparticles.

Figures 3 and **4** depict the effect of λ on the $f'(\eta)$ and $g(\eta)$ profile. It is clear from both the figures that an increase in λ decreases the momentum boundary layer thickness resulting in velocity decrease. It is also noted that $g(\eta)$ decreases smoothly with the increase in the

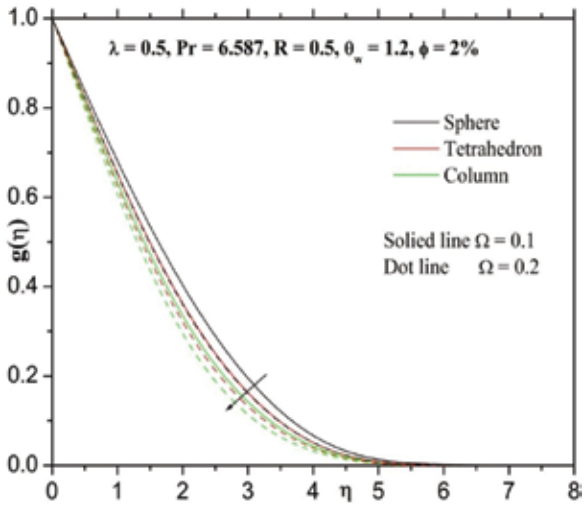

Figure 2. Influence of Ω on $g(\eta)$.

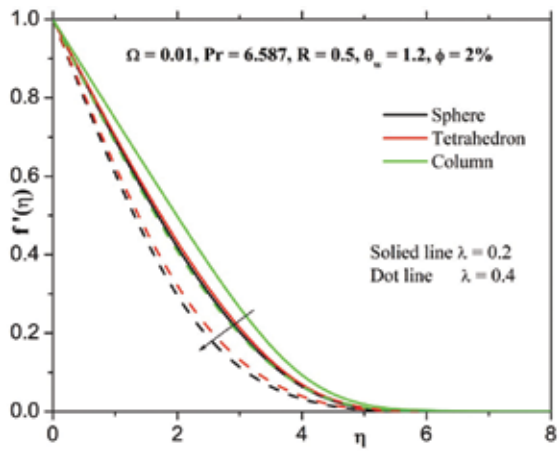

Figure 3. Influence of λ on $f'(\eta)$.

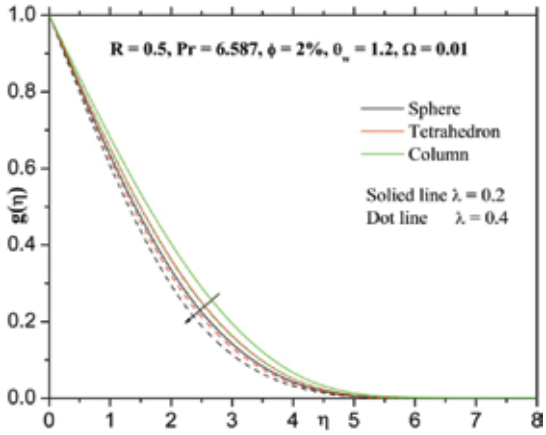

Figure 4. Influence of λ on $g(\eta)$.

unsteadiness parameter. This shows an important fact that the rate of cooling is much faster for higher values of λ, whereas it may take a longer time in steady flows.

Influence of the solid volume fraction parameter (ϕ) on temperature profiles $\theta(\eta)$ can be visualized in **Figure 5**. It is observed that the temperature profile increases by increasing values of the solid volume fraction parameter. This is due to the fact that the volume occupied by the dust particles per unit volume of mixture is higher so that it raises the rate of heat transfer. It was noticed that the development in the temperature profiles of column-shaped nanoparticles is high when compared to temperature profiles of sphere- and tetrahedron-shaped nanoparticles due to the increase in volume fraction of nanoparticles.

The effect of temperature ratio parameter (θ_w) on temperature profile is shown in **Figure 6**. The influence of temperature ratio parameter enriches the temperature profile and corresponding boundary layer thickness. This may happen due to the fact that the fluid temperature is much

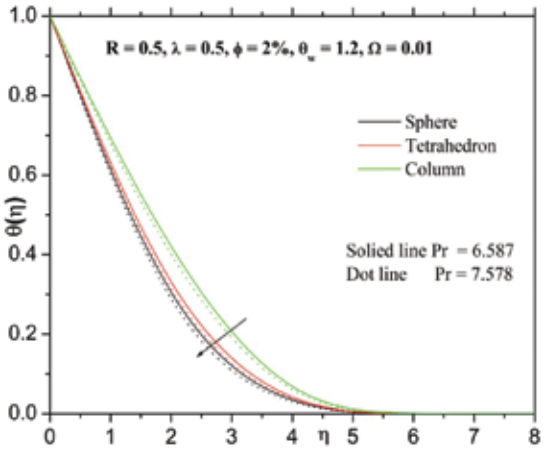

Figure 5. Influence of Pr on $\theta(\eta)$.

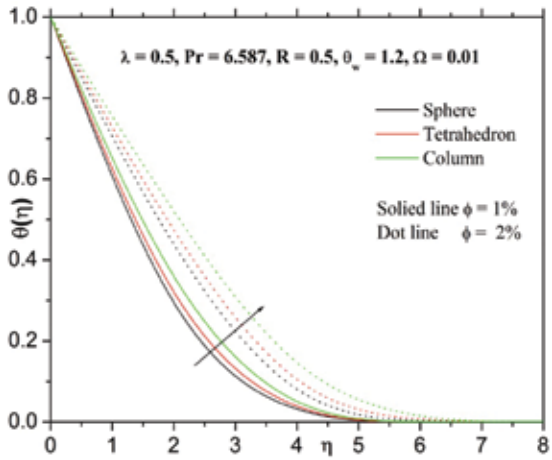

Figure 6. Influence of ϕ on $\theta(\eta)$.

higher than the ambient temperature for increasing values of θ_w, which increases the thermal state of the fluid. It is also observed that the rate of heat transfer is higher in the column-shaped nanoparticles than that of tetrahedron- and sphere-shaped nanoparticles.

Figure 7 demonstrates the effect of the Prandtl number (Pr) on temperature profiles of $\theta(\eta)$. The above mentioned graph elucidate that the temperature profile and corresponding thermal boundary layer thickness decrease rapidly with increasing values of Pr. Physically, the Prandtl number is the ratio of momentum diffusivity to thermal diffusivity. In fact, the larger Prandtl number means that the lower thermal diffusivity. A decrease in the thermal diffusivity leads to a decrease in the temperature and its associated boundary layer thickness.

The temperature distribution $\theta(\eta)$ for various values of radiation parameter (R) is shown in **Figure 8**. This figure reveals that the larger values of radiation parameter increase the temperature profile and thermal boundary layer thickness. Generally, higher values of

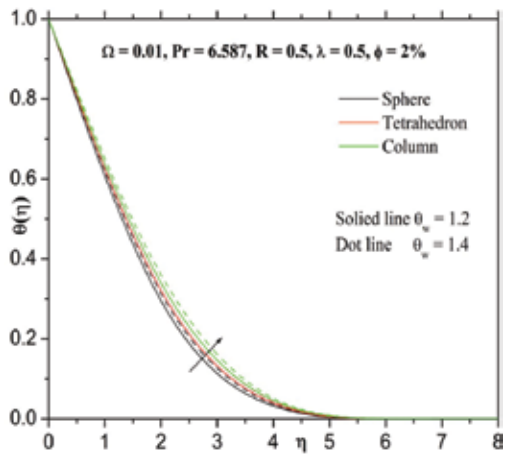

Figure 7. Influence of θ_w on $\theta(\eta)$.

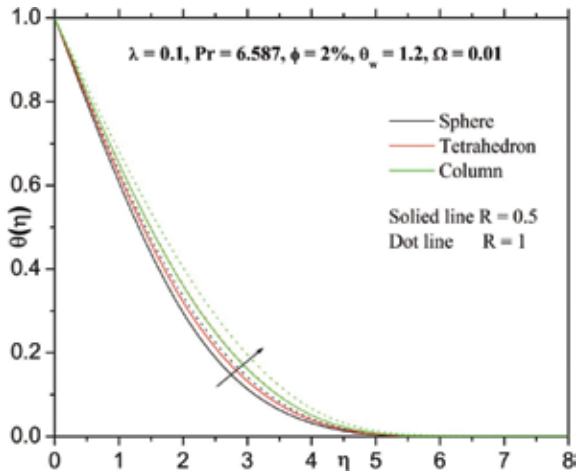

Figure 8. Influence of R on $\theta(\eta)$.

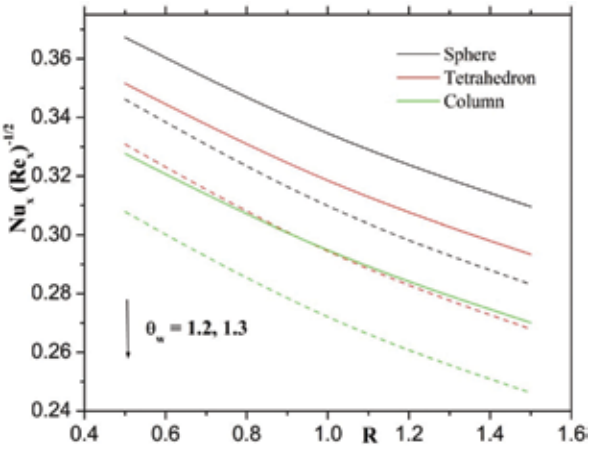

Figure 9. Influence of θ_w and R on Nusselt number.

radiation parameter produce additional heat to the operating fluid that shows associate enhancement within the temperature field. We have noticed an improvement within the temperature profile because of increase in the radiation parameter. Moreover, the rate of heat transfer at the wall is less in case of the sphere-shaped particles when compared to the tetrahedron- and column-shaped nanoparticles.

Figure 9 shows the effect of θ_w and R on the skin friction coefficient. Here, we observed that the skin friction coefficient decreases for larger values of θ_w and R. **Figure 10** delineates the influence of ϕ and Ec on Nusselt number. One can observe from the figure that Nusselt number decreases for larger values of ϕ and Ec. It is also perceived from these figures that the maximum decrease in the rate of heat transfer of nanofluid is motivated by the column-shaped, followed by

http://dx.doi.org/10.5772/intechopen.74807

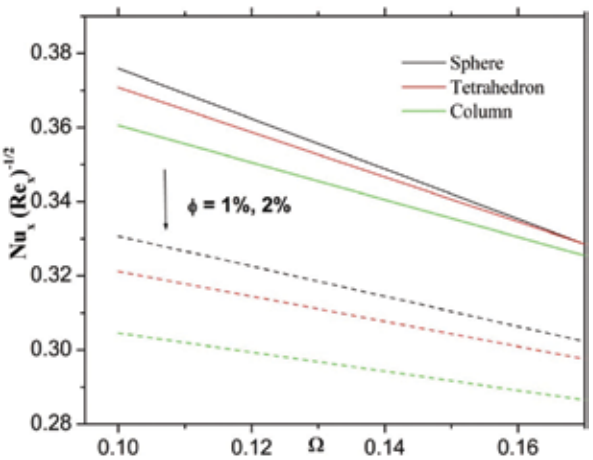

Figure 10. Influence of ϕ and Ω on Nusselt number.

tetrahedron- and sphere-shaped nanoparticles, respectively. It is just because of the nanofluid which contains column-shaped nanoparticles having maximum thermal conductivity than nanofluids containing tetrahedron- and sphere-shaped nanoparticles. **Table 3** presents the numerical values of Nusselt number for various values physical parameter values. It is observed that Nusselt number increases with increasing Pr. Further, from **Table 3**, we observe that Nusselt number decreases with increasing values of θ_w, R, ϕ and λ.

5. Conclusions

In the present analysis, impact nonlinear radiative heat transfer of Cu-water nanoparticles over an unsteady rotating flow under the influence of particle shape is considered. Effects of various parameters are studied graphically. The main points of the present simulations are listed as follows:

- The highlight of this study is that temperature profile is more enhanced in column-shaped nanoparticles when compared to tetrahedron- and sphere-shaped nanoparticles.
- Temperature profile and thermal boundary layer thickness increase with increasing values of R and θ_w.
- The thermal boundary layer thickness and temperature profile enhance with increasing values of ϕ.
- Higher values of rotating parameter enhance the velocity profile and corresponding boundary layer thickness. It has quite opposite behavior in angular velocity profile.
- Unsteady parameter increases the velocity profile and corresponding boundary layer thickness.

Author details

K. Ganesh Kumar[1], B.J. Gireesha[1] and S. Manjunatha[2]*

*Address all correspondence to: manjubhushana@gmail.com

1 Department of Studies and Research in Mathematics, Kuvempu University, Shimoga, Karnataka, India

2 Department of Engineering Mathematics, Faculty of Engineering, Christ University, Bengaluru, India

References

[1] Hayat T, Muhammad T, Alsaedi A, Alhuthali MS. Magnetohydrodynamic three-dimensional flow of viscoelastic nanofluid in the presence of nonlinear thermal radiation. Journal of Magnetism and Magnetic Materials. 2015;**385**:222-229

[2] Shehzad SA, Hayat T, Alsaedi A, Mustafa AO. Nonlinear thermal radiation in three-dimensional flow of Jeffrey nanofluid: A model for solar energy. Applied Mathematics and Computation. 2014;**248**:273-286

[3] Mustafa M, Mushtaq A, Hayat T, Alsaedi A. Radiation effects in three-dimensional flow over a bi-directional exponentially stretching sheet. Journal of the Taiwan Institute of Chemical Engineers. 2015;**47**:43-49

[4] Kafoussias NG, Williams EW. Thermal-diffusion and diffusion-thermo effects on mixed free-forced convective and mass transfer boundary layer flow with temperature dependent viscosity. International Journal of Engineering Science. 1995;**33**(9):1369-1384

[5] Srinivasacharya D, Kaladhar K. Mixed convection flow of couple stress fluid in a non-darcy porous medium with Soret and Dufour effects. Journal of Applied Science and Engineering. 2012;**15**:415-422

[6] Rudraswamy NG, Kumar KG, Gireesha BJ, Gorla RSR. Soret and Dufour effects in three-dimensional flow of Jeffery nanofluid in the presence of nonlinear thermal radiation. Journal of Nanoengineering and Nanomanufacturing. 2017;**6**(4):278-287

[7] Kumar KG, Rudraswamy NG, Gireesha BJ, Krishnamurthy MR. Influence of nonlinear thermal radiation and viscous dissipation on three-dimensional flow of Jeffrey nano fluid over a stretching sheet in the presence of joule heating. Nonlinear Engineering. 2017;**6**(3): 207-219

[8] Kumar KG, Gireesha BJ, Manjunatha S, Rudraswamy NG. Effect of nonlinear thermal radiation on double-diffusive mixed convection boundary layer flow of viscoelastic nanofluid over a stretching sheet. International Journal of Mechanical and Materials Engineering. 2017;**12**(1):18

[9] Kumar KG, Rudraswamy NG, Gireesha BJ, Manjunatha S. Nonlinear thermal radiation effect on Williamson fluid with particle-liquid suspension past a stretching surface. Results in Physics. 2017;**7**:3196-3202

[10] Makinde OD, Kumar KG, Manjunatha S, Gireesha BJ. Effect of nonlinear thermal radiation on MHD boundary layer flow and melting heat transfer of micro-polar fluid over a stretching surface with fluid particles suspension. Defect and Diffusion Forum. 2017;**378**: 125-136

[11] Rosca NC, Pop I. Mixed convection stagnation point flow past a vertical flat plate with a second order slip: Heat flux case. International Journal of Heat and Mass Transfer. 2013; **65**:102-109

[12] Choi CUS. Enhancing thermal conductivity of fluids with nanoparticles. Siginer DA, Wang HP, editors. Development and Applications of Non-Newtonian Flows. Vol. 231. MD: ASME; 1995. pp. 99-10

[13] Maiga SEB, Palm SJ, Nguyen CT, Roy G, Galanis N. Heat transfer enhancement by using nanofluids in forced convection flows. International Journal of Heat and Fluid Flow. 2005; **26**:530-546

[14] Khan W, Pop I. Boundary-layer flow of a nanofluid past a stretching sheet. International Journal of Heat and Fluid Flow. 2010;**53**(11–12):2477-2483

[15] Rudraswamy NG, Shehzad SA, Ganesh Kumar KG, Gireesha BJ. Numerical analysis of MHD three-dimensional Carreau nanoliquid flow over bidirectionally moving surface. Journal of the Brazilian Society of Mechanical Sciences and Engineering. 2017;**39**(12):5037-5047

[16] Kumar KG, Gireesha BJ, Prasannakumara BC, Ramesh GK, Makinde OD. Phenomenon of radiation and viscous dissipation on Casson nanoliquid flow past a moving melting surface. Diffusion Foundations. 2017;**11**:33-42

[17] Kumar KG, Ramesh GK, Gireesha BJ, Gorla RSR. Characteristics of Joule heating and viscous dissipation on three-dimensional flow of Oldroyd B nanofluid with thermal radiation. Alexandria Engineering Journal. 2017. DOI: 10.1016/j.aej.2017.06.006

[18] Prasannakumara BC, Gireesha BJ, Krishnamurthy MR, Kumar KG. MHD flow and nonlinear radiative heat transfer of Sisko nanofluid over a nonlinear stretching sheet. Informatics in Medicine Unlocked. 2017;**9**:123-132

[19] Kumar KG, Gireesha BJ, Prasannakumara BC, Makinde OD. Impact of chemical reaction on marangoni boundary layer flow of a Casson nano liquid in the presence of uniform heat source sink. Diffusion Foundations. 2017;**11**:22-32

[20] Ellahi R, Zeeshan A, Hassan M. Shape effects of nanosize particles in Cu-H_2O nanofluid on entropy generation. International Journal of Heat and Mass Transfer. 2015;**81**:449-456

[21] Ghosh MM, Ghosh S, Pabi SK. Effects of particle shape and fluid temperature on heat-transfer characteristics of nanofluids. Journal of Materials Engineering and Performance. 2013;**22**(6):1525-1529

[22] Jeong J, Li C, Kwon Y, Lee J, Kim SH, Yun R. Particle shape effect on the viscosity and thermal conductivity of ZnO nanofluids. International Journal of Refrigeration. 2013; **36**(8):2233-2241

[23] Timofeeva EV, Routbort JL, Singh D. Particle shape effects on thermophysical properties of alumina nanofluids. Journal of Applied Physics. 2009;**106**(1):014304-1-014304-10

[24] Ji Y, Wilson C, Chen H, Ma H. Particle shape effect on heat transfer performance in an oscillating heat pipe. Nanoscale Research Letters. 2011;**6**:296

[25] Sheikholeslami M, Gorji-Bandpay M, Ganji DD. Investigation of nanofluid flow and heat transfer in presence of magnetic field using KKL model. Arabian Journal for Science and Engineering. 2014;**39**(6):5007-5016

Chapter 11

Thermal Conductivity of Graphite-Based Polymer Composites

Teboho Clement Mokhena,
Mokgaotsa Jonas Mochane, Jeremia Shale Sefadi,
Setumo Victor Motloung and
Dickson Mubera Andala

Additional information is available at the end of the chapter

http://dx.doi.org/10.5772/intechopen.75676

Abstract

It is well known that polymers are insulators, which limit their usage in other applications where thermal conductivity is essential for heat to be efficiently dissipated or stored. In the past, the improvement in the thermal conductivity of polym.rs with conductive fillers has been investigated by researchers. Carbon-based materials such as graphite, graphene and carbon nanotube, which feature excellent properties such as a high mechanical strength, a high thermal conductivity and a tailorable electronic configuration, have been added to different polymer matrices to enhance their thermal conductivity. Amongst others, graphite more especially expanded graphite merits special interest because of its abundant availability at a relatively low cost and lightweight when compared to other carbon allotropes. Herein, we describe the thermal conductivity of polymer/graphite composites and their applications.

Keywords: polymer, graphite composites, thermal conductivity, functionalization, applications

1. Introduction

Polymers can be moulded into various shapes and forms which afford their application in different fields [1–3]. This is owing to their unique properties such as lightweight, durability and low production cost. Polymers have substituted natural materials (e.g. steel and glass) in most of their former uses [1–3]. Besides these unique features, their success in certain applications

is hindered by their poor electrical, thermal and mechanical properties. The incorporation of different fillers has been subject to researchers and scientists as a suitable solution to overcome these limitations. However, the resulting composite properties were found to be directly dependent on several aspects such as matrix-type, filler-type, interaction between the filler and polymer as well as the distribution of the filler within the polymeric matrix [4].

Research has escalated on the use of conductive fillers to improve not only the electrical and thermal conductivities but also the overall physical properties of the resulting composite product. Different conductive fillers such as metal powder, carbon black, carbon nanotubes (CNTs) and natural graphite were employed as reinforcing fillers of various polymeric materials [5, 6]. Amongst all these fillers, graphite garnered in much interest owing to its unique properties such as abundant availability, low cost and easy functionalization [7].

The polymer/graphite composites exhibited a high thermal conductivity and an electrical conductivity at a fairly low concentration. Polymer/graphite composites have been used in many applications including structural, aerospace and sporting goods. Most recently, researchers have focused their attention on the development of polymer/graphite composites for applications whereby thermal conductivity is needed [8, 9]. It is documented [7] in the study that the significance of thermal conductivity and/or thermal diffusivity in polymer composites is related to the need for considerable levels of thermal conductivity in circuit boards and heat exchangers. According to the studies [10], conductive composites are frequently used in wide applications such as heating elements, temperature-dependent sensors, self-limiting electrical heaters, switching devices, antistatic materials for electromagnetic interferences and shielding of electronic devices. This chapter reviews recent development on the thermal conductivity of polymer/graphite composites.

2. Graphite

Graphite is a carbon-based layered material whose structure is composed of successive layers of graphene sheets (carbon) and received much interest owing to its exceptional thermal, mechanical and electrical properties [5, 11, 12]. It is thermodynamically stable and soft with the successive layers being parallel to the base plane. The layers are bonded together by van der Waals forces. Graphite consists of carbons that are hexagonally bound to each other by covalent bonds with an interatomic separation of 0.142 nm and an interlayer separation of 0.335 nm. It is sp^2-hybridized with three of four valence electrons of hexagonally attached carbons that are linked to the valence electrons of the neighbouring carbon by σ-bonding. Therefore, the fourth electron resonates freely within the graphene layer but it is no longer interacting with a specific carbon atom. Van der Waals forces acting between adjacent graphene layers result from the delocalization of π-electrons. Thus, the interatomic interaction within the single graphene layer is stronger, that is, 75 times when compared to the interaction between the adjacent layers [11]. Hence, there has been much graphite modification that takes place in between the layers in order to improve its dispersion in different polymeric materials. Graphite can be classified into two types: natural and synthetic graphite as shown in **Figure 1**.

http://dx.doi.org/10.5772/intechopen.75676

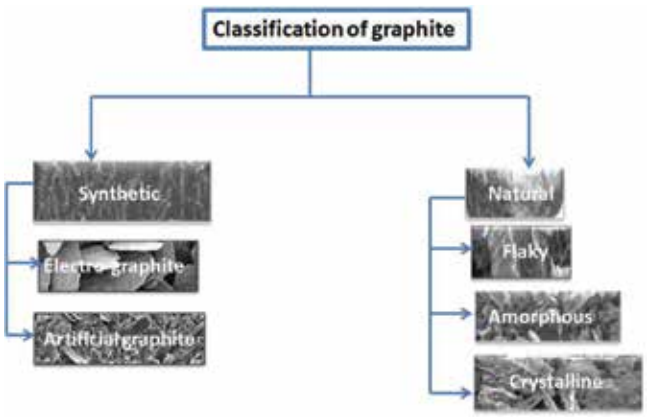

Figure 1. Schematic representation of graphite classification.

2.1. Natural graphite

Naturally occurring abundant graphite is classified into three categories depending on the geological environment, that is, amorphous, flake and highly crystalline [11]. Amorphous graphite has a content of graphite ranging from 25 to 85% depending on the geological conditions. It is usually derived from mesomorphic environment such as shale, slate and coal. Amorphous graphite is regarded as the less pure form of graphite with lack of considerable ordering and presence of microcrystalline structure. It has been applied in different applications where graphite is often utilized; however, its utilization depends on the degree of purity. Flake graphite is formed in either metamorphic or igneous geologic environments. It is obtained through froth floatation which results in 80–90% graphite. Flake graphite is less abundant as compared to amorphous graphite and has good electrical properties. It has been employed in various applications of graphite such as secondary steel manufacture, lubricants, pencils, powder metallurgy and coatings. Despite being found almost all over the world, crystalline (Vein/lump) graphite is commercially mined in Sri Lanka. It originates from crude oil deposits that through time, temperature and pressure were converted to graphite. As reflected by its name, it has a higher degree of crystallinity due to its direct deposition from a high-temperature fluid phase and its purity is more than 90%. Thus, it has good electrical and thermal conductivity. Vein graphite enjoyed its success in different applications such as batteries, lubricants, grinding wheels and powder metallurgy.

2.2. Synthetic graphite

Synthetic graphite is produced by treating carbonaceous precursors such as coal, petroleum and synthetic or natural organic chemicals in inert atmosphere to temperatures above 2400°C as well as thermal treatment of nongraphitic carbons, graphitization or chemical vapour deposition (CVD) from hydrocarbons under temperatures of 1883°C [11]. High temperatures are often employed to facilitate solid-state phase transition effect in order to produce graphite

crystals. The production method is the primary factor that influences the resulting graphite properties. Synthetic graphite can also be categorized into two, that is, electro-graphite and artificial graphite. Electro-graphite is a pure carbon-shaped graphite produced from coal tar pitch and calcined petroleum pitch in the electric furnace, while artificial graphite results from the thermal treatment of calcined petroleum pitch at 2800°C. In general, the synthetic graphite has a low density, a high electrical resistance and porosity. Synthetic graphite is employed in different applications such as energy storage, carbon brushes and aerospace. Further modifications are often not required for its application in various fields. To avoid confusion, graphite will be used in this document without discriminate, whether it is synthetic or natural-based.

3. Modification of graphite

Modification of graphite has been subject of research in order to afford interaction with large polymer molecules and to achieve a better graphite dispersion [5, 11]. Many efforts have been done to overcome the absence of functional groups on the surface of graphite (or graphene sheets) and space between the sheets. There are three classic forms of modified graphite, that is, graphite-intercalated compounds (GICs), graphene oxide (graphite oxide (GO)) and expanded graphite (EG).

Graphite-intercalated compounds (*GICs*): GICs result from the insertion of atomic or molecular layers of different chemical species called intercalant between graphene sheets of the host graphite material [5, 12–14]. GIC can be categorized into two depending on the character of their bonding, that is, covalent GICs and ionic GICs. Covalent GICs include graphite oxide (GO), carbon monofluoride and tetracarbon monofluoride, whereas ionic GICs include graphite salts, graphite-alkali-metal compounds, graphite-halogen compounds and graphite-metal chloride compounds. Ionic GICs received much interest due to the capability of changing the electronic properties of graphite. The latter result in the presence of π-bonds in graphite that can accept/donate electrons from/to the intercalation. Further classification of ionic GICs depends on the staging of the GIC which is associated with the number of graphite layers between each intercalant layer. In the first stage (stage 1), the intercalant and graphite layers are alternating in which one layer of graphite is separated by one layer of intercalant. In a stage 2 GIC, there are two adjacent layers of graphite sheets between each intercalant layer. The intercalation of graphite results in increasing its interlayer spacing, weakening the interlayer interactions. The latter facilitate the exfoliation of the GICs by mechanical or thermal treatments.

Graphite oxide (*GO*): GOs are known as pseudo-two dimensional solid materials with covalent between the layers. Graphite oxide is often prepared by heat treatment of graphite flakes with oxidizing agents such that polar groups are introduced on the graphite surface [5, 15, 16]. This treatment also widens the interlayer spacing between the graphene sheets.

Expanded graphite (*EG*): The exposure of intercalated graphite to thermal treatment beyond critical temperature or microwave radiation leads to a large expansion of graphite flakes along the *c*-axis than in-plane direction as shown in **Figure 2**. The resulting material, which is known

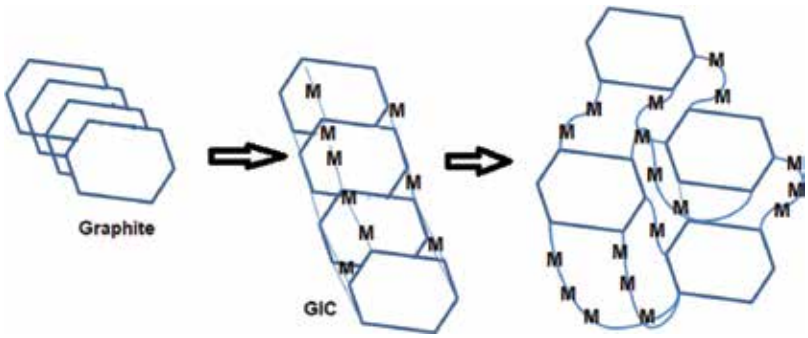

Figure 2. Schematic presentation of the preparation of expanded graphite (EG).

as expanded graphite (EG), has a vermicular or a worm-like structure with a low density, a high-temperature resistance and a high conductivity [6, 17, 18]. A mixture of sulphuric acid and nitric acid is usually employed for graphite intercalation followed by heat or microwave treatment to produce expanded graphite [5, 19].

Graphene: Graphene is a monolayer of sp^2-hybridized carbon atoms arranged in a two-dimensional lattice. It has been produced using different methods such as growth by chemical vapour deposition (both of discrete monolayers onto substrate and agglomerated powders), micro-mechanical exfoliation of graphite, and growth on crystalline silicon carbide [5]. These methods afford defect-free material with excellent physical properties; however, the yield is not large enough for use as a composite filler. The thermal conductivity of graphene ranges between 600 and 5000 W m^{-1} K^{-1} with Young modulus of 1 TPa and a tensile strength of 130 GPa [20].

4. Graphite composites

In order to broaden the applications of polymers, the incorporation of a suitable filler with required functionality is the most cost-effective and reliable method [17]. Some of the polymers fall short when it comes to electrical, thermal and mechanical as compared to ceramics and steel. However, the unique properties of polymers such as lightweight and mouldability into different shapes make them suitable candidates for various applications. Amongst other fillers, graphite features unique properties such as a high thermal and electrical conductivity, a low coefficient of thermal expansion, an exceptional thermal resistance, a high thermal shock resistance, improved stiffness and an increased strength. It is abundantly available and easily functionalized to afford various applications. The thermal conductivity of the graphite and/or its composites is of significant importance considering the demands as thermal conductance in heat exchangers, circuit boards, machinery, electronic appliances and many other applications as explained in Section 1.

4.1. Preparation of graphite composites

Beside the modification of graphite, the major contributor to the distribution of graphite in the polymeric matrix relies on the selected preparation method. Classic preparation methods for graphite/polymer composites are *in situ* polymerization, melt intercalation and solution-casting techniques [21–24]. Complete dispersion of the graphite particles leads to poor thermal conductivity due to lack of conductive network path within the composite product. **Figure 3** shows a schematic presentation of the resulting morphologies depending on the preparation method.

4.1.1. In situ polymerization

In situ polymerization involves the polymerization of monomer (or/and oligomer) in the presence of the filler [6, 21, 24–26]. This method is one of the most effective processes to facilitate the dispersion of the filler in the polymeric material. Moreover, it enhances strong interaction between the composite component; hence, the mechanical properties of the resulting composite are superior to the composite prepared by either solution casting or melt intercalation [25]. This technique, however, is associated with some limitations such as polymer and filler selection and limited to laboratory scale. Moreover, it is environmentally unfriendly process which makes it not feasible for composite preparation.

4.1.2. Solution casting

In solution casting, the polymer is dissolved in suitable solvents and then the filler is added into the polymer solution [22, 27]. In order to improve the dispersion of the fillers, the sonication step is usually adopted [27, 28]. Some polymers are, however, not soluble in most available solvents which then limit the choice of a polymer for this technique. This process is not environmentally friendly due to the fact that the solvent has to be evaporated from the system which can be harmful except if the solvent is water. For industrial production, this technique will be expensive with regard to the recovery of the solvent used. Nevertheless, the mechanical

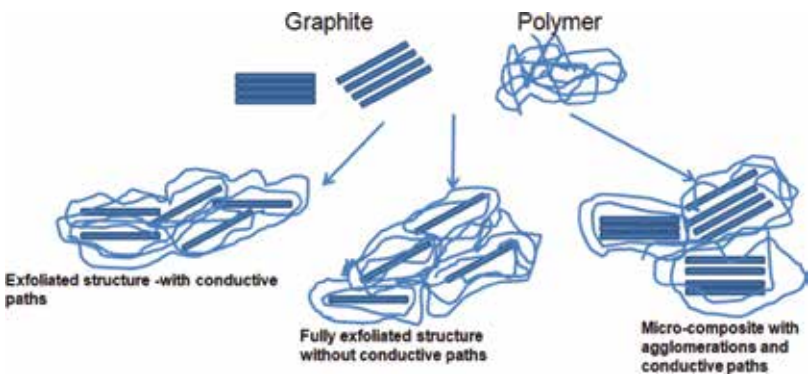

Figure 3. Different types of composites arising from and interaction between the host polymer and graphite layers obtained from different preparation methods.

properties of the resulting composites are superior to melt intercalation due to the sufficient time given for the filler to interact with each other as well as the polymeric matrix. A comparison between solution casting as well as solution casting followed by melt pressing was conducted by Bai et al. [22]. It was reported that solution-casted samples had high ability to form the percolated filler network as compared to solution casting followed by melt pressing. The percolation network is essential for the conduction paths within the composite material. However, the appropriate solvent can be chosen to avoid the formation of micro-voids within the composite [29]. The solution casting followed by hot pressing serves as a good procedure to eradicate the voids within the composite material [29].

4.1.3. Melt intercalation

Melt intercalation is the most favourable process with regard to industrial and environmental perspectives [23, 30, 31]. Polymer and filler are mixed together in the melt-compounding technique which leads to exposure to high shear and heat. The mixture is heated to a temperature above the melting temperature of the polymer for certain period to allow homogeneity. Classic compounding techniques include a single-screw extruder, a twin-screw extruder and an internal mixer. All these techniques can be utilized alone or in combination to afford better dispersion of the fillers. Injection moulding and/or melt pressing are usually used to mould the composite for characterization. In general, the percolation threshold is little bit higher than the other processing techniques, that is, solution casting and in situ polymerization [30]. Interestingly, the balance between the mechanical properties and other properties such as electrical conductivity can be achieved through this method which is of significance towards the commercialization of the resulting composite products. Its limitations involve the choice of polymer/filler, limited filler distribution and thermal degradation of the host polymer [23]. The properties of the polymer such as molecular weight, viscosity and chain length play a major role on the properties of the resulting composite product, hence influencing conclusions reached by different authors [11].

4.1.4. Other processing techniques

The combination of solution casting followed by melt intercalation/pressing has also been reported [28, 32, 33]. The main was to ensure the interaction between the fillers in order to promote the conductance path network within the host matrix. On the other hand, electrospun graphite composites were also reported in the study [34]. Despite the advantages associated with these techniques, *viz*. cost-effective, possibility of scaling up, control over the morphology of the resulting fibres and almost all polymers can be processed, there are only few studies based on the electrospun graphite composites [34, 35]. In situ melt mixing was carried out by mixing low-temperature expendable graphite with LDPE [36]. The expandable graphite expanded during the mixing process which is of significant importance considering the contact between the graphite particles. It is, however, recognized that such a process can lead to a large number of agglomeration with an increase in the filler's content. In the case of adhesive resins (e.g. epoxy resin), curing at a certain temperature over a certain period is usually utilized to prepare the composite products [37, 38].

5. Thermal conductivity

5.1. Graphite composites

Numerous researchers studied the thermal conductivity of polymer composites with regard to their importance to reach appreciable levels of thermal conductance in circuit boards, heat exchangers, appliances and machinery as summarized in **Table 1** [7, 17, 39]. Amongst all thermal conductive fillers, graphite merits special interest not only due to its high thermal conductivity, that is, 25–470 W m^{-1} K^{-1}, but high thermal stability, exceptional chemical resistance and mechanical properties [40]. A comparative study of the thermal conductivity between graphite and other conductive fillers (*viz*. copper powder (Cu), aluminium powder (Al), silver powder (Ag), zinc oxide (ZnO), boron nitride (BN), aluminium oxide (Al_2O_3) and diamond) particles was done by Fu et al. [37]. It was reported that the highest thermal conductivity was obtained at the filling load of 44.3 wt% of graphite due to the layered structure of graphite forming heat pathways within the matrix. The thermal conductivities of diamond (29.14%), Cu (68.25%), Al (69.69%), Al_2O_3 (67%) and BN (35.5%) were 0.35, 0.74, 1.11, 0.57 and 0.59 W m^{-1} K^{-1}, respectively. Although the resulting thermal conductivities were not true reflection of the thermal conductivity of the particles, this was related to the different structural arrangement within the particles which controls the contact between them. The

System	Maximum particle content	Preparation method	Thermal conductivity (W m^{-1} K^{-1})	Refs.
LDPE/graphite	10 vol.%	Melt mixing	6.5	[39]
HDPE/graphite	7%	Melt mixing	1.59	[40]
LDPE/low-temperature expandable graphite	50 wt%	Melt mixing followed by pan milling and dilution with neat LDPE	5.04	[51]
LDPE/untreated low-temperature expandable graphite	50 wt%	Melt mixing	7.02	[51]
LDPE/low-temperature expandable graphite (LTEG)	37 vol% (60 wt%)	Melt mixing	11.24	[36]
Ethylene vinyl acetate/natural graphite	7.5	Melt mixing	~0.29	[52]
Ethylene vinyl acetate/expanded graphite (EG)	7.5	Melt mixing	~0.31	[52]
Ethylene vinyl acetate/expanded graphite (EG)	4 phr	Solution casting followed by melt pressing	0.87	[33]
Ethylene vinyl acetate/natural graphite (NG)	4 phr	Solution casting followed by melt pressing	0.48	[33]
Epoxy resin/graphite	44.3 wt%	Oven curing	1.68	[37]
Epoxy resin/graphite	4.5 wt%	Oven curing	1.0	[38]
Epoxy resin/graphite	2 wt%	Oven curing	1.0	[50]

Table 1. Selected studies based on the thermal conductivity of graphite composites.

graphite being a cheaper material performed better than other expensive conductive particles. In general, the thermal conductivity increases almost linearly with an increase in graphite content, regardless of processing method as shown in **Figure 1** [39–43]. This can be attributed to the high thermal conductivity of the graphite when compared to pristine polymeric matrix.

Mu and Feng [41] prepared graphite/silicone rubber composites using solution-casting and melt-mixing processing techniques. They reported that the thermal conductivity increased with an increase in graphite content; however, solution-casted composites had a high conductivity as compared to melt-mixed ones. The authors reported that the thermal conductivity of solution-casted composites reached a value of 0.32 W m^{-1} K^{-1} at 9 per hundred rubber (phr) of graphite, whereas for melt-mixed it was only 0.24 W m^{-1} K^{-1}, which is the conductivity level similar to solution-casted composite at 4 phr. This was attributed to the conducting path networks created by contact between the graphite layers at a fairly low content in the case of solution casting compared to the reduction of surface-to-volume ratio in the case of melt mixing as shown in **Figure 4**. The latter resulted in a higher content of graphite required so that they can abut or contact in order to form the conducting paths. A comparison between two commercial graphite (EG-10, synthetic graphite, SGL Carbon, UK, and KS-15, synthetic graphite, Lonza, Switzerland) in two different polymeric matrices (high-density polyethylene (HDPE) and polystyrene (PS)) was conducted by Krupa and Chodák [7]. They reported a nonlinear increase of thermal conductivity with an increase in graphite content regardless of matrix and graphite type. It was, however, reported that the graphite KS displayed higher thermal conductivities than the thermal conductivities of EG-filled material especially for PS composites at a higher graphite content. The graphite KS had smaller particles with a narrow particle size distribution as well as a higher specific surface than graphite EG which corroborate the fact that the size of the particles did not influence the thermal conductivity, however, the contact between the graphite particles even if they are agglomerated. In another study, it was reported that the crystallinity of the polymer also plays a major role on the thermal conductivity of the resulting composite product [44]. It was reported that high-density polyethylene (HDPE)-based composites displayed high thermal conductivities over the whole graphite composition as compared to less crystalline low-density polyethylene (LDPE). Similarly, Deng et al. investigated the effect of chain structure on the thermal conductivity of expanded graphite/polymer composites [45]. Expanded graphite (EG) was blended with three different polymers, that is, polyphenylene sulphide (PPS), syndiotactic polystyrene (sPS) and amorphous polystyrene (aPS). The thermal conductivities of the neat aPS, sPS and PPS

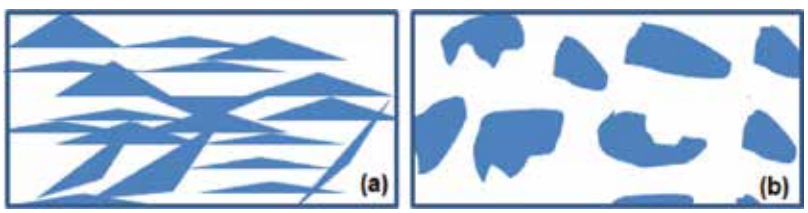

Figure 4. Schematic presentation of the proposed mechanism for thermal conductive paths for (a) solution-casted and (b) melt-mixed samples.

samples were reported as 0.18, 0.23 and 0.24, respectively. This was ascribed to the crystallinity of polymers. Similar result of observation was reported elsewhere in the study [46, 47]. The EG/PPS composites showed the highest thermal conductivity throughout the whole range in comparison to the two counterpart composites (**Figure 5**). The observed behaviour was attributed to the difference in polymer matrices with varied chain structures which may result in different crystallizations and interactions of composites.

Sefadi et al. [48] studied the influence of graphite treatment with sodium dodecyl sulphate (SDS) in water on the thermal conductivity. Moreover, the authors exposed the samples to 50-KGy electron beam irradiation to improve the interaction between graphite and ethylene vinyl acetate (EVA), as host matrix. They reported an increase in thermal conductivity with an increase in filler content due to high conductivity of graphite, regardless of the treatment. However, the thermal conductivity of the irradiated samples was slightly lower than unirradiated samples. This was attributed to the restriction of the polymer chains *via* cross-linking which reduced the vibration of phonons. There are a number of factors which contribute to the overall thermal conductivity of a composite product such as the dispersion of filler, matrix crystallinity and crystal structure, degree of interfacial thermal contact between the components, and scattering of phonons. Thus, these factors may counterbalance each other such that the obtained thermal conductivity does not reflect the percentage of the conductive filler added into the host matrix. For instance, Shen et al. [49] reported that the

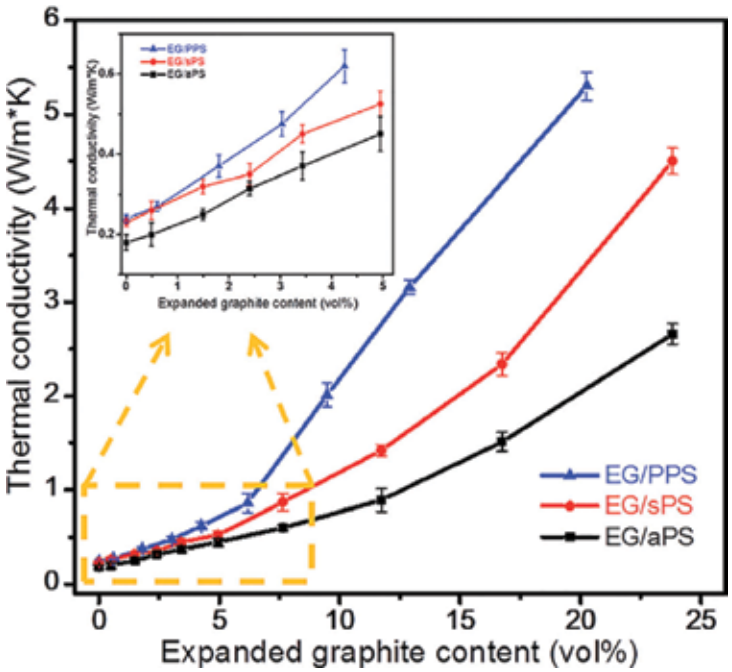

Figure 5. The thermal conductivity of EG/polymer composites as a function of EG volume contents (the error bar is marked). The inset shows the thermal conductivity at a low content [45].

functionalization of the filler can promote dispersion as well as interaction between composite components, but at the expense of thermal conductivity. Hence, it is of significant importance to choose functionalization of the filler while taking into account the lateral size of the filler for high thermal conductive materials. Li et al. [50] also reported that the treatment of the graphite with UV/O_3 did not have an influence on the thermal conductivity of the resulting composite materials. On the contrary, Wang and Tsai [20] reported that functionalized fillers exhibited superior thermal enhancements more than pristine filler. This was attributed to the increase in interfacial thermal conductivity (ITC) between the filler and the host matrix.

5.2. Graphite with other fillers (ternary systems)

There has been an ever-increasing interest in incorporating additional conductive filler into a graphite composite product to overcome the limitation of these materials [22, 31, 53–55]. It can be argued that the maximum thermal conductivity value achieved in graphite composites is 11.24 W m^{-1} K^{-1} (see **Table 1**). It is envisaged that the incorporation of the second filler can further enhance the thermal conductivity of the resulting composite products [31, 53, 56]. Lebedev et al. [53] reported that the inclusion of 1 wt% of carbon nanotubes (CNT) into polylactic acid (PLA)/natural graphite composites improved thermal conductivity by more than 40% of magnitude. The thermal conductivity was increased from 0.93 W m^{-1} K^{-1} for neat polymer to 2.73 W m^{-1} K^{-1} after the addition of 30 wt% graphite, whereas after the inclusion of 1 wt% CNT, the thermal conductivity value reached 3.8 W m^{-1} K^{-1}. This is ascribed to the additional CNT bridges which closely adjoin the surface of graphite. A similar study using HDPE as the polymeric matrix was recent conducted by Che et al. [31]. The authors reported that the thermal conductivity further increased with the addition of CNT compared to that with EG composites. In another study, it was demonstrated that a small content of a second filler, that is, below 2 wt%, has no significant influence on the thermal conductivity when compared to EG composites due to the fillers being wrapped in between the graphite layers [57]. A maximum increase of 38.5% compared to single filler-based composite was achieved at 5 wt% of the second filler. Self-hybrid composites of EG by crushing EG using a high-speed crusher to obtain different particle sizes were recently studied by Kim et al. [54]. The composites were prepared by mixing the crushed EG and raw EG with polycarbonate (PC) using melt extrusion. Hybrid composites (10 wt% crushed EG and raw EG) displayed a higher thermal conductivity by 12 and 20.7% compared to 20 wt% raw EG and crushed EG composites. The thermal conductivity value reached 2.62 W m^{-1} K^{-1} compared to 2.34 and 2.17 W m^{-1} K^{-1} for raw-EG and crushed EG-based composites due to synergistic effect. Various thermal conductive particles rather than carbon-based ones can also be used to enhance the thermal conductivity. Kostagiannakopoulou et al. [58] also reported that the thermal conductivity of the epoxy system increased significantly by increasing the filler content. However, the inclusion of the second filler, that is, multiwalled carbon nanotubes (MWCNTs) did improve the thermal conductivity at a higher graphite content (5, 10 and 15%). The highest enhancement percentage was 48 at 15% of graphite. The highest increase of ~176 was achieved in the case of 15% wt of the filler. A combination of graphite and aluminium nitride (AIN) was reported by Yuan et al. [59] and the thermal conductivity reached a value of

2.77 W m^{-1} K^{-1} that was 14.6 times that of neat polymeric matrix by combining only 50 wt% AIN and 6 wt% graphite.

6. Conclusions and remarks

The design of composites from graphite is inexpensive and available in abundance. This has initiated new ideas in the field of science for the development of a wide range of novel functional materials. Generally, the addition of graphite improved the thermal conductivity of the host polymer matrix irrespective of filler functionalization, the type of polymer and the method of preparation. Various processing techniques such as solvent casting melt blending and pan milling and masterbatch melt mixing have been used for the preparation of graphite composites. The type of mixing method seemed to have had an effect on the resultant thermal conductivity of the graphite/polymer composites. For instance, solution-casted composites had a high thermal conductivity as compared to melt-mixed system. It is understood that during solution casting, the EG particles will have a sufficient surface-to-volume ratio; as a result, they can contact easily and form conducting path networks at low EG contents. However, for melt mixing, one is of the idea that the EG particles' shape is changed during the melt-mixing process, resulting in a decrease of surface-to-volume ratio. Therefore, only a higher content of EG can contact and form conductive paths. Furthermore, the type of polymer had an influence on the thermal conductivity of the polymer/graphite composites, with the crystalline polymers having a higher thermal in the composites. It was further observed that the type of treatment on the graphite or its polymer composites also played a significant role in the improvement or non-improvement of the thermal conductivity of the polymer graphite composites. For example, the silane-treated graphite composites showed a higher thermal conductivity than the non-silane-treated graphite composites. In some cases, the treatment of the graphite with UV/O_3 did not have an influence on thermal conductivity of the resulting composite materials. Lately, the incorporation of the second filler with graphite can further enhance the thermal conductivity of the resulting composite products and widen the application of graphite composites.

Author details

Teboho Clement Mokhena[1], Mokgaotsa Jonas Mochane[1], Jeremia Shale Sefadi[2]*, Setumo Victor Motloung[3] and Dickson Mubera Andala[4]

*Address all correspondence to: jeremia.sefadi@spu.ac.za

1 Department of Chemistry, University of Zululand, KwaDlangezwa, KwaZulu Natal, South Africa

2 Department of Chemistry, Sol Plaatje University, South Africa

3 Sefako Makgatho Health Science University, Medunsa, South Africa

4 Chemistry Department, Multimedia University of Kenya, Nairobi, Kenya

References

[1] Ho BT, Roberts TK, Lucas S. An overview on biodegradation of polystyrene and modified polystyrene: The microbial approach. Critical Reviews in Biotechnology. 2017;**38**(2):308-320. DOI: 10.1080/07388551.2017.1355293

[2] Restrepo-Flórez J-M, Bassi A, Thompson MR. Microbial degradation and deterioration of polyethylene-a review. International Biodeterioration & Biodegradation. 2014;**88**:83-90. DOI: 10.1016/j.ibiod.2013.12.014

[3] Wei R, Zimmermann W. Microbial enzymes for the recycling of recalcitrant petroleum-based plastics: How far are we? Microbial Biotechnology. 2017;**10**(6):1308-1322. DOI: 10.1111/1751-7915.12710

[4] Yasmin A, Luo J-J, Daniel IM. Processing of expanded graphite reinforced polymer nanocomposites. Composites Science and Technology. 2006;**66**(9):1182-1189. DOI: 10.1016/j.compscitech.2005.10.014

[5] Potts JR, Dreyer DR, Bielawski CW, Ruoff RS. Graphene-based polymer nanocomposites. Polymer. 2011;**52**(1):5-25. DOI: 10.1016/j.polymer.2010.11.042

[6] Chen G, Weng W, Wu D, Wu C. PMMA/graphite nanosheets composite and its conducting properties. European Polymer Journal. 2003;**39**(12):2329-2335. DOI: 10.1016/j.eurpolymj.2003.08.005

[7] Krupa I, Chodák I. Physical properties of thermoplastic/graphite composites. European Polymer Journal. 2001;**37**(11):2159-2168. DOI: 10.1016/S0014-3057(01)00115-X

[8] Ezquerra T, Kulescza M, Balta-Calleja F. Electrical transport in polyethylene-graphite composite materials. Synthetic Metals. 1991;**41**(3):915-920. DOI: 10.1016/0379-6779(91)91526-G

[9] Blaszkiewicz M, McLachlan DS, Newnham RE. The volume fraction and temperature dependence of the resistivity in carbon black and graphite polymer composites: An effective media-percolation approach. Polymer Engineering & Science. 1992;**32**(6):421-425. DOI: 10.1002/pen.760320606

[10] Klason C, MCQueen DH, Kubát J. Electrical Properties of Filled Polymers and Some Examples of Their Applications, Macromolecular Symposia. Manhattan, America: Wiley Online Library. 1996;**24**(2):110-117. DOI: 10.1002/masy.1996108012

[11] Nasir A, Kausar A, Younus A. Polymer/graphite nanocomposites: Physical features, fabrication and current relevance. Polymer-Plastics Technology and Engineering. 2015;**54**(7):750-770. DOI: 10.1080/03602559.2014.979503

[12] Dresselhaus MS, Dresselhaus G. Intercalation compounds of graphite. Advances in Physics. 2002;**51**(1):1-186. DOI: 10.1080/00018730110113644

[13] Smith RP, Weller TE, Howard CA, Dean MP, Rahnejat KC, Saxena SS, Ellerby M. Superconductivity in graphite intercalation compounds. Physica C: Superconductivity and Its Applications. 2015;**514**:50-58. DOI: 10.1016/j.physc.2015.02.029

[14] Xu J, Dou Y, Wei Z, Ma J, Deng Y, Li Y, Liu H, Dou S. Recent progress in graphite intercalation compounds for rechargeable metal (Li, Na, K, Al)-ion batteries. Advanced Science. 2017;**4**(10):1-14. DOI: 10.1002/advs.201700146

[15] Olanipekun O, Oyefusi A, Neelgund GM, Oki A. Synthesis and characterization of reduced graphite oxide–polymer composites and their application in adsorption of lead. Spectrochimica Acta Part A: Molecular and Biomolecular Spectroscopy. 2015;**149**:991-996. DOI: 10.1016/j.saa.2015.04.071

[16] Shin HJ, Kim KK, Benayad A, Yoon SM, Park HK, Jung IS, Jin MH, Jeong H-K, Kim JM, Choi J-Y, Lee YH. Efficient reduction of graphite oxide by sodium borohydride and its effect on electrical conductance. Advanced Functional Materials. 2009;**19**(12):1987-1992. DOI: 10.1002/adfm.200900167

[17] Mochane MJ, Motaung TE, Motloung SV. Morphology, flammability, and properties of graphite reinforced polymer composites. Systematic review. Polymer Composites. 2017. DOI: 10.1002/pc.24379

[18] Tsai K-C, Kuan H-C, Chou H-W, Kuan C-F, Chen C-H, Chiang C-L. Preparation of expandable graphite using a hydrothermal method and flame-retardant properties of its halogen-free flame-retardant HDPE composites. Journal of Polymer Research. 2011;**18**(4): 483-488. DOI: 10.1007/s10965-010-9440-2

[19] Shen X, Lin X, Jia J, Wang Z, Li Z, Kim J-K. Tunable thermal conductivities of graphene oxide by functionalization and tensile loading. Carbon. 2014;**80**:235-245. DOI: 10.1016/j.carbon.2014.08.062

[20] Wang T-Y, Tsai J-L. Investigating thermal conductivities of functionalized graphene and graphene/epoxy nanocomposites. Computational Materials Science. 2016;**122**:272-280. DOI: 10.1016/j.commatsci.2016.05.039

[21] Milani MA, González D, Quijada R, Basso NR, Cerrada ML, Azambuja DS, Galland GB. Polypropylene/graphene nanosheet nanocomposites by in situ polymerization: Synthesis, characterization and fundamental properties. Composites Science and Technology. 2013; **84**:1-7. DOI: 10.1016/j.compscitech.2013.05.001

[22] Bai Q-q, Wei X, Yang J-h, Zhang N, Huang T, Wang Y, Zhou Z-w. Dispersion and network formation of graphene platelets in polystyrene composites and the resultant conductive properties. Composites Part A: Applied Science and Manufacturing. 2017;**96**:89-98. DOI: 10.1016/j.compositesa.2017.02.020

[23] Anandhan S, Bandyopadhyay S. Polymer nanocomposites: From synthesis to applications. In: Nanocomposites and Polymers with Analytical Methods. Rijeka: InTech; 2011. DOI: 10.5772/17039

[24] Ding P, Su S, Song N, Tang S, Liu Y, Shi L. Highly thermal conductive composites with polyamide-6 covalently-grafted graphene by an in situ polymerization and thermal reduction process. Carbon. 2014;**66**:576-584. DOI: 10.1016/j.carbon.2013.09.041

[25] Patole AS, Patole SP, Kang H, Yoo J-B, Kim T-H, Ahn J-H. A facile approach to the fabrication of graphene/polystyrene nanocomposite by in situ microemulsion polymerization. Journal of Colloid and Interface Science. 2010;**350**(2):530-537. DOI: 10.1016/j.jcis.2010.01.035

[26] Zheng G, Wu J, Wang W, Pan C. Characterizations of expanded graphite/polymer composites prepared by in situ polymerization. Carbon. 2004;**42**(14):2839-2847. DOI: 10.1016/j.carbon.2004.06.029

[27] Guo H, Li X, Li B, Wang J, Wang S. Thermal conductivity of graphene/poly (vinylidene fluoride) nanocomposite membrane. Materials & Design. 2017;**114**:355-363. DOI: 10.1016/j.matdes.2016.11.010

[28] Zhang W-B, Zhang Z-x, Yang J-H, Huang T, Zhang N, Zheng X-T, Wang Y, Zhou Z-W. Largely enhanced thermal conductivity of poly (vinylidene fluoride)/carbon nanotube composites achieved by adding graphene oxide. Carbon. 2015;**90**:242-254. DOI: 10.1016/j.carbon.2015.04.040

[29] Ding P, Zhang J, Song N, Tang S, Liu Y, Shi L. Anisotropic thermal conductive properties of hot-pressed polystyrene/graphene composites in the through-plane and in-plane directions. Composites Science and Technology. 2015;**109**:25-31. DOI: 10.1016/j.compscitech.2015.01.015

[30] Han Y, Wu Y, Shen M, Huang X, Zhu J, Zhang X. Preparation and properties of polystyrene nanocomposites with graphite oxide and graphene as flame retardants. Journal of Materials Science. 2013;**48**(12):4214-4222. DOI: 10.1007/s10853-013-7234-8

[31] Che J, Wu K, Lin Y, Wang K, Fu Q. Largely improved thermal conductivity of HDPE/expanded graphite/carbon nanotubes ternary composites *via* filler network-network synergy. Composites Part A: Applied Science and Manufacturing. 2017;**99**:32-40. DOI: 10.1016/j.compositesa.2017.04.001

[32] Xiao Y-j, Wang W-y, Chen X-j, Lin T, Zhang Y-t, Yang J-h, Wang Y, Zhou Z-w. Hybrid network structure and thermal conductive properties in poly (vinylidene fluoride) composites based on carbon nanotubes and graphene nanoplatelets. Composites Part A: Applied Science and Manufacturing. 2016;**90**:614-625. DOI: 10.1016/j.compositesa.2016.08.029

[33] George JJ, Bhowmick AK. Ethylene vinyl acetate/expanded graphite nanocomposites by solution intercalation: Preparation, characterization and properties. Journal of Materials Science. 2008;**43**(2):702-708. DOI: 10.1007/s10853-007-2193-6

[34] Huang Z-X, Liu X, Wong S-C, Qu J-p. Electrospinning polyvinylidene fluoride/expanded graphite composite membranes as high efficiency and reusable water harvester. Materials Letters. 2017;**202**:78-81. DOI: 10.1016/j.matlet.2017.05.067

[35] Tu Z, Wang J, Yu C, Xiao H, Jiang T, Yang Y, Shi D, Mai Y-W, Li RKY. A facile approach for preparation of polystyrene/graphene nanocomposites with ultra-low percolation

threshold through an electrostatic assembly process. Composites Science and Technology. 2016;**134**:49-56. DOI: 10.1016/j.compscitech.2016.08.003

[36] Wu H, Lu C, Zhang W, Zhang X. Preparation of low-density polyethylene/low-temperature expandable graphite composites with high thermal conductivity by an in situ expansion melt blending process. Materials & Design (1980-2015). 2013;**52**:621-629. DOI: 10.1016/j.matdes.2013.05.056

[37] Fu Y-X, He Z-X, Mo D-C, Lu S-S. Thermal conductivity enhancement with different fillers for epoxy resin adhesives. Applied Thermal Engineering. 2014;**66**(1-2):493-498. DOI: 10.1016/j.applthermaleng.2014.02.044

[38] Wang Z, Qi R, Wang J, Qi S. Thermal conductivity improvement of epoxy composite filled with expanded graphite. Ceramics International. 2015;**41**(10):13541-13546. DOI: 10.1016/j.ceramint.2015.07.148

[39] Lebedev SM, Gefle OS. Evaluation of electric, morphological and thermal properties of thermally conductive polymer composites. Applied Thermal Engineering. 2015;**91**:875-882. DOI: 10.1016/j.applthermaleng.2015.08.046

[40] Ye CM, Shentu BQ, Weng ZX. Thermal conductivity of high density polyethylene filled with graphite. Journal of Applied Polymer Science. 2006;**101**(6):3806-3810. DOI: 10.1002/app.24044

[41] Mu Q, Feng S. Thermal conductivity of graphite/silicone rubber prepared by solution intercalation. Thermochimica Acta. 2007;**462**(1-2):70-75. DOI: 10.1016/j.tca.2007.06.006

[42] Mochane M, Luyt A. The effect of expanded graphite on the flammability and thermal conductivity properties of phase change material based on PP/wax blends. Polymer Bulletin. 2015;**72**(9):2263-2283. DOI: 10.1007/s00289-015-1401-9

[43] Mochane M, Luyt A. The effect of expanded graphite on the thermal stability, latent heat, and flammability properties of EVA/wax phase change blends. Polymer Engineering & Science. 2015;**55**(6):1255-1262. DOI: 10.1002/pen.24063

[44] Krupa I, Novák I, Chodák I. Electrically and thermally conductive polyethylene/graphite composites and their mechanical properties. Synthetic Metals. 2004;**145**(2-3):245-252. DOI: 10.1016/j.synthmet.2004.05.007

[45] Deng S, Wang J, Zong G, Chen F, Chai S, Fu Q. Effect of chain structure on the thermal conductivity of expanded graphite/polymer composites. RSC Advances. 2016;**6**(12):10185-10191. DOI: 10.1039/c5ra26272k

[46] Hay J, Luck D. The conformation of crystalline poly (phenylene sulphide). Polymer. 2001; **42**(19):8297-8301. DOI: 10.1016/S0032-3861(01)00335-4

[47] Langer L, Billaud D, Issi J-P. Thermal conductivity of stretched and annealed poly (p-phenylene sulfide) films. Solid State Communications. 2003;**126**(6):353-357. DOI: 10.1016/S0038-1098(03)00110-8

[48] Sefadi JS, Luyt AS, Pionteck J, Piana F, Gohs U. Effect of surfactant and electron treatment on the electrical and thermal conductivity as well as thermal and mechanical properties of

ethylene vinyl acetate/expanded graphite composites. Journal of Applied Polymer Science. 2015;**132**(32). DOI: 10.1002/app.42396

[49] Shen X, Wang Z, Wu Y, Liu X, Kim J-K. Effect of functionalization on thermal conductivities of graphene/epoxy composites. Carbon. 2016;**108**:412-422. DOI: 10.1016/j.carbon.2016.07.042

[50] Li J, Sham ML, Kim J-K, Marom G. Morphology and properties of UV/ozone treated graphite nanoplatelet/epoxy nanocomposites. Composites Science and Technology. 2007;**67**(2):296-305. DOI: 10.1016/j.compscitech.2006.08.009

[51] Wu H, Sun X, Zhang W, Zhang X, Lu C. Effect of solid-state shear milling on the physicochemical properties of thermally conductive low-temperature expandable graphite/low-density polyethylene composites. Composites Part A: Applied Science and Manufacturing. 2013;**55**:27-34. DOI: 10.1016/j.compositesa.2013.08.009

[52] Tavman I, Çeçen V, Ozdemir I, Turgut A, Krupa I, Omastova M, Novak I. Preparation and characterization of highly electrically and thermally conductive polymeric nanocomposites. Archives of Materials Science. 2009;**40**(2):84-88

[53] Lebedev S, Gefle O, Amitov E, Berchuk DY, Zhuravlev D. Poly (lactic acid)-based polymer composites with high electric and thermal conductivity and their characterization. Polymer Testing. 2017;**58**:241-248. DOI: 10.1016/j.polymertesting.2016.12.033

[54] Kim HS, Na JH, Jung YC, Kim SY. Synergistic enhancement of thermal conductivity in polymer composites filled with self-hybrid expanded graphite fillers. Journal of Non-Crystalline Solids. 2016;**450**:75-81. DOI: 10.1016/j.jnoncrysol.2016.07.038

[55] Kim HS, Kim JH, Yang C-M, Kim SY. Synergistic enhancement of thermal conductivity in composites filled with expanded graphite and multi-walled carbon nanotube fillers via melt-compounding based on polymerizable low-viscosity oligomer matrix. Journal of Alloys and Compounds. 2017;**690**:274-280. DOI: 10.1016/j.jallcom.2016.08.141

[56] Yu A, Ramesh P, Sun X, Bekyarova E, Itkis ME, Haddon RC. Enhanced thermal conductivity in a hybrid graphite nanoplatelet–carbon nanotube filler for epoxy composites. Advanced Materials. 2008;**20**(24):4740-4744. DOI: 10.1002/adma.200800401

[57] Wu K, Xue Y, Yang W, Chai S, Chen F, Fu Q. Largely enhanced thermal and electrical conductivity via constructing double percolated filler network in polypropylene/expanded graphite-multi-wall carbon nanotubes ternary composites. Composites Science and Technology. 2016;**130**:28-35. DOI: 10.1016/j.compscitech.2016.04.034

[58] Kostagiannakopoulou C, Fiamegkou E, Sotiriadis G, Kostopoulos V. Thermal conductivity of carbon nanoreinforced epoxy composites. Journal of Nanomaterials. 2016;**2016**:1-12. DOI: 10.1155/2016/1847325

[59] Yuan W, Xiao Q, Li L, Xu T. Thermal conductivity of epoxy adhesive enhanced by hybrid graphene oxide/AlN particles. Applied Thermal Engineering. 2016;**106**:1067-1074. DOI: 10.1016/j.applthermaleng.2016.06.089

Edited by Aamir Shahzad

This book is intended to provide a deep understanding on the advanced treatments of thermal properties of materials through experimental, theoretical, and computational techniques. This area of interest is being taught in most universities and institutions at the graduate and postgraduate levels. Moreover, the increasing modern technical and social interest in energy has made the study of thermal properties more significant and exciting in the recent years. This book shares with the international community a sense of global motivation and collaboration on the subject of thermal conductivity and its wide spread applications in modern technologies. This book presents new results from leading laboratories and researchers on topics including materials, thermal insulation, modeling, steady and transient measurements, and thermal expansion. The materials of interest range from nanometers to meters, bringing together ideas and results from across the research field.

Published in London, UK

IntechOpen

ISBN 978-1-83881-689-6